AN INVESTIGATION OF THE ELECTROMAGNETIC BEHAVIOR OF A MICROWAVE PLASMA SOURCE OVER A WIDE RANGE OF PRESSURES AND FLOW RATES

Dissertation for the Degree of Ph. D.
MICHIGAN STATE UNIVERSITY
RAGHUVEER MALLAVARPU
1976





This is to certify that the

thesis entitled

AN INVESTIGATION OF THE ELECTROMAGNETIC BEHAVIOR OF A MICROWAVE PLASMA SOURCE OVER A WIDE RANGE OF PRESSURES AND FLOW RATES

presented by

Raghuveer Mallavarpu

has been accepted towards fulfillment of the requirements for

Ph.D degree in Electrical Engineering

Major professor

Date July 23, 1976

O-7639

,	•		
			`
			
- .			

ABSTRACT

AN INVESTIGATION OF THE ELECTROMAGNETIC BEHAVIOR OF A MICROWAVE PLASMA SOURCE OVER A WIDE RANGE OF PRESSURES AND FLOW RATES

By

Raghuveer Mallavarpu

The electromagnetic behavior of a microwave plasma source is experimentally examined over a wide range of pressures and flow rates.

The plasma source under study is a variable length microwave cavity partially filled with a cold, lossy, isotropic, homogeneous plasma column enclosed in a quartz tube. A small signal linear theory which neglects the flow rate of the gases, but takes into account the pressure dependence of the discharge, is used to qualitatively explain some of the observed experimental results.

Three different types of experiments are conducted on the plasmacavity to demonstrate its use as a versatile microwave plasma source. Two plasma cavities, i.e., Cavity 1 and Cavity 2 operating at incident powers of 30W and 1.2 KW respectively, are used to perform these experiments. Cavity 1 maintains a stable, low pressure, non-flowing plasma. It is suitable for examining the linear and non-linear behavior of the plasma and is amenable to conventional plasma diagnostics. A high pressure (over 1 atm.), flowing plasma can be maintained in Cavity 2 and is suitable for studying the absorbed power characteristics of the plasma source.

In the first of these experiments, unusual EM phenomena of the plasma source are examined using Cavity 1. The presence of two plasma density operating points for a single eigenlength in the $\mathrm{TE}_{111}^{\star}$ mode is experimentally verified. This unusual behavior is explained as resulting from the presence of a backward wave region in the ω - k diagram of the TE_{11}^{\star} mode for non-zero losses. The coupling of EM energy to space charge waves, resulting in the formation of long plasma columns, is experimentally demonstrated and this phenomena is qualitatively explained from the eigenlength vs. $(\omega_{\mathrm{pe}}/\omega)^2$ and $(\nu_{\mathrm{e}}/\omega)$ curves. Short wavelength standing waves of the $\mathrm{TM}_{00\mathrm{p}}$ mode are also excited, as predicted by the theory. Two different types of sidebands are detected in the reflected power spectrum of the $\mathrm{TE}_{111}^{\star}$ mode, and the occurrence of one of these is qualitatively explained as being caused by a fluctuation in the average plasma density as a function of time.

The second phase of the experimentation involves diagnostics on the plasma source. The average electron density, $N_{\rm O}$, and the electron temperature, $T_{\rm e}$, are measured over the pressure range 0.04 - 20 torr using the $TM_{\rm O10}$ frequency shift, double floating probe and disc diagnostic techniques. A knowledge of these parameters is used in calculating the effective electric field $E_{\rm e}$ and the reduced field $E_{\rm e}/p$ in the plasma. The shape of the $N_{\rm O}$, $T_{\rm e}$, $E_{\rm e}$ and $E_{\rm e}/p$ vs. pressure curves follow the same general variation with pressure as those exhibited by other investigators in He gas.

In the third type of experiments, the absorbed power characteristics of the plasma source are examined over a wide range of pressures, flow rates, and incident power levels. The absorbed power characteristics of a flowing plasma are shown to be significantly different from those of a

non-flowing plasma. The absorbed power is shown to increase directly as a function of the flow rate at low flow rates and then reach a saturation at high flow rates. This phenomena is qualitatively explained as being caused by the shielding effect of the high density plasma layer adjacent to the quartz tube.

The variation of the absorbed power as a function of pressure is shown to be more uniform in this plasma source than in other types of plasma sources. No tuning stubs are required to provide an impedance match between the external microwave system and cavity. Plasmas can be sustained in argon gas beyond 1 atm. and the gas flow rate can be varied to as high as 14,000 cc/min. It is possible to couple more than 90% of the incident power to the plasma by optimizing the length, discharge pressure and the gas flow rate of the plasma source.

AN INVESTIGATION OF THE ELECTROMAGNETIC BEHAVIOR OF A MICROWAVE PLASMA SOURCE OVER A WIDE RANGE OF PRESSURES AND FLOW RATES

Ву

Raghuveer Mallavarpu

A DISSERTATION

Submitted to
Michigan State University
in partial fulfillment of the requirements
for the degree of

DOCTOR OF PHILOSOPHY

Department of Electrical Engineering and Systems Science

To my parents

Mr. & Mrs. M. Nageswara Rao

ACKNOWLEDGMENTS

The author wishes to express his sincere gratitude to his major professor, Dr. J. Asmussen, for his able guidance, encouragement and invaluable advice during the course of this investigation. Special thanks are also due to the other members of the guidance committee, Drs. K. M. Chen, D. P. Nyquist, M. Siegel and G. L. Pollack, for their time and interest in this work.

The author also acknowledges the support of Detroit Edison Company,
Kimberly-Clark Corporation, and the Division of Engineering research
at Michigan State University for financing part of this research.

TABLE OF CONTENTS

Chapt	<u>er</u>	age
LIST	OF FIGURES	vi
I	INTRODUCTION	1
II	DERIVATION OF THE MODES ON A CONCENTRIC LOSSY COLD PLASMA ROD INSIDE A CYLINDRICAL METAL WAVEGUIDE	6
	2.1 Introduction	6
	2.2 Basic Equations	7
	2.3 Derivation of the Characteristic Equation	12
	2.4 ω - k Diagrams	22
	2.5 Summary	61
III	POWER ABSORBED IN A PLASMA WAVEGUIDE	63
	3.1 Introduction	63
	Waveguide Modes	66
	Waveguide Modes	70
	3.2.2 TM ₀₁ Mode	73
	3.3 Power Flow and Power Absorbed for TE op Waveguide Modes	75
	3.4 Power Flow and Power Absorbed for TE 11 Waveguide Modes	80
IV	ELECTROMAGNETIC AND SPACE CHARGE MODES OF A COLD LOSSY PLASMA ROD INSIDE A CYLINDRICAL CAVITY	88
	4.1 Introduction	88
	4.1 Introduction	93
	4.2.1 Classification and Description of the Plasma-	73
	Cavity Modes	93
	4.2.2 Rotationally Symmetric Modes, TM ₀₁₁	94
	and TE ₀₁₁ * 4.2.3 Dipole Modes: TE ₁₁₁ and TM ₁₀₁	95
	4.2.3 Dipote riodes: 1E111 and 1rt 101.	-
	4.2.4 Space Charge Modes TM _{OOp}	97
	4.3 Summary	99
1	V EXPERIMENTAL SYSTEMS	100

Chapter		Page
	5.1 Introduction	. 100
	Cavity 1	. 105
	5.2.5 The External Microwave System for Cavity 2	. 110
	5.2.6 Diagnostic Circuits for Cavity 2	. 112
VI	EXPERIMENTAL PERFORMANCE OF THE MICROWAVE PLASMA SOURCE	. 114
	6.1 Introduction	. 114
	6.2 Linear and Non-Linear Operation of Cavity 1	. 116
	6.2.1 Introduction	. 116
	Single Resonant Length	. 117
	6.2.3 Formation of Long Plasma Columns	. 119
	6.2.4 Excitation of Short Wavelength ($\lambda = 1 \text{cm}$) Standing Waves	
	6.2.5 Detection of Sidebands in the Reflected Spectrum	. 129
	6.3 Measurement of N_0 , T_e and Calculation of E_e	
	in the #1 Plasma-Cavity	. 132
	6.3.1 Introduction	. 132
	Electron Densities	. 133
	6.3.1.2 Floating Double Probe Method	
	Conductivity	
	and Te	
	6.3.2 Experimental Results	
	Microwave Plasma Source	
	6.4.1 Introduction	
VII	SUMMARY AND CONCLUSIONS	. 185
	APPENDIX A	. 189
	ITST OF REFERENCES	191

LIST OF FIGURES

Figure		Page
2.1	An infinitely long metal waveguide with three concentric dielectric regions. Region 1: Cold, lossy, homogeneous, isotropic plasma of radius a. Region 2: Quartz tube of outer radius b. Region 3: Air space from ρ = b to ρ = c. Region 4: The outer boundary of the metal waveguide	13
2.2a	$\omega/\omega_{\rm pe}$ vs. $\beta/k_{\rm c}$ for the TM_{00} mode. $f_{\rm pe} = 6.0$ GHz, $\omega_{\rm pe}/\omega_{\rm c} = 3.47$. Waveguide dimensions: $a = 0.3$ cms., $b = 0.3875$ cms., $c = 5.08$ cms	26
2.2b	$\omega/\omega_{\rm pe}$ vs. $\alpha/k_{\rm c}$ for the TM ₀₀ mode. $f_{\rm pe}$ = 6.0 GHz, $\omega_{\rm pe}/\omega_{\rm c}$ = 3.47. Waveguide dimensions: a = 0.3 cms., b = 0.3875 cms., c = 5.08 cms	27
2.3a	$ω/ω$ pe vs. $β/k$ for the TM_{00} mode for $ω/ω$ pe $≤ 0.9$. $f_{pe} = 4.5 \text{ GHz}$, $ω_{pe}/ω_{c} = 2.6$. Waveguide dimensions: $a = 0.3 \text{ cms.}$, $b = 0.3875 \text{ cms.}$, $c = 5.08 \text{ cms.}$	28
2.3b	$ω/ω_{pe}$ vs. $α/k_{c}$ for the TM_{00} mode for $ω/ω_{pe} \le 0.9$. $f_{pe} = 4.5$ GHz, $ω_{pe}/ω_{c} = 2.6$. Waveguide dimensions: a = 0.3 cms., $b = 0.3875$ cms., $c = 5.08$ cms	29
2.4a	ω/ω _{pe} vs. $β/k$ _c for the TM ₀₀ mode for $ω/ω$ _{pe} $≤$ 0.9. f _{pe} = 6.0 GHz, $ω$ _{pe} / $ω$ _c = 3.47. Waveguide dimensions: a = 0.3 cms., b = 0.3875 cms., c = 5.08 cms	30
2.4b	$\omega/\omega_{\rm pe}$ vs. $\alpha/k_{\rm c}$ for the TM mode for $\omega/\omega_{\rm pe} \le 0.9$. $f_{\rm pe} = 6.0$ GHz, $\omega_{\rm pe}/\omega_{\rm c} = 3.47$. Waveguide dimensions: a = 0.3 cms., $b = 0.3875$ cms., $c = 5.08$ cms	31
2.4c	ω/ω _{pe} vs. $β/k$ _c for the TM ₀₀ mode for $ω/ω$ _{pe} < 0.1. f _{pe} = 6.0 GHz, $ω$ _{pe} / $ω$ _c = 3.47. Waveguide dimensions: a = 0.3 cms., b = 0.3875 cms., c = 5.08 cms	32

Figure		Page
2.4d	ω/ω_{pe} vs. α/k_{c} for the TM ₀₀ mode for ω/ω_{pe} < 0.1. f_{pe} = 6.0 GHz, ω_{pe}/ω_{c} = 3.47. Waveguide dimensions: a = 0.3 cms., $b = 0.3875$ cms., $c = 5.08$ cms	33
2.5a	$\omega/\omega_{\rm pe}$ vs. $\beta/k_{\rm c}$ for the TM_{00} mode for $\omega/\omega_{\rm pe} \le 0.9$. $f_{\rm pe}$ = 10.5 GHz, $f_{\rm pe}/f_{\rm c}$ = 6.1. Waveguide dimensions: a = 0.3 cms., b = 0.3875 cms., c = 5.08 cms	34
2.5b	$\omega/\omega_{\rm pe}$ vs. $\alpha/k_{\rm c}$ for the TM ₀₀ mode for $\omega/\omega_{\rm pe} \le 0.9$. $f_{\rm pe} = 10.5$ GHz, $\omega_{\rm pe}/\omega_{\rm c} = 6.1$. Waveguide dimensions: a = 0.3 cms., $b = 0.3875$ cms., $c = 5.08$ cms	35
2.6	Field distribution and charge perturbation for circularly symmetric surface wave on isotropic plasma column. Reproduced from Trivelpiece 12	38
2.7-		30
2.7a	Real part of plasma dielectric constant ε_r vs. ω/ω_{pe} and ν_e/ω_{pe} . ε_r for ε_r	40
2.7b	Imaginary part of plasma dielectric constant ϵ_{i} vs. ω/ω_{pe} and ν_{e}/ω_{pe} . ϵ_{pe} = 6.0 GHz	41
2.8a	ω/ω _{pe} vs. $β/k$ _c for the TM ₀₁ mode. f _{pe} = 10.5 GHz, $ω$ _{pe} / $ω$ _c = 6.1. Waveguide dimensions: a = 0.3 cms., b = 0.3875 cms., c = 5.08 cms	44
2.8b	$\omega/\omega_{\rm pe}$ vs. $\alpha/k_{\rm c}$ for the TM ₀₁ mode. $f_{\rm pe}$ = 10.5 GHz, $\omega_{\rm pe}/\omega_{\rm c}$ = 6.08. Waveguide dimensions: a = 0.3 cms., b = 0.3875 cms., c = 5.08 cms	45
2.8c	$ω/ω_{pe}$ vs. $β/k_{c}$ for the TM_{01} mode for $ω/ω_{pe} < 0.24$. $f_{pe} = 10.5$ GHz, $ω_{pe}/ω_{c} = 6.1$. Waveguide dimensions: a = 0.3 cms., $b = 0.3875$ cms., $c = 5.08$ cms	46
2.8d	$ω/ω$ pe vs. $α/k$ for the TM_{01} mode for $ω/ω$ pe $≤ 0.20$. $f_{pe} = 10.5$ GHz, $ω_{pe}/ω_{c} = 6.08$. Waveguide dimensions: a = 0.3 cms., $b = 0.3875$ cms., $c = 5.08$ cms	47
2.8e	Real part of plasma dielectric constant ε_r vs. ω/ω_{pe} and v_e/ω_{pe} . $f_{pe} = 10.5$ GHz	48
2.8f	Imaginary part of plasma dielectric constant ε_i vs. ω/ω_{pe} and v_e/ω_{pe} . $f_{pe} = 10.5 \text{ GHz.} \dots$	49

Figure		Page
2.9a	ω/ω _{pe} vs. $β/k$ _c for the TM ₀₁ mode. f _{pe} = 20 GHz, ω _{pe} / $ω$ _c = 11.6. Waveguide dimensions: a = 0.3 cms., b = 0.3875 cms., c = 5.08 cms	50
2.9ь	$\omega/\omega_{\rm pe}$ vs. $\alpha/k_{\rm c}$ for the TM ₀₁ mode. $f_{\rm pe}$ = 20 GHz, $\omega_{\rm pe}/\omega_{\rm c}$ = 11.6. Waveguide dimensions: a = 0.3 cms., b = 0.3875 cms., c = 5.08 cms	51
2.10a	$ω/ω$ _{pe} vs. $β/k$ _c for TM_{10}^* and TE_{11}^* modes. $f_{pe} = 5.3$ GHz, $ω$ _{pe} / $ω$ _c = 3.07. Waveguide dimensions: $a = 0.3$ cms., $b = 0.3875$ cms., $c = 5.08$ cms	54
2.10ъ	$ω/ω$ vs. $α/k$ for TM_{10}^* and TE_{11}^* modes. $f_{pe} = 5.3$ GHz, $ω_{pe}/ω_{c} = 3.07$. Waveguide dimensions: $a = 0.3$ cms., $b = 0.3875$ cms., $c = 5.08$ cms	55
2.10c	$ω/ω$ _{pe} vs. $β/k$ _c for the TE_{11}^* mode for $ω/ω$ _{pe} < 0.35 and $ν_e/ω$ _{pe} = 0.2. f _{pe} = 5.3 GHz. $ω$ _{pe} / $ω$ _c = 3.07. Waveguide dimensions: a = 0.3 cms., b = 0.387 cms., c = 5.08 cms.	56
2.10d	$ω/ω$ pe vs. $α/k$ for the TE_{11}^* mode for $ω/ω$ pe < 0.35 and $ν/ω$ = 0.2. $f_{pe} = 5.3$ GHz, $ω$ $ω$ $ω$ = 3.07. Waveguide dimensions: $a = 0.3$ cms., $b = 0.3875$ cms., $c = 5.08$ cms.	57
2.10e	Real part of plasma dielectric constant ε_r vs. ω/ω_{pe} and v_e/ω_{pe} . $f_{pe} = 5.3$ GHz	59
2.10f	Imaginary part of plasma dielectric constant ε_i vs. ω/ω_{pe} and v_e/ω_{pe} . $f_{pe} = 5.3$ GHz	60
3.1	Arbitrarily-shaped metallic waveguide of unit length S_1 and S_2 are waveguide cross sections at $Z = 0$ and $Z = 1$	64
3.2	Normalized absorbed power $P_a/ A ^2$ vs. ω/ω_{pe} and v_e/ω_{pe} for the TM_{00} mode. Waveguide dimensions:	
3.3	a = 0.3 cms., b = 0.3875 cms., c = 5.08 cms. $f_{pe} = 6$ GHz. Normalized absorbed power in the resistor $P_a/ I ^2$ vs. $\omega/2\pi$ for a parallel RLC circuit driven by an ideal current source. L = 10uH. C = 10 pf	71 72
		, 4

Figure		Page
3.4	Normalized absorbed power $P_a/ A ^2$ vs. ω/ω_{pe} and v_e/ω_{pe} for the TM_{01} mode. Waveguide dimensions: $a = 0.3$ cms., $b = 0.3875$ cms., $c = 5.08$ cms., $f_{pe} = 10.5$ GHz	74
3.5	Normalized absorbed power $P_a/ A ^2$ vs. ω/ω_{pe} and v_e/ω_{pe} for the TE_{01} mode. $f_{pe} = 10.5$ GHz. Wave-	
	guide dimensions: a = 0.3 cms., b = 0.3875 cms., c = 5.08 cms	79
3.6	Normalized absorbed power $P_a/ A ^2$ vs. ω/ω_{pe} and v_e/ω_{pe} for the TE_{11}^* mode. $f_{pe} = 5.3$ GHz. Waveguide dimensions: $a = 0.3$ cms., $b = 0.3875$ cms., $c = 5.08$ cms	86
4.1a	Resonant length L_s vs. the plasma density $(\omega_{pe}/\omega)^2$ for the modes TM_{00p} , TM_{011} , TM_{101}^* , and TE_{111}^* . Operating frequency fixed at $\omega/2\pi = 3.03$ GHz. Waveguide dimensions: $a = 0.3$ cms., $b = 0.3875$ cms., $c = 5.08$ cms	90
4.1b	Resonant length L_s vs. $(\omega_{pe}/\omega)^2$ for the cold plasma modes, TM_{00p} and TM_{10p}^* . Operating frequency $\omega/2\pi = 3.03$ GHz. Waveguide dimensions: $a = 0.3$ cms., $b = 0.3875$ cms., $c = 5.08$ cms	91
4.2	Resonant length vs. plasma density $(\omega_{\rm pe}/\omega)^2$ and $\nu_{\rm e}/\omega$ for a cavity of radius 10.146 cm., plasma radius of 1.248 cm., and an operating frequency of 2.45 GHz	92
5.1	Cross section of the cylindrical cavity, 30 watt microwave source, and plasma diagnostic circuits	101
5.2	Resonant frequency versus cavity size. Waveguide dimensions: c = 5.08 cms	102
5.3	$ω/2π$ vs. f and $ν_e/ω$ for the TM_{010} mode. Waveguide dimensions: $a = 0.3$ cms., $b = 0.3875$ cms., $c = 5.08$ cms	106
5.4	The #2 plasma-cavity system. (a) Cross section of plasma cavity (b) Isometric drawing	108

Figure		Page
5.5	The external microwave system for the #2 plasma-cavity	111
6.1	Comparison of the theoretical and experimental curves of the cavity resonant length L vs.	
	$(\omega_{\rm pe}/\omega)^2$ for the TE $^*_{111}$ mode. Waveguide dimen-	
•	sions: a = 0.3 cms., b = 0.3875 cms., c = 5.08 cms	118
6.2	Plasma being ejected out of cavity as a result of efficient coupling to the space charge wave through an electromagnetic excitation of the cavity (TE ₁₁₁ or TM _{O11} mode)	120
6.3	Absorbed power vs. the discharge pressure for the TM_{011} mode, with the incident power P_1 held constant.	
	The cavity resonant length L _s = 8.6 cms	122
6.4	Absorbed power vs. the discharge pressure for the ${\rm TM}_{011}$ mode, with the incident power P held constant.	
	The cavity resonant length $L_s = 8.1 \text{ cms.} \dots \dots$	123
6.5	Absorbed power vs. the discharge pressure for the TE_{111}^* mode, with the incident power P_i held constant.	
	The cavity resonant length $L_s = 5.92$ cms	124
6.6	Excitation of 8 half-wave resonances of the TM 00p	
	mode for an off resonance electromagnetic excitation of the cavity (TE_{111}^* mode)	127
6.7	Excitation of 3 half-wave resonances of the TM 00p	
	mode for a large off resonance electromagnetic excitation of the cavity (TE* mode)	128
6.8a	Sidebands detected on the spectrum analyzer in the TE_{111}^{\star} mode with the operating frequency $\omega/2\pi$ = 3.03 GHz.	
	Cavity resonant length $L_s = 6$ cms. Discharge pressure=	
	12 mtorr. Power absorbed = 14.2 watts. Plasma electron density $(\omega_{\rm pe}/\omega)^2$ fluctuated between 2.04 - 3.16. Fre-	
	quency scale: 0.2 MHz/cm	130

Figure		Page
6.8b	Sidebands detected on the spectrum analyzer in the ${{ ext{TE}}^{m{\star}}_{111}}^{m{\star}}$ mode with the operating frequency	
	$\omega/2\pi = 3.03$ GHz. Cavity resonant length L _s =	
	6.02 cms. Discharge pressure = 12 mtorr. Power absorbed = 14.1 watts. Plasma electron density $(\omega_{pe}/\omega)^2$ = 2.95. Frequency scale:	
•	2.0 MHz/cm	131
6.9	The effective collision frequency in A as a function of velocity and frequency. Reproduced from Whitmer and Herman ⁵⁰	140
6.10a	Normalized electron density $(\omega_{pe}/\omega)^2$ vs. dis-	
	charge pressure P_0 and the absorbed power P_a	
	using the TM ₀₁₀ frequency shift method	142
6.10ь	Effective electric field E vs. discharge pressure	
	P_{o} and absorbed power P_{a} , from the TM_{010} frequency	
	shift method	143
6.10c	Reduced field E_e/P_o vs. discharge pressure P_o and	
	absorbed power P_a , from the TM_{010} frequency shift	
	method	144
6.11a	Typical floating double probe I-V characteristics at a discharge pressure of 86 mtorr. Absorbed power P = 20 W	146
6.11b	Typical floating double probe I-V characteristics	
	for pressures above 1 torr. Absorbed power P = 20 W	147
6.11c	Typical floating double probe I-V characteristics at a discharge pressure of 140 mtorr and different	
	absorbed power levels	148
6.11d	Typical floating double probe I-V characteristics at a discharge pressure of 730 mtorr and different absorbed power levels	149
6.12a	Normalized electron density $(\omega_{pe}/\omega)^2$ vs. discharge	
	pressure P and absorbed power P, from the floating	
	double probe measurements	151

Figure		Page
6.12b	Electron temperature T_e vs. discharge pressure P_o and absorbed power P_a , from the floating double probe measurements	152
6.12c	Effective electric field E_e vs. discharge P_o and absorbed power P_a , from the floating double probe measurements	153
6.12d	Reduced field E_e/P_o vs. discharge pressure P_o and absorbed power P_a , from floating double probe measurements	154
6.13a	Normalized electron density $(\omega_{pe}/\omega)^2$ vs. discharge pressure P _o and absorbed power P _a , from measurements using discs	156
6.13b	Electron temperature T_e vs. discharge pressure P_o and absorbed power P_a , from measurements using discs	157
6.13c	Effective electric field $E_{\rm e}$ vs. discharge pressure $P_{\rm o}$ and absorbed power $P_{\rm a}$, from measurements using discs	158
6.13d	Reduced field E_e/P_o vs. discharge pressure P_o and absorbed power P_a , from measurements using discs	159
6.14a	Normalized electron density $(\omega_{pe}/\omega)^2$ vs. discharge pressure P_o and absorbed power P_a over the pressure range 40 mtorr - 20 torr, from three different diagnostic methods	160
6.14b	Electron temperature T _e vs. discharge pressure P _o and absorbed P _a over the pressure range 0.1 - 20 torr, from two different diagnostic methods	161
6.14c	Reduced field E_e/P_o vs. discharge pressure P_o and absorbed power P_a over the pressure range 0.04 - 20 torr, from three different diagnostic methods	162
6.15	Absorbed power P_a vs. eigenlength L_s and different discharge pressures P_o , for the TE_{011} mode plasma of Cavity 2. Flow rate = 1000 cc/min., Incident power P_i = 1.2 KW	166

Figure		Page
6.16	Power absorbed P_a vs. eigenlength L_s , and flow rate (cc/min) for the TE_{011} mode plasma of Cavity 2. Discharge pressure, P_o = 10 torr. Incident power P_i = 1.2 KW	169
6.17	TE ₀₁₁ resonant length vs. plasma density $(\omega_{pe}/\omega)^2$ and collision frequency (ν_e/ω) for Cavity 2. $\omega/2\pi = 2.45$ GHz	170
6.18	Power absorbed P_a vs. discharge pressure P_o and incident power P_i for the TE_{112}^* mode plasma of Cavity 2. Flow rate = 147 cc/min. Gas: argon	173
6.19	Power absorbed P_a vs. discharge pressure P_o and incident power P_i for the TE_{112}^* mode plasma of Cavity 2. Flow rate = 520 cc/min. Gas: argon	174
6.20	Power absorbed P_a vs. discharge pressure P_o and incident power P_i for the TE_{112}^* mode plasma of Cavity 2. Flow rate = 955 cc/min. Gas: argon	175
6.21	Power absorbed P_a vs. discharge pressure P_o and incident power P_i for the TE_{112}^* mode plasma of Cavity 2. Flow rate = 1480 cc/min. Gas: argon	176
6.22	Power absorbed P_a vs. discharge pressure P_o and incident power P_i for the TE_{112}^* mode plasma of Cavity 2. Flow rate = 2500 cc/min. Gas: argon	177
6.23	Power absorbed P vs. discharge pressure P and flow rate for the TE_{112}^* mode plasma of Cavity 2. Incident power P = 966 W. Gas: argon	178
6.24	Power absorbed P vs. discharge pressure P and flow rate for the TE mode plasma of Cavity 2. Incident power P = 759 W. Gas: argon	179
6.25	Percentage peak-absorbed power vs. flow rate for the TE* 112 plasma of Cavity 2. Incident power P; = 966 W	180

Figure		Page
6.26	Plot of absorbed microwave power vs. pressure for argon plasmas at various incident powers. Reproduced from Bosisio et.al. ⁵⁴	182

CHAPTER I

INTRODUCTION

Microwave discharges have been investigated for over 25 years 1 and applications have been suggested in the areas of plasma chemistry², laser discharges³, and RF heating in thermonuclear fusion research⁴. Despite this interest, experimentally versatile steady-state microwave discharges at pressures greater than 1 torr have not been available until recently⁵. In most investigations the microwave plasma formation is restricted by the metal coupling structure. For example, certain coupling structures produce plasmas that are small in comparison to the electromagnetic wavelength^{6,7}, resulting in maximum plasma volumes of only about 50 cm 3. Also, many experiments can only operate over restricted pressure ranges^{7,8}, and are able to achieve densities which are only slightly higher than the critical density N_c , corresponding to plasma resonance at the exciting frequency 8,9. Furthermore, most plasma coupling structures are complex and difficult to analyze electromagnetically 6,7,8. This electromagnetic complexity makes direct measurement of the plasma characteristics, such as electron density, temperature, etc., difficult without disturbing the plasma and electromagnetic fields. Thus, from an experimental and practical point of view, there is a need for an RF plasma source which is able to provide a high variable plasma density, which is capable of maintaining a microwave discharge over large changes in background pressure and gas flow rate, which is able to be analyzed electromagnetically, and which is amenable to diagnostic

measurement techniques for the quantification of microwave plasma parameters. In addition, many industrial applications will require a plasma source having a volume much larger than $50~\rm cm^3$.

Recently, a large-volume microwave plasma source was developed⁵. By means of a slow, traveling-wave structure, microwave energy of up to 2.5 kW was coupled to a 19 mm outside diameter quartz tube obtaining plasmas exceeding 2000 cm³. This microwave plasma system was shown to possess a good match at many different incident power levels without external tuning systems for pressures of 1 torr up to 1 atm. in argon gas. Thus, this system appears to overcome the tuning problems of previous microwave plasma sources while producing a large-volume plasma over a wide pressure range.

In this thesis the experimental properties of still another microwave plasma source is described 10. Here the plasma is part of a cylindrical waveguiding system and either fast or slow waves are able to sustain a plasma. The waveguiding system is terminated at one end by a fixed short and at the other by a variable short, consequently, forming a plasma cavity. Microwave power is then coupled to the resonances of the plasma cavity, imposing the requirement for a physical length tuning mechanism. However, this tuning is a fast, simple adjustment that seems justified in view of the higher electric field (an important parameter in many plasma chemistry experiments) obtained at the cavity resonances.

A linear, lossy, cold plasma theory is used in modeling the microwave plasma source and is described in Chapters II-IV. Attempts are made in Chapter VI to qualitatively explain the experimental results by comparing with this theory.

The basic equations which will be used to mathematically describe a cold, lossy, homogeneous, isotropic plasma are introduced in Chapter II. From this set of equations a dispersion relation for the propagation of electromagnetic and cold plasma modes is derived for a quartz-enclosed plasma concentrically located in an infinite metal waveguide. $\omega-\beta \text{ and }\omega-\alpha \text{ diagrams are explained for the different modes, with the electron density and the electron-neutral collision frequency as the variable plasma parameters. Regions of forward and backward waves are identified on the <math display="inline">\omega-k$ diagrams.

The Poynting vector is evaluated in Chapter III for the lossy plasma modes that were discussed in Chapter II. From this Poynting vector a normalized power absorbed per unit waveguide length is derived for the modes. The power absorbed is studied as a function of the frequency with the electron density and the electron collision frequency as the variable plasma parameters. Volume and surface resonances of the plasma are identified and the power absorbed by the plasma at the resonant frequencies is discussed.

The characteristic equation derived in Chapter II is used in Chapter IV to obtain an eigenlength vs. plasma density and electron collision frequency plot for the various modes of a cylindrical plasma-cavity. The behavior of these modes at low and high values of the plasma densities and for a range of collision frequencies is discussed. Slow-wave and backward-wave resonances are identified on the eigenlength plot. The region of intersection of EM resonances with slow wave resonances is also discussed.

The experimental apparatus is presented in Chapter V. The design of two different cavities used in performing experimental work from

10 mtorr to 500 torr is discussed. The driving microwave circuits and the probe and microwave diagnostic circuits are explained.

The experimental results are discussed in Chapter VI. The actual experiments are done in two different cavities. Experiments are carried out in the pressure range 10 mtorr to 20 torr and incident power levels up to 30 W with Cavity 1. In experiments on Cavity 2, the pressure range is 1 torr - 500 torr, flow rate is varied from 0-2500 cc/min and incident power levels up to 1.3 KW are used. Eigenlength curves of the TE 111 mode are verified and the coupling of EM and plasma modes is demonstrated. Non-linear effects in the form of sidebands in the reflected spectrum of the TE 111 mode are observed. The reason for the occurrence of one of these sidebands is explained.

For many experiments involving applications of a gas discharge, it is important to evaluate an effective electric field in the plasma. The determination of this quantity requires a knowledge of the electron density and the collisional frequency in the plasma. These plasma parameters are measured as a function of pressure in the range 100 mtorr to 20 torr using microwave, probe and disc diagnostic techniques. The limitations of these methods and the accuracy of the results is also presented.

Experiments on a flowing gas are conducted on Cavity 2, which is capable of handling incident powers of up to 1.3 KW. Power absorbed vs. cavity eigenlength are obtained for the TE_{011} mode with flow rate and the gas pressure as the variable parameters. Another set of experiments are conducted with a $\mathrm{TE}_{112}^{\star}$ mode where the absorbed power is measured as a function of the gas pressure with the incident power and the gas flow rate as the externally variable parameters. All these

experiments show that the absorbed power characteristics of a flowing plasma differ significantly from those of a non-flowing plasma.

Chapter VII summarizes the work presented in the thesis and suggests further investigations where required.

CHAPTER II

DERIVATION OF THE MODES ON A CONCENTRIC LOSSY COLD PLASMA ROD INSIDE A CYLINDRICAL METAL WAVEGUIDE

2.1 Introduction

The general problem of propagating waves in a plasma waveguide has been examined by several workers. The problem can be divided into two specific cases which depend on the exact plasma volume occupying the waveguide:

- 1) A plasma totally filling the waveguide, and
- 2) A plasma partially filling the waveguide.

Allis, Buschsbaum and Bers¹¹ obtained the ω - k diagram for the various propagating modes in a lossy, cold plasma completely filling a circular waveguide. Only EM waves can propagate in such a plasma-waveguide system. Surface waves are not present because they require charge accumulation on the plasma surface.

Trivelpiece ¹² and Gould made a quasistatic analysis to show that surface wave propagation is possible in a circular waveguide partially filled by a concentric, <u>cold lossless</u> plasma rod. Agdur and Eneander ¹³ solved the complete electromagnetic problem by deriving the characteristic equation for the waveguide modes and solved for the cavity resonances for several important resonant modes; i.e., TE₁₁₁, TM₀₁₀, etc. Shohet ¹⁴ extended their results to include electron-neutral collisional losses and solved for cavity resonant frequency as a function of electron density and collisional losses.

Wave propagation along warm plasma columns in free space and partially filling circular waveguides has been examined by Diament, Granatstein and Schlesinger 15, Vandenplas 16 and Fredericks 17. They have shown that the cold plasma theory is not valid in and beyond the region where the phase velocity equals the electron thermal velocity and that a warm plasma description is more accurate. They also describe warm plasma modes 15, Tonks-Dattner or temperature resonances, and demonstrate experimentally the coupling of EM modes to these resonances.

In this chapter, solutions to the characteristic equation of a lossy plasma waveguide are studied in greater detail than in previous investigations. For example, the dispersion curves for a number of propagating modes in such a plasma-waveguide are obtained for both the lossless and the lossy cases. These curves will show that in addition to forward EM and cold-plasma waves, it is also possible to have frequency regions where backward waves propagate. Using this complete electromagnetic description, the power absorbed per unit length has also been calculated and is discussed in detail in Chapter III.

2.2 Basic Equations

Consider a cold, homogeneous, isotropic, lossy plasma of infinite extent. An electromagnetic analysis of such a plasma is well known and can be carried out by treating it as a material with a complex dielectric constant. The latter is easily derived from a consideration of the cold plasma fluid equations and the associated Maxwell's equations that describe the electromagnetic fields in the plasma.

A set of basic fluid equations obtained from the first two velocity moments of the Boltzmann equation for both electrons and ions are shown below. In these equations the pressure term is neglected since $T_e = T_i = 0$, in the cold plasma approximation.

$$\frac{\partial N_e}{\partial t} + \nabla \cdot (N_e \vec{V}_e) = 0$$
 2.1

$$m_{e} \frac{\partial \vec{v}_{e}}{\partial t} + m_{e} (\vec{v}_{e} \cdot \nabla) \vec{v}_{e} = -e(\vec{E} + \vec{v}_{e} \times \vec{B}) - (v_{e} \vec{v}_{e}) m_{e}$$
2.2

$$\frac{\partial N_i}{\partial t} + \nabla \cdot (N_i \vec{V}_i) = 0$$
 2.3

$$m_{i} \frac{\partial \vec{v}_{i}}{\partial t} + m_{i} (\vec{v}_{i}.\nabla) \vec{v}_{i} = e (\vec{E} + \vec{v}_{i} \times \vec{B}) - (v_{i}\vec{v}_{i}) m_{i}$$
2.4

where

 N_{ρ} = electron number density

N₁ = ion number density

 \vec{V}_{e} = macroscopic electron velocity

 \vec{V}_i = macroscopic ion velocity

m_e = electron mass

m, = ion mass

È = electric field

 \vec{B} = magnetic field

e = electronic charge

 $v_{\rm e}$ = effective electron-neutral particle collision frequency

 v_4 = effective ion-neutral particle collision frequency.

Equations 2.1 to 2.4 express the conservation of mass for electrons, conservation of momentum for electrons, conservation of mass for ions and conservation of momentum for ions, respectively. The electron-neutral particle collisional losses within the plasma are accounted for by a non-zero value of ν_e . The associated Maxwell's equations in such a plasma are:

$$\nabla \times \vec{E} = -\mu_0 \frac{\partial \vec{H}}{\partial t}$$
 2.5

$$\nabla. \stackrel{\rightarrow}{E} = e \frac{(N_i - N_e)}{\epsilon_o}$$

$$\nabla \mathbf{x} \dot{\mathbf{H}} = \mathbf{e} (\mathbf{N}_{i} \dot{\mathbf{V}}_{i} - \mathbf{N}_{e} \dot{\mathbf{V}}_{e}) + \varepsilon_{o} \frac{\partial \dot{\mathbf{E}}}{\partial \mathbf{t}}$$
2.7

$$\nabla \cdot \vec{H} = 0$$
.

In the above equations the constitutive relations are given by,

$$\vec{D} = \varepsilon_0 \vec{E}$$

$$\vec{B} = \mu_0 \vec{H} . \qquad 2.10$$

These relations are valid under the assumption that the electrons and ions are free and are present in a free space medium, i.e., there is no bound charge present as in a dielectric.

Assuming a time-variation of the form $e^{j\omega t}$ and expressing the variable quantities as the sum of a dc term and a perturbed ac term, the variables become:

$$N_e = N_{oe} + n_e e^{j\omega t}$$
 2.11

$$N_{i} = N_{oi} + n_{i} e^{j\omega t}$$
 2.12

$$\vec{V}_e = \vec{V}_e e^{j\omega t}$$
 assuming no dc electron drift 2.13

$$\vec{V}_i = \vec{V}_i e^{j\omega t}$$
 assuming no dc ion drift 2.14

$$\vec{E} = \vec{E} e^{j\omega t}$$
 assuming no static electric field 2.15

$$\frac{1}{H} = \frac{1}{H} e^{j\omega t}$$
 assuming no static magnetic field. 2.16

 N_{oe} and N_{oi} are the unperturbed electron and ion particle densities respectively, and they are equal for both electrons and ions in a homogeneous plasma, i.e., $N_{oe} = N_{oi} = N_{oi}$.

Using Equations 2.11 through 2.16, the first velocity moment equation for electrons as given by Equation 2.2 can now be reduced to,

$$j\omega \vec{V}_{e}m_{e} = q_{e}\vec{E} - v_{e}m_{e}\vec{V}_{e}. \qquad 2.17$$

In Equation 2.17, the $(\vec{V}_e \times \vec{B})$ term and the non-linear term $(\vec{V}_e \cdot \nabla) \vec{V}_e$ have been neglected. These approximations are justified provided we study those wave solutions for which $V_e << V_{\phi}$, where V_{ϕ} is the phase velocity of the wave. The $\vec{V}_e \times \vec{B}$ term can be simplified by using Maxwell's curl equation for \vec{E} , to become:

$$\frac{\vec{v}_e}{\vec{v}_\phi} \times \hat{n} \times \vec{E}$$

where \hat{n} is a unit vector in the direction of propagation.

The non-linear term $(\vec{V}_e.\nabla)\vec{V}_e$ upon simplification, becomes:

$$j\omega^{m}_{e} \frac{(\vec{v}_{e} \cdot \hat{n})\vec{v}_{e}}{v_{\phi}}$$
.

Under the assumption that $V_e << V_{\phi}$, (perturbation theory), these terms are very small compared to other terms in Equation 2.2: i.e.,

and the omission of these terms from Equation 2.17 is justified. Cold plasma theory, however, fails if $V_{\phi} \sim V_{th}$ where V_{th} is the electron thermal velocity. In that case, a warm plasma description is more accurate.

From Equation 2.17, the macroscopic electron velocity is easily obtained as,

$$\vec{v}_{e} = -\left(\frac{e \vec{E}}{m_{e}(j\omega + v_{e})}\right). \qquad 2.18$$

The high frequency plasma phenomena are of interest in this study. Thus, under the high frequency approximation, the plasma ion frequency ω_{pi} is very small compared to the operating frequency ω . The motion of the ions can be considered to be negligible and, therefore, the contribution to the current density, J, comes entirely from the electron motion. Thus,

$$\vec{J} = -N_0 e \vec{V}_e. \qquad 2.19$$

Using Equation 2.18 in Equation 2.19,

$$\vec{J} = \frac{N_0 e^{2\vec{E}}}{m_0 (j\omega + v_0)} \qquad 2.20$$

Since also $\vec{J} = \vec{\sigma E}$, an equivalent plasma conductivity $\vec{\sigma}$ can be defined as,

$$\sigma = \frac{N_0 e^2 (v_e - j\omega)}{m_0 (v_e^2 + \omega^2)}.$$
 2.21

Substituting for σ from Equation 2.21, into Maxwell's curl equation for the magnetic field in the plasma, we have

$$\nabla \times \vec{H} = j\omega \varepsilon_{o} \vec{E} + \vec{J}$$

$$= j\omega \varepsilon_{o} \vec{E} + \sigma \vec{E} = j\omega \varepsilon_{o} \left[1 + \frac{\sigma}{j\omega \varepsilon_{o}} \right] \vec{E}$$
2.22

or
$$\nabla \times \hat{H} = j\omega \varepsilon_0 \left[1 - \frac{\omega_{pe}^2}{v_e^2 + \omega^2} - j \frac{v_e}{\omega} \frac{\omega_{pe}^2}{v_e^2 + \omega^2} \right] \hat{E}$$
 2.23

where $\omega_{pe} = \sqrt{\frac{N_{o}e^{2}}{m_{e}\epsilon_{o}}}$, is the plasma electron frequency.

Equation 2.23 is of the form $\nabla \times \hat{H} = j\omega \in \hat{E}$. Thus, we can define an equivalent dielectric constant for the plasma as,

$$\varepsilon = \varepsilon_{0} \left\{ 1 - \frac{\omega_{p_{e}}^{2}}{v_{e}^{2} + \omega^{2}} \right\} - j \frac{v_{e}}{\omega} \frac{\omega_{p_{e}}^{2}}{v_{e}^{2} + \omega^{2}}$$

$$= \varepsilon_{0} \left(\varepsilon_{r} + j \varepsilon_{j} \right)$$
2.24

where

$$\varepsilon_{\mathbf{r}} = 1 - \frac{\omega_{\mathbf{pe}}^2}{(v_{\mathbf{e}}^2 + \omega^2)}$$
 and $\varepsilon_{\mathbf{i}} = -\frac{v_{\mathbf{e}}}{\omega} \frac{\omega_{\mathbf{pe}}^2}{(v_{\mathbf{e}}^2 + \omega^2)}$.

For a lossless plasma, v_e = 0 and ε is purely real.

2.3 Derivation of the Characteristic Equation

We next consider an infinite metal waveguide of inner radius c, concentric with a homogeneous, isotropic lossy plasma rod of radius a, enclosed in a thin quartz tube of radius b. A generalized characteristic equation, dependent on the plasma parameters $\boldsymbol{\omega}_{\text{pe}}$ and $\boldsymbol{\nu}_{\text{e}}$ and describing the eigenmodes of such a waveguide, will be derived here. The effect of the finite thickness of the quartz tube will be included in this derivation.

Since the plasma is assumed homogeneous, isotropic and lossy, Maxwell's Equation 2.5, 2.6, 2.8, and 2.23 describe the electromagnetic behavior within the plasma rod. The problem then reduces to a boundary value problem of three concentric dielectric regions in a metal waveguide as shown in Figure 2.1. Region 1 is the homogeneous, isotropic, lossy plasma; region 2 is the quartz dielectric that encloses the plasma; and region 3 is free space. The theory for such a problem is well known 18. The fields in the three regions are expressed in terms of electric and magnetic scalar potential functions, ψ^{e1} , ψ^{e2} , ψ^{e3} , ψ^{m1} , ψ^{m2} and ψ^{m3} . A

-			

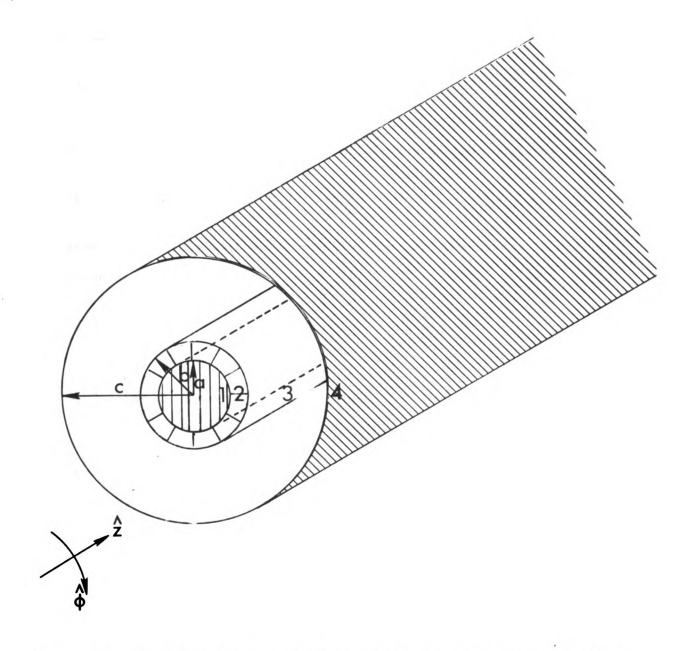


Figure 2.1. An infinitely long metal waveguide with three concentric dielectric regions. Region 1: Cold, lossy, homogeneous, isotropic plasma of radius a. Region 2: Quartz tube of outer radius b. Region 3: Air space from ρ = b to ρ = c. Region 4: The outer boundary of the metal waveguide.

scalar Helmholtz equation in cylindrical coordinates is formulated for each of the potential functions in the three regions. These equations are solved subject to boundary conditions on the perfectly conducting boundary r = c, at the free space-quartz interface r = b and at the quartz-plasma interface, r = a. Expressed in terms of a general ψ , the scalar Helmholtz equation is,

$$\frac{1}{\rho} \frac{\partial}{\partial \rho} \left(\rho \frac{\partial \psi}{\partial \rho} \right) + \frac{1}{\rho^2} \frac{\partial^2 \psi}{\partial \phi^2} + \frac{\partial^2 \psi}{\partial z^2} + k^2 \psi = 0$$
 2.25

where k relates the longitudinal and radial propagation constants as

$$k^2 = \omega^2 \mu \varepsilon = k_\rho^2 + k_z^2.$$

The general solutions to the magnetic and electric potentials in each of the three regions are,

$$\psi^{\text{ml}} = AJ_n(k_{\rho_1}r) \cos \varphi e$$
2.26

$$\psi^{m2} = \left[BJ_n(k_{\rho_2}r) + CN_n(k_{\rho_2}r)\right] \cos n\phi e^{-jk_z z}$$
2.27

$$\psi^{m3} = \left[DJ_n(k_{\rho_3}r) + EN_n(k_{\rho_3}r) \right] \cos n\phi e^{-jk_z z}$$
2.28

$$\psi^{e1} = FJ_n(k_{\rho_2}r) \sin n\phi e^{-jk_z z}$$
2.29

$$\psi^{e2} = \left[GJ_n(k_{\rho_2}r) + HN_n(k_{\rho_2}r) \right] \quad \sin n\phi e^{-jk_z z}$$
 2.30

$$\psi^{e3} = \left[IJ_n(k_{\rho_3}r) + KN_n(k_{\rho_3}r) \right] \sin n\phi e^{-jk_z z}$$
2.31

In each of the three regions, the associated electric and magnetic fields for the TM and TE modes can then be derived from the following general relations:

TM Mode

$$E_{\rho} = \frac{1}{\hat{y}} \frac{\partial^2 \psi^{m}}{\partial \rho \partial z}$$
 2.32

$$E_{\phi} = \frac{1}{\hat{y} \rho} \frac{\partial^2 \psi^m}{\partial \psi \partial z}$$
 2.33

$$E_{z} = \frac{1}{\hat{y}} \left(\frac{\partial^{2}}{\partial z^{2}} + k^{2} \right) \psi^{m}$$

$$H_{\rho} = \frac{1}{\rho} \frac{\partial \psi^{m}}{\partial \phi}$$
 2.35

$$H_{\psi} = -\frac{\partial \psi^{m}}{\partial \rho}$$
 2.36

$$H_{z} = 0 2.37$$

TE Mode

$$E_{O} = -\frac{1}{O} \frac{\partial \psi^{e}}{\partial \phi}$$
 2.38

$$E_{\phi} = \frac{\partial \psi^{e}}{\partial \rho}$$
 2.39

$$E_{z} = 0$$
 2.40

$$H_{\rho} = \frac{1}{\hat{z}} \frac{\partial^2 \psi^{e}}{\partial \rho \partial z}$$
 2.41

$$H_{\phi} = \frac{1}{\hat{z}\rho} \frac{\partial^2 \psi^{e}}{\partial \phi \partial z}$$
 2.42

$$H_z = \frac{1}{2} \left(\frac{\partial^2}{\partial z^2} + k^2 \right) \psi^e$$
 2.43

where $\hat{y} = j\omega \epsilon$ and $\hat{z} = j\omega \mu$.

In each region the potential functions must also satisfy the separation relations:

Region 1.
$$k_{\rho_1}^2 + k_z^2 = k_1^2 = (\frac{\omega}{c})^2 \epsilon_1$$
 2.44

Region 2.
$$k_{\rho_2}^2 + k_z^2 = k_2^2 = (\frac{\omega}{c})^2 \epsilon_2$$
 2.45

Region 3.
$$k_{\rho_3}^2 + k_z^2 = k_3^2 = (\frac{\omega}{c})^2$$
. 2.46

 ϵ_1 is the plasma permittivity and is given by Equation 2.24, and ϵ_2 is the permittivity of the quartz tube.

The solutions to the Helmholtz equation must satisfy the following boundary conditions:

- 1) The tangential components of \vec{E} and \vec{H} must be continuous across the plasma-quartz tube interface; i.e., at ρ = a, E_z , H_z , E_φ and H_φ must be continuous.
- 2) The tangential components of \vec{E} and \vec{H} must be continuous across the quartz tube free space interface; i.e., at ρ = b, E_z , H_z , E_{ϕ} and H_{ϕ} must be continuous.
- 3) The tangential components of \vec{E} must vanish on the outer metal boundary; i.e., at $\rho = b$, $E_z = 0$, $E_{\phi} = 0$.

In this class of problems the fields cannot be divided into pure TE or TM modes; thus, both $\rm E_z$ and $\rm H_z$ will be necessary to satisfy the boundary conditions for any given mode. This will ensure a general solution. Except for the case of rotionally symmetric modes, which can be thought of as pure TE or TM, the other modes are hybrid in character.

Using equations 2.26 through 2.46, subject to the boundary conditions as given above, we arrive at the following 8 simultaneous equations

$$Fk_{\rho_1}^2 J_n(k_{\rho_1} a) = Gk_{\rho_2}^2 J_n(k_{\rho_2} a) + Hk_{\rho_2}^2 N_n(k_{\rho_2} a)$$
 2.47

$$A\epsilon_2 k_{\rho_1}^2 J_n(k_{\rho_1} a) = B \epsilon_1 k_{\rho_2}^2 J_n (k_{\rho_2} a) + C\epsilon_1 k_{\rho_2}^2 N_n(k_{\rho_2} a)$$
 2.48

$$A k_{\rho_{1}} J_{n}^{"} (k_{\rho_{1}} a) + F \frac{k_{z}^{n}}{\omega \mu_{o}^{a}} J_{n}(k_{\rho_{1}} a) = B k_{\rho_{2}} J_{n}^{"} (k_{\rho_{2}} a) + C k_{\rho_{2}} N_{n}^{"} (k_{\rho_{2}} a)$$

$$+ G \frac{k_{z}^{n}}{\omega \mu_{o}^{a}} J_{n}(k_{\rho_{2}} a) + H \frac{k_{z}^{n}}{\omega \mu_{o}^{a}} N_{n}(k_{\rho_{2}} a)$$
2.49

$$A \frac{k_{z}^{n}}{\omega \epsilon_{1}^{a}} J_{n}(k_{\rho_{1}}^{a}) + F k_{\rho_{1}}^{J'_{n}(k_{\rho_{1}}^{a})} = B \frac{k_{z}^{n}}{\omega \epsilon_{2}^{a}} J_{n}(k_{\rho_{2}}^{a}) + C \frac{k_{z}^{n}}{\omega \epsilon_{2}^{a}} N_{n}(k_{\rho_{2}}^{a})$$

+
$$G k_{\rho_2} J_n^{\dagger} (k_{\rho_2} a)$$
 + $H k_{\rho_2} N_n^{\dagger} (k_{\rho_2} a)$ 2.50

$$G k_{\rho_2}^2 J_n(k_{\rho_2} b) + H k_{\rho_2}^2 N_n (k_{\rho_2} b) = K' k_{\rho_3}^2 F_2$$
 2.51

$$B \epsilon_{3}^{2} k_{\rho_{2}}^{2} J_{n} (k_{\rho_{2}}^{b}) + C\epsilon_{3}^{2} k_{\rho_{2}}^{2} N_{n} (k_{\rho_{2}}^{b}) = E' \epsilon_{2}^{2} k_{\rho_{3}}^{2} F_{1}$$
2.52

$$B \ k_{\rho_2} J_n' \ (k_{\rho_2} b) \ + \ C \ k_{\rho_2} N_n' \ (k_{\rho_2} b) \ + \ G \ \frac{k_z n}{\omega \mu_o b} \ J_n \ (k_{\rho_2} b) \ + \ H \ \frac{k_z n}{\omega \mu_o b} \ N_n \ (k_{\rho_2} b)$$

= E'
$$k_{\rho_3} F_3 + K' \frac{k_z n}{\omega \mu_o b} F_2$$
 2.53

$$B \frac{k_{z}^{n}}{\omega \epsilon_{2}^{b}} J_{n} (k_{\rho_{2}^{b}}^{b}) + C \frac{k_{z}^{n}}{\omega \epsilon_{2}^{b}} N_{n} (k_{\rho_{2}^{b}}^{b}) + C k_{\rho_{2}^{o}}^{j} (k_{\rho_{2}^{b}}^{b}) +$$

$$H k_{\rho_{2}} N_{n}' (k_{\rho_{2}} b) = E' \frac{k_{z} n}{\omega \epsilon_{3} b} F_{1} + K' k_{\rho_{3}} F_{4}$$
2.54

where

$$E' = -E/J_n (k_{\rho_3} c)$$
 2.55

$$K' = - K/J_n' (k_{\rho_3} c)$$
 2.56

$$F_1 = J_n (k_{\rho_3} b) N_n (k_{\rho_3} c) - J_n (k_{\rho_3} c) N_n (k_{\rho_3} b)$$
 2.57

$$F_2 = J_n (k_{\rho_3} b) N_n' (k_{\rho_3} c) - J_n' (k_{\rho_3} c) N_n (k_{\rho_3} b)$$
 2.58

$$F_{3} = J_{n}^{\prime}(k_{\rho_{3}}b) N_{n}(k_{\rho_{3}}c) - J_{n}(k_{\rho_{3}}c) N_{n}^{\prime}(k_{\rho_{3}}b)$$
 2.59

$$F_4 = J_n^{\dagger} (k_{\rho_3} b) N_n^{\dagger} (k_{\rho_3} c) - J_n^{\dagger} (k_{\rho_3} c) N_n^{\dagger} (k_{\rho_3} b).$$
 2.60

For a non-trivial solution to the simultaneous equations 2.47 through 2.54, the determinant of the coefficients must be identically zero. Hence, it follows that,

•	•	
V	0	
	•	
_	.1	

•
0

0	0	0	0	$-k_{\rho_3}^2 F_2$	0	$\frac{-nk_z}{\omega \nu_o b} F_2$	-k F4
-k ² N (k _p a)	. 0	$\frac{-k}{\omega U_0} \frac{n}{a} \frac{N}{n} \left(k_{D_0} a\right)$	$-k$ _D $\frac{N'(k_{\rm p}a)}{2}$	$k_{\rho_2}^2 N(k_{\rho_2}b)$	0	$\frac{k_z^n}{\omega \mu_o^b} N_n(k_p^b)$	k _ρ N' (k _ρ b)
-k ² J ₁ (k ₂ a)	0	$\frac{-k}{\omega \mu} \frac{n}{a} \int_{0}^{\infty} (k_{\rho} a)$	$-k$ _{ρ} $\frac{1}{n}$ $(k$ _{ρ} $a)$	$k_{\rho_2}^2 \int_{\Omega} (k_{\rho_2} b)$	C	$\frac{k_{z}}{\omega u_{o}} \int_{0}^{\infty} J_{u}(k_{o}b)$	k J'(k b)
k ² J (k _ρ a)	. 0	$\frac{k_{a}}{\omega \nu_{o}} \frac{1}{a} \int_{0}^{a} (k_{a})$	k J'(k a)	0	0	0	0
0	0	0	0	0	$-\epsilon_2 k_{\rho_3}^2 F_1$	-k _p F ₃	$\frac{-k}{\omega \epsilon_3 b} F_1$
0	$-\epsilon_1 k_{\Omega}^2 N (k_{\Omega} a)$	-k _p N'(k _p a)	$\frac{-k}{\omega \epsilon} \frac{n}{2^a} \frac{(k_p a)}{n}$	0	$\epsilon_{3}^{k_{\rho}^{2}}_{\rho_{2}^{2}}^{N}(k_{\rho}^{b}) - \epsilon_{2}^{k_{\rho}^{2}}_{\rho_{3}^{3}}^{F_{1}}$	k _{o N} ' (k _o b)	$\frac{k_2}{\omega \epsilon_2 b} N_{\alpha} (k_{\rho_2} b) \frac{1}{\omega_2}$
0	$-\epsilon_1 k_{\rho_2}^2 J_n(k_{\rho_2}a)$	$-k \int_{0}^{1} (k a)$	$\frac{-k}{\omega \epsilon_2^a} \int_0^1 (k_\rho a)$	0	$\epsilon_3 k_{\rho_2}^2 J_n(k_{\rho_2}b)$	κ _{ρ J'} (κ _{ρ b)}	$\frac{k_z^n}{\omega \epsilon_2^b} J_n(k_{\rho_2^b})$
0	ε ₂ k _{ρ Jn (k_{ρ a)}}	k _{ρ J} n (k _{ρ a})	$\frac{k_n}{\omega \epsilon_1 a_n} (k_{\rho} a)$	0	0	0	0

Upon simplifying the above determinant we obtain the following characteristic equation for the three dielectric boundary value problem

$$\left[\frac{\varepsilon_1}{\varepsilon_2} \frac{k_{\rho_2}}{k_{\rho_1}} \frac{J_n'(k_{\rho_1}a)}{J_n(k_{\rho_1}a)} \left(\varepsilon_3 k_{\rho_2} F_3 F_7 - \varepsilon_2 k_{\rho_3} F_1 F_8\right) - \left(\varepsilon_3 k_{\rho_2} F_3 F_5 - \varepsilon_2 k_{\rho_3} F_1 F_6\right)\right].$$

$$\left[\frac{k_{\rho_{2}}}{k_{\rho_{1}}} \frac{J_{n}^{\prime}(k_{\rho_{1}}a)}{J_{n}(k_{\rho_{1}}a)} \left(k_{\rho_{3}} F_{2}F_{8}-k_{\rho_{2}}F_{4}F_{7}\right) - \left(k_{\rho_{3}}F_{2}F_{6} - k_{\rho_{2}}F_{4}F_{5}\right)\right]$$

$$= \frac{n^2 k_2^2}{\omega^2 \mu_0 \varepsilon_2 a^2} \frac{(k_{\rho_1}^2 - k_{\rho_2}^2)^2}{k_{\rho_1}^4 k_{\rho_2}^2} \left[\varepsilon_3 k_{\rho_2} k_{\rho_3} F_2 F_3 F_7 F_8 - \varepsilon_3 k_{\rho_2}^2 F_3 F_4 F_7^2 \right]$$

+
$$\epsilon_{2}^{k} \rho_{2}^{k} \rho_{3}^{F_{1}F_{4}F_{7}F_{8}} - \epsilon_{2}^{k^{2}} \rho_{3}^{F_{1}F_{2}F_{8}}^{2}$$

$$-\frac{J_{n}^{'2}(k_{\rho_{1}}a)}{J_{n}^{2}(k_{\rho_{1}}a)} \epsilon_{1}k_{\rho_{2}}^{2}F_{1}F_{2}F_{7}^{2} \Bigg] + \Bigg[\frac{n^{2}k_{z}^{2}}{\omega^{2}\mu_{o}\epsilon_{2}ab} \frac{(k_{\rho_{1}}^{2} - k_{\rho_{2}}^{2})(k_{\rho_{2}}^{2} - k_{\rho_{3}}^{2})}{k_{\rho_{1}}^{4}k_{\rho_{2}}^{4}k_{\rho_{3}}^{2}} \Bigg].$$

$$\left[2\epsilon_{2} k_{\rho_{1}}^{2} k_{\rho_{2}}^{2} k_{\rho_{3}}^{2} F_{1}F_{2}F_{9}F_{10} + \frac{n^{2}k_{z}^{2}}{\omega^{2}\mu_{o}ab} (k_{\rho_{1}}^{2} - k_{\rho_{2}}^{2}) (k_{\rho_{2}}^{2} - k_{\rho_{3}}^{2}) F_{1}F_{2}F_{7}^{2}\right]$$

$$F_{5} = J_{n}^{\prime}(k_{\rho_{2}}a) N_{n}(k_{\rho_{2}}b) - N_{n}^{\prime}(k_{\rho_{2}}a) J_{n}(k_{\rho_{2}}b)$$
 2.63

$$F_{6} = J_{n}^{\prime}(k_{\rho_{2}}a) N_{n}^{\prime}(k_{\rho_{2}}b) - N_{n}^{\prime}(k_{\rho_{2}}a) J_{n}^{\prime}(k_{\rho_{2}}b)$$
 2.64

$$F_7 = J_n(k_{\rho_2}a) N_n(k_{\rho_2}b) - N_n(k_{\rho_2}a) J_n(k_{\rho_2}b)$$
 2.65

$$F_8 = J_n(k_{\rho_2}a) N_n'(k_{\rho_2}b) - N_n(k_{\rho_2}a) J_n'(k_{\rho_2}b)$$
 2.66

$$F_9 = J_n'(k_{\rho_2}a) N_n(k_{\rho_2}a) - N_n'(k_{\rho_2}a) J_n(k_{\rho_2}a)$$
 2.67

$$F_{10} = J_n(k_{\rho_2}b) N_n'(k_{\rho_2}b) - N_n(k_{\rho_2}b) J_n'(k_{\rho_2}b).$$
 2.68

For rotationally symmetric modes, n=0 and the right side of Equation 2.62 becomes zero. The left hand side is a product of two expressions, each of which when equated to zero yields the TM and TE mode solutions, respectively. When $n \neq 0$ the entire Equation 2.62 must be used in obtaining a solution, since the modes are hybrid in nature; i.e., they have both E_z and H_z field components. If the enclosing quartz tube thickness were assumed zero, i.e. if we set b=a in Equation 2.62 and if $v_e=0$, then we would obtain the two dielectric problem characteristic equation, as has been derived by others 13.

It is apparent that for finite losses within the plasma almost all the terms in the transcedental equation above are complex, including the Bessel's functions which are functions with complex arguments. Details of the numerical techniques involved in evaluating the roots of such an equation are explained in Appendix A.

Since the plasma under study is lossy, k_z , in general, is complex, i.e., $k_z = \beta - j\alpha$, where β is the propagation constant and α the attenuation constant in the z - direction. By solving the characteristic equation for ω vs. k_z , with ω_{pe} and ν_e specified, $\omega - \beta$ and $\omega - \alpha$ diagrams can be generated for each mode. Interesting electromagnetic properties can be obtained from such diagrams and these will be the subject of discussion in the following section.

2.4 ω-k Diagrams

This section presents the ω - k diagrams for the various propagating modes in the inhomogenous waveguide. This diagram gives a useful insight into the fast wave and slow wave solutions to this boundary value problem. It explains some modes that exist without a plasma and the transformation of electromagnetic modes in the presence of the plasma and also predicts the appearance of modes that do not exist in the empty waveguide.

Both fast wave $(V_{\varphi} > c)$ and slow wave $(V_{\varphi} < c)$ solutions are found to exist in this type of waveguide, because of the coaxially located dielectric enclosed plasma rod. In general, both TE and TM modes are needed to satisfy boundary conditions. Thus, the modes are hybrid in nature, except in the rotationally symmetric case where TE and TM modes uncouple and exist independently. The propagating modes for this boundary value problem can be broadly classified into two categories 10,13,16,17 .

- 1) <u>Fast wave electromagnetic modes</u>: These are empty waveguide electromagnetic modes that have been perturbed by the presence of the plasma and have a phase velocity greater than the speed of light. They can be further subdivided into two classes.
- (a) $\frac{\text{TE}}{\text{om}}$ or $\frac{\text{TM}}{\text{om}}$: m > 0. These are rotationally symmetric modes and hence, they are pure TE or TM in nature. They are labeled the same

as the corresponding modes in the empty circular waveguide 13,16,17 . At high plasma densities, i.e., $\omega_{pe} >> \omega$, and all losses these modes approach the coaxial waveguide mode that has the same index as the empty circular waveguide mode 10 . At high frequencies, i.e., $\omega >> \omega_{pe}$, and all losses these modes approach the corresponding empty circular waveguide modes.

- (b) $\frac{\text{TE}_{nm}^*}{\text{or TM}_{nm}^*}$: $\frac{\text{n}>0$, m>0. These are hybrid modes, the asterisk denoting their hybrid nature. They are labeled with respect to the TE or TM modes in a circular waveguide, into which they reduce when the plasma density goes to zero. At high plasma densities and zero losses, the TE_{nm}^* $\left(\text{TM}_{nm}^*\right)$ mode approaches the TM_{nm} $\left(\text{TE}_{nm+1}\right)$ mode in a coaxial waveguide with a metallic center conductor. At high plasma densities and finite losses, however, the TE_{nm}^* $\left(\text{TM}_{nm}^*\right)$ mode approaches the TE_{nm} $\left(\text{TM}_{nm}^*\right)$ coaxial waveguide mode. At high frequencies, and finite losses the TE_{nm}^* $\left(\text{TM}_{nm}^*\right)$ mode approaches the empty circular waveguide TE_{nm} $\left(\text{TM}_{nm}^*\right)$ mode.
- 2) Slow wave plasma modes: These modes do not exist in an empty waveguide and have a phase velocity smaller than the velocity of light over a wide range of plasma densities. They can be further subdivided into two classes of modes.
- (a) $\underline{\text{TM}}_{00}$: This mode is circularly symmetric and does not exist in the empty waveguide. However, it is classified with respect to the circularly symmetric TM modes of an empty waveguide. This is also called a surface wave or a space charge wave. At large plasma densities and low losses the $\underline{\text{TM}}_{00}$ mode approaches the TEM mode of a coaxial waveguide with its phase velocity approaching the speed of light, whereas at large plasma densities and high losses it deviates from the TEM mode and becomes more of a slow wave.
- (b) $\underline{\text{TM}}_{\text{no}}^*$. These are hybrid modes that are ϕ dependent. They are slow waves in a lossless plasma and for small losses. At high

plasma densities they asymptotically approach the coaxial TE_{n1} mode. For finite losses, however, the TM_{n0}^{\star} mode becomes degenerate with the TE_{n1}^{\star} mode and its asymptotic behavior at high plasma densities and high frequencies, is same as that of the TE_{n1}^{\star} mode.

The following sub-sections deal with a detailed study of the normalized ω - k diagrams, i.e., ω/ω_{pe} vs. β/k_c and ω/ω_{pe} vs. α/k_c with ω_{pe}/ω_{c} and ν_{e}/ω_{pe} as variable parameters, for the TM_{00} , TM_{01} , TM_{10}^* , TE_{11}^* modes. ω_{c} and k_c are the cutoff frequency and cutoff wave number, respectively, of the TE_{11} mode in an empty circular waveguide. These diagrams have been plotted for experimental waveguide dimensions: a = 0.3 cms., b = 0.3875 cms., c = 5.08 cms. The experimental operating frequency $\frac{\omega}{2\pi} = 3.03$ GHz is also shown in these curves. For these waveguide dimensions, $\frac{c}{2\pi} = 1.73$ GHz and $k_c = 0.362$ cm⁻¹.

TM_{00} mode.

Space charge or electromechanical waves propagate in a stationary plasma of finite cross-section, due to a perturbation either of the average volume charge density or of the surface charge density 12. Propagation of slow waves in a cold plasma due to a volume charge perturbation is possible only in the presence of a d-c magnetic field. Surface waves can propagate on a quartz-enclosed plasma rod, partially filling a metal waveguide, with or without a d-c magnetic field.

The TM_{00} mode is a surface wave that propagates in the absence of a d-c magnetic field. The dispersion relation for the TM_{0m} mode can be obtained as a special case of equation 2.62, by setting n = 0. The resulting equation is shown on the following page.

$$\frac{\varepsilon_{1}}{\varepsilon_{2}} \frac{k_{\rho_{2}}}{k_{\rho_{1}}} \frac{J_{0}^{\prime}(k_{\rho_{1}}a)}{J_{0}(k_{\rho_{1}}a)} = \frac{\varepsilon_{3}^{k_{\rho_{2}}} F_{3}F_{5} - \varepsilon_{2}^{k_{\rho_{3}}} F_{1}F_{6}}{\varepsilon_{3}^{k_{\rho_{2}}} F_{3}F_{7} - \varepsilon_{2}^{k_{\rho_{3}}} F_{1}F_{8}}$$
2.69

where,

 F_1 , F_3 , F_5 , F_6 , F_7 and F_8 are as given in equations 2.57, 2.59, 2.63 to 2.66 with n = 0. The first root (m = 0) of equation 2.69 is the solution to the TM_{00} mode, the second root (m = 1) that of the TM_{01} mode and so on. The TM_{00} mode has basically three field components: longitudinal and radial electric fields E_z and E_p respectively, and a circular magnetic field H_{ϕ} . E_z would be predominant for those frequencies when the TM_{00} mode is a space charge wave and E_z would become zero whenever the TM_{00} mode approaches the TEM mode.

The ω - k diagram for the TM $_{00}$ mode is obtained from equation 2.69, with ν_e/ω_{pe} and ω_{pe}/ω_{c} as running parameters. Several interesting features of the plots of ω/ω_{pe} vs. β/k_c (figures 2.2a, 2.3a, 2.4a, 2.4c, 2.5a) and ω/ω_{pe} vs. α/k_c (figures 2.2b, 2.3b, 2.4b, 2.4d, 2.5b) will now be explained. Figures 2.2a and 2.2b show the lossy TM $_{00}$ waves for f_{pe} = 6.0 GHz and ν_e/ω_{pe} = 0.1 over the entire frequency range. In Figure 2.2a, the ω - k diagram is separated into four regions. Region 1 is the slow wave portion of the curve. In region 2, the TM $_{00}$ mode is a backward wave. Region 3 shows that the TM $_{00}$ mode is almost cut off in this frequency range. In region 4, this mode is an EM wave which eventually becomes asymptotic to the light line. Figures 2.3a, 2.4a, 2.5a show the ω/ω_{pe} vs. β/k_c diagrams and figures 2.3b, 2.4b, 2.5b show the ω/ω_{pe} vs. α/k_c diagrams for the different plasma densities of f_{pe} = 4.5 GHz, 6.0 GHz and 10.5 GHz and for a range of collision frequencies. The ν_e/ω_{pe} = 0.03 curves in figures 2.5a, and 2.5b have the same

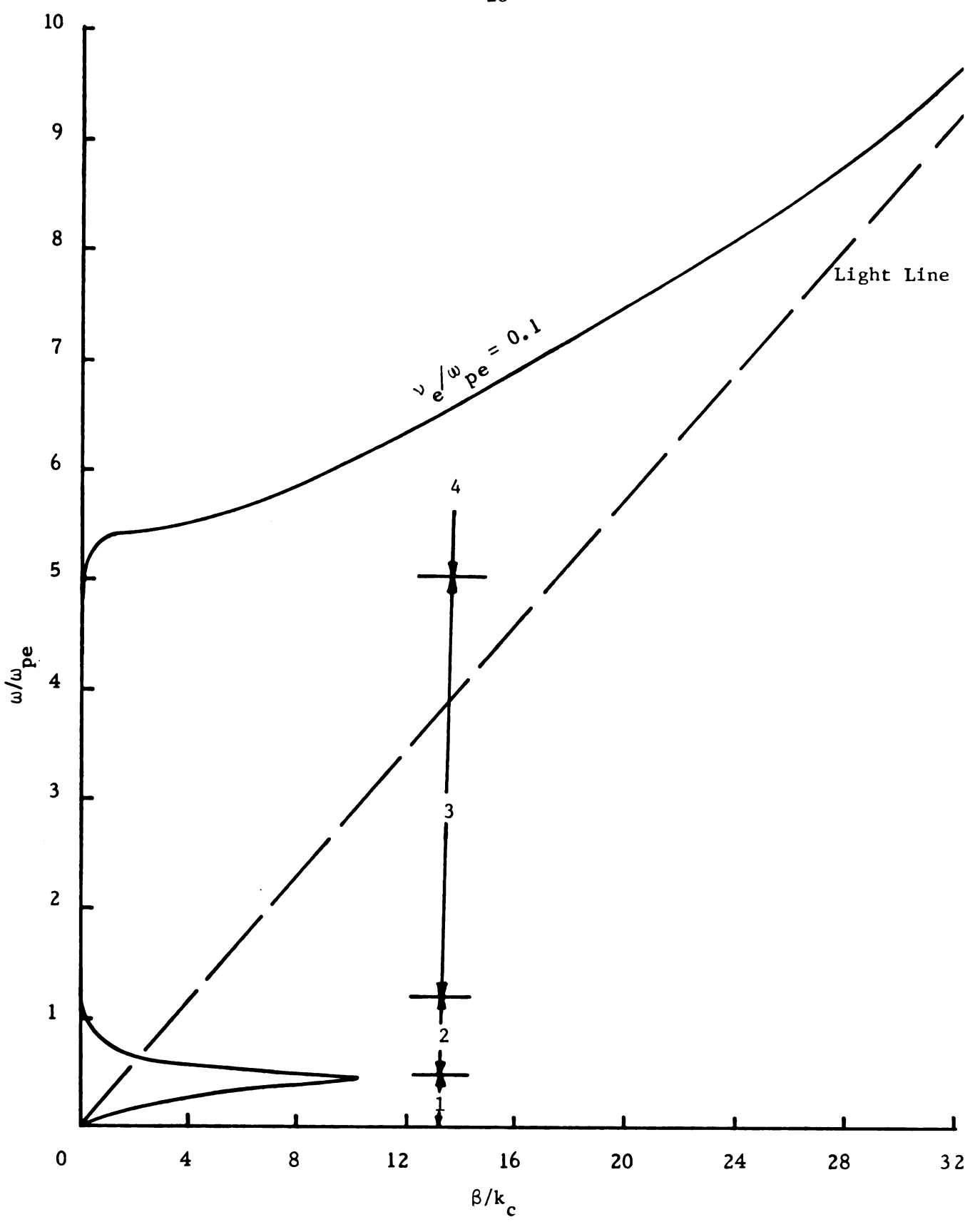


Figure 2.2a. ω/ω_{pe} vs. β/k_{c} for the TM $_{00}$ mode. f_{pe} =6.0 GHz. ω_{pe}/ω_{c} =3.47. Waveguide dimensions: a = 0.3 cms., b = 0.3875 cms., c = 5.08 cms.

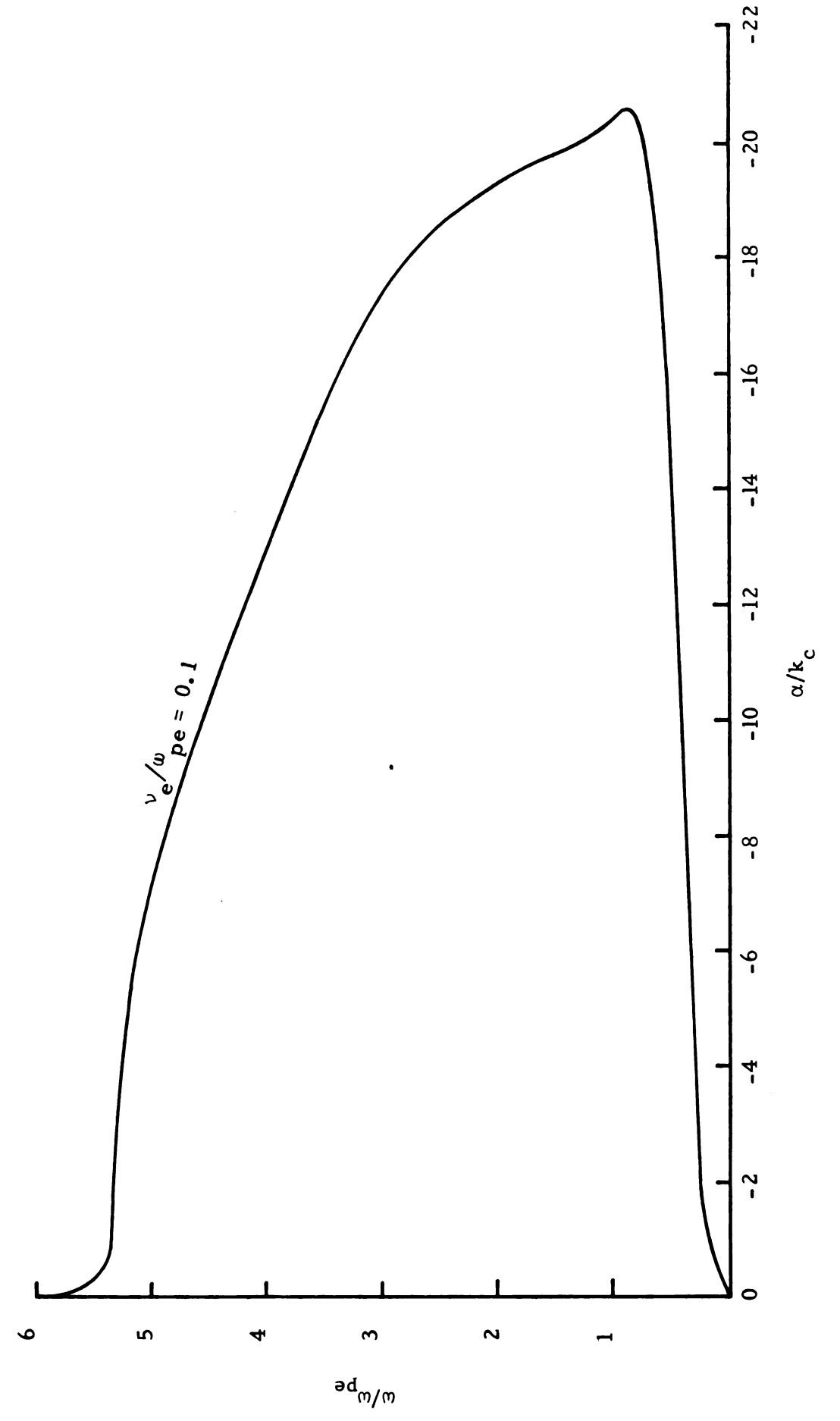


Figure 2.2b. $\omega/\omega_{\rm pe}$ vs. $\alpha/k_{\rm c}$ for the TM $_{00}$ mode. $f_{\rm pe}=6.0~{\rm GHz},~\omega_{\rm pe}/\omega_{\rm c}=3.47.$ Waveguide dimensions: a = 0.3 cms., b = 0.3875 cms., c = 5.08 cms.

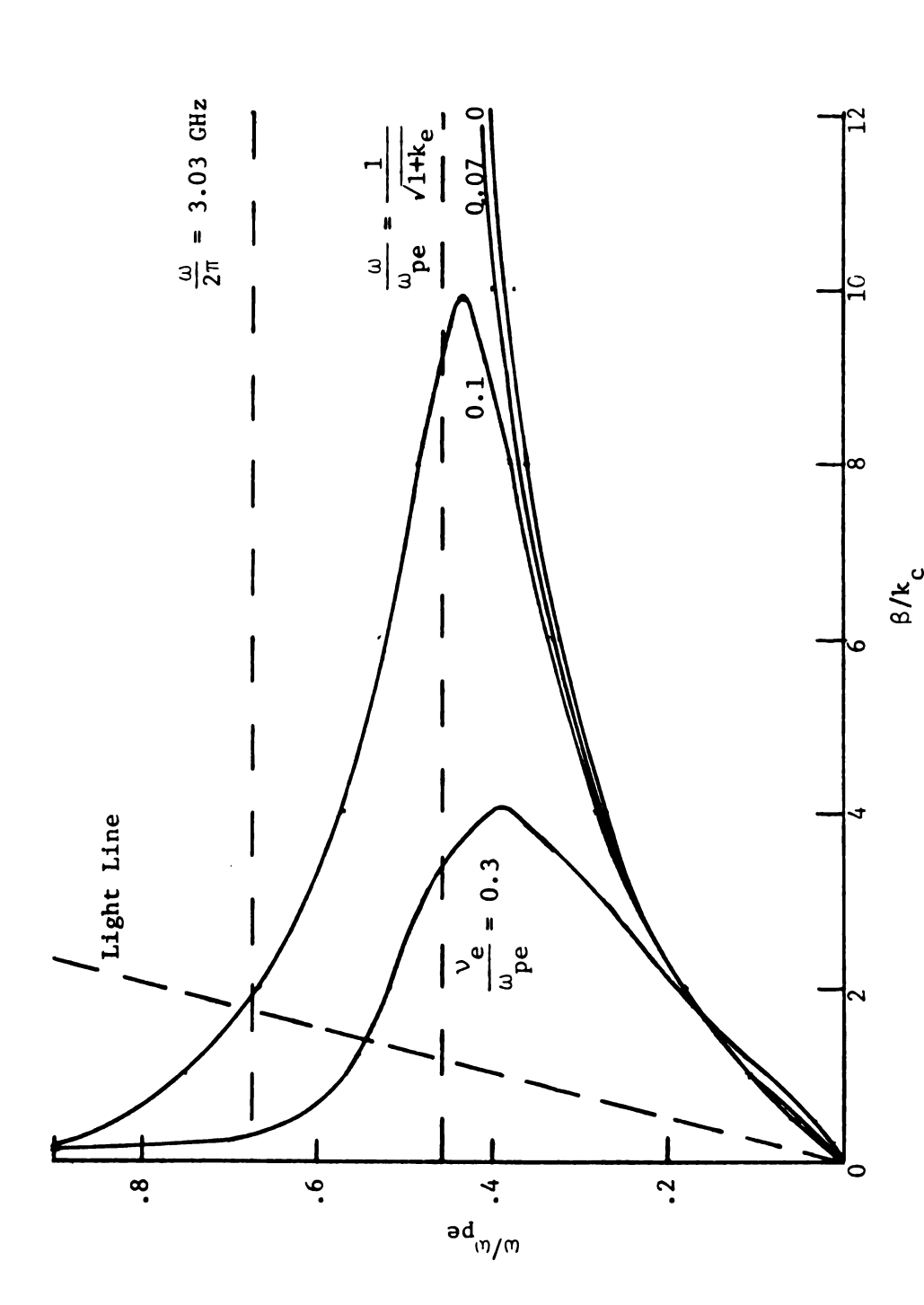


Figure 2.3a. ω/ω_{pe} vs. β/k_c for the TM $_{00}$ mode for $\omega/\omega_{pe} \le 0.9$. f = 4.5 GHz, ω_{pe}/ω_{c} = 2.6. Waveguide

dimensions: a = 0.3 cms., b = 0.3875 cms., c = 5.08 cms.

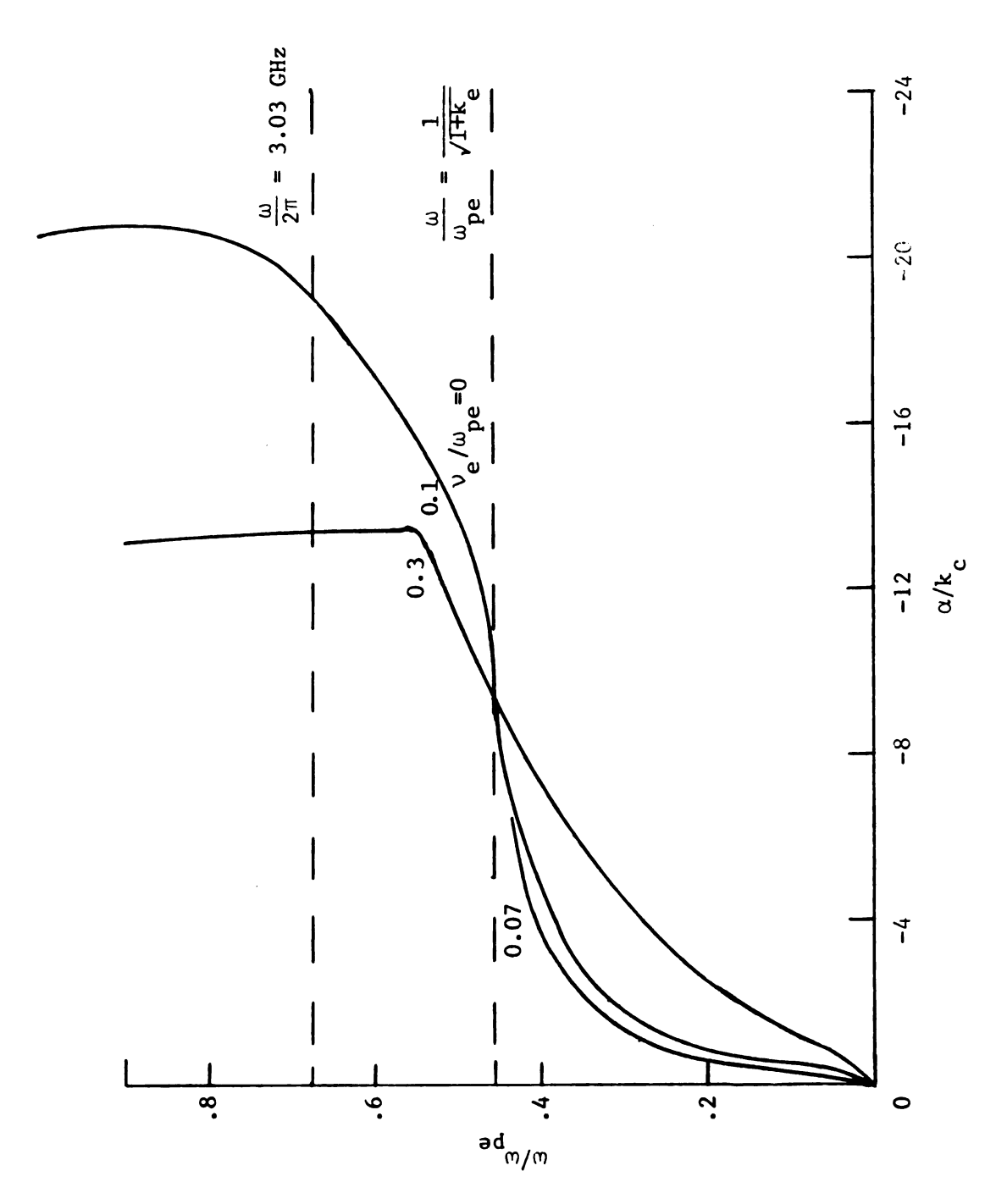


Figure 2.3b. ω/ω_p vs. α/k_c for the TM $_{00}$ mode for $\omega/\omega_p < 0.9$. f = 4.5 GHz, $\omega_p = 2.6$. Waveguide dimensions: a = 0.3 cms., b = 0.3875 cms., c = 5.08 cms.

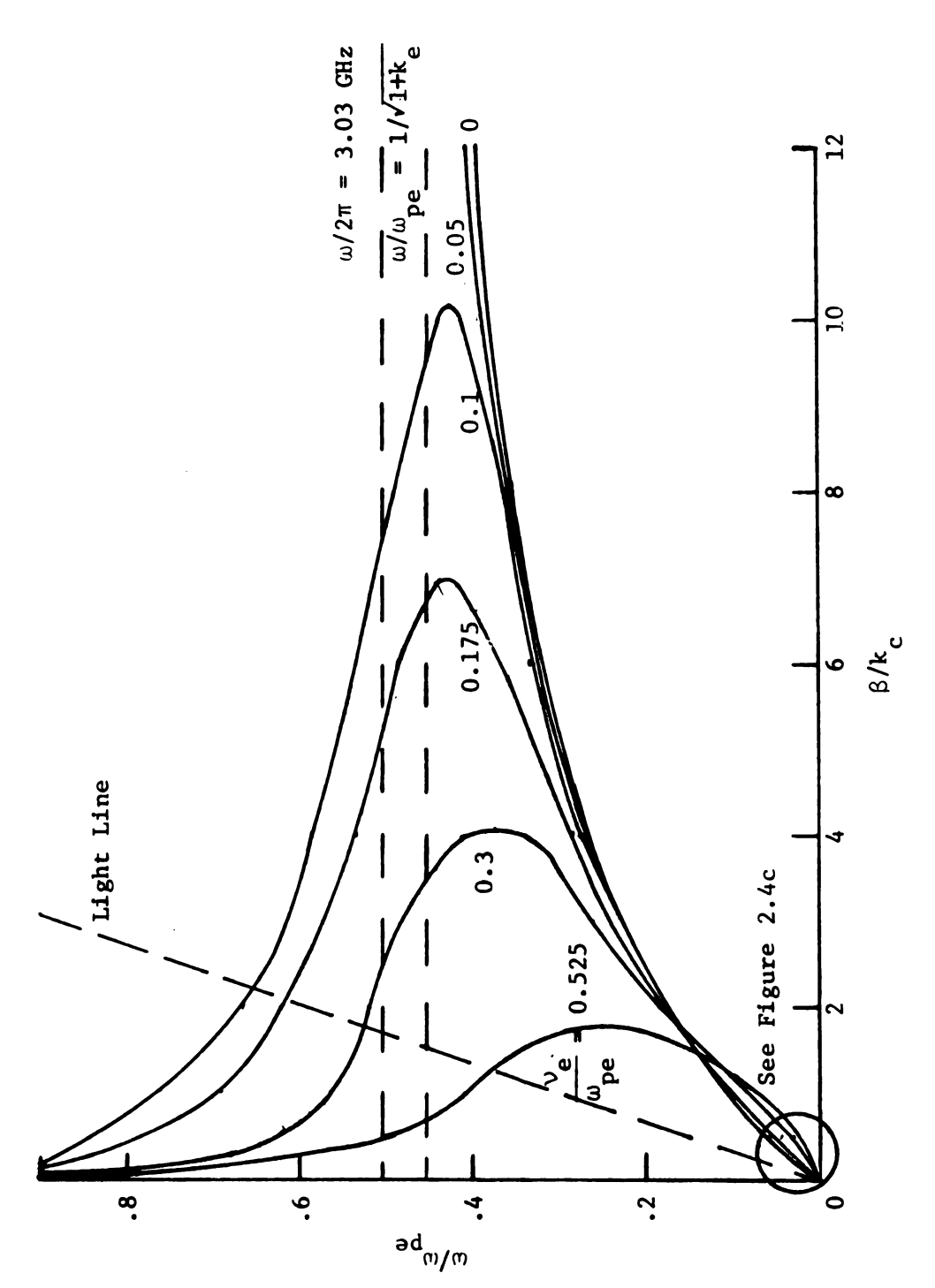


Figure 2.4a. $\omega/\omega_{\rm pe}$ vs. $\beta/k_{\rm c}$ for the TM $_{00}$ mode for $\omega/\omega_{\rm pe} \le 0.9$. f = 6.0 GHz. $\omega_{\rm pe}/\omega_{\rm c} = 3.47$. Waveguide dimensions: a = 0.3 cms., b = 0.3875 cms., c = 5.08 cms.

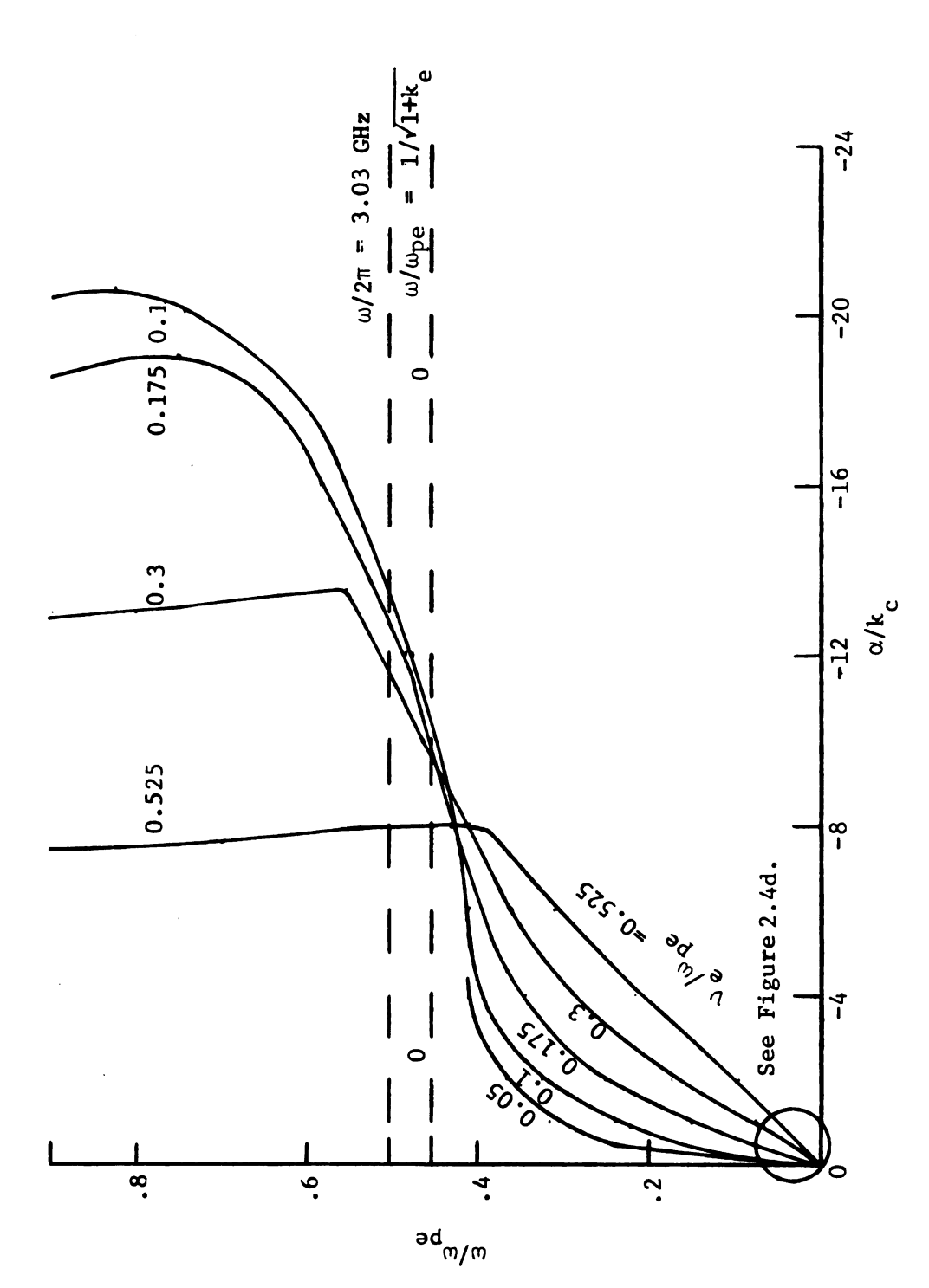


Figure 2.4b. $\omega/\omega_{\rm pe}$ vs. $\alpha/k_{\rm c}$ for the TM $_{00}$ mode for $\omega/\omega_{\rm pe} \le 0.9$. f = 6.0 GHz, $\omega_{\rm pe}/\omega_{\rm c}$ = 3.47. Waveguide dimensions: a = 0.3 cms., b = 0.3875 cms., c = 5.08 cms.

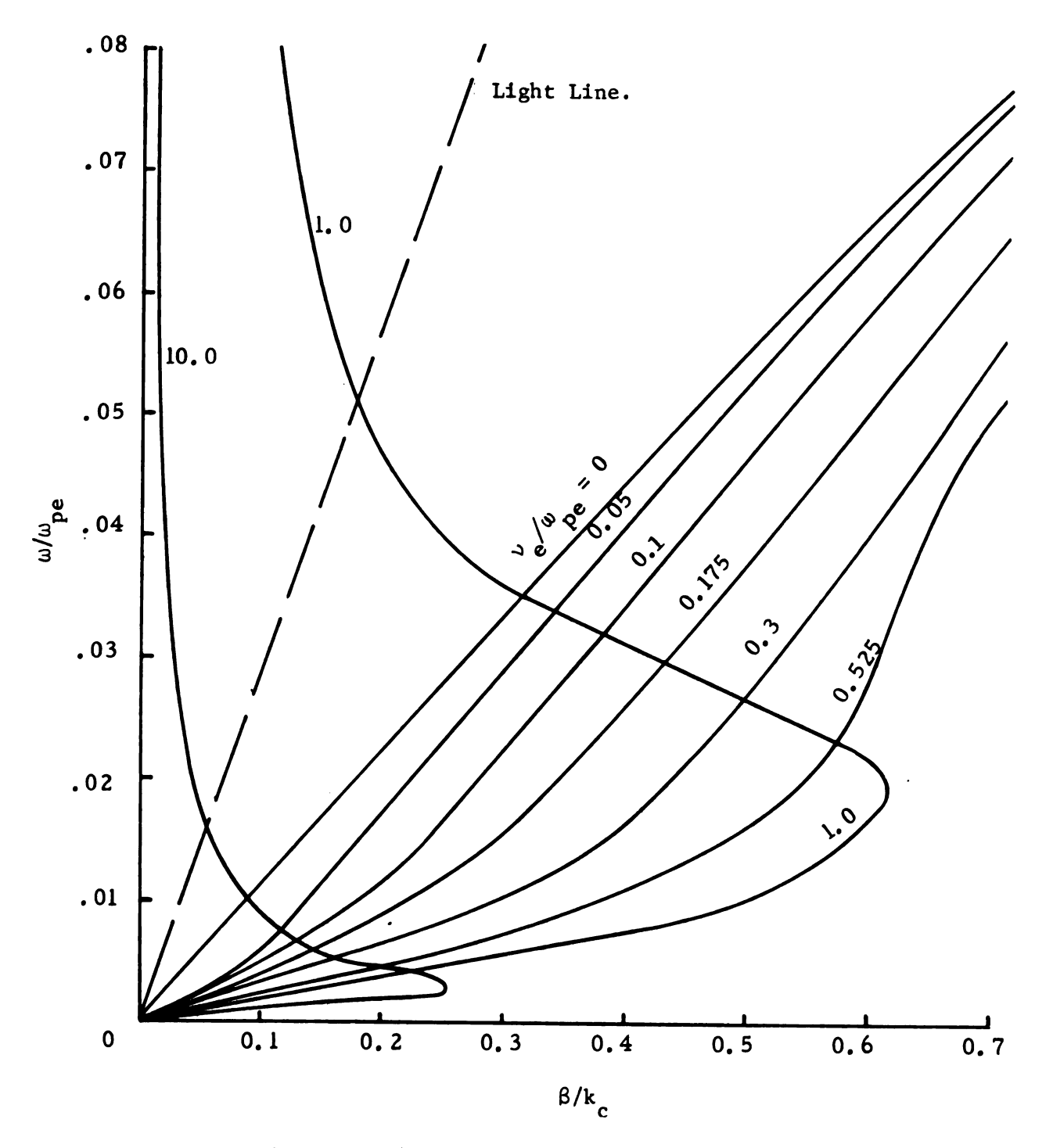


Figure 2.4c. ω/ω_{pe} vs. β/k_{c} for the TM $_{00}$ mode for ω/ω_{pe} < 0.1. f = 6.0 GHz, ω_{pe}/ω_{c} = 3.47. Waveguide dimensions: a = 0.3 cms., b = 0.3875 cms., c = 5.08 cms.

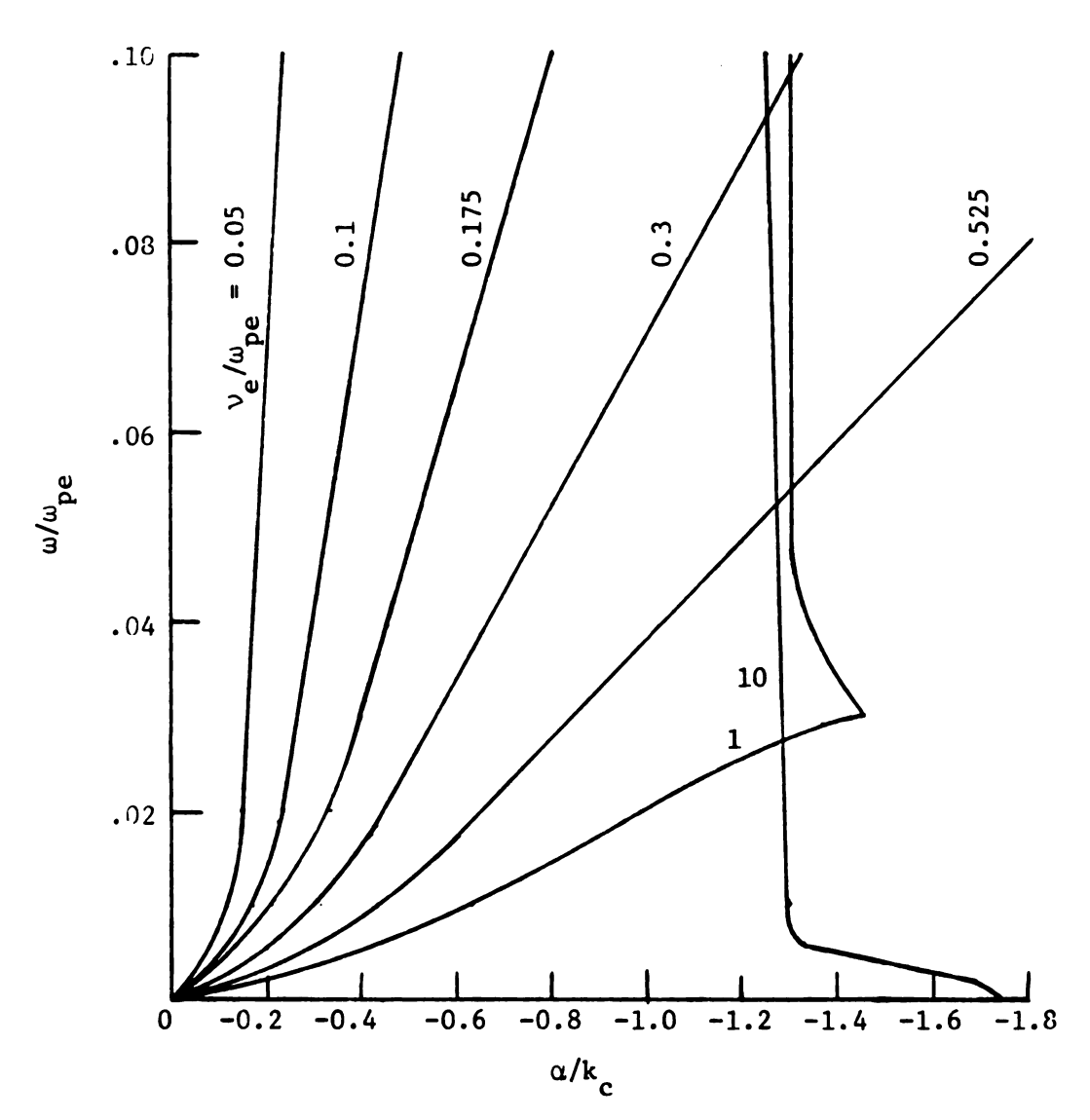


Figure 2.4d. ω/ω_{pe} vs. α/k_{c} for the TM_{00} mode for ω/ω_{pe} < 0.1. f = 6.0 GHz, ω_{pe}/ω_{c} = 3.47. Waveguide dimensions: a = 0.3 cms., b = 0.3875 cms., c = 5.08 cms.

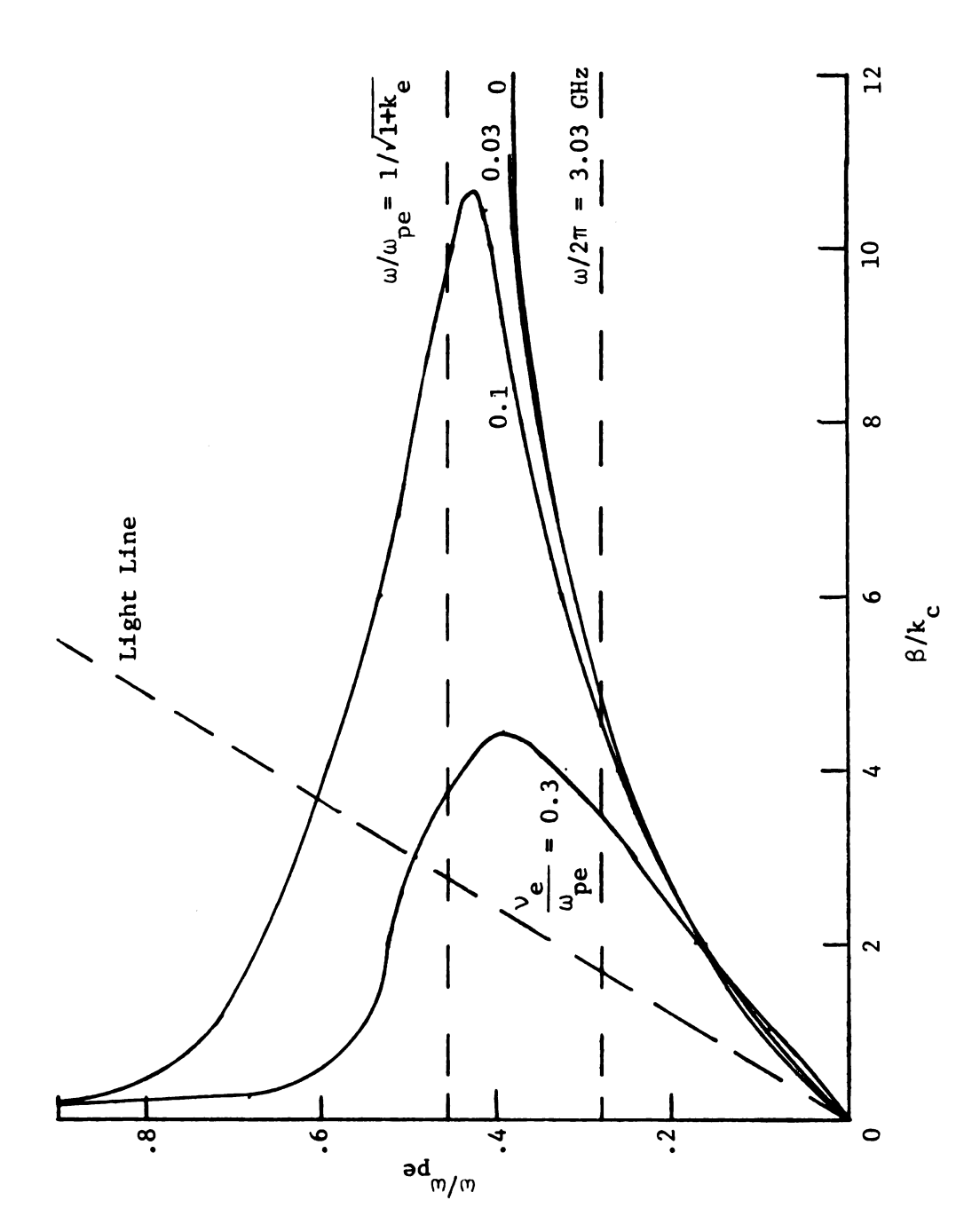


Figure 2.5a. $\omega/\omega_{\rm pe}$ vs. $\beta/k_{\rm c}$ for the TM $_{00}$ mode for $\omega/\omega_{\rm pe} \le 0.9$ f = 10.5 GHz, f $_{\rm pe}/f_{\rm c}$ = 6.1. Waveguide dimensions: a = 0.3 cms., b = 0.3875 cms., c = 5.08 cms.

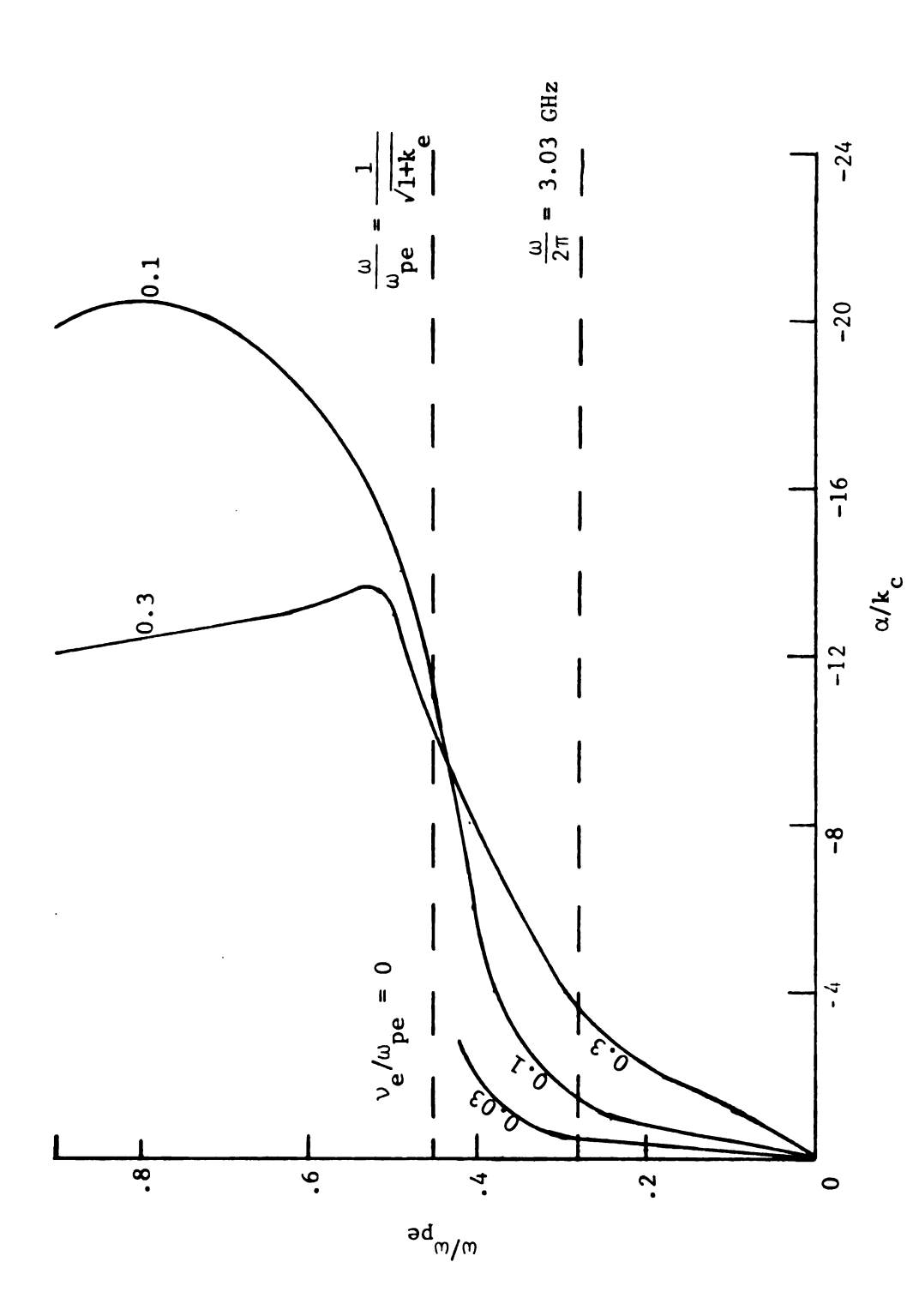


Figure 2.5b. $\omega/\omega_{\rm pe}$ vs. $\alpha/k_{\rm c}$ for the TM $_{00}$ mode for $\omega/\omega_{\rm pe} < 0.9$. f = 10.5 GHz, $\omega_{\rm pe}/\omega_{\rm c}$ = 6.1. Waveguide dimensions: a = 0.3 cms., b = 0.3875 cms., c = 5.08 cms.

collisional loss as the $v_e/w_{pe} = 0.052$ curves in figures 2.4a and 2.4b and the $v_e/w_{pe} = 0.07$ curves in figures 2.3a and 2.3b. Similarly, the $v_e/w_{pe} = 0.1$ and $v_e/w_{pe} = 0.3$ curves in figures 2.5a and 2.5b have the same collisional loss as the $v_e/w_{pe} = 0.175$ and $v_e/w_{pe} = 0.525$ curves respectively, in figures 2.4a and 2.4b. Figures 2.4c and 2.4d are enlargements of the circled areas of figures 2.4a and 2.4b, respectively. They show the low-frequency $(\omega/\omega_{pe} < 0.1)$ details for $f_{pe} = 6.0$ GHz.

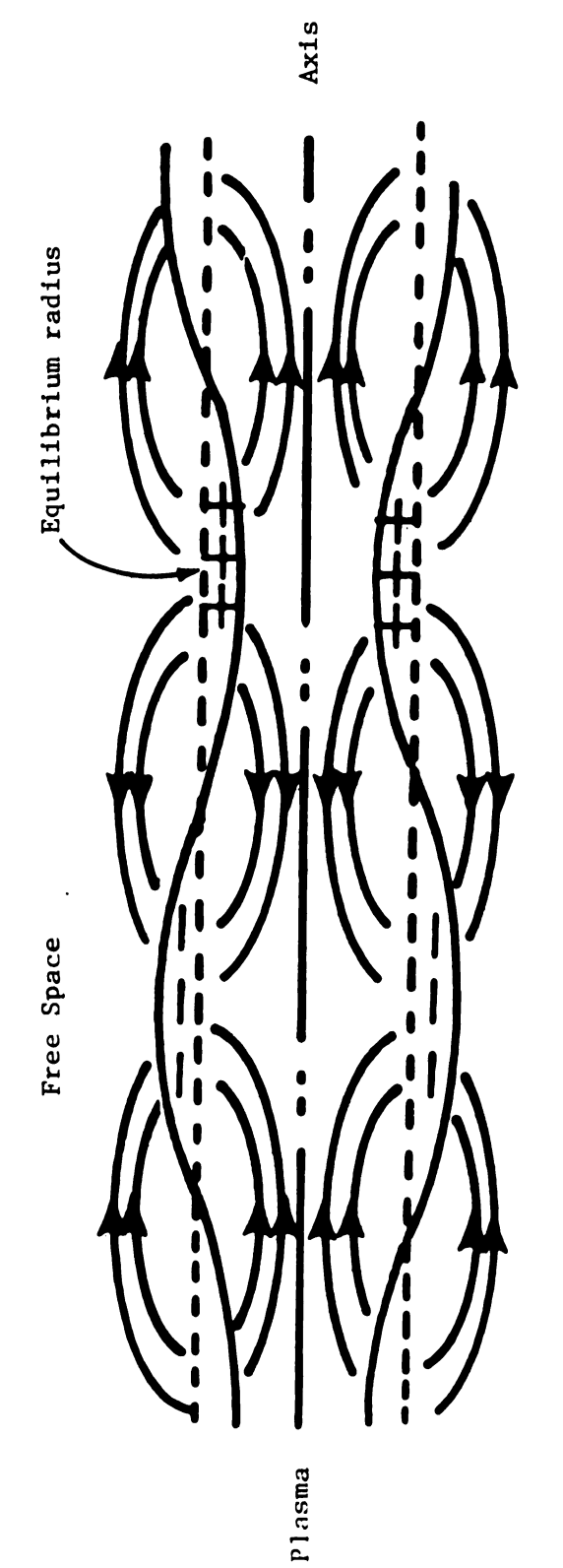
(a) Lossless plasma or $v_e/\omega_{pe} = 0$. Trivelpiece 12 has investigated this case extensively. The ω - k diagram (figures 2.3a, 2.4a, 2.4c, 2.5a) show that when $v_e/w_p = 0$, propagation is possible from zero frequency up to the slow wave resonance frequency $\omega = \omega_{pe} / \sqrt{1+k_e}$, where k_{ρ} is the relative dielectric constant of the quartz tube. For $k_{\rho} = 1$, i.e., free space or no quartz tube, $\omega = \omega_{pe} / \sqrt{2}$. The effect of the quartz tube is essentially to lower the frequency of the slow wave resonance. The TM_{00} mode $(v_e/\omega_{pe}=0)$ is a slow wave and lies entirely to the right of the light line. As $\omega \rightarrow \omega_{pe}/\sqrt{1+k_e}$, both the phase velocity and the group velocity $\mathbf{V}_{\underline{\varphi}}$ and $\mathbf{V}_{\underline{g}}$ respectively, approach zero. Thus, at $\omega = \omega_{pe} / \sqrt{1+k_e}$, this mode become a non-propagating space charge oscillation. However, as $\omega \rightarrow \omega_{pe}/\sqrt{1+k_e}$, there are limitations to the cold plasma theory. For $T_{\rho} \neq 0$, i.e., a warm plasma, and as β/k_{c} approaches the thermal velocity line, warm plasma effects will alter the results and for still large $\beta/k_{_{\rm C}}$'s collisionless Landau damping becomes predominant. In this region, the cold plasma theory no longer holds.

This mode can propagate only if the plasma partially fills the metallic waveguide since its propagation depends on surface charge accumulation. This would require that a dielectric region separate the plasma column and the circular waveguide. In most practical cases, the

separating dielectric region is a combination of free space and a dielectric tubing containing the plasma. The electric field and charge 12 on such an isotropic plasma column are shown in Figure 2.6. At frequencies close to the slow wave resonance frequency $\omega^*\omega_{\rm pe}$ / $\sqrt{1+k_{\alpha}}$, β is large. If $\beta t \approx 1$, where t = thickness of the quartz dielectric, then the fields would be confined entirely to the dielectric and the plasma 12 . The phase velocity at these frequencies is, thus, determined by the thickness of the dielectric, the value of the dielectric constant k_{α} , and the properties of the plasma. At low frequencies or high plasma densities, ω/ω_{pe} <<1, βa is small (Figures 2.3a, 2.4a, and 2.5a) and the effect of the quartz dielectric is negligible. The plasma assumes conductor-like properties and fields exist primarily in the region between the plasma and the metallic boundary. The surface currents on the plasma penetrates a thin outer shell into the plasma just as surface currents on the inner wall of the outer metallic waveguide penetrates a skin-depth layer. The TM_{00} mode, in this case, approaches the TEM mode. The TM_{00} lossless curve gets closer to the light line with increasing f_{ne} and, as a result, the frequency range of the TEM mode operation also increases.

Trivelpiece 12 has shown that it is possible to have a backward wave region for the lossless case, by using a thin dielectric of high permittivity. However, the dielectric thickness, permittivity and waveguide dimensions chosen here are such that this region does not exist in the ω - β diagrams of figures 2.3a, 2.4a, and 2.5a.

(b) Lossy plasma or $v_e/\omega_{pe} \neq 0$. In practical gas discharges where energy losses due to electron-neutral collisions cannot be ignored, it is important to study the propagation of space charge modes as v_e , the effective collision frequency is varied. The study of the



Field distribution and charge perturbation for circularly symmetric $_{\rm 12}$ surface wave on isotropic plasma column. Reproduced from Trivelpiece $^{\rm 12}$ Figure 2.6.

lossy TM₀₀ mode is divided into three frequency regions: (ω/ω_{pe}) < 0.1, $0.1<(\omega/\omega_{pe})<1/\sqrt{1+k_e}$, and $(\omega/\omega_{pe})>1/\sqrt{1+k_e}$.

The low frequency behavior, $\omega/\omega_{\rm pe}$ <0.1, for a typical plasma density fpe = 6.0 GHz is shown in figures 2.4c and 2.4d. As density increases, the lossless curve shifts towards the light line. For small losses, $v_e/\omega_{\rm pe} \leq 0.1$, the difference between the lossy curve and the lossless curve is negligible. As $v_e/\omega_{\rm pe}$ becomes greater than 0.1, the deviation of the lossy curves from the lossless curve is more significant. At low frequencies and high collisional losses ($v_e/\omega_{\rm pe}$ =0.525, 1, 10) the departure of the curves from the lossless TEM mode of operation is apparent (figures 2.4c and 2.4d). This is consistent with the values of the complex dielectric constant for frequencies in the region ($\omega/\omega_{\rm pe}$) \leq 0.1 (figures 2.7a and 2.7b) because at high collision frequencies the plasma properties approach that of a lossy dielectric. The attenuation curves at low frequencies are shown in figures 2.3b, 2.4d, and 2.5b.

For frequencies in the range $0.10 < \omega/\omega_{pe} < 1/\sqrt{1+k_e}$, the deviation of the small loss curves, $v_e/\omega_{pe} < 0.1$, from the lossless curve is negligible (figures 2.3a, 2.4a and 2.5a). The wave damping due to collisions in this frequency range and for $v_e/\omega_{pe} < 0.1$ is also small as shown by the ω/ω_{pe} vs. α/k_c curves (figures 2.3b, 2.4b and 2.5b). For instance, for the following given plasma parameters: $f_{pe} = 6.0$ GHz, $v_e/\omega_{pe} = 0.05$ and $\omega/\omega_{pe} = 0.35$, a wave of unit amplitude is attenuated in a distance of one wavelength to 0.285. The approximate frequency range $0.25 < \omega/\omega_{pe} < 1/\sqrt{1+k_e}$ would correspond to a region where an experimental generation of space charge waves would be possible.

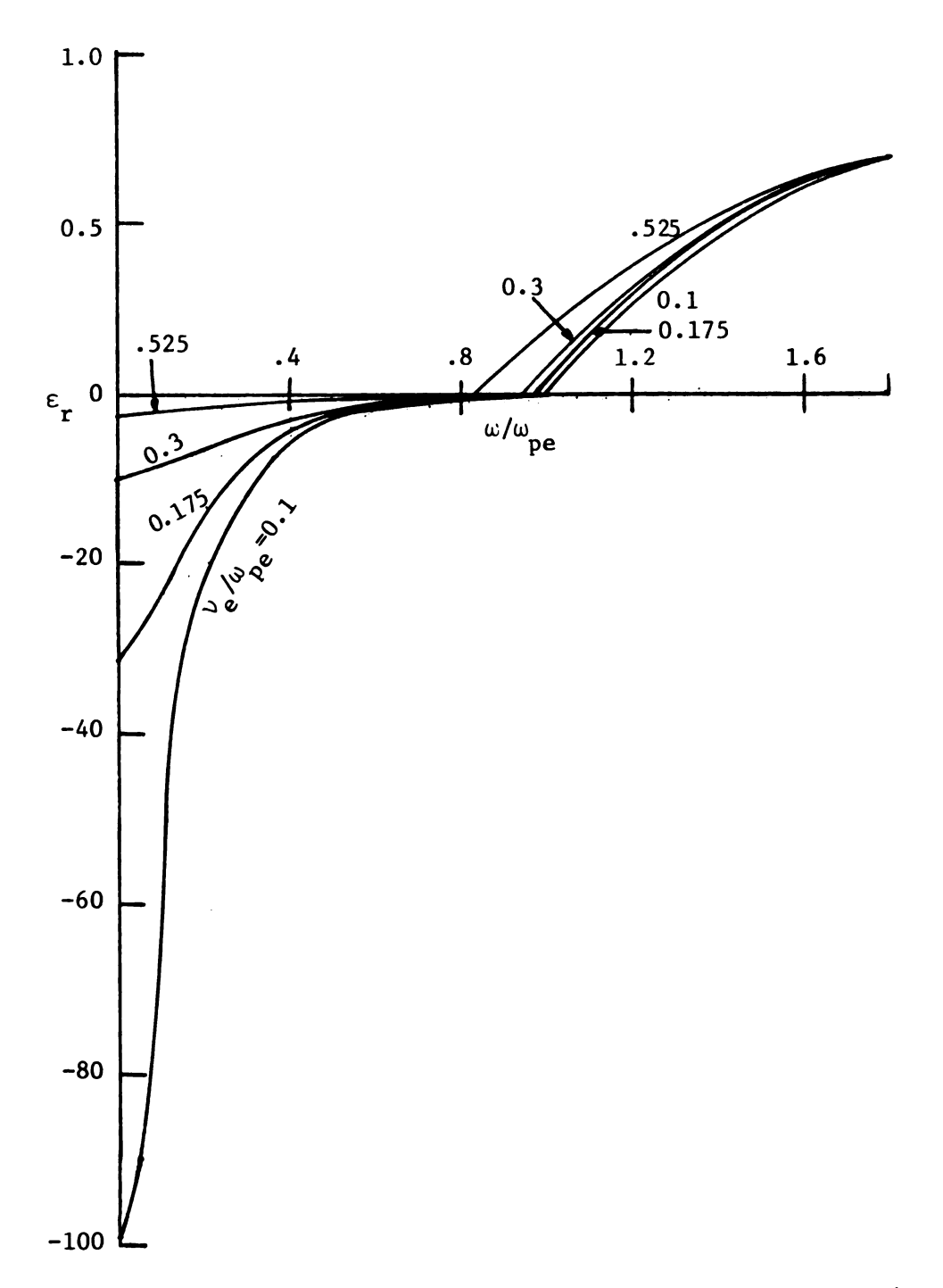


Figure 2.7a. Real part of plasma dielectric constant ϵ_r vs. ω/ω_{pe} and v_e/ω_{pe} . f_{pe} = 6 GHz.

•

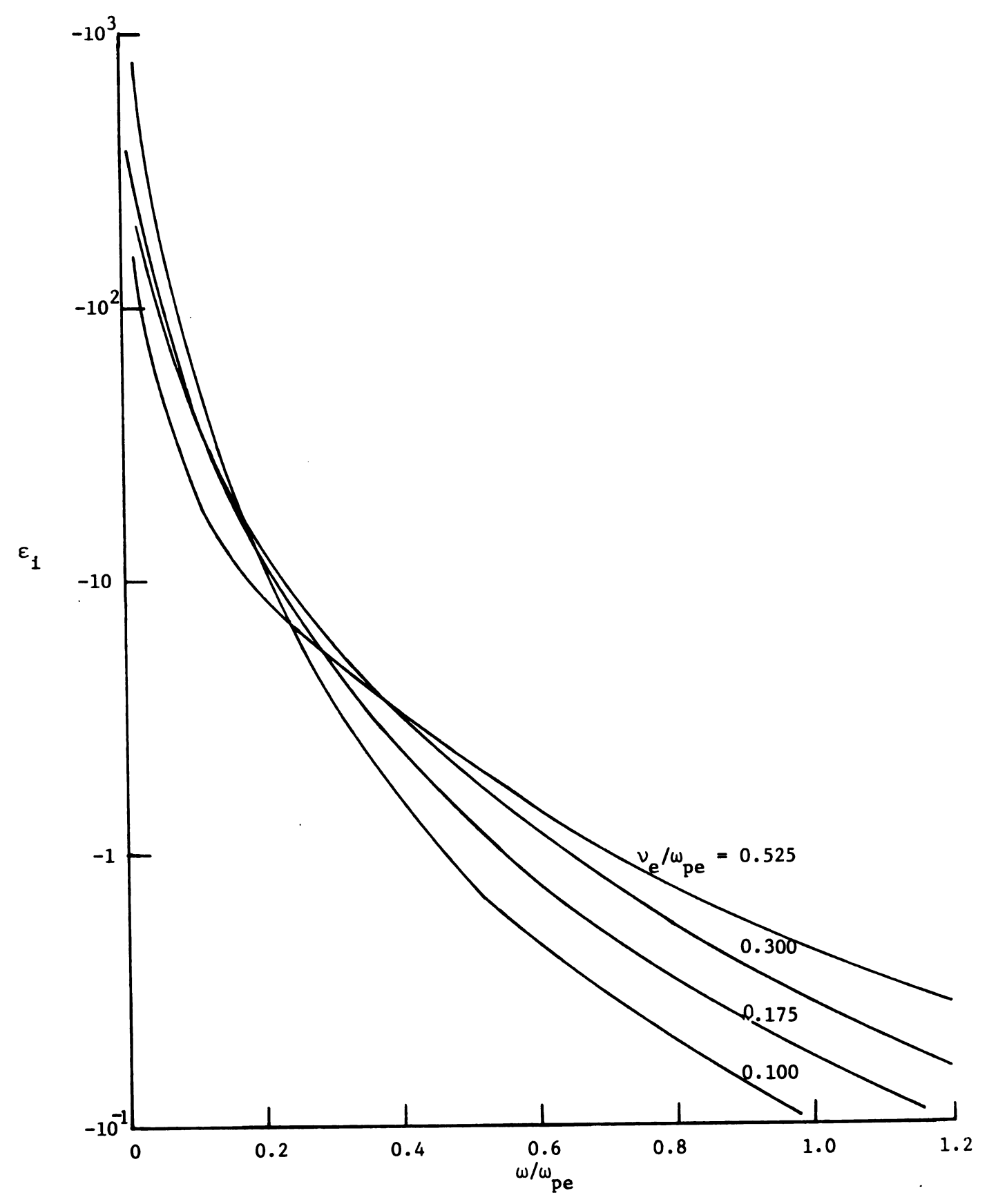


Figure 2.7b. Imaginary part of plasma dielectric constant ϵ_i vs. ω/ω_{pe} and ν_e/ω_{pe} . f_{pe} = 6.0 GHz.

The lossy curve, unlike the lossless curve, does not become asymptotic to $\omega = \omega_{pe} / \sqrt{1+k_e}$, at high values of β/k_c . A non-zero value of (v_e/ω_{pe}) removes the singularity 19 of the lossless curve at the frequency $(\omega/\omega_{pe}) = 1/\sqrt{1+k_e}$. Therefore, in the presence of losses, (β/k_c) decreases with frequency for $\omega > \omega_{\rm pe} / \sqrt{1+k_{\rm e}}$. It crosses the light line, becomes a fast wave and at very high frequencies becomes asymptotic to the light line, (see figure 2.2a). The lossy curve thus, becomes a backward wave in the frequency range $1/\sqrt{1+k_e} \le \omega/\omega_{\rm ne} \lesssim 0.9$ (figures 2.3a, 2.4a and 2.5a). This backward wave region, however, is highly damped as shown by the ω/ω_{pe} vs. α/k_c curves (figures 2.3b, 2.4b, and 2.5b) and is no longer a true wave phenomenon. For example, for the following given plasma parameters: $f_{pe} = 6.0 \text{ GHz}$, $v_e/\omega_{pe} = 0.1 \text{ and } \omega/\omega_{pe}$ = 0.44, a wave of unit amplitude is attenuated in a distance of one wavelength to 0.0031. These curves also indicate that for very small losses, say $v_e/\omega_{pe} \leq 0.01$, it might be possible to have a frequency range where the backward space charge waves are not altogether damped. Computation problems prevented the generation of such curves.

As seen in figure 2.2b, beyond $\omega=\omega_{pe}/\sqrt{1+k_e}$, α/k_c increases with ω/ω_{pe} for a given ν_e/ω_{pe} , reaches a maximum then decreases and eventually tends to zero at very high frequencies. At very high frequencies, $\omega/\omega_{pe}>>1$, all the lossy TM_{00} curves asymptotically approach the light line. Figures 2.2a and 2.2b show this behavior for $f_{pe}=6.0$ GHz, and $\nu_e/\omega_{pe}=0.1$. This high frequency part of the curve is consistent with the value of the complex dielectric constant of the plasma at such frequencies and losses, (figures 2.7a and 2.7b). For an $f_{pe}=6.0$ GHz and a given (ν_e/ω_{pe}) , ε_r+1 and ε_1+0 as ω becomes very large. At these frequencies, the plasma waveguide becomes an empty circular waveguide and the TM_{00} mode behaves as a circular waveguide mode.

$\frac{\text{TM}}{01} \frac{\text{mode}}{1}$:

This is a rotationally symmetric mode and, hence, purely transverse magnetic. Its characteristic equation is given by equation 2.69. Its field pattern is easily analyzed even in the presence of the plasma. It has radial and longitudinal electric fields E_p and E_z , respectively, and a circular magnetic field H_{φ} . The dispersion equation is solved for ω/ω_{pe} vs. β/k_c with ω_{pe}/ω_c and ν_e/ω_{pe} as variable parameters. Figures 2.8a, 2.9a, 2.8b and 2.9b show ω/ω_{pe} vs. β/k_c and ω/ω_{pe} vs. α/k_c for f_{pe} = 10.5 GHz and f_{pe} = 20.0 GHz, respectively, and a range of losses. Figures 2.8c and 2.8d show the low frequency details of the ω/ω_{pe} vs. β/k_c and ω/ω_{pe} vs. α/k_c diagrams for f_{pe} = 10.5 GHz.

- (a) Lossless plasma or $v_e/w_{pe}=0$. As seen in figure 2.8a, for $f_{pe}=10.5$ GHz, this mode is cut off below $\omega/\omega_{pe}=0.23$ or f=2.42 GHz. An increase in the plasma density to $f_{pe}=20.0$ GHz as shown in figure 2.9a, raises the cut off frequency to $\omega/\omega_{pe}=0.134$ or f=2.68 GHz. The TM $_{01}$ coaxial mode cut off frequency for the waveguide dimensions chosen is f=2.92 GHz. Thus, the TM $_{01}$ cut off frequency is seen to approach f=2.92 GHz at very high plasma densities. The dispersion curves (figures 2.8a and 2.9a) are typical fast-wave electromagnetic solutions when $v_e/\omega_{pe}=0$. At high frequencies, the curves asymptotically approach the light line and become the TM $_{01}$ empty waveguide mode.
- (b) Lossy plasma or $v_e/\omega_{pe} \neq 0$. As shown in figures 2.8a and 2.9a, at high frequencies all the loss curves are asymptotic to the light line and deviate very little from the lossless curve. Also, the collisional damping at these frequencies is negligible, see figures 2.8b and 2.9b. As ω/ω_{pe} approaches the region $\omega/\omega_{pe} \approx 0.23$ in figure 2.8a, the deviation of the lossy curve from the $v_e/\omega_{pe} = 0$ curve is more significant. The

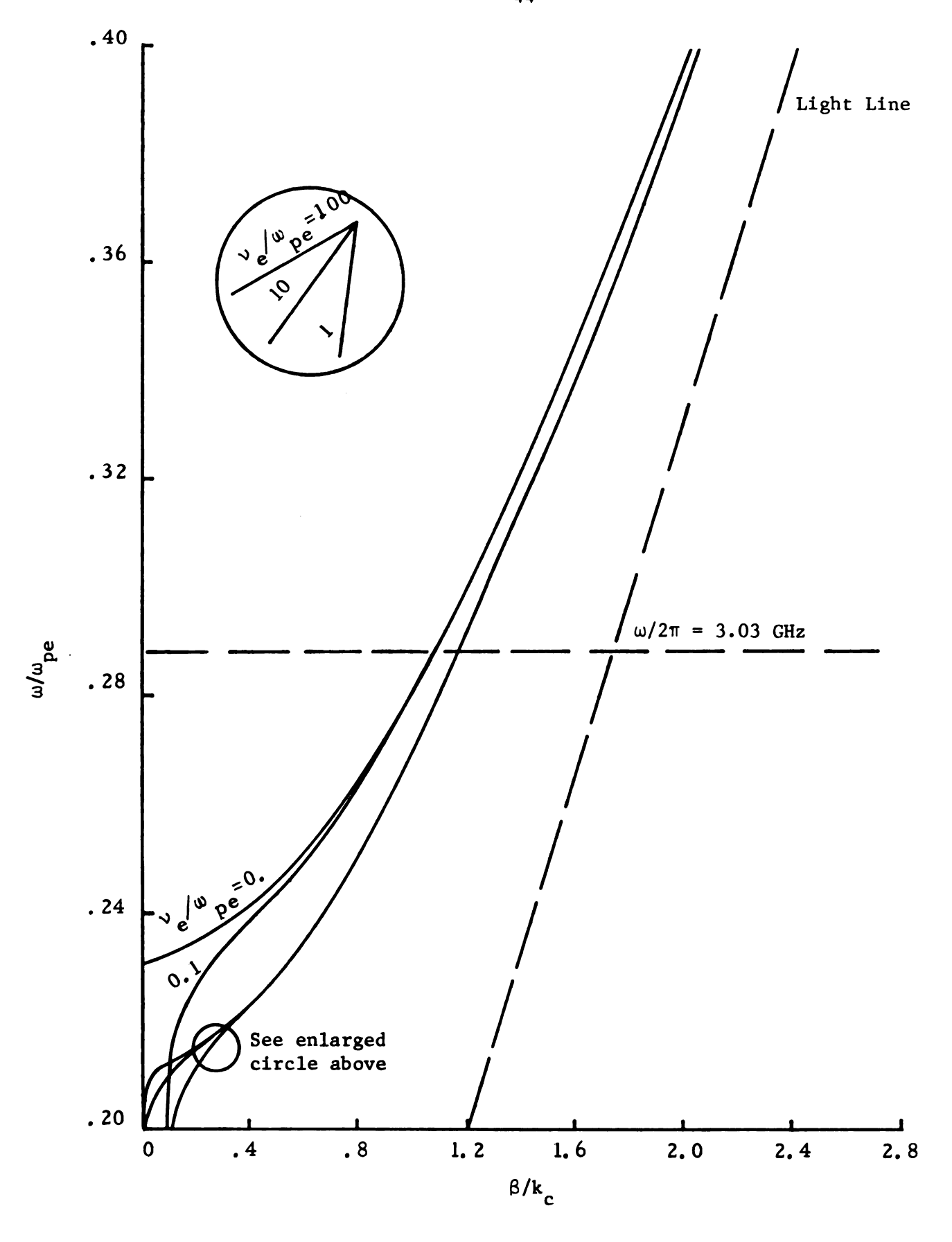


Figure 2.8a. $\omega/\omega_{\rm pe}$ vs. $\beta/k_{\rm c}$ for the TM $_{01}$ mode. $f_{\rm pe}$ = 10.5 GHz, $\omega_{\rm pe}/\omega_{\rm c}$ = 6.1. Waveguide dimensions: a = 0.3 cms., b = 0.3875 cms., c = 5.08 cms.

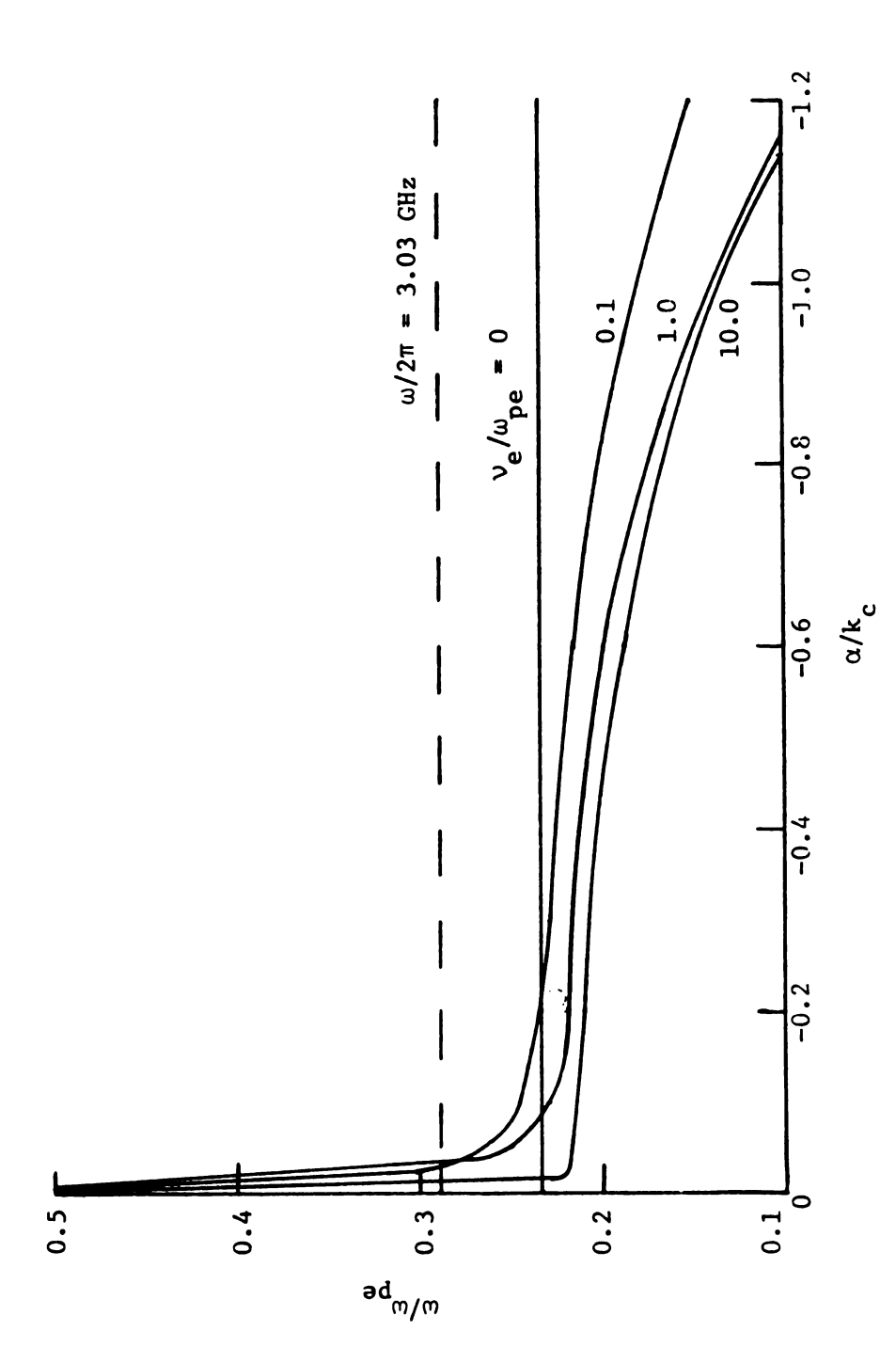


Figure 2.8b. ω/ω vs. α/k for the TM mode. f = 10.5 GHz, ω ω ω = 6.08. Waveguide dimensions: a = 0.3 cms., b = 0.3875 cms., c = 5.08 cms.

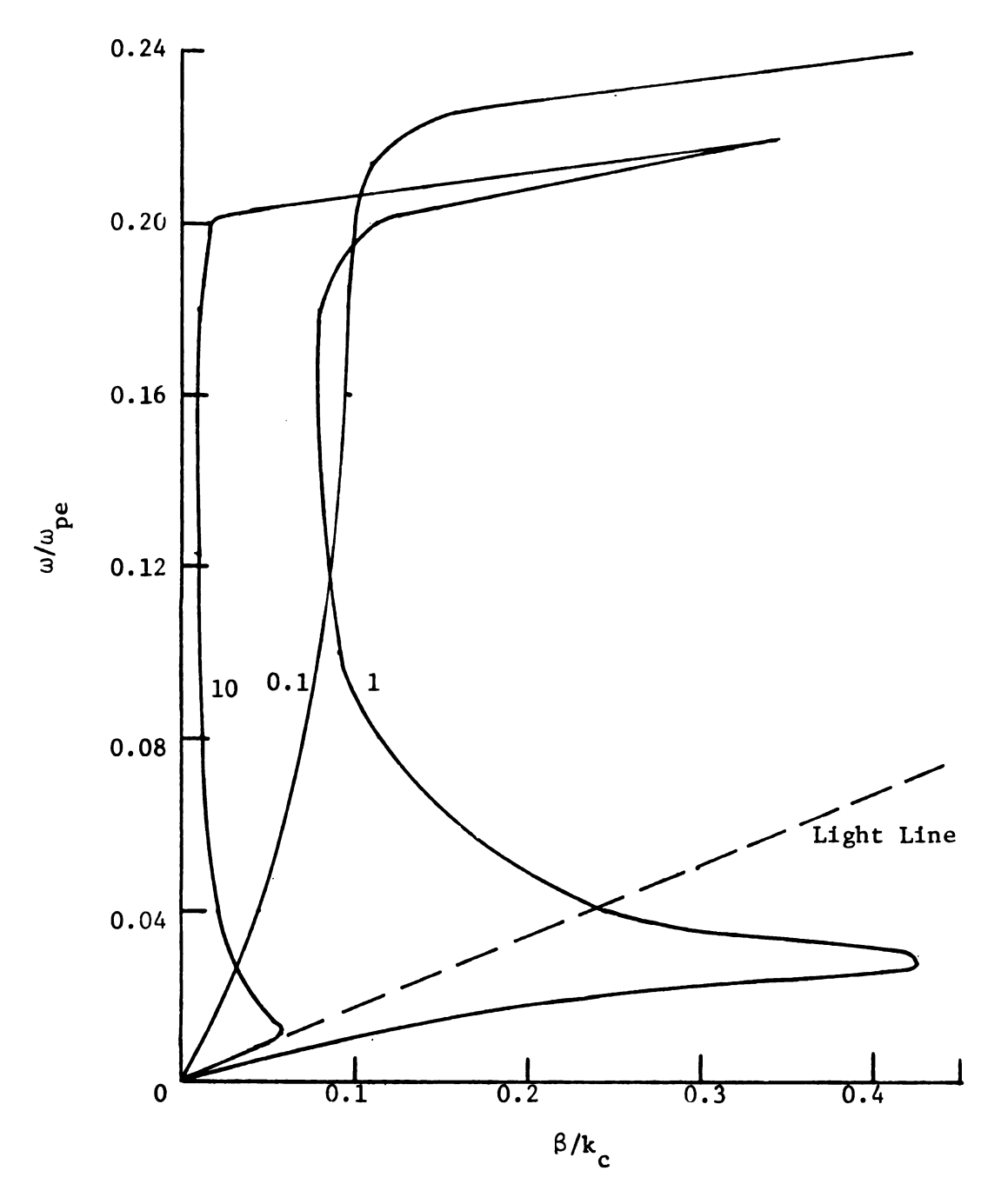


Figure 2.8c. $\omega/\omega_{\rm pe}$ vs. $\beta/k_{\rm c}$ for the TM $_{01}$ mode for $\omega/\omega_{\rm pe}$ < 0.24. f = 10.5 GHz, $\omega_{\rm pe}/\omega_{\rm c}$ = 6.1. Waveguide dimensions: a = 0.3 cms., b = 0.3875 cms., c = 5.08 cms.

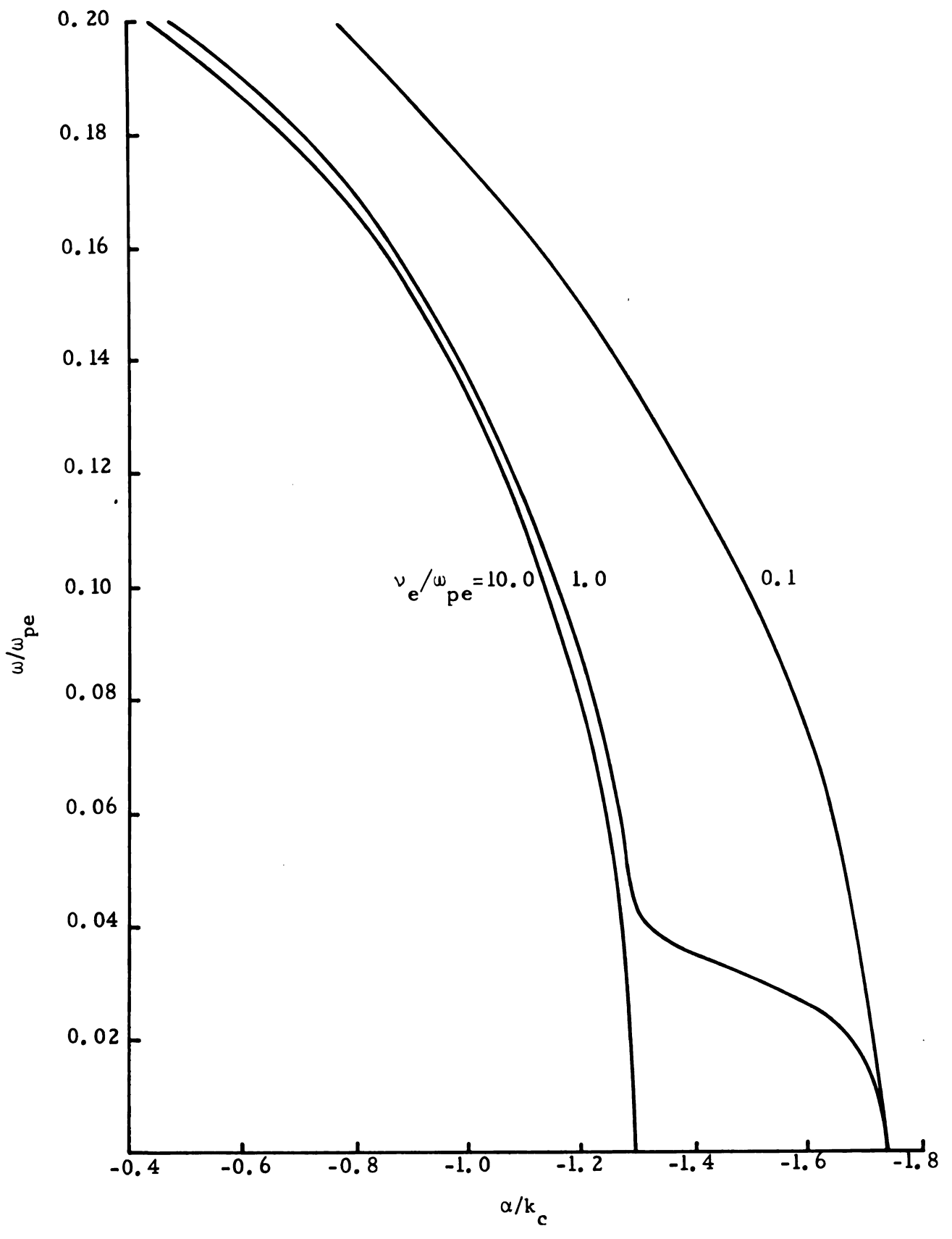


Figure 2.8d. $\omega/\omega_{\rm pe}$ vs. $\alpha/k_{\rm c}$ for the TM₀₁ mode for $\omega/\omega_{\rm pe} \le 0.20$. $f_{\rm pe} = 10.5$ GHz, $\omega_{\rm pe}/\omega_{\rm c} = 6.08$. Waveguide dimensions: a = 0.3 cms., b = 0.3875 cms., c = 5.08 cms.

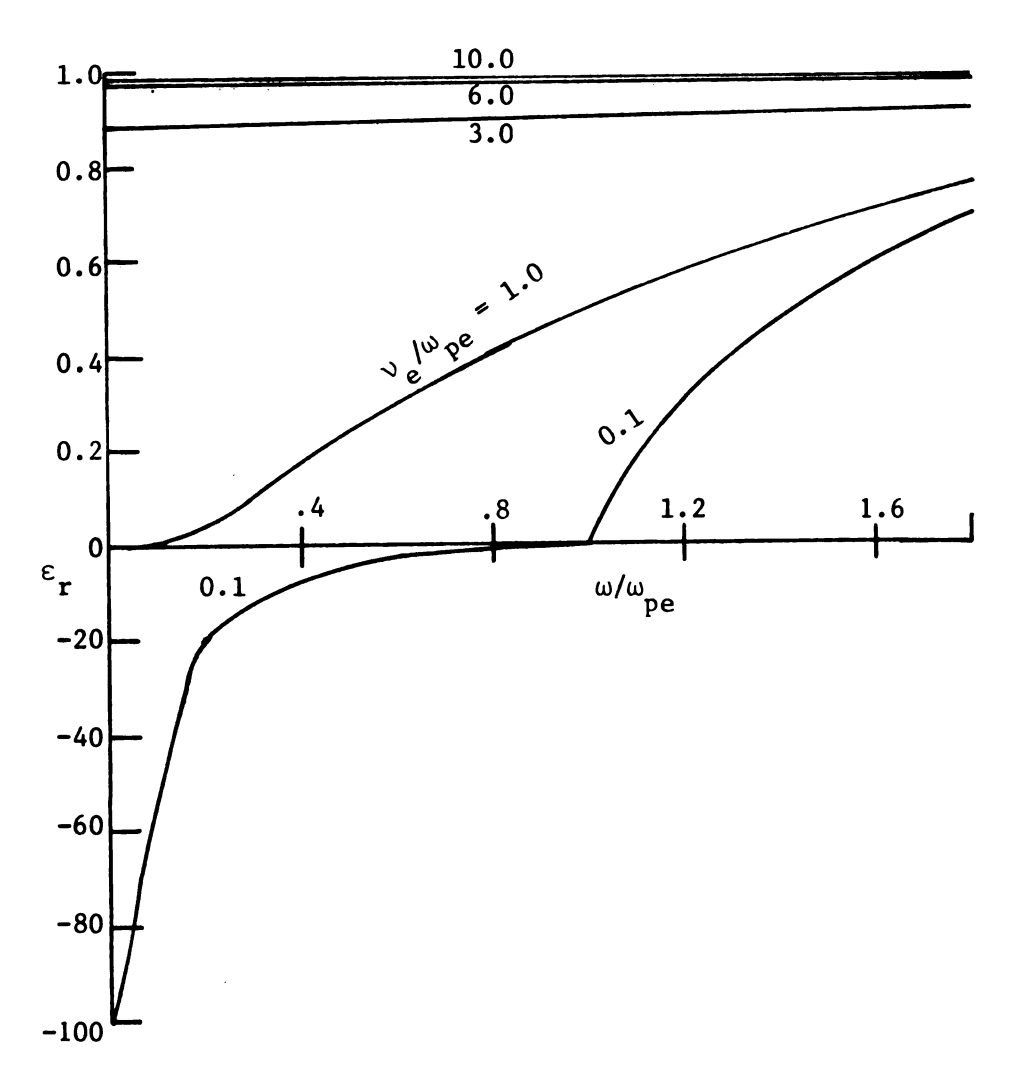


Figure 2.8e. Real part of plasma dielectric constant $\epsilon_{\rm r}$ vs. $\omega/\omega_{\rm pe}$ and $v_{\rm e}/\omega_{\rm pe}$. $f_{\rm pe}$ = 10.5 GHz.

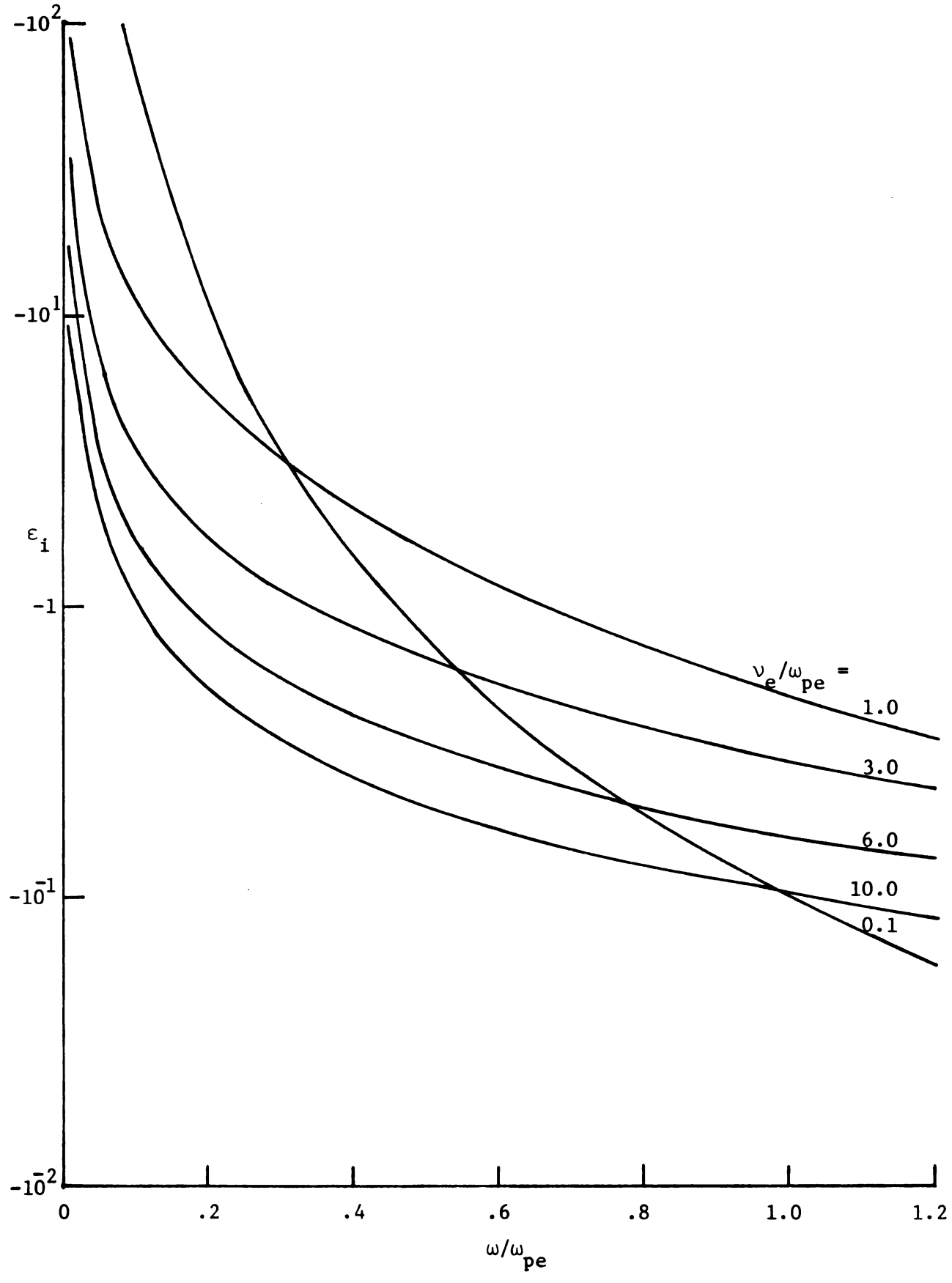


Figure 2.8f. Imaginary part of plasma dielectric constant ϵ_i vs. ω/ω_{pe} and v_e/ω_{pe} . f_{pe} = 10.5 GHz.

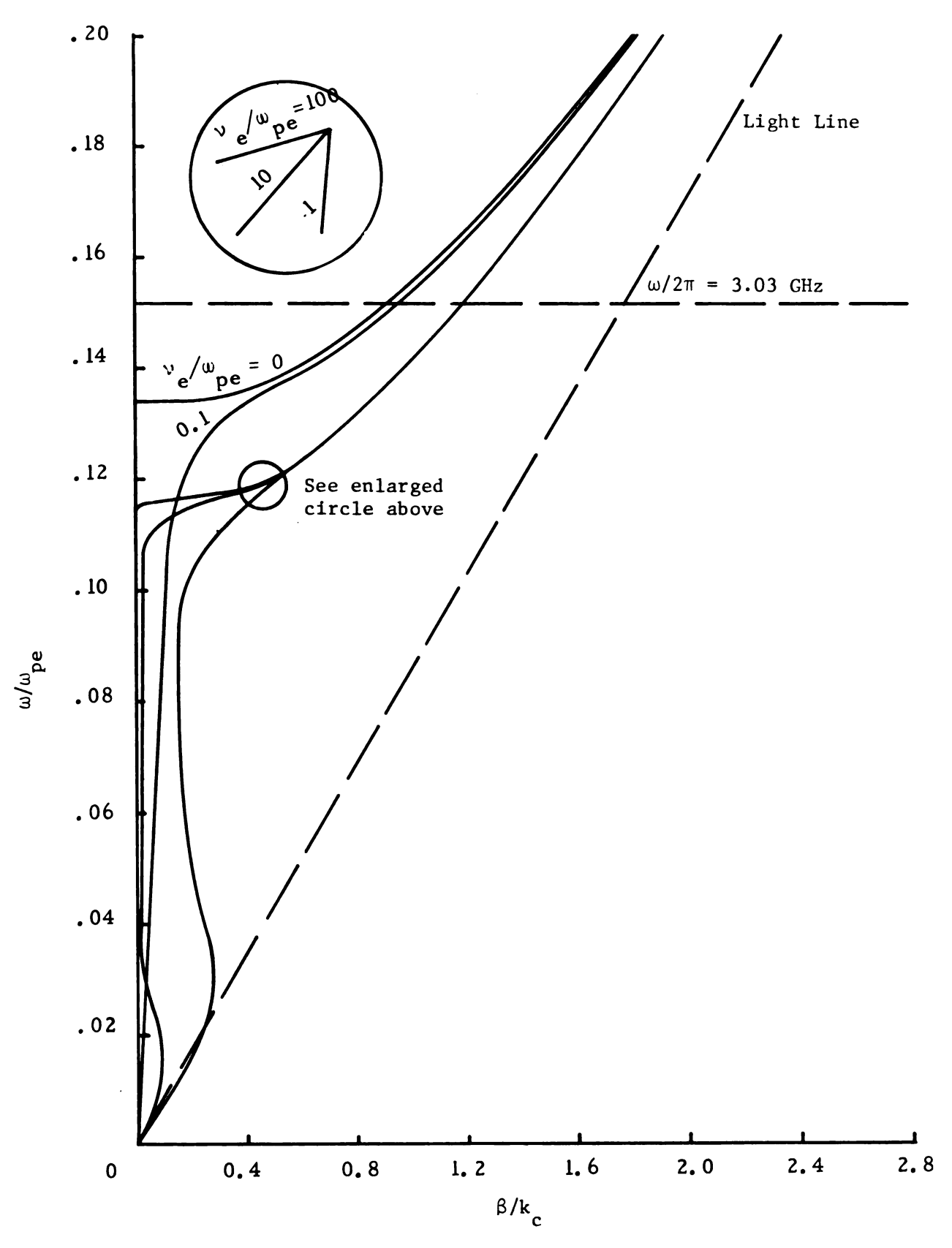


Figure 2.9a. $\omega/\omega_{\rm pe}$ vs. $\beta/k_{\rm c}$ for the TM $_{01}$ mode. $f_{\rm pe}$ = 20 GHz, $\omega_{\rm pe}/\omega_{\rm c}$ = 11.6. Waveguide dimensions: a = 0.3 cms., b = 0.3875 cms., c = 5.08 cms.

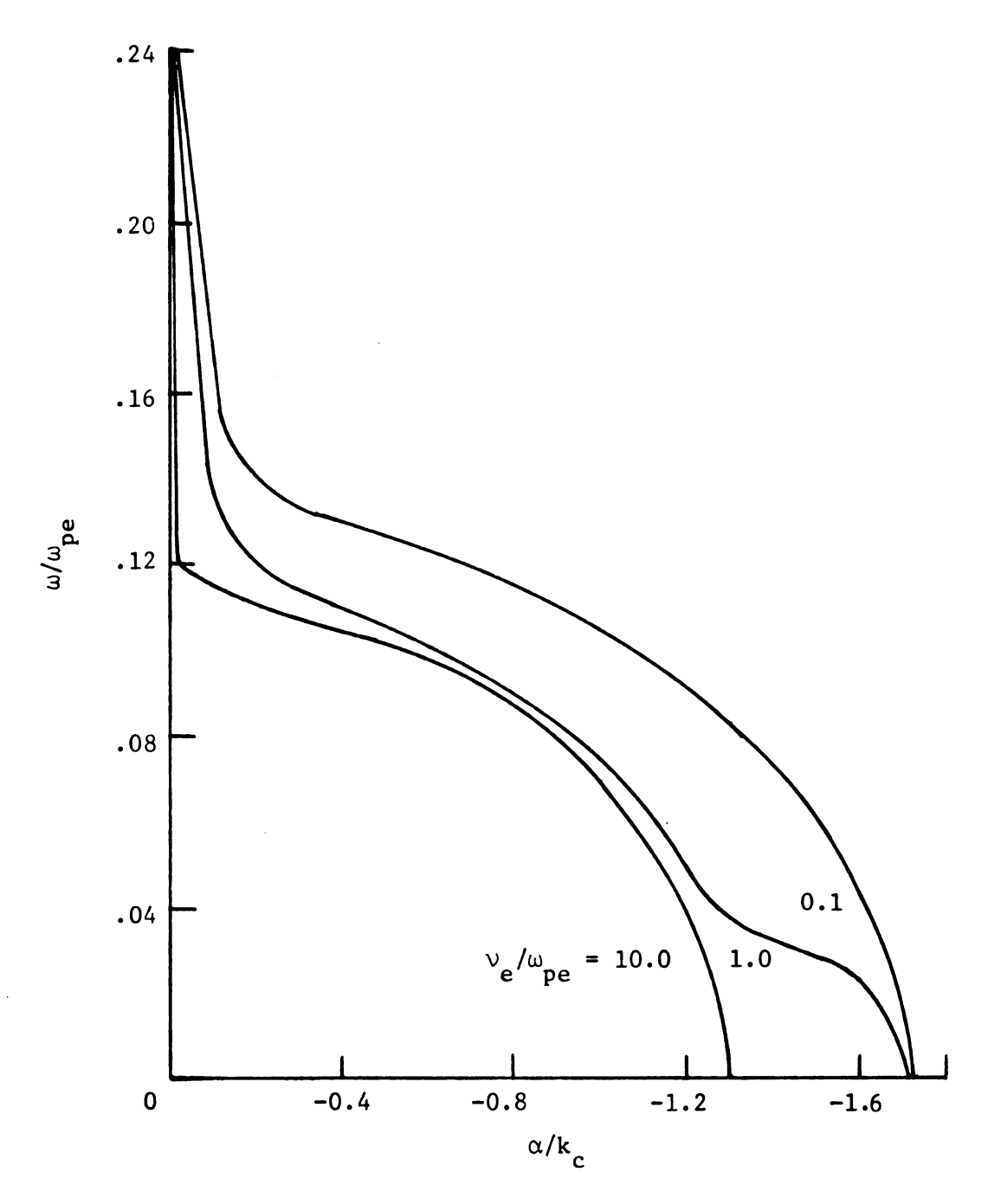


Figure 2.9b. $\omega/\omega_{\rm pe}$ vs. $\alpha/k_{\rm c}$ for the TM $_{01}$ mode. f = 20 GHz, $\omega_{\rm pe}/\omega_{\rm c}$ = 11.6. Waveguide dimensions: a = 0.3 cms., b = 0.3875 cms., c = 5.08 cms.

lossy curve has no cut off frequency. β/k decreases with ω/ω and becomes zero when $\omega/\omega_{\rm pe}$ = 0, as shown in figures 2.8c and 2.9a. The attenuation per unit wavelength for all the lossy curves for frequencies below ω/ω_{pe} = 0.21 in figure 2.8c and below ω/ω_{pe} = 0.115 in figure 2.9a is very high. For instance, for the following given plasma parameters: $f_{pe} = 10.5 \text{ GHz}$, $v_e/\omega_{pe} = 0.1 \text{ and } \omega/\omega_{pe} = 0.20$, a wave of unit amplitude is attenuated in a distance of one wavelength to 7×10^{-23} . The curves for small losses v_e/ω_{pe} = 0.1 (figures 2.8a and 2.9a) almost coincide with the lossless curves above the cut off frequency. As v_e/w_{pe} is increased through the range 1 to 100 (figure 2.8a), the difference between the lossy and lossless curves above the cut off frequency is more apparent. For very high losses $v_e/\omega_{pe} = 100$ (figure 2.8a), the mode appears to be practically cut off for frequencies below ω \leq 0.208 $\omega_{_{\mbox{\footnotesize{De}}}}$ or f = 2.2 GHz. So with the plasma density fixed and as $v_e/w_{pe}^{\to\infty}$ the cut off frequency of this mode approaches that of the TM_{01} circular waveguide mode. This behavior is consistent with the value of the complex dielectric at (ω/ω_{pe}) ~0.208 and f = 10.5 GHz (figures 2.8e and 2.8f). As (v_e/ω_{pe}) increases at this frequency, ε_r^{-1} and ε_i^{-0} .

At high frequencies, i.e., a large $\omega/\omega_{\rm pe}$, $\varepsilon_{\rm r}^{\to 1}$, $\varepsilon_{\rm i}^{\to 0}$ (figures 2.8e and 2.8f) and this mode approaches the ${\rm TM}_{01}$ waveguide mode without a plasma. As $\omega \to 0$, $\varepsilon_{\rm r}$ remains finite and $\varepsilon_{\rm i}^{\to -\infty}$. The plasma becomes a lossy conductor and the ${\rm TM}_{01}$ mode is, thus, highly damped at very low frequencies.

TE11 and TM10 modes.

The dispersion relation for these modes is obtained by putting n = 1 in equation 2.62. Because of their hybrid nature, these modes

have all the possible electric and magnetic field components, i.e., $E_{\rho}, \ E_{\phi}, \ E_{z} \ \text{and} \ H_{\rho}, \ H_{\phi}, \ H_{z}, \ \text{respectively.} \ \text{The dispersion equation is}$ solved for ω/ω_{pe} vs. β/k_{c} with ω_{pe}/ω_{c} and ν_{e}/ω_{pe} as variable parameters. Figures 2.10a, 2.10b, 2.10c and 2.10d show the ω/ω_{pe} vs. β/k_{c} and ω/ω_{pe} vs. α/k_{c} for a typical plasma density of f_{pe} = 5.3 GHz. Several features of these curves will now be explained.

(a) Lossless plasma or $v_e/\omega_{pe}=0$. For $f_{pe}=5.3$ GHz, the TE_{11}^* mode has a cut off frequency at $\omega=0.58~\omega_{pe}$ for the guide dimensions of a = 3 cms., b = 0.3875 cms. c = 5.08 cms. This mode has the lowest cut off frequency in both the circular and coaxial waveguides. It is a typical fast electromagnetic wave, eventually becoming asymptotic to the light line. At very high plasma densitities, the cut off frequency of this mode approaches the TM_{11} coaxial mode cut off frequency. $(\omega/\omega_{pe}=0.68)$.

The TM $_{10}^{\pi}$ mode, which does not exist in the empty circular waveguide, has a cut off frequency at $\omega = 0.33~\omega_{pe}$ for waveguide dimensions: a=0.3 cms., b = 0.3875 cms., c = 5.08 cms. β/k_c increases with ω/ω_{pe} and this mode behaves like a fast wave up to $\beta = 1.86~k_c$. For $\beta>1.86~k_c$, this mode becomes a slow wave and eventually becomes asymptotic to the frequency of dipole resonance. This frequency obtained from the quasi static formula $\frac{16}{3}$.

static formula¹⁶,
$$\left(\omega_{pe}/\omega\right)^2 = 1 + \varepsilon_2 \frac{1 - \left(\frac{a}{b}\right)^2}{1 + \left(\frac{a}{b}\right)^2} \frac{1 + \left(\frac{a}{b}\right)^2}{1 + \left(\frac{a}{b}\right)^2}$$

is $\omega \simeq \omega_{pe} / \sqrt{3}$. In the formula, a = plasma radius, b = outer radius of

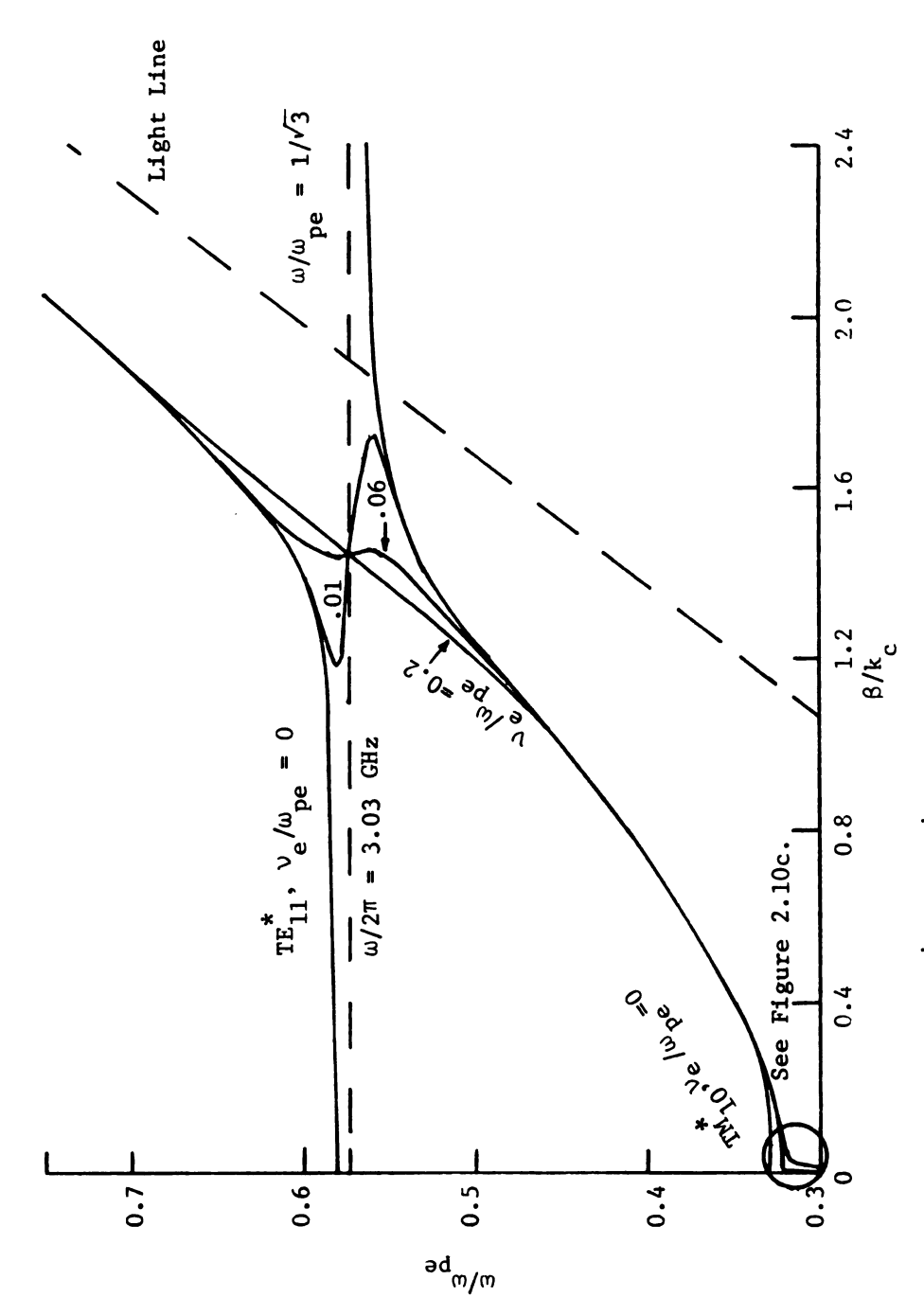


Figure 2.10a. ω/ω_{pe} vs. β/k_c for TM and TE $_{11}$ modes. f $_{pe}$ = 5.3 GHz, ω_{pe}/ω_{c} = 3.07. Waveguide dimensions: a = 0.3 cms., b = 0.3875 cms., c = 5.08 cms.

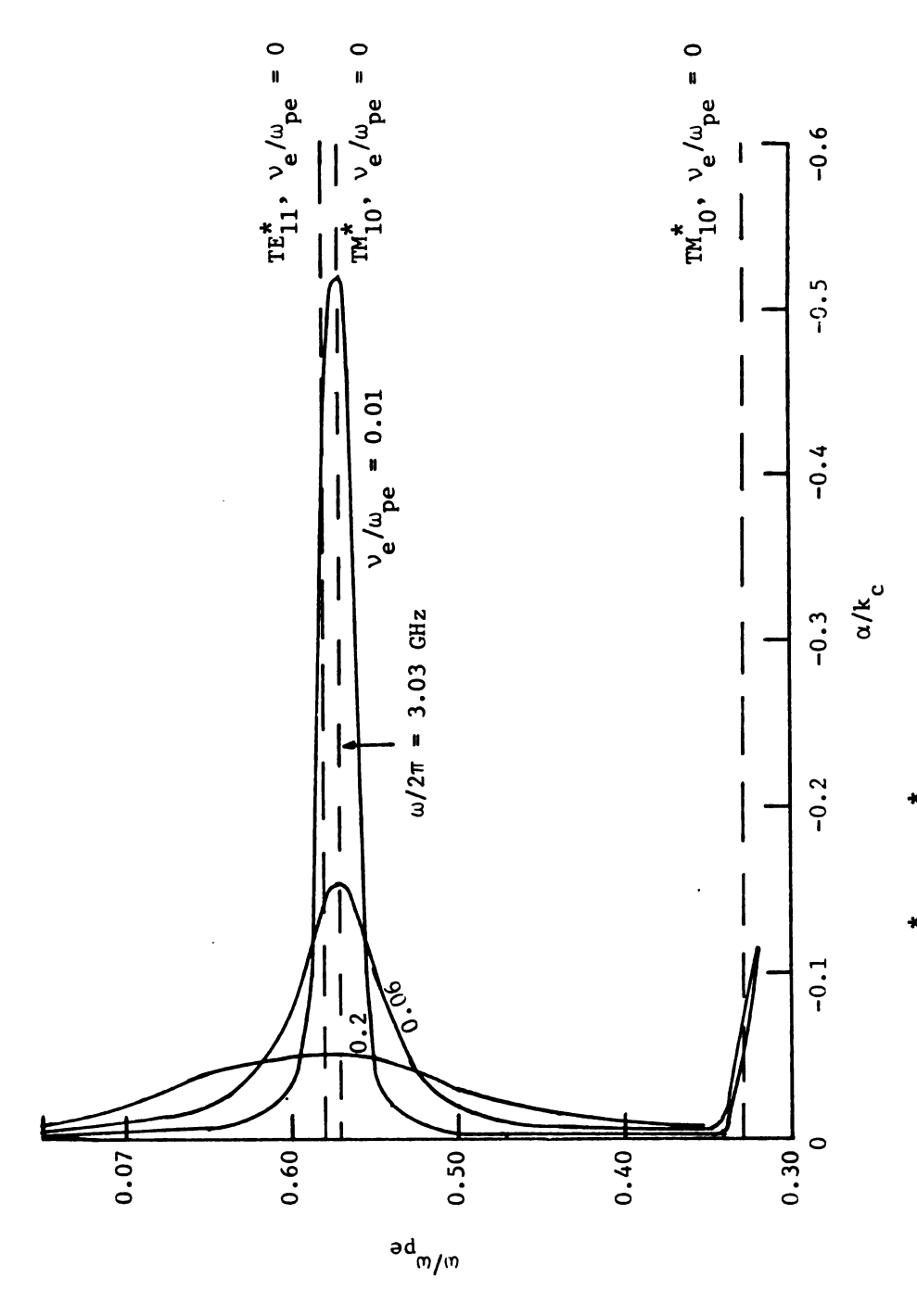


Figure 2.10b. ω/ω vs. α/k for TM and TE modes. f = 5.3 GHz, $\omega_{\rm pe}/\omega_{\rm c}$ = 3.07. Waveguide dimensions: a = 0.3 cms., b = 0.3875 cms., c = 5.08 cms.

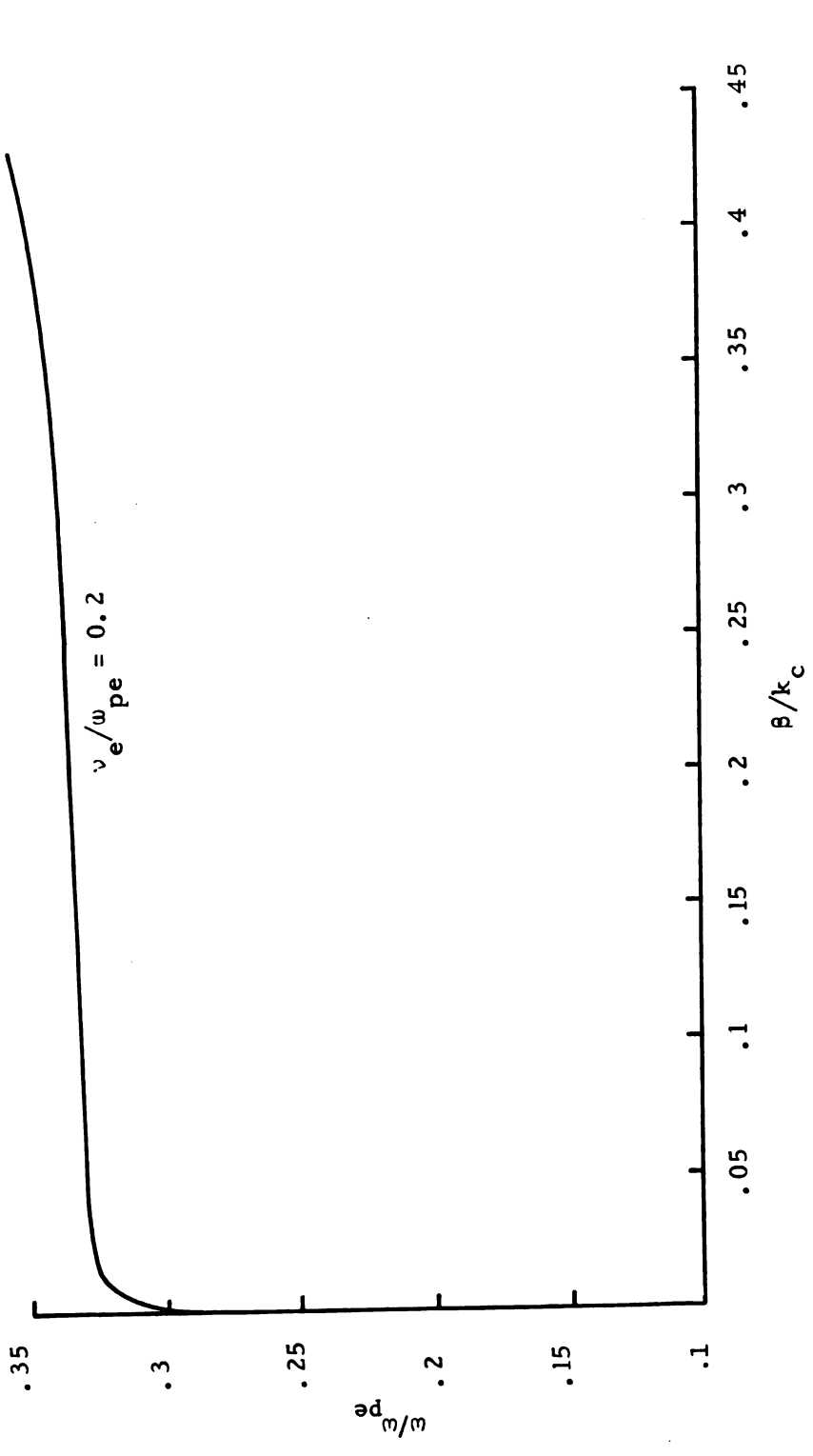


Figure 2.10c. ω/ω_p vs. β/k_c for the TE_{11}^* mode for $\omega/\omega_p < 0.35$ and $v_e/\omega_p = 0.2$ fpe = 5.3 GHz, $\omega_p = 0.2$ from $\omega_p = 0.2$ Waveguide dimensions: a = 0.3 cms., b = 0.3875 cms., c = 5.08 cms.

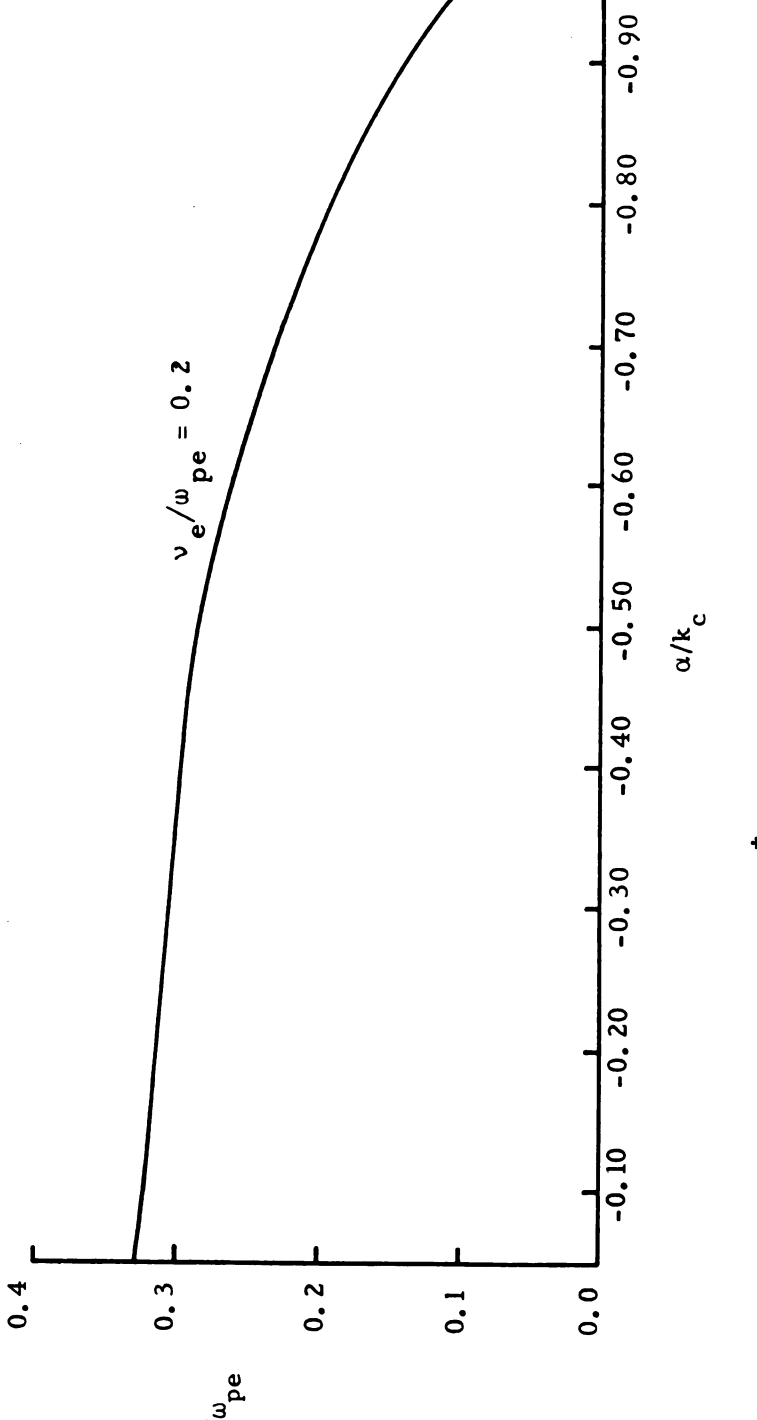


Figure 2.10d. ω/ω vs. α/k for the TE $_{11}^{\star}$ mode for ω/ω < 0.35 and v_e/ω = 0.2. f = 5.3 GHz, ω/ω = 3.07. Waveguide dimensions: a = 0.3 cms., b = 0.3875 cms., c = 5.08 cms.

dielectric tubing, and ε_2 = permittivity of the dielectric. Without the quartz dielectric this mode would have been asymptotic to the line $\omega = \omega_{\rm pe}/\sqrt{2}$. As ω approaches $\omega_{\rm pe}/\sqrt{3}$, the phase and group velocities $V_{\rm p}$ and $V_{\rm g}$ approach zero and the space charge oscillations are highly attenuated (Figure 2.10a). However, as $\omega \to \omega_{\rm pe}/\sqrt{3}$, $\beta/k_{\rm c}$ becomes large and the cold plasma theory is not valid in this region. Warm plasma theory considerably modifies the dispersion curve near $V_{\rm p} = V_{\rm th}$, where $V_{\rm th}$ = electron thermal velocity. For still larger $\beta/k_{\rm c}$'s when the wavelength becomes the same order of magnitude as $\lambda_{\rm de}$, the debye length, collisionless Landau damping becomes predominant. Thus, the present theory is not valid in that region for the lossless TM_{10}^* mode.

(b) Lossy plasma or $v_e/\omega_{pe} \neq 0$. When v_e/ω_{pe} is non-zero, the singularity of the TM $^*_{10}$ mode at the frequency of dipole resonance is removed. The TE $^*_{11}$ and the TM $^*_{10}$ modes have one distinct solution in the presence of losses.

As shown in Figure 2.10a, for very small collisional losses $(\nu_e/\omega_{pe}=0.01) \text{ and for } \omega > 0.334 \; \omega_{pe} \text{ the } \omega/\omega_{pe} \text{ vs. } \beta/k_c \text{ curve closely follows the lossless TM}^*_{10} \text{ curve up to } \omega = 0.55 \; \omega_{pe}. \quad \text{For } \omega > 0.55 \; \omega_{pe}, \\ \beta/k_c \text{ first decreases then increases and the dispersion curve becomes asymptotic to the lossless TE}^*_{11} \text{ mode solution.} \quad \text{A backward wave region is, thus, seen to exist in the frequency range } 0.565\omega_{pe} \leq \omega \leq 0.575 \; \omega_{pe}. \\ \text{The behavior of this curve below the frequency } \omega = 0.33 \; \omega_{pe} \text{ is shown in Figure 2.10c.} \quad \text{The lossy curve for small losses has no cut off frequency.} \\ \beta/k_c \text{ goes to zero as } \omega/\omega_{pe} \text{ tends to zero.}$

At higher losses ($v_e/w_{pe} = 0.2$), the backward wave region is not too prominent, but the asymptotic behavior of this curve outside the frequency range 0.55 ω_{pe} < ω <0.060 ω_{pe} remains the same. An examination of

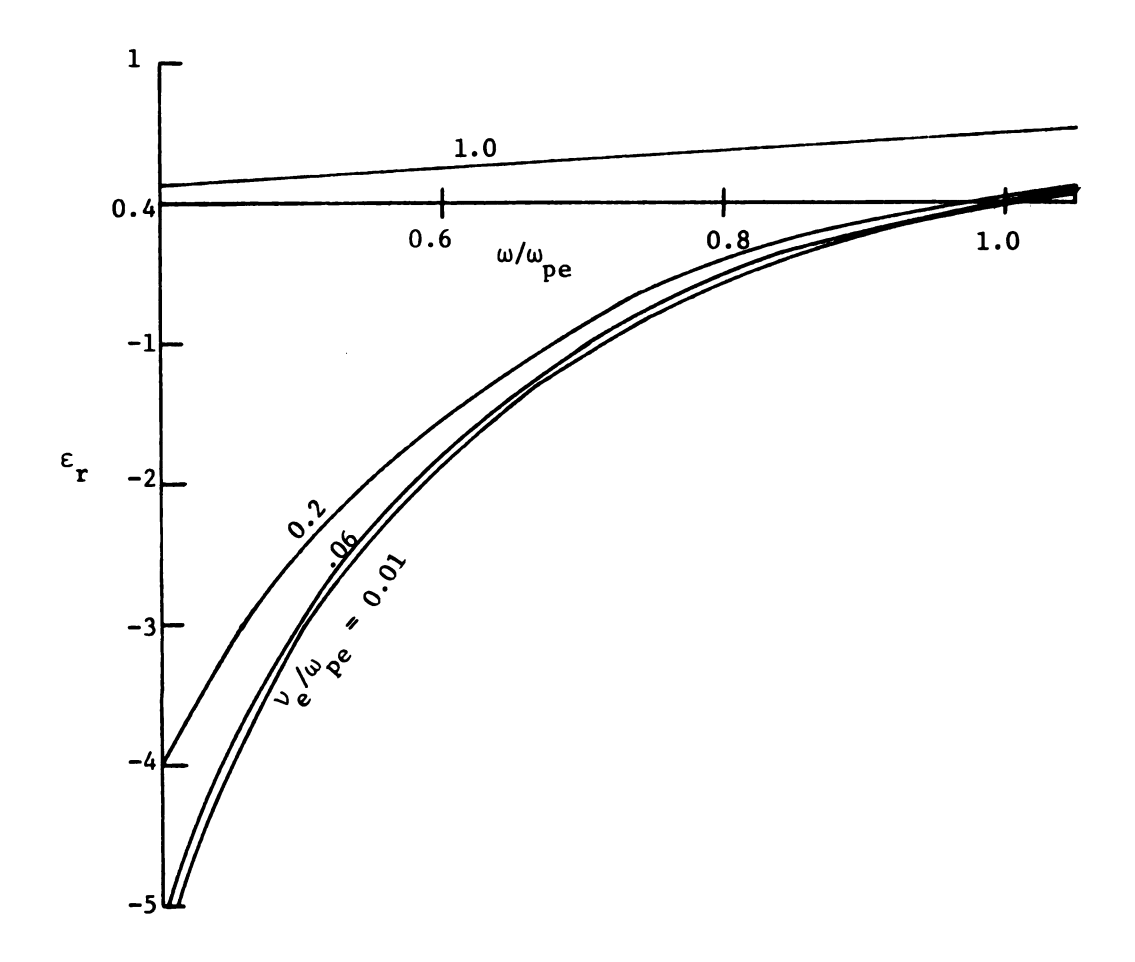


Figure 2.10e. Real part of plasma dielectric constant ϵ_r vs. ω/ω_{pe} and ν_e/ω_{pe} . f_{pe} = 5.3 GHz.

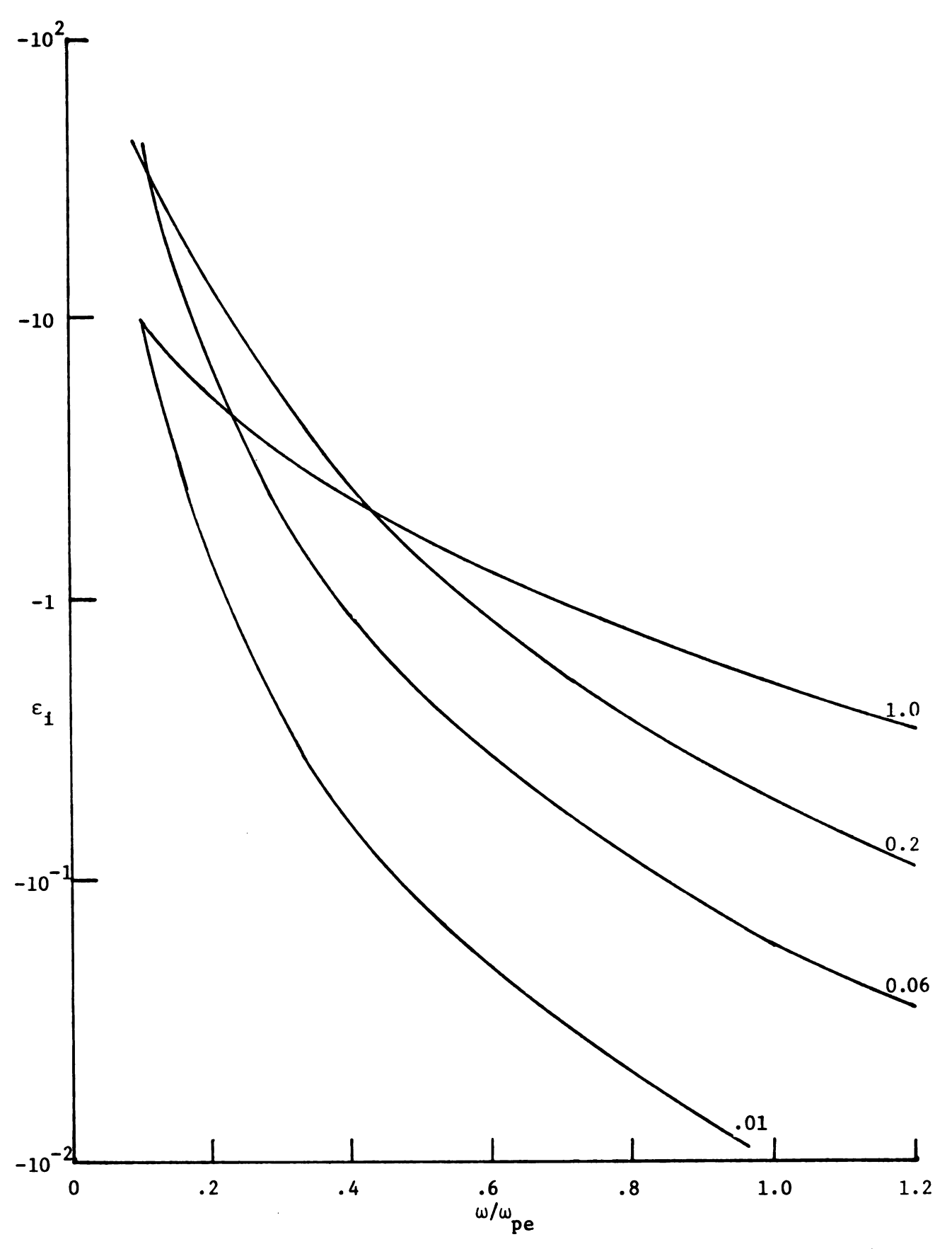


Figure 2.10f. Imaginary part of plasma dielectric constant ϵ_i vs. ω/ω_{pe} and v_e/ω_{pe} . f_{pe} = 5.3 GHz.

the ω/ω_{pe} vs. α/k_c curve (Figure 2.10b) reveals that there is a peak in attenuation in the backward wave region defined by 0.55 ω_{pe} $< \omega < 0.60 \omega_{pe}$. Attenuation in this region is a maximum for low effective collison frequencies. In the limit of v_e/ω_{pe} $\rightarrow 0$, the attenuation $\rightarrow \infty$, and the TE $_{11}^*$ and TM $_{10}^*$ modes become distinct. The backward wave region suggests that it might be possible to excite unstable waves in this frequency range by operating at low discharge pressures and driving the plasma with strong RF fields.

Attenuation is almost negligible for $\omega>0.60~\omega_{pe}$ and in the range 0.55 $\omega_{pe}<\omega<0.33~\omega_{pe}$ for the v_e/ω_{pe} 's shown in Figure 2.10b. Below $\omega=0.33\omega_{pe}$ collisional damping rises steeply (Figure 2.10c).

The asymptotic behavior of these curves is consistent with the values of the plasma complex dielectric constant as a function of the frequency (Figures 2.10e and 2.10f).

For f_{pe} = 5.3 GHz and with $(v_e/\omega_{pe})^{\to\infty}$ the cut off frequency of the TE $_{11}^{\star}$ mode approaches that of the TE $_{11}$ circular waveguide mode at $(\omega/\omega_{pe}$ = 0.326). An examination of Figures 2.10e and 2.10f reveals that at ω/ω_{pe} \approx 0.326, $\varepsilon_r^{\to}1$, and $\varepsilon_i^{\to}0$ as $(v_e/\omega_{pe})^{\to\infty}$ and the plasma waveguide becomes an empty waveguide. As (ω/ω_{pe}) becomes large, $\varepsilon_r^{\to}1$ and $\varepsilon_i^{\to}0$ for a fixed collision frequency (Figures 2.10e and 2.10f) and the TE $_{11}^{\star}$ mode becomes the TE $_{11}^{\star}$ circular waveguide mode.

2.5 Summary

The dispersion curves of this chapter describe the propagation characteristics of EM and space charge waves in a waveguide partially filled with a concentric lossy plasma rod. The ω - k diagrams for a lossless plasma waveguide have been studied by others 12,17 . In this chapter, the

emphasis has been on the study of dispersion curves in the presence of collisional losses and how these curves differ from the curves for the lossless case.

The introduction of losses removes the singularity 19 of the lossless $^{7M}_{00}$ mode at the slow wave resonance frequency and of the lossless $^{7M}_{10}$ mode at the dipole resonance frequency. Furthermore, $^{7E}_{11}$ and $^{7M}_{10}$ modes have one distinct solution to the characteristic equation in the presence of losses. Also, a backward wave region appears in the lossy dispersion curves of $^{7M}_{00}$ and $^{7E}_{11}$ modes. The asymptotic behavior of the dispersion curves for very large and very small values of the normalized frequency $(\omega/\omega_{\rm pe})$ and the normalized collisional frequency $(\psi_{\rm e}/\omega_{\rm pe})$ has been described.

The properties of the dispersion curves of this chapter will be used in the following chapters in studying the power absorbed in a lossy plasma waveguide and in examining the eigenmodes of a plasma cavity.

CHAPTER III

POWER ABSORBED IN A PLASMA WAVEGUIDE

3.1 Introduction

The propagation characteristics of EM and space charge waves in a plasma-waveguide (see Figure 2.1) was described in the last chapter. The energy carried by these waves is absorbed by the plasma due to collisions between electrons and neutral particles. A useful insight into the energy relationships in a plasma waveguide can be obtained by applying the complex Poynting theorem to this problem. Assuming an e^{jωt} variation and a small signal approximation, the general form of this theorem is:

$$\nabla \cdot (\frac{1}{2} \stackrel{?}{E} \times \stackrel{?}{H} \stackrel{*}{}) -j\omega (\frac{1}{2} \varepsilon E^2 - \frac{1}{2} \mu H^2) = \frac{1}{2} \stackrel{?}{E} \cdot \stackrel{?}{J} \stackrel{*}{}. \qquad 3.1$$

Integrating the above equation over a volume of unit length of a metallic waveguide (see Figure 3.1), we have

$$\frac{1}{2} \int \overrightarrow{E} \times \overrightarrow{H}^* \cdot \hat{z} ds - j\omega \int (\frac{1}{2} \varepsilon E^2 - \frac{1}{2} \mu H^2) dv = \frac{1}{2} \int \overrightarrow{E} \cdot \overrightarrow{J}^* dv \qquad 3.2$$

where s_1 and s_2 are the waveguide cross-sectional areas at z=0 and z=1 and v=1 and v=1 are the waveguide volume. The contribution to the surface integrals from the perfectly conducting metallic surface of the waveguide is zero.

Equation 3.2 can be further specialized for the case of a unit length of the plasma waveguide, as shown in Figure 2.1, Chapter II.

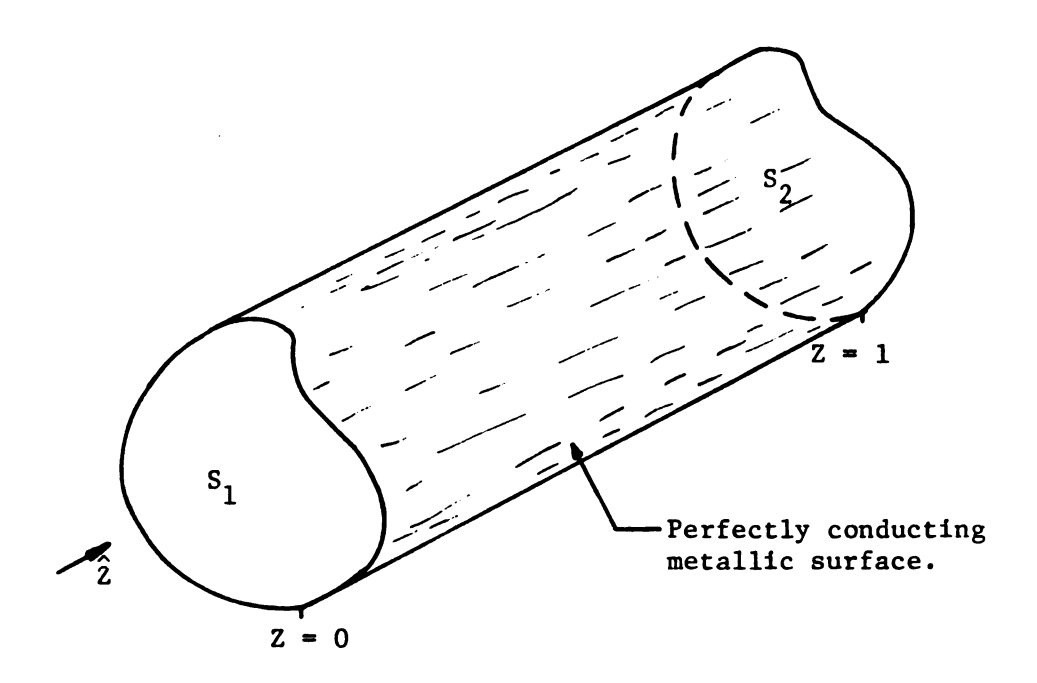


Figure 3.1. Arbitrarily-shaped metallic waveguide of unit length. S_1 and S_2 are waveguide cross sections at Z=0 and Z=1.

Substituting for J from the plasma conduction current for electrons (Equation 2.20, Chapter II) and rearranging the terms we have:

$$\frac{1}{2} \int \overrightarrow{E} \times \overrightarrow{H} \stackrel{*}{\sim} \widehat{z} \, ds - j\omega \int_{\mathbf{V}_{1}} (\frac{1}{2} \varepsilon E^{2} - \frac{1}{2} \mu H^{2}) \, dv - j\omega \int_{\mathbf{V}_{2}} \frac{N_{0} e^{2}}{(v_{e}^{2} + \omega^{2})} E^{2} \, dv$$

$$= \frac{1}{2} \int_{\mathbf{V}_{2}} \frac{v_{e} N_{0} e^{2}}{(v_{e}^{2} + \omega^{2})} E^{2} \, dv$$
3.3

where \mathbf{v}_1 represents integration over the entire plasma-waveguide volume and \mathbf{v}_2 represents integration over the plasma volume. The real part of the first term on the left hand side of the equation i.e.,

represents the time-average power transferred to the unit-length plasma waveguide volume and is equal to the collisional heating term on the right hand side of the equation, i.e., the time average power transferred to the plasma particles in \mathbf{v}_2 .

$$\frac{1}{2}$$
 Im $\int \vec{E} \times \vec{H} \cdot \hat{z} ds$,
 $s_1 + s_2$

is equal to the sum of the time-averaged stored electric, magnetic and kinetic energies per unit time as given by the second and third terms on the left hand side of the equation.

In this chapter the expressions for the time average power absorbed/unit length are derived from

$$P_{a} = \frac{1}{2}Re \int \vec{E} \times \vec{H}^{*} \cdot \hat{z} ds$$

$$3.4$$

for the TM_{op} , p=0, 1, 2, etc., TE_{op} , p=1, 2, 3, etc., and TE_{11}^{\star} modes. The numerical results of Chapter II are used in studying the behavior of P_a as a function of the plasma parameters (ω/ω_{pe}) and (v_e/ω_{pe}) . It will be shown that, in general, the absorbed power per unit length is a direct function of the losses in the plasma. For modes that have an electric field component normal to the cylindrical plasma column volume, surface resonances are observed. It is also shown that the power absorbed at all resonances varies inversely as the collision frequency.

3.2 Power flow and power absorbed for TM waveguide modes

A cross-section of the quartz-enclosed plasma in a cylindrical waveguide is shown in Figure 2.1. The TM_{op} wave functions and the electric and magnetic field components for regions 1, 2 and 3 of the plasma-waveguide are obtained by putting n=0 in equations 2.26, 2.27, and 2.28 and using equations 2.32 through 2.37. Assuming a time variation of the form $e^{j\omega t}$, these equations are:

Region 1:
$$o < r \le a$$

$$\psi^{m1} = AJ_o(k_{\rho_1}r) e$$
3.5

$$E_{r} = -(Ak_{z}k_{\rho_{1}}/\omega\epsilon_{1})J_{o}'(k_{\rho_{1}}r)e$$
3.6

$$H_{\phi} = -Ak_{\rho_1} J_{o}'(k_{\rho_1} r) e^{-jk_z z}$$
3.7

$$E_{z} = -\frac{jAk^{2}_{\rho_{1}}}{\omega \varepsilon_{1}} J_{o}(k_{\rho_{1}}r)e^{-jk_{z}z}$$
3.8

Region 2: $a \le r \le b$

$$\psi^{m2} = [BJ_o(k_{\rho_2}r) + CN_o(k_{\rho_2}r)]e^{-jk_zz}$$
3.9

$$E_{\mathbf{r}} = -\frac{\mathbf{k}}{\omega \varepsilon_{2}} \left[B \mathbf{k}_{\rho_{2}} J_{o}^{\prime}(\mathbf{k}_{\rho_{2}} \mathbf{r}) + C \mathbf{k}_{\rho_{2}} N_{o}^{\prime}(\mathbf{k}_{\rho_{2}} \mathbf{r}) \right] e^{-j k_{2} z}$$
3.10

$$H_{\phi} = -k_{\rho_2} [BJ_o' (k_{\rho_2} r) + CN_o' (k_{\rho_2} r)] e^{-jk_z^z}$$
3.11

$$E_{z} = -\frac{jk_{\rho}^{2}}{\omega \varepsilon_{2}} \left[BJ_{o}(k_{\rho} r) + CN_{o}(k_{\rho} r)\right] e^{-jk_{z}^{2}}$$
3.12

Region 3: $b \le r \le c$

$$\psi^{m3} = [DJ_o(k_{\rho_3}r) + EN_o(k_{\rho_3}r)] e^{-jk_z^z}$$
3.13

$$E_{r} = -\frac{k_{z}}{\omega \epsilon_{3}} \left[Dk_{\rho_{3}} J_{o}'(k_{\rho_{3}}r) + Ek_{\rho_{3}} N_{o}'(k_{\rho_{3}}r) \right] e^{-jk_{z}z}$$
 3.14

$$H_{\phi} = -k_{\rho_{3}} [DJ_{o}'(k_{\rho_{3}}r) + EN_{o}'(k_{\rho_{3}}r)] e^{-jk_{z}^{z}}$$
3.15

$$E_{z} = -\frac{jk_{\rho}^{2}}{\omega \varepsilon_{3}} \left[DJ_{o}(k_{\rho_{3}}r) + EN_{o}(k_{\rho_{3}}r)\right] e^{-jk_{z}z}.$$
3.16

The above equations involve five arbitrary constants: A, B, C, D, and E. The constants can be expressed in terms of one arbitrary constant, namely A, by applying the boundary conditions: continuity of E_z and H_{φ} at r=a, r=b, and E_z =0 at r=c. In terms of A, these constants are: $B=F_{11}A$, $C=F_{12}A$, $D=F_{14}A$, $E=F_{13}A$

where,

$$F_{11} = (k_{\rho_1} F_6 / k_{\rho_2} F_1)$$
 3.17

$$F_{12} = (k_{\rho_1} F_7 / k_{\rho_2} F_1)$$
 3.18

$$F_{13} = (k_{\rho_1} F_5 F_6 J_0 (k_{\rho_3} c) / k_{\rho_3} F_1 F_8)$$
3.19

$$F_{14} = -F_{13}N_0(k_{\rho_3}c)/J_0(k_{\rho_3}c)$$
3.20

and

$$F_1 = J_o(k_{\rho_2}a) N_o(k_{\rho_2}a) - J_o(k_{\rho_2}a) N_o(k_{\rho_2}a)$$
 3.21

$$F_2 = J_o(k_{\rho_3}c) N_o(k_{\rho_3}b) - J_o(k_{\rho_3}b) N_o(k_{\rho_3}c)$$
3.22

$$F_{3} = J_{o}(k_{\rho_{3}}c) N_{o}'(k_{\rho_{3}}b) - N_{o}(k_{\rho_{3}}c) J_{o}'(k_{\rho_{3}}b)$$
3.23

$$F_{5} = J_{o} (k_{\rho_{2}} b) N_{o}^{\dagger} (k_{\rho_{2}} b) - N_{o} (k_{\rho_{2}} b) J_{o}^{\dagger} (k_{\rho_{2}} b)$$
3.24

$$F_6 = (\epsilon_2 k_{\rho_1} / \epsilon_1 k_{\rho_2}) J_o(k_{\rho_1} a) N_o'(k_{\rho_2} a) - J_o'(k_{\rho_1} a) N_o(k_{\rho_2} a)$$
 3.25

$$F_7 = J_0(k_{\rho_2}a) J_0'(k_{\rho_1}a) - (\epsilon_2 k_{\rho_1}/\epsilon_1 k_{\rho_2}) J_0(k_{\rho_1}a) J_0'(k_{\rho_2}a)$$
 3.26

$$F_8 = (\epsilon_2 k_{\rho_3} / \epsilon_3 k_{\rho_2}) F_2 N_0' (k_{\rho_2} b) - F_3 N_0 (k_{\rho_2} b).$$
 3.27

Using the Poynting vector the time-average power flow in the z direction P_z , can now be written as:

$$P_z = \frac{1}{2}Re \int_{S} \vec{E} \times \vec{H}^* \cdot \hat{z} da$$

$$= \frac{1}{2} \operatorname{Re} \int_{0}^{a} \int_{0}^{2\pi} E_{r} H_{\phi}^{*} da + \int_{a}^{b} \int_{0}^{2\pi} E_{r} H_{\phi}^{*} da + \int_{b}^{c} \int_{0}^{2\pi} E_{r} H_{\phi}^{*} da$$

$$= {}^{1}_{2}Re \left[P_{z1} + P_{z2} + P_{z3} \right]$$
3.28

where,

$$\begin{split} P_{z1} &= \int_{0}^{a} \int_{0}^{2\pi} E_{r} H_{\phi}^{*} da \\ &= 2\pi |A|^{2} \frac{k_{\rho} k_{\rho}^{*} k_{z}}{k_{\rho} k_{z}} e^{-2\alpha z} \int_{0}^{a} J_{o}^{!} (k_{\rho_{1}} r) J_{o}^{**} (k_{\rho_{1}} r) r dr \\ P_{z2} &= \int_{0}^{b} \int_{0}^{2\pi} E_{r} H_{\phi}^{*} da \\ &= 2\pi |A|^{2} \frac{k_{\rho} k_{\rho}^{*} k_{z}}{\omega c_{z}} e^{-2\alpha z} \left[F_{11} F_{11}^{*} \int_{a}^{b} J_{o}^{!} (k_{\rho_{2}} r) J_{o}^{**} (k_{\rho_{2}} r) r dr \\ &+ F_{11} F_{12}^{*} \int_{a}^{b} J_{o}^{!} (k_{\rho_{2}} r) N_{o}^{**} (k_{\rho_{2}} r) r dr \\ &+ F_{12} F_{11}^{*} \int_{a}^{b} N_{o}^{!} (k_{\rho_{2}} r) J_{o}^{**} (k_{\rho_{2}} r) r dr \\ &+ F_{12} F_{12}^{*} \int_{a}^{b} N_{o}^{!} (k_{\rho_{2}} r) J_{o}^{**} (k_{\rho_{2}} r) r dr \\ &+ F_{12} F_{12}^{*} \int_{a}^{b} N_{o}^{!} (k_{\rho_{2}} r) N_{o}^{**} (k_{\rho_{2}} r) r dr \\ &+ F_{12} F_{12}^{*} \int_{a}^{b} \int_{a}^{b} N_{o}^{!} (k_{\rho_{2}} r) N_{o}^{**} (k_{\rho_{2}} r) r dr \\ &+ F_{12} F_{13}^{*} \int_{a}^{b} \int_{a}^{b} (k_{\rho_{3}} r) N_{o}^{**} (k_{\rho_{3}} r) r dr \\ &+ F_{14} F_{13}^{*} \int_{a}^{b} \int_{a}^{b} J_{o}^{!} (k_{\rho_{3}} r) N_{o}^{**} (k_{\rho_{3}} r) r dr \\ &+ F_{14} F_{13}^{*} \int_{a}^{b} J_{o}^{!} (k_{\rho_{3}} r) N_{o}^{**} (k_{\rho_{3}} r) r dr \\ &+ F_{14} F_{13}^{*} \int_{a}^{b} J_{o}^{!} (k_{\rho_{3}} r) N_{o}^{**} (k_{\rho_{3}} r) r dr \end{split}$$

+ $F_{13}F_{14}^* \int_0^c N_0'(k_{\rho_3}r) J_0'^*(k_{\rho_3}r) r dr$

+
$$F_{13}F_{13}^{*}\int_{b}^{c}N_{o}^{\prime}(k_{\rho_{3}}r)N_{o}^{\prime*}(k_{\rho_{3}}r)rdr$$
]. 3.31

The power absorbed per unit length P_a for the TM mode is:

$$P_a = (P_z |_{z=0} - P_z |_{z=1})$$
 3.32

As is evident from the expressions for P_{z1} , P_{z2} , and P_{z3} , the power absorbed/unit length P_a is a function of the square of the amplitude of the wave function in the plasma $|A|^2$, the incident frequency ω , the electron plasma frequency ω_{pe} and the collisional frequency v_e . P_{z1} , P_{z2} , P_{z3} are numerically integrated and plots of the normalized power absorbed/unit length, $P_a/|A|^2$, vs. the plasma parameters (ω/ω_{pe}) and (v_e/ω_{pe}) for a fixed ω_{pe} are obtained for the TM₀₀ and TM₀₁ modes. These are explained in detail in the sections that follow.

3.2.1 TM mode

Figure 3.2 shows $P_a/|A|^2$ vs. (ω/ω_{pe}) for $(v_e/\omega_{pe})=0.05$, 0.1, 0.175, 0.3, 0.525, and $f_{pe}=6$ GHz for the TM_{00} mode. The (ω/ω_{pe}) vs. (β/k_c) and (ω/ω_{pe}) vs. (α/k_c) diagrams for these values of the electron density and the normalized collisional frequency were shown in Figures 2.4a and 2.4b.

It is clear from Figure 3.2 that the $P_a/|A|^2$ curves for the TM_{00} mode have two resonances. One of these occurs near the frequency of slow wave resonance $(\omega/\omega_{pe}) = 1/\sqrt{1+k_e} = 0.46$ while the other resonance occurs at $(\omega/\omega_{pe}) = 1$.

The resonance at $(\omega/\omega_{pe})^{\simeq}$ 0.46 peaks only when the normalized collisional frequency is very small, i.e., when (v_e/ω_{pe}) = 0.1, 0.05, etc.



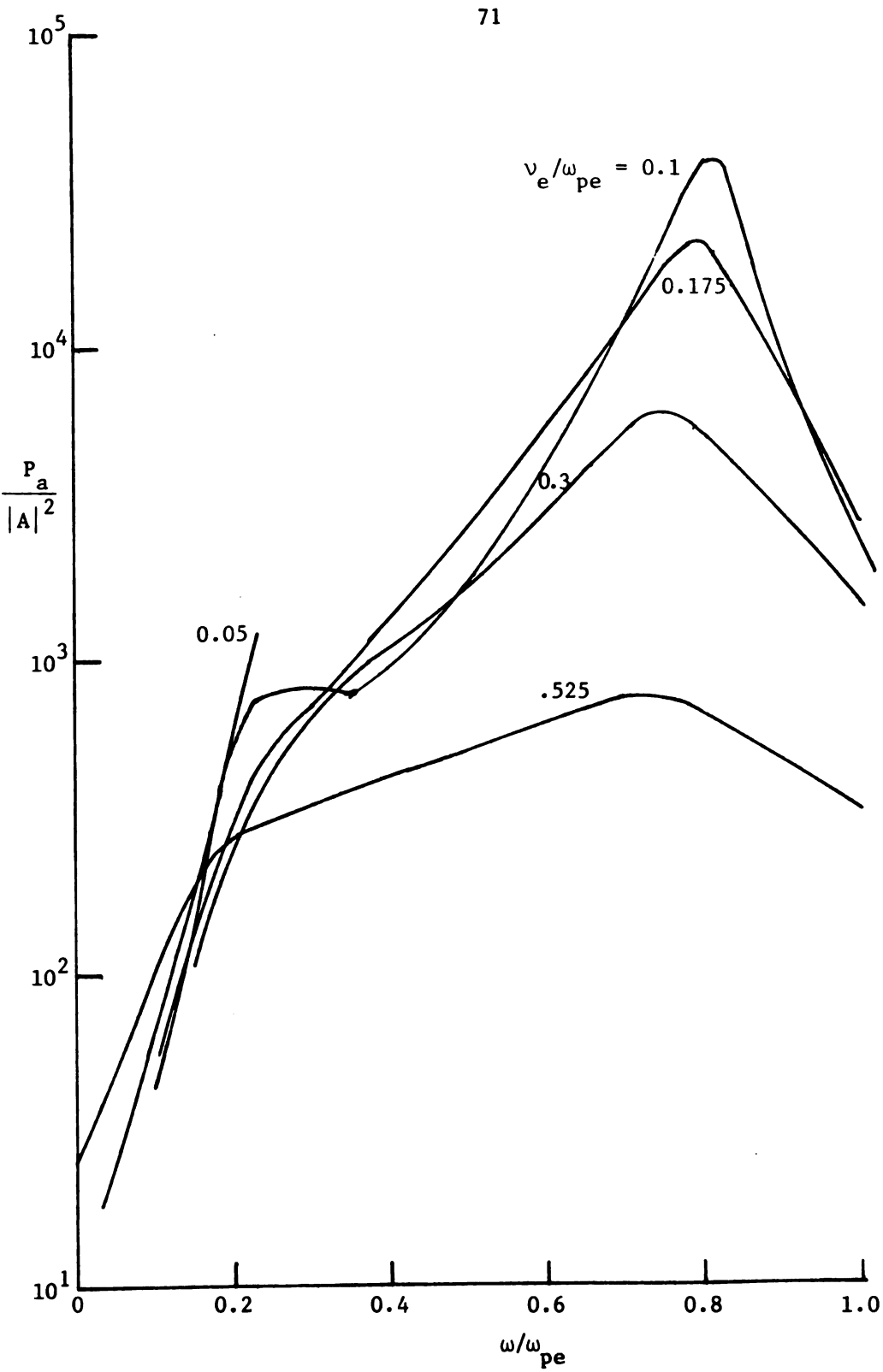


Figure 3.2. Normalized absorbed power $P_a/|A|^2$ vs. ω/ω_{pe} and v_e/ω_{pe} for the TM_{00} mode. Waveguide dimensions: a=0.3 cms., b=0.3875 cms., c=5.08 cms. f_{pe} = 6 GHz.

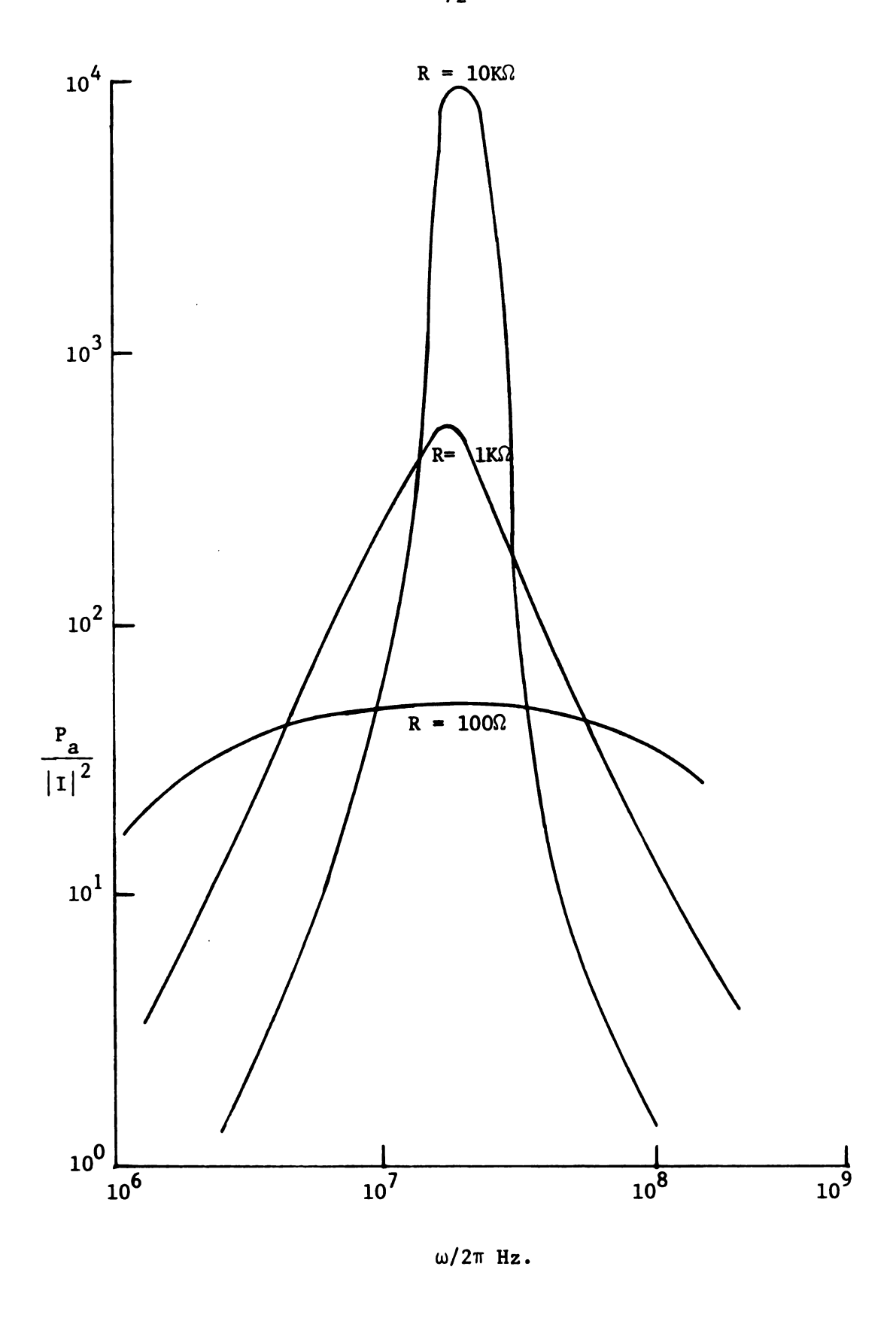


Figure 3.3. Normalized absorbed power in the resistor $P_a/|I|^2$ vs. $\omega/2\pi$ for a parallel RLC circuit driven by an ideal current source. $L=10\mu H$, C=10 pf.

This indicates that surface waves can be strongly excited when the frequency and plasma density are such that (ω/ω_{pe}) =0.46 and when the collisional frequency is very small.

The resonance at the plasma frequency $\omega^*\omega_{pe}$ is a volume resonance. The expressions for P_{z1} , P_{z2} , P_{z3} (Equations 3.29, 3.30, 3.31) reveal that these quantities reach a maximum in the neighborhood of $\omega=\omega_{pe}$, giving rise to a peak in the absorbed power. It should be noted that these curves were computed with constant A. In practice, however, this does not occur because the coupling of the incident power varies with plasma density.

A study of the two resonances described above shows that the losses in the plasma increase with decreasing v_e/ω_{pe} . This behavior is analogous to the power absorbed by a resistor at resonance in a series or parallel RLC circuit driven by an ideal voltage or current source, respectively. Typical curves for absorbed power in a resistor of a parallel RLC circuit driven by an ideal current source are shown in Figure 3.3. As damping in the circuit goes to zero, i.e., as $R^{+\infty}$, the absorbed power in the resistor at resonance becomes very large.

3.2.2 <u>TM</u>₀₁ mode

The power absorbed curves for this mode are shown in Figure 3.4 for the collisional losses (v_e/ω_{pe}) = 0.1, 1.0, 3.0, 6.0 and 10.0. The electron plasma frequency f_{pe} is fixed at 10.5 GHz. The (ω/ω_{pe}) vs. (β/k_c) and (ω/ω_{pe}) vs. (α/k_c) curves for the same electron plasma frequency were shown in Chapter II in Figures 2.8a, 2.8b, 2.8c and 2.8d.

The behavior of the power absorbed curves of this mode can be understood by studying the variation of the plasma permittivity ϵ_1 with the frequency. The real and imaginary parts of ϵ_1 vs. (ω/ω_{pe}) are

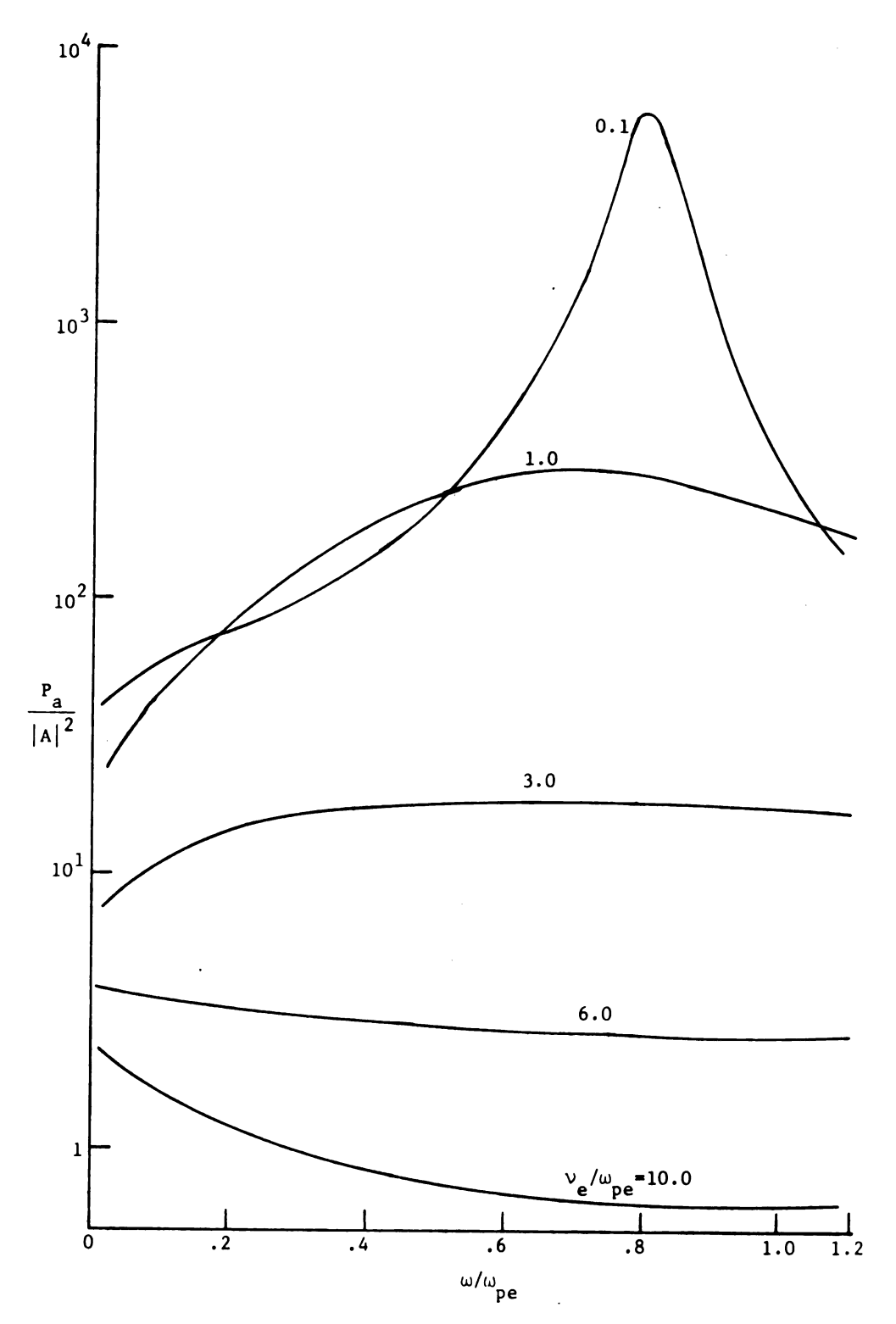


Figure 3.4. Normalized absorbed power $P_a/|A|^2$ vs. ω/ω_{pe} and v_e/ω_{pe} for the TM₀₁ mode. Waveguide dimensions: a=0.3 cms., b=0.3875 cms., C=5.08 cms. f_{pe} = 10.5 GHz.

shown in Figures 2.8e and 2.8f. By comparing Figures 2.8e and 2.8f with Figure 3.4, it is evident that the power absorbed is a direct function of the lossiness of the plasma. This mode also has a volume resonance at $\omega = \omega_{\rm pe}$, and is prominent for small collisional losses $(v_{\rm e}/\omega_{\rm pe}=0.1)$.

3.3 Power flow and power absorbed for TE waveguide modes

Consider the cylindrical plasma-waveguide with regions 1, 2, and 3 as shown in Figure 2.1. Assuming a time variation of the form $e^{\mathbf{j}\omega t}$, the TE op wave functions and the electric and magnetic field components for the three regions of Figure 2.1 are:

Region 1: $o < r \le a$

$$\psi^{e1} = AJ_0(k_{\rho_1}r) e^{-jk_z z}$$
3.33

$$E_{\phi} = A k_{\rho} J_{o}^{\dagger}(k_{\rho} r) e^{-jk_{z}z}$$
3.34

$$H_{\mathbf{r}} = -A k_{\rho} k_{\mathbf{z}} J_{\mathbf{o}}^{\dagger} (k_{\rho} \mathbf{r}) e^{-jk_{\mathbf{z}} \mathbf{z}}$$

$$\frac{-jk_{\mathbf{z}} \mathbf{z}}{\omega \mu_{\mathbf{o}}}$$
3.35

$$H_{z} = -jA k_{\rho}^{2} J_{o}(k_{\rho} r) e^{-jk_{z}z}$$

$$\frac{-jk_{z}z}{\omega \mu_{o}}$$
3.36

Region 2: $a \le r \le b$

$$\psi^{e2} = [BJ_0(k_{\rho_2}r) + CN_0(k_{\rho_2}r)] e^{-jk_z z}$$
3.37

$$E_{\phi} = k_{\rho_{2}} [BJ_{o}'(k_{\rho_{2}}r) + CN_{o}'(k_{\rho_{2}}r)] e^{-jk_{z}z}$$
3.38

$$H_{r} = \frac{-k_{\rho} k_{z}}{\omega \mu_{o}} [BJ_{o}^{\dagger}(k_{\rho} r) + CN_{o}^{\dagger}(k_{\rho} r)] e$$
3.39

$$H_{z} = \frac{-j k_{\rho}^{2}}{\omega \mu_{o}} [BJ_{o}(k_{\rho} r) + CN_{o}(k_{\rho} r)] e^{-jk_{z}z}$$
3.40

Region 3: b≤r≤c

$$\psi^{e3} = [DJ_o(k_{\rho_3}r) + EN_o(k_{\rho_3}r)] = e^{-jk_z z}$$
3.41

$$E_{\phi} = k_{\rho_{3}} [DJ_{o}'(k_{\rho_{3}}r) + EN_{o}'(k_{\rho_{3}}r)] e^{-jk_{z}z}$$
3.42

$$H_{r} = \frac{-k_{\rho} k_{z}}{\omega \mu_{o}} \left[DJ_{o}'(k_{\rho_{3}}r) + EN_{o}'(k_{\rho_{3}}r) \right] e^{-jk_{z}z}$$
3.43

$$H_{z} = \frac{-jk_{\rho}}{\omega\mu_{o}} \left[DJ_{o}(k_{\rho_{3}}r) + EN_{o}(k_{\rho_{3}}r)\right] = \frac{-jk_{z}z}{e}.$$
 3.44

The above equations involve five arbitrary constants: A, B, C, D, and E. All the constants can be expressed in terms of A by applying the following boundary conditions: continuity of E_{ϕ} and H_z at r=a, r=b, and $E_{\phi}=o$ at r=c. The arbitrary constants in terms of A are: $B=F_{11}A$, $C=F_{12}A$, $D=F_{13}A$, and $E=F_{14}A$, where

$$F_{11} = (k_{\rho_1} F_6 / k_{\rho_2} F_1)$$
 3.45

$$F_{12} = (k_{\rho_1} F_7 / k_{\rho_2} F_1)$$
 3.46

$$F_{13} = -N_o'(k_{\rho_3}c) F_{14}/J_o'(k_{\rho_3}c)$$
 3.47

$$F_{14} = (k_{\rho_2} F_5 J_0' (k_{\rho_3} c) F_{11} / k_{\rho_3} F_8)$$
3.48

and

$$F_{1} = J_{o}(k_{\rho_{2}}a)N_{o}'(k_{\rho_{2}}a) - J_{o}'(k_{\rho_{2}}a)N_{o}(k_{\rho_{2}}a)$$
3.49

$$F_2 = J_0'(k_{\rho_3}c)N_0(k_{\rho_3}b) - J_0(k_{\rho_3}b)N_0'(k_{\rho_3}c)$$
3.50

$$F_{3} = J_{o}^{\prime}(k_{\rho_{3}}c)N_{o}^{\prime}(k_{\rho_{3}}b) - J_{o}^{\prime}(k_{\rho_{3}}b)N_{o}^{\prime}(k_{\rho_{3}}c)$$
3.51

$$F_{5} = J_{o}(k_{\rho_{2}}b)N_{o}'(k_{\rho_{2}}b) - N_{o}(k_{\rho_{2}}b)J_{o}'(k_{\rho_{2}}b)$$
3.52

$$F_{6} = (k_{\rho_{1}}/k_{\rho_{2}}) J_{o}(k_{\rho_{1}}a) N_{o}'(k_{\rho_{2}}a) - J_{o}'(k_{\rho_{1}}a)N_{o}(k_{\rho_{2}}a)$$
3.53

$$F_7 = J_o(k_{\rho_2} a) J_o'(k_{\rho_1} a) - (k_{\rho_1}/k_{\rho_2}) J_o(k_{\rho_1} a) J_o'(k_{\rho_2} a)$$
3.54

$$F_8 = (k_{\rho_3}/k_{\rho_2})F_2N_0'(k_{\rho_2}b) - F_3N_0'(k_{\rho_2}b).$$
 3.55

Using the expressions for E and H in the Poynting Vector, the time average power flow in the z direction $P_{\overline{z}}$ can be written as:

$$P_z = \frac{1}{2}Re \int \hat{E} \times \hat{H}^* \cdot \hat{z} da$$

$$= {}^{1}_{2} \operatorname{Re} \int_{0}^{a} \int_{0}^{2\pi} -E_{\phi}H_{\mathbf{r}}^{*} \operatorname{rd} \operatorname{rd} \phi + \int_{a}^{b} \int_{0}^{2\pi} -E_{\phi}H_{\mathbf{r}}^{*} \operatorname{rd} \operatorname{rd} \phi + \int_{b}^{c} \int_{0}^{2\pi} -E_{\phi}H_{\mathbf{r}}^{*} \operatorname{rd} \operatorname{rd} \phi$$

$$= \frac{1}{2} \operatorname{Re} \left[P_{z1} + P_{z2} + P_{z3} \right]$$
 3.56

where

$$P_{z1} = 2\pi |A| \frac{{}^{2} k_{\rho} k_{z}^{*} k_{z}^{*}}{\omega \mu_{o}} e^{-2\alpha z} \int_{0}^{a} J_{o}^{*}(k_{\rho_{1}} r) J_{o}^{**}(k_{\rho_{1}} r) r dr$$
 3.57

$$P_{z2} = 2\pi |A|^{2} \frac{k_{\rho} k_{\rho}^{*} k_{z}^{*}}{\omega \mu_{o}} e^{-2\alpha z} \left[F_{11}F_{11}^{*} \int_{a}^{b} J_{o}^{*}(k_{\rho_{z}}r) J_{o}^{**}(k_{\rho_{z}}r) r dr\right]$$

$$+ F_{11}F_{12}^{*} \int_{a}^{b} J_{o}^{'}(k_{\rho_{2}}r) N_{o}^{'*}(k_{\rho_{2}}r) r dr$$

$$+ F_{12}F_{11}^{*} \int_{a}^{b} N_{o}^{'}(k_{\rho_{2}}r) J_{o}^{'*}(k_{\rho_{2}}r) r dr$$

$$+ F_{12}F_{12}^{*} \int_{a}^{b} N_{o}^{'}(k_{\rho_{2}}r) N_{o}^{'*}(k_{\rho_{2}}r) r dr$$

$$3.58$$

$$P_{z3} = 2\pi |A|^{2} \frac{k_{\rho_{3}}^{k_{\rho_{3}}} k_{z}^{k}}{\omega \mu_{o}} e^{-2\alpha z} \left[F_{13} F_{13}^{*} \int_{b}^{c} J_{o}^{\prime}(k_{\rho_{3}} r) J_{o}^{\prime *}(k_{\rho_{3}} r) r dr \right]$$

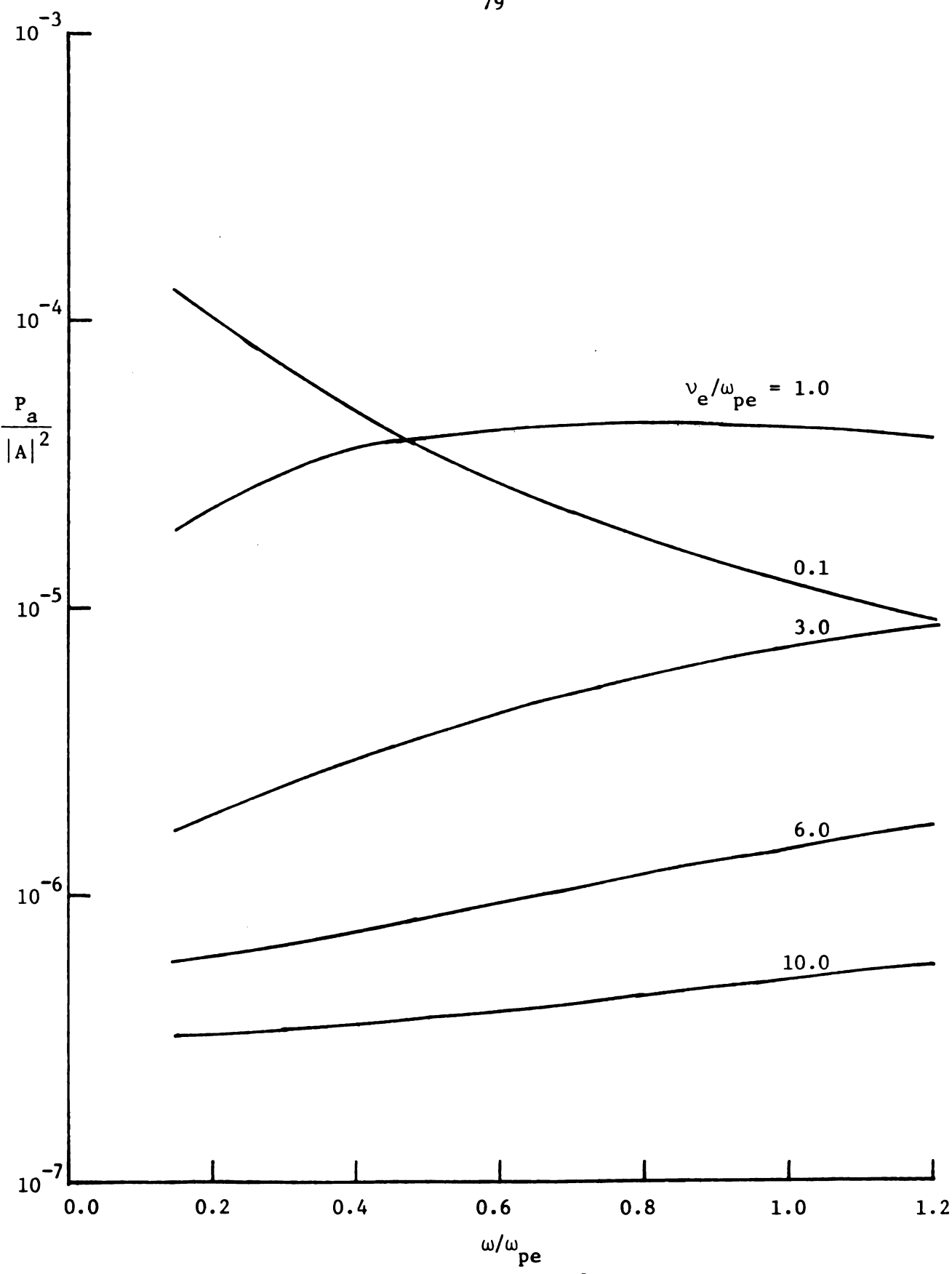
$$+ F_{13}F_{14}^{*} \int_{b}^{c} J'_{o}(k_{\rho_{3}}r) N'_{o}(k_{\rho_{3}}r) r dr$$

$$+ F_{14}F_{13}^{*} \int_{b}^{c} N'_{o}(k_{\rho_{3}}r) J'_{o}(k_{\rho_{3}}r) r dr$$

$$+ F_{14}F_{14}^{*} \int_{b}^{c} N'_{o}(k_{\rho_{3}}r) N'_{o}(k_{\rho_{3}}r) r dr$$

$$+ F_{14}F_{14}^{*} \int_{b}^{c} N'_{o}(k_{\rho_{3}}r) N'_{o}(k_{\rho_{3}}r) r dr$$
3.59

The power absorbed per unit length P_a , for the TE_{op} mode is given by Equation 3.32. A comparison between the absorbed power expressions for the TM_{op} mode (Equations 3.29 - 3.31) and the TE_{op} mode (Equations 3.57 - 3.59) reveals that these expressions are very similar. This is due to the dual nature of these two modes. E_r and H_{ϕ} contribute to the power flow in the TM_{op} mode while E_{ϕ} and H_r do the same in the TE_{op} mode.



Normalized absorbed power $P_a/|A|^2$ vs. ω/ω_{pe} and v_e/ω_{pe} for the TE₀₁ mode. f_{pe} = 10.5 GHz. Waveguide dimensions: a=0.3 cms., Figure 3.5. b=0.3875 cms., c=5.08 cms.

The normalized power absorbed per unit length $P_a/|A|^2$ for the TE_{01} mode is plotted against (ω/ω_{pe}) for (v_e/ω_{pe}) = 0.1, 1.0, 3.0, 6.0 and 10.0 and f_{pe} = 10.5 GHz as shown in Figure 3.5.

The variation of the plasma permittivity ε_1 (see Figures 2.8e and 2.8f), with frequency explains the behavior of the normalized absorbed power $P_a/\left|A\right|^2$. It is evident that in general the normalized absorbed power is a direct function of the losses in the plasma. No surface or volume resonances are observed for this mode, since there is no electric field component normal to the plasma column.

3.4 Power flow and power absorbed for TE* waveguide modes

In this derivation, the thickness of the quartz tube enclosing the plasma is neglected due to the complexity of the three region problem. Thus, there are only two dielectric regions in the plasma-waveguide. Region 1 is the cold, lossy, homogenous, isotropic plasma of radius a. Region 2 is the free space extending from r = a to r = b, the perfectly conducting boundary of the cylindrical waveguide. Assuming a time variation of the form $e^{j\omega t}$, the TE_{11}^* wave functions and the electric and magnetic field components for the regions 1 and 2 can be written as:

Region 1: $o < r \le a$

$$\psi^{\text{ml}} = \text{AJ}_{1}(k_{\rho_{1}}r) \cos \phi e^{-jk_{z}z}$$
3.60

$$\psi^{el} = DJ_1(k_{\rho_1}r) \sin \phi e$$
3.61

$$E_{r} = -\left[\frac{D}{r}J_{1}(k_{\rho_{1}}r) + \frac{A_{1}k_{\rho_{1}}}{\omega\varepsilon_{1}}J_{1}'(k_{\rho_{1}}r)\right]\cos\phi e^{-jk_{z}z}$$
3.62

$$E_{\phi} = \left[Dk_{\rho_1} J_1'(k_{\rho_1} r) + \frac{A^k z}{\omega \epsilon_1 r} J_1(k_{\rho_1} r) \right] \quad \sin \phi \quad e^{-jk_z z}$$
3.63

$$E_{z} = \frac{-jA}{\omega \varepsilon_{1}} k_{\rho_{1}}^{2} J_{1}(k_{\rho_{1}}r) \cos \phi e^{-jk_{z}z}$$
3.64

$$H_{r} = -\left[\frac{Dk_{\rho_{1}}^{k_{z}}}{\omega \mu_{o}} J_{1}^{\prime}(k_{\rho_{1}}r) + \frac{A}{r} J_{1}(k_{\rho_{1}}r)\right] \sin \phi e^{-jk_{z}z}$$
3.65

$$H_{\phi} = -\left[\frac{Dk_{z}}{\omega\mu_{o}r} J_{1}(k_{\rho_{1}}r) + Ak_{\rho_{1}}J_{1}'(k_{\rho_{1}}r)\right] \cos\phi e^{-jk_{z}z}$$
3.66

$$H_{z} = -jD \frac{k_{\rho}^{2}}{\omega \mu_{o}} J_{1}(k_{\rho_{1}}r) \quad \sin \phi \quad e^{-jk_{z}z}$$
3.67

Region 2: $a \le r \le b$

$$\psi^{m2} = \left[BJ_{1}(k_{\rho_{2}}r) + CN_{1}(k_{\rho_{2}}r)\right] \cos\phi e^{-jk_{z}z}$$
3.68

$$\psi^{e2} = \left[EJ_{1}(k_{\rho_{2}}r) + FN_{1}(k_{\rho_{2}}r) \right] \sin\phi e^{-jk_{z}z}$$
3.69

$$E_{\mathbf{r}} = -\left[\frac{1}{\mathbf{r}} \cdot \left(EJ_{1}(k_{\rho_{2}}\mathbf{r}) + FN_{1}(k_{\rho_{2}}\mathbf{r})\right)\right]$$

$$+\frac{k_{\rho}k_{z}}{\omega\varepsilon_{z}}\left(BJ_{1}'(k_{\rho}r) + CN_{1}'(k_{\rho}r)\right)\right]\cos\phi e^{-jk_{z}z}$$
3.70

$$E_{\phi} = \left[k_{\rho_{2}}\left(EJ_{1}'(k_{\rho_{2}}r) + FN_{1}'(k_{\rho_{2}}r)\right) + \frac{k_{z}}{\omega\varepsilon_{2}r}\left(BJ_{1}(k_{\rho_{2}}r) + CN_{1}(k_{\rho_{2}}r)\right)\right] \sin\phi e^{-jk_{z}z}$$
3.71

$$E_{z} = -j \frac{k_{\rho}^{2}}{\omega \varepsilon_{2}} \left[BJ_{1}(k_{\rho_{2}}r) + CN_{1}(k_{\rho_{2}}r) \right] \cos \phi e^{-jk_{z}z}$$
3.72

		:

$$H_{r} = -\left[\frac{k_{\rho} k_{z}}{\omega \mu_{o}} \left(EJ_{1}'(k_{\rho_{z}}r) + FN_{1}'(k_{\rho_{z}}r)\right) + \frac{1}{r} \cdot \left(BJ_{1}(k_{\rho_{z}}r) + CN_{1}(k_{\rho_{z}}r)\right)\right] \sin \phi e^{-jk_{z}z}$$

$$3.73$$

$$H_{\phi} = -\left[\frac{k}{\omega \mu_{o} r} \left(EJ_{1}(k_{\rho_{2}} r) + FN_{1}(k_{\rho_{2}} r)\right)\right]$$

$$+ k_{\rho_{2}} \left(B J_{1}'(k_{\rho_{2}} r) + CN_{1}'(k_{\rho_{2}} r) \right) \cos \phi e^{-jk_{2}z}$$
3.74

$$H_z = -j \frac{k_\rho^2}{\omega \mu_o} \left[EJ_1(k_{\rho_2}r) + FN_1(k_{\rho_2}r) \right] \sin \phi e^{-jk_z z}$$
 3.75

The above equations can be expressed in terms of the arbitrary constant A by applying the following boundary conditions: Continuity of E_{φ} , E_{z} , H_{φ} and H_{z} at r=a, and $E_{\varphi}=0$, $E_{z}=0$ at r=b. The arbitrary constants in terms of A are: $B=F_{12}A$, $C=F_{11}A$, $D=F_{13}A$, $E=F_{15}A$, and $F=F_{14}A$, where

$$F_{11} = -\left(\epsilon_{2} k_{\rho_{1}}^{2} / \epsilon_{1} k_{\rho_{2}}^{2} F_{1}\right) J_{1} (k_{\rho_{1}} a) J_{1} (k_{\rho_{2}} b)$$
3.76

$$F_{12} = -F_{11} \left(N_1(k_{\rho_1}b) / J_1(k_{\rho_2}b) \right)$$
 3.77

$$F_{13} = \left[\left(F_{12} k_{\rho_1} J_1'(k_{\rho_2} a) - k_{\rho_1} J_1'(k_{\rho_1} a) + k_{\rho_2} F_{11} N_1'(k_{\rho_2} a) \right) / \right]$$

$$\frac{k_z}{\omega \mu_o a} \left(1 - \frac{k_\rho^2}{k_\rho^2} \right) J_1(k_\rho_1 a)$$
3.78

$$F_{14} = -\left[F_{13}k_{\rho_1}^2J_1(k_{\rho_1}a)J_1'(k_{\rho_2}b) / k_{\rho_2}^2F_2\right]$$
3.79

$$F_{15} = -\left[F_{14}N_1'(k_{\rho_2}b) / J_1'(k_{\rho_2}b)\right]$$
3.80

and

$$F_{1} = \left[J_{1}(k_{\rho_{2}}a)N_{1}(k_{\rho_{2}}b) - J_{1}(k_{\rho_{2}}b)N_{1}(k_{\rho_{2}}a)\right]$$
3.81

$$F_{2} = \left[J_{1}(k_{\rho_{2}}a)N_{1}'(k_{\rho_{2}}b) - N_{1}(k_{\rho_{2}}b)J_{1}'(k_{\rho_{2}}b)\right].$$
3.82

Using the Poynting vector the time-average power flow in the z direction, $\mathbf{P}_{_{\mathbf{Z}}}$, can be written as:

$$P_z = \frac{1}{2}Re \int \vec{E} \times \vec{H}^* \cdot \hat{z} da$$

$$= {}^{1}_{2}Re \left[\int_{0}^{a} \int_{0}^{2\pi} (E_{r}H_{\varphi}^{*} - E_{\varphi}H_{r}^{*})r \, dr \, d\varphi + \int_{a}^{b} \int_{0}^{2\pi} (E_{r}H_{\varphi}^{*} - E_{\varphi}H_{r}^{*})r \, dr \, d\varphi \right]$$

$$= {}^{1}_{2}Re \left[P_{z1} + P_{z2} \right]$$
3.83

where

$$P_{z1} = \int_{0}^{a} \int_{0}^{2\pi} (E_{r}H_{\phi}^{*} - E_{\phi}H_{r}^{*})r \, dr \, d\phi$$

$$= |A|^{2} \pi e^{-2\alpha z} \left[\left(\frac{F_{13}F_{13}^{*} k_{z}^{*}}{\omega \mu_{o}} + \frac{k_{z}}{\omega \epsilon_{1}} \right)_{0} \int_{0}^{a} \frac{J_{1}(k_{\rho_{1}}r)J_{1}^{*}(k_{\rho_{1}}r)}{r} \, dr + \left(F_{13}k_{\rho_{1}}^{*} + \frac{k_{\rho}^{*} k_{z}k_{z}^{*}}{\omega \mu_{z}} \right)_{0} \int_{0}^{a} J_{1}(k_{\rho_{1}}r)J_{1}^{*}(k_{\rho_{1}}r) \, dr$$

$$\begin{split} &+\left(\frac{F_{13}^{*}k_{\rho_{1}}^{*}k_{z}^{*}k_{z}^{*}}{\frac{\sigma}{\omega}\mu_{0}\epsilon_{1}}^{*}+F_{13}k_{\rho_{1}}\right)_{0}\int_{0}^{a}J_{1}^{*}(k_{\rho_{1}}r)J_{1}^{*}(k_{\rho_{1}}r)dr\\ &+\left(\frac{k_{\rho_{1}}^{*}k_{\rho_{1}}^{*}k_{z}}{\omega\epsilon_{1}}^{*}+\frac{F_{13}F_{13}^{*}k_{\rho_{1}}k_{\rho_{1}}^{*}k_{z}^{*}}{\omega\mu_{0}^{*}}\right)_{0}\int_{0}^{a}J_{1}^{*}(k_{\rho_{1}}r)J_{1}^{*}(k_{\rho_{1}}r)rdrdr\\ &+\left(\frac{k_{\rho_{1}}^{*}k_{\rho_{1}}^{*}k_{z}}{\omega\epsilon_{1}}^{*}+\frac{F_{13}F_{13}^{*}k_{\rho_{1}}k_{\rho_{1}}^{*}k_{z}^{*}}{\omega\mu_{0}^{*}}\right)_{0}\int_{0}^{a}J_{1}^{*}(k_{\rho_{1}}r)J_{1}^{*}(k_{\rho_{1}}r)rdrdr\\ &=|A|^{2}\pi e^{-2\alpha z}\left[\left(\frac{F_{15}F_{15}^{*}k_{z}^{*}}{\left(\frac{F_{15}F_{15}^{*}k_{z}^{*}}{\omega\epsilon_{2}}\right)_{a}+\frac{F_{12}F_{12}^{*}k_{z}^{*}}{\omega\epsilon_{2}}\right)_{a}\int_{0}^{b}J_{1}\frac{(k_{\rho_{1}}r)J_{1}^{*}(k_{\rho_{2}}r)J_{1}^{*}(k_{\rho_{2}}r)}{r}dr\\ &+\left(\frac{F_{15}F_{14}^{*}k_{z}^{*}}{\omega\mu_{0}}^{*}+\frac{F_{12}F_{13}^{*}k_{\rho_{2}}^{*}k_{z}^{*}k_{z}^{*}}{\omega\mu_{0}\epsilon_{2}}\right)_{a}\int_{0}^{b}J_{1}(k_{\rho_{2}}r)J_{1}^{*}(k_{\rho_{2}}r)dr\\ &+\left(F_{15}F_{13}^{*}k_{\rho_{2}}^{*}+\frac{F_{12}F_{12}^{*}k_{2}^{*}k_{\rho_{2}}}{\omega\mu_{0}\epsilon_{2}}\right)_{a}\int_{0}^{b}J_{1}(k_{\rho_{2}}r)J_{1}^{*}(k_{\rho_{2}}r)dr\\ &+\left(\frac{F_{14}F_{13}^{*}k_{z}^{*}}{\omega\mu_{0}}^{*}+\frac{F_{11}F_{12}k_{z}}{\omega\epsilon_{2}}\right)_{a}\int_{0}^{b}N_{1}(k_{\rho_{2}}r)J_{1}^{*}(k_{\rho_{2}}r)dr\\ &+\left(\frac{F_{14}F_{13}^{*}k_{z}^{*}}{\omega\mu_{0}}^{*}+\frac{F_{11}F_{12}k_{z}}{\omega\epsilon_{2}}\right)_{a}\int_{0}^{b}N_{1}(k_{\rho_{2}}r)J_{1}^{*}(k_{\rho_{2}}r)\cdot\frac{1}{r}\cdot dr\\ &+\left(\frac{F_{14}F_{12}^{*}k_{\rho_{2}}^{*}}{\omega\mu_{0}}+\frac{F_{11}F_{12}k_{z}}{\omega\epsilon_{2}}\right)_{a}\int_{0}^{b}N_{1}(k_{\rho_{2}}r)J_{1}^{*}(k_{\rho_{2}}r)\cdot\frac{1}{r}\cdot dr\\ &+\left(\frac{F_{14}F_{12}^{*}k_{\rho_{2}}^{*}}{\omega\mu_{0}}+\frac{F_{11}F_{12}k_{z}}{\omega\epsilon_{2}}\right)_{a}\int_{0}^{b}N_{1}(k_{\rho_{2}}r)J_{1}^{*}(k_{\rho_{2}}r)J_{1}^{*}(k_{\rho_{2}}r)dr\\ &+\left(\frac{F_{14}F_{12}^{*}k_{\rho_{2}}^{*}}{\omega\mu_{0}}+\frac{F_{11}F_{12}k_{z}}{\omega\epsilon_{2}}\right)_{a}\int_{0}^{b}N_{1}(k_{\rho_{2}}r)J_{1}^{*}(k_{\rho_{2}}r)J_{1}^{*}(k_{\rho_{2}}r)dr\\ &+\left(\frac{F_{14}F_{12}^{*}k_{\rho_{2}}^{*}}{\omega\mu_{0}}+\frac{F_{11}F_{12}k_{\rho_{2}}k_{\rho_{2}}^{*}}{\omega\mu_{0}}\right)_{a}\int_{0}^{b}N_{1}(k_{\rho_{2}}r)J_{1}^{*}(k_{\rho_{2}}r)J_{1}^{*}(k_{\rho_{2}}r)dr\\ &+\left(\frac{F_{14}F_{12}^{*}k_{\rho_{2}}^{*}}{\omega\mu_{0}}+\frac{F_{11}F_{12}k_{\rho_{2}}k_{\rho_{2}}k_{\rho_{2}}^{*}}{\omega\mu_{0}}\right)_{a}\int_{0}^{b}N_{1}(k_{\rho_{2}}r)J_{1}$$

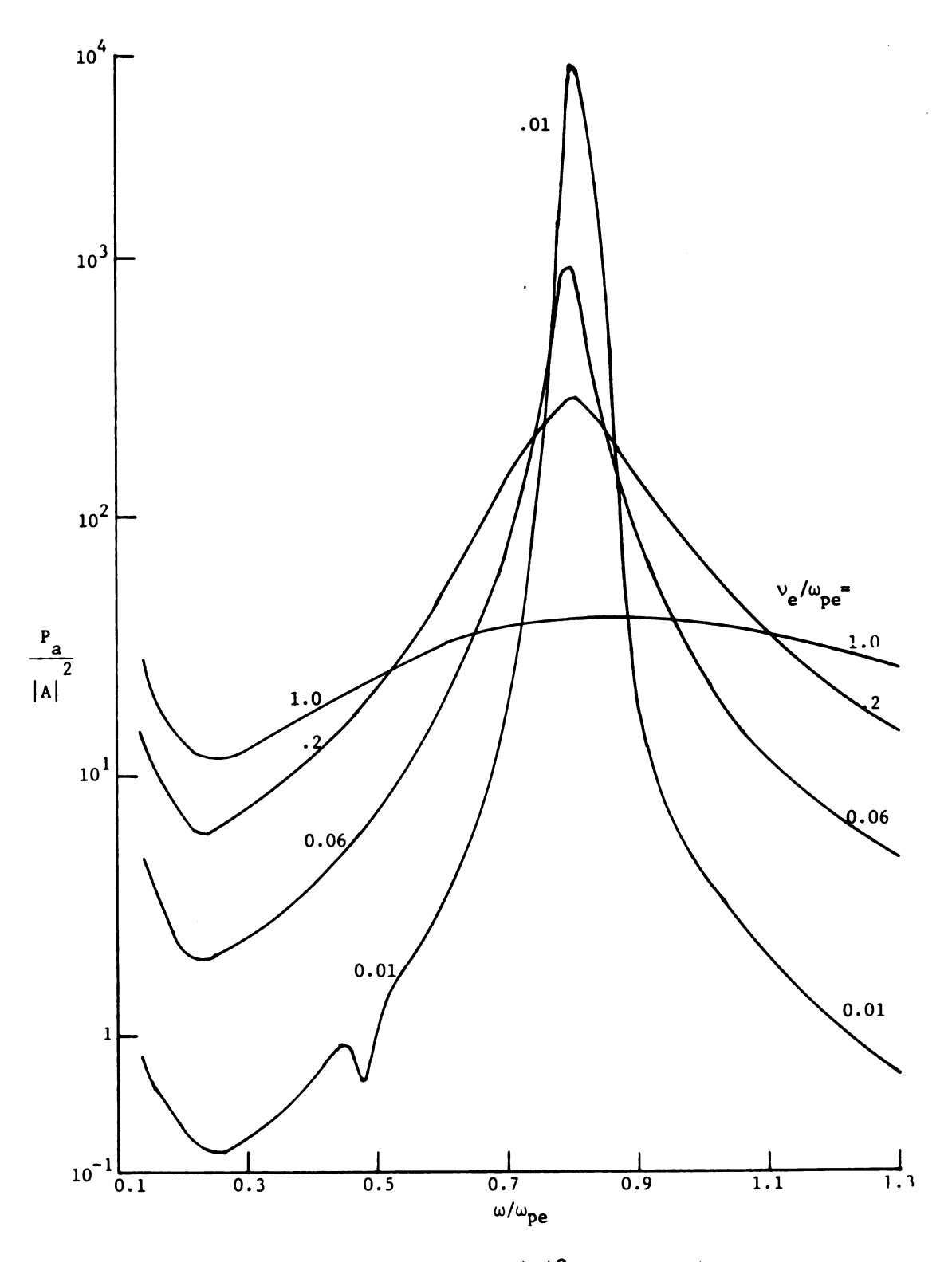


Figure 3.6. Normalized absorbed power $P_a/|A|^2$ vs. ω/ω_{pe} and v_e/ω_{pe} for the TE $_{11}^{\star}$ mode. f_{pe} = 5.3 GHz. Waveguide dimensions: a=0.3 cms., b=0.3875 cms., c=5.08 cms.

The power absorbed/unit length P_a , for the TE_{11}^* mode is given by Equation 3.32. The integrals involved in the expressions for P_{z1} and P_{z2} are numberically integrated and a plot of the normalized power absorbed/unit length, $P_a/|A|^2$, vs. the plasma parameters (ω/ω_{pe}) and (ν_e/ω_{pe}) for a fixed f_{pe} are obtained for this mode. Figure 3.6 shows this plot for f_{pe} = 5.3 GHz and (ν_e/ω_{pe}) = 0.01, 0.06, 0.2, and 1.0.

A study of the power absorbed curves of the TE_{11}^* mode (Figure 3.6) together with the variation of the plasma permittivity as a function of frequency (Figures 2.10e and 2.10f) shows that for most frequencies the power absorbed varies according to the lossiness of the plasma. A plasma volume resonance is present at $\omega = \omega_{\rm pe}$, as in the TM_{00} and TM_{01} modes. Also, seen in Figure 3.6 is a small peak for the $(v_{\rm e}/\omega_{\rm pe}) = 0.01$ curve in the neighborhood of the dipole resonance. This resonance does not appear to be prominent for the plasma-waveguide dimensions chosen here.

CHAPTER IV

ELECTROMAGNETIC AND SPACE CHARGE MODES OF A COLD LOSSY PLASMA ROD INSIDE A CYLINDRICAL CAVITY

4.1 Introduction

The dispersion curves of Chapter II are useful to develop an understanding of the electromagnetic and cold plasma modes of a microwave plasma cavity. The literature reports a considerable amount of work that has been done relating to this problem. Brown and Rose discussed the effects of plasmas in microwave cavities in the early 1950's. Later Agdur and Eneander theoretically solved the problem of a lossless cold plasma cylinder concentrically located in a cylindrical cavity. Shohet the extended their results to include losses and obtained the eigenfrequencies of a plasma cavity. Fredericks for obtained the eigenfrequencies and eigenlengths for cold and warm plasma modes in a lossless plasma partially filling a cylindrical cavity. Leprince has studied the cold and warm plasma resonances of a cylindrical plasma located inside a cylindrical cavity. Additionally, he extensively studied some observed parametric instabilities in the plasma. More recently, Moisan, Beaudry, and Leprince have reported the production of long plasma columns in a re-entrant cavity.

The plasma cavity under study here is formed from a length $L_{_{\rm S}}$ of the plasma-waveguide considered in Chapter II. As before, the motion of the ions is neglected ($\omega_{_{
m pi}}$ =0) and the plasma is assumed to be homogeneous, isotropic and lossy. The waveguide is fitted with metal ends. One end is movable so that the length $L_{_{
m S}}$ can be varied. The metal boundary ends

set up standing waves along the plasma column-cavity system, with the longitudinal propagation constant for any particular mode given by $\beta = p \ 2\pi/2L_s, \text{ where } p = 0, \ 1, \ 2. \quad \text{If the driving frequency } \omega \text{ is fixed for a given value of } p, \text{ the characteristic equation (Equation 2.62) can be solved for } k_z \text{ with } (\omega_{pe}/\omega)^2 \text{ and } \nu_e/\omega \text{ as variable parameters. } k_z, \text{ in general, is complex and is written as: } k_z = \beta - j\alpha \text{ where } \beta = \text{longitudinal propagation constant and } \alpha = \text{longitudinal attenuation constant. The cavity length } L_s \text{ can be obtained from } \beta \text{ provided the damping of the standing waves in a unit wavelength is negligibly small i.e., if } e^{-2\alpha} \approx 1.$

Eigenlength curves are generated for the TM_{00p} , TM_{011} , TE_{011} , TM_{10p}^* , TE_{111}^* and TM_{111}^* modes, and are plotted for two different experimental waveguide dimensions in Figures 4.1 and 4.2. Figure 4.1a shows the eigenlength curves for a = 0.3 cms., b = 0.3875 cms., c = 5.08 cm., and an operating frequency of f = 3.03 GHz. Figure 4.2 shows the eigenlength curves for a = b = 1.248 cms. (quartz thickness is neglected), c = 5.08 cms. and an operating frequency of f = 2.45 GHz. Different portions of these curves correspond to fast waves, slow waves, or backward waves as described in the ω - k diagrams of Chapter II. Also of special interest are the regions where two different modes intersect, indicating where cavity resonances are degenerate.

Figure 4.2 is a very general eigenlength curve since it includes all the possible fundamental modes. Figure 4.1a is a more specialized curve since some of the modes (TE_{011} , TM_{111}^*) are cut off for the chosen operating frequency, f = 3.03 GHz. A detailed description of each of the eigenlength curves of Figure 4.1a is given in the next section. Most of the descriptions are also applicable to the curves of Figure 4.2.

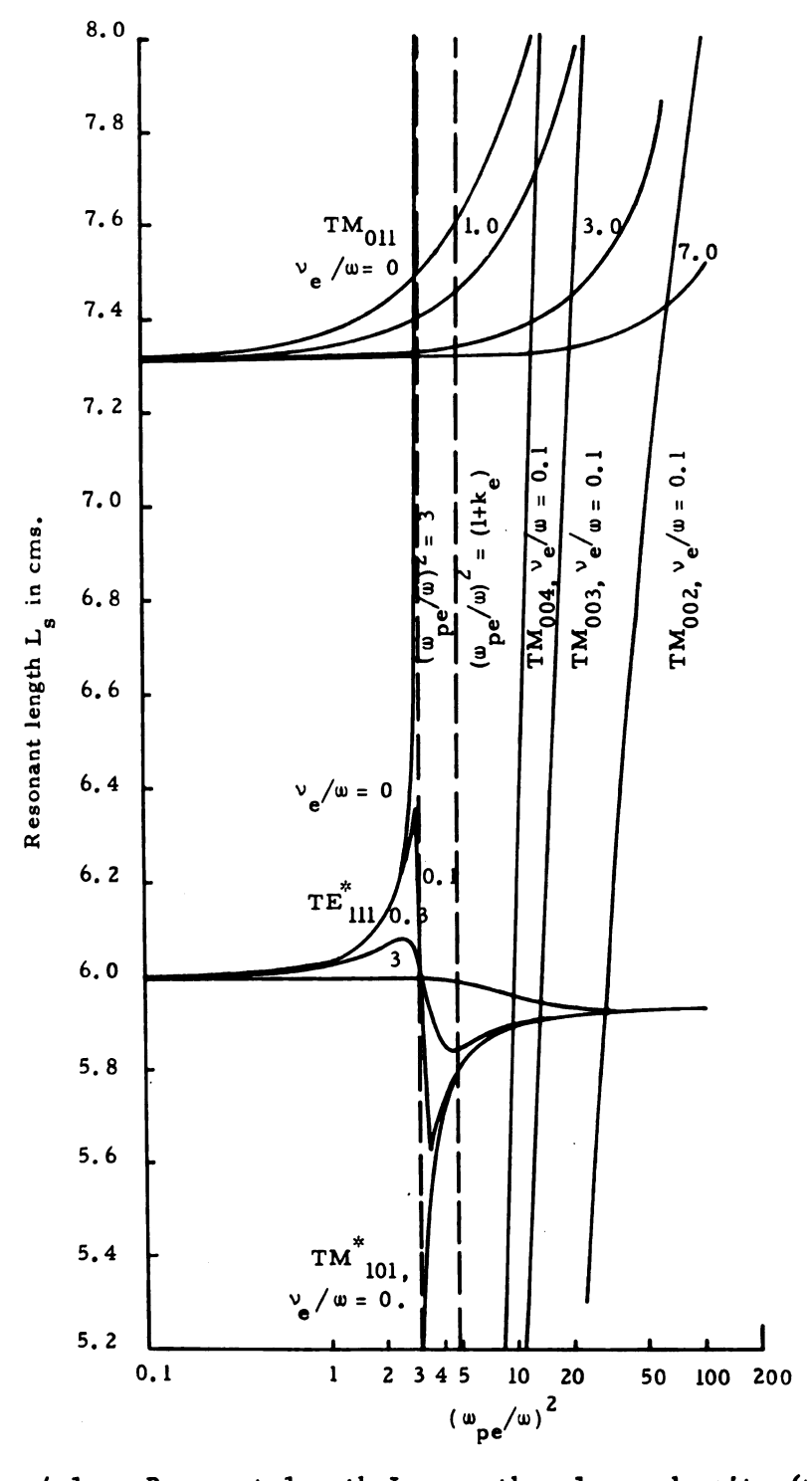


Figure 4.1a. Resonant length L vs. the plasma density $(\omega_{pe}/\omega)^2$ for the modes TM_{00p} , TM_{011} , TM_{101} , and TE_{111}^* . Operating frequency fixed at $\omega/2\pi$ = 3.03 GHz. Waveguide dimensions: a = 0.3 cms., b = 0.3875 cms., c = 5.08 cms.

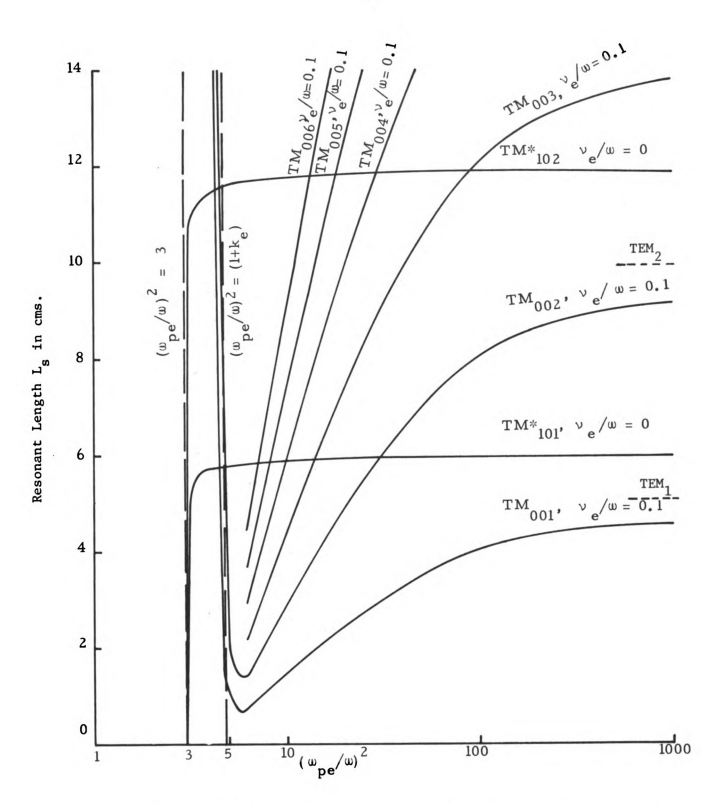


Figure 4.1b. Resonant length $L_{\rm s}$ vs. $(\omega_{\rm pe}/\omega)^2$ for the cold plasma modes, $TM_{00\rm p}$ and $TM_{10\rm p}^*$. Operating frequency $\omega/2\pi$ = 3.03 GHz. Waveguide dimensions: a = 0.3 cms., b = 0.3875 cms., c = 5.08 cms.

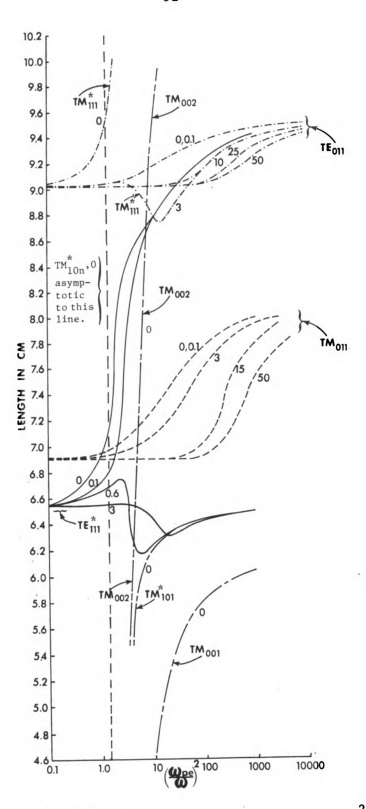


Figure 4.2. Resonant length vs. plasma density $(\omega_{pe}/\omega)^2$ and ν_e/ω for a cavity of radius 10.146 cm., plasma radius of 1.248 cm., and an operating frequency of 2.45 GHz.

4.2 Theoretical Cavity Mode

4.2.1 Classification and Description of the Plasma-Cavity Modes

It is convenient to classify the resonant lengths of the plasmacavity into three groups 10.

1) "Perturbed" cylindrical cavity resonances.

These resonances are the empty cavity electromagnetic resonances which are "perturbed" by the presence of the plasma. Thus, the forward and backward traveling waveguide modes associated with these resonances always have a phase velocity greater than the speed of light, i.e., they are fast wave electromagnetic modes. This group of resonances can be further divided into two subclasses of modes:

a)
$$TE_{Omp}$$
 or TM_{Omp} ; $m > 0$.

These resonances are pure TE or TM resonances since they are \$\phi\$ independent and thus, they are labeled with respect to the TE or TM modes on a circular waveguide. At high plasma densitites and for high losses, these modes approach the coaxial mode that has the same index as the empty cavity.

b)
$$TE_{nmp}^*$$
 or TM_{nmp}^* ; $n > 0$, $m > 0$

These modes are hybrid resonances. They are labeled with respect to the TE or TM modes in an empty circular waveguide into which they degenerate when the plasma density equals zero. It is useful to note that for high plasma densities and zero losses, (i.e., $v_e/\omega=0$) the TE_{nmp}^* resonance (or TM_{nmp}^* resonance) approaches the TM_{nmp} resonance (or $TE_{n,m+1,p}$ resonance) in a coaxial waveguide with a metallic center conductor. The TE_{111}^* mode shown in Figure 4.1a belongs to this family of modes. However, for large values of collision frequency, the resonant length increases, decreases, and then increases again returning to the TE_{111} coaxial cavity resonant length.

2) Cold-plasma resonances (TM_{001} and TM_{n01}^* ; n > 0)

These resonances do not exist in the empty cavity and are affected by the finite electron temperature only when the wave phase velocity V_{φ} is approximately equal to the thermal velocity $V_{th} = \sqrt{3KT_e/m_e}$ and $\omega > \omega_{pe}$. Thus, they are called cold-plasma modes.

Each of the modes classified above are now described in detail.

4.2.2 Rotationally Symmetric Modes, TM₀₁₁ and TE₀₁₁

(a) Lossless Plasma. $v_e/\omega=0$. As shown in Figure 4.1a, the TM₀₁₁ mode is comprised of a single half-wave resonance of the TM₀₁ waveguide mode discussed in Chapter II and has an empty cavity resonant length of $L_s=7.32$ cms. With increase in plasma density $(\omega_{pe}/\omega)^2$, the eigenlength increases slowly at first and then increases steeply in an almost linear fashion. At very high plasma densities, when the plasma rod behaves more like a conductor, the eigenlength curve becomes horizontally asymptotic to the TM₀₁₁ coaxial cavity resonant length line. This region occurs at $L_s=8$ cms. for the cavity with dimensions a=b=1.248 cms. and c=10.146 cms., as shown in Figure 4.2. For the eigenlength curves of Figure 4.1a, the TM₀₁₁ coaxial cavity resonance occurs at $L_s=19.1$ cms. and is not shown in the latter figure.

For the operating frequency and waveguide dimensions of Figure 4.1a, the ${\rm TE}_{011}$ mode is cut off. It is shown in the more general curve of Figure 4.2. It has an empty cavity resonant length of ${\rm L_s}$ = 9.02 cms. In a manner similar to the ${\rm TM}_{011}$ mode, the ${\rm TE}_{011}$ mode at high plasma densities, approaches the ${\rm TE}_{011}$ coaxial cavity resonance of ${\rm L_s}$ = 9.55 cms.

(b) Lossy plasma $v_e/\omega \neq 0$. As shown in Figure 4.1a, the eigenlength of the TM₀₁₁ mode at low plasma densities, $(\omega_{pe}/\omega)^2 = 0.1$, is

 $L_{\rm s}$ = 7.32 cms. The asymptotic behavior and the general form of the curve is almost identical to the lossless curve. For a given eigenlength, however, the lossy curve operates at a higher plasma density than the lossless curve. At very high plasma densities it becomes asymptotic to the TM_{011} coaxial cavity resonant length $L_{\rm s}$ = 19.1 cms.

The behavior of the eigenlength curves is consistent with the ω - k diagrams for the TM $_{01}$ mode shown in Figures 2.8a and 2.9a. The effect of the quartz tubing has been to reduce the empty cavity resonant length from L $_{_{\rm S}}$ \approx 7.42 cms. to L $_{_{\rm S}}$ = 7.32 cms.

For dimensions of the experimental cavity of Figure 4.1a, this mode appears to have a large variation in both the resonant length and the electron density. The eigenlength curves suggest that it might be possible to vary the length of the plasma column from 7.4 cms. to 18 cms. and the average plasma density from $(\omega_{pe}/\omega)^2 = 3$ to at least $(\omega_{pe}/\omega)^2 = 100$, if the required RF input power were available.

The behavior of the lossy ${\rm TE}_{011}$ mode resembles that of the ${\rm TM}_{011}$ mode. As shown in Figure 4.2, at high plasma densities the lossy curves become asymptotic to the ${\rm TE}_{011}$ coaxial resonance given by ${\rm L}_{\rm s}$ = 9.55 cms.

4.2.3 <u>Dipole modes; TE</u>* and TM*101

(a) Lossless plasma. $v_e/\omega=0$. As shown in Figure 4.1a, the TE $^*_{11}$ mode has an empty cavity resonant length of L $_s=5.99$ cms. The lossless eigenlength curve at first rises slowly with increasing plasma density, then very steeply in the neighborhood of $\omega_{pe} < \sqrt{3} \omega$ and eventually becomes vertically asymptotic to the dipole resonance line given by $(\omega_{pe}/\omega)^2=3$. If the effect of the quartz had been neglected, this curve would have been asymptotic to $(\omega_{pe}/\omega)^2=2$. For densities beyond $(\omega_{pe}/\omega)^2=3$, this eigenlength curve would normally be horizontally

asymptotic to the TM₁₁₁ coaxial mode eigenlength line 17. The TM₁₁₁ mode, however, is cut off at the chosen experimental operating frequency, f = 3.03 GHz. The general case is shown in Figure 4.2 where the lossless $\operatorname{TE}_{111}^{\star}$ curve asymptotically approaches the TM_{111} coaxial resonance, $L_s = 9.55$ cms. at very high plasma densities. The TM_{101}^* mode, (see Figure 4.1a), i.e., the first half wavelength resonance of the TM_{10}^{*} mode, does not exist in the empty cavity. It is present only in the presence of a plasma and for densities ω_{pe} > $\sqrt{3}$ $\omega.$ It is vertically asymptotic to the line, $(\omega_{pe}/\omega)^2 = 3$. With increase in plasma density the eigenlength increases and the curve eventually becomes asymptotic to $L_{_{\mbox{\scriptsize S}}}$ = 5.925 cms., the TE_{111} coaxial cavity resonant length. In the neighborhood of $(\omega_{pe}/\omega)^2 = 3$, this mode is essentially a slow space charge wave as described in Chapter II. It behaves as a fast electromagnetic wave for $L_s \ge 5.8$ cms. The TM_{10p}^* modes, for $p = 2, 3 \dots$ are also vertically asymptotic to $(\omega_{\rm pe}/\omega)^2$ = 3, and horizontally asymptotic to L_s = 5.96 p, p = 2, 3, etc., respectively, as shown in detail in Figure 4.1b.

- (b) Lossy plasma, $v_e/\omega \neq 0$. For this case the TM_{101}^* mode and the TE_{111}^* mode have identical eigenlength solutions. This mode can best be studied by further subdividing the losses.
- 1. Small losses $v_e/\omega=0.1$. As shown in Figure 4.1a, the low plasma density $[(\omega_{pe}/\omega)^2=0.1]$ eigenlength is $L_s=5.99$ cms. The eigenlength increases slowly with plasma density up to $(\omega_{pe}/\omega)^2=1.5$. In the neighborhood of $(\omega_{pe}/\omega)^2=3$, the eigenlength increases, then decreases sharply and rises again. It eventually becomes asymptotic to $L_s=5.925$ cms., the TE_{111} coaxial cavity resonant length. The region in which the eigenlength decreases with increasing plasma density $(2.8 \le (\omega_{pe}/\omega)^2 \le 3.3)$ corresponds to a backward wave (see Figure 4.1a). The backward wave region for the TE_{11}^* waveguide mode was described in Chapter II.

It is useful to observe that for $(\omega_{pe}/\omega)^2 < 3$ and for $(\omega_{pe}/\omega)^2 > 3$, there are operating regions where it is possible to have two plasma densities for a fixed eigenlength. As shown in the ω/ω_{pe} vs. α/k_c diagrams for this mode (Figure 2.10b) wave attenuation is high in the backward wave region.

2. High Losses $v_e/\omega=3.0$. At such high collision frequencies, the resonant length of the TE_{111}^{\star} mode is relatively insensitive to variations in the plasma density. For small values of $(\omega_{\text{pe}}/\omega)^2$ the plasma is essentially a lossy dielectric and the eigenlength is close to that of the TE_{111} empty cavity mode, $L_s=5.99$ cms. As $(\omega_{\text{pe}}/\omega)^2$ becomes large the plasma becomes a lossy conductor. The resonant length of this mode approaches that of the TE_{111} coaxial cavity mode, $L_s=5.925$ cms.

It is clear from Figure 4.1a that the eigenlength is almost constant for density variations above $(\omega_{\rm pe}/\omega)^2 > 10$. This is true for all collision frequencies. This region would be suitable for operating RF discharges with practically no tuning of the length 10 . It would seem that a plasma with pressures varying from low to high values can be formed in this region without jumping out of resonance. This would make this mode practical for flowing and fluctuating plasmas in plasma chemistry applications or as a general RF plasma source 10 .

4.2.4 Space Charge Modes TM 00p

These modes do not exist in the empty cavity. In the presence of the plasma, however, they exist over a wide range of resonant lengths. Figure 4.1a shows the eigenelength curves of several modes, TM_{002} , TM_{003} , TM_{004} in the region of experimental operation i.e., $L_{\rm s}$ = 5.2 cms. to $L_{\rm s}$ = 8.0 cms. It is in this range of resonant length, in which these modes intersect with two electromagnetic modes TM_{011} and TE_{111}^{\star} . These

regions of mode intersection are of special experimental importance. It will be discussed in experimental sections to follow.

Small losses $v_e/\omega = 0.1$. The behavior of these modes is best studied by looking at the eigenlength curves of ${\rm TM}_{\rm OOp}$ for very small losses, say v_e/ω = 0.1. At high plasma densities the TM_{00p} curves for p = 1, 2, 3 etc., are horizontally asymptotic to the TEM resonant length given by $L_s = p$ 4.95 cm. as shown in Figure 4.1b. With a decrease in plasma density the eigenlength of these modes falls steadily at first and then drops very steeply for small decreases in plasma density. The almost vertical drop of the TM_{00p} eigenlength curve with decreasing plasma density continues until it approaches the region $\omega_{pe} > \sqrt{1+k_e} \omega$, where $k_{\rho} = 3.78$ is the quartz dielectric constant. In this region the curve reaches a point of zero slope, after which the eigenlength increases very sharply with a further decrease in the plasma density. This curve cannot approach the horizontal asymptote of an EM mode, because that mode is cut off at the operating frequency, f = 3.03 GHz, (Figures 4.1a and 4.1b). The TM_{002} mode is not shown in its entirety in Figure 4.1a. This same type of behavior, however, is true for all losses and a typical eigenlength curve for TM_{002} , v_e/ω = 0.1 is shown in Figure 4.1b.

The TM_{00p} lossless curves for p = 1, 2 ... almost coincides with the TM_{00p} v_e/ω = 0.1 curves; the difference being that the lossless curves eventually become asymptotic to the line $(\omega_{pe}/\omega)^2$ = $(1+k_e)$ = 4.78, and do not rise again with a decrease in plasma density. The behavior of TM_{00p} curves is consistent with the ω - k diagrams for the TM_{00} waveguide modes described in Chapter II (Figures 2.2, 2.3, 2.4 and 2.5).

As can be inferred from the ω/ω_{pe} vs. α/k_{c} (Figures 2.3b, 2.4b and 2.5b) curves of Chapter II for the TM_{00} modes, only the forward space

charge region ($\omega_{\rm pe}$ > 4.78 ω) with small collisional losses ($\nu_{\rm e}/\omega$ = 0.1) has low damping. The backward wave region, i.e., when the eigenlength increases with decreasing plasma density, is not of significance as a wave phenomena because of heavy damping. However, it still might be possible to experimentally couple energy to the plasma in this region.

4.3 Summary

The lossy cold plasma theory of Chapter II has been used here to obtain the eigenlengths of EM and space charge modes of a microwave-plasma cavity. The eigenlength curves suggest that it might be possible to operate the plasma-cavity over a wide range of electron densities, collision frequencies and in a number of different modes. The primary EM modes of operation are TM_{011} , TE_{011} and TE_{111}^* . A plasma source operated in these modes has applications in plasma chemistry experiments and in pumping gas lasers. Also, the TM_{011} mode, which as electric fields in the form of an axial quadropole, is capable of exerting radio frequency forces on a plasma for confinement purposes 23 .

The backward wave region in the lossy TE_{111}^{\star} eigenlength curves suggests that it might be possible to have two plasma density operating points for a single eigenlength. Also, of interest are the regions where the eigenlength curves of the space charge modes TM_{00p} intersect with those of the EM modes TM_{011} and TE_{111}^{\star} , suggesting that it might be possible to couple the EM energy to space charge waves. These observations and the usefulness of the plasma-cavity as a RF plasma source will be experimentally studied in Chapter VI.

CHAPTER V

EXPERIMENTAL SYSTEMS

5.1 Introduction

Two microwave cavities have been used to experimentally study the linear resonances, the non-linear behavior and the absorbed power characteristics of the microwave plasma source. Both cavities are cylindrical, have a sliding short for tuning and a screened window for viewing purposes. The two cavities, however, differ in size. Cavity 1 has a radius of 5.08 cms. and operates at the available incident power of 30W while cavity 2 has a radius of 10.15 cms. and operates at incident powers of up to 1.3KW.

5.2 The Two Plasma-Cavity Systems

5.2.1 The #1 Plasma-Cavity System

A cross-section of Cavity 1 is shown in Figure 5.1. This variable length cavity has been designed to excite several resonances in the 2 to 4 GHz frequency range. The waveguide dimensions have been chosen so that when operating in the TE_{111}^* cavity mode the ratio of the resonant length to radius is approximately one for a 3.03 GHz signal. A cavity radius of 5.08 cms. satisfies this design requirement.

Several of the resonant modes of this cylindrical cavity are shown in Figure 5.2. In this figure, the resonant frequency is shown as a function of the cavity length. Also, shown in Figure 5.2 are a few of the coaxial cavity modes. These modes are of interest because a very dense cylindrical plasma has electrical properties similar to a metal rod inside the cavity.

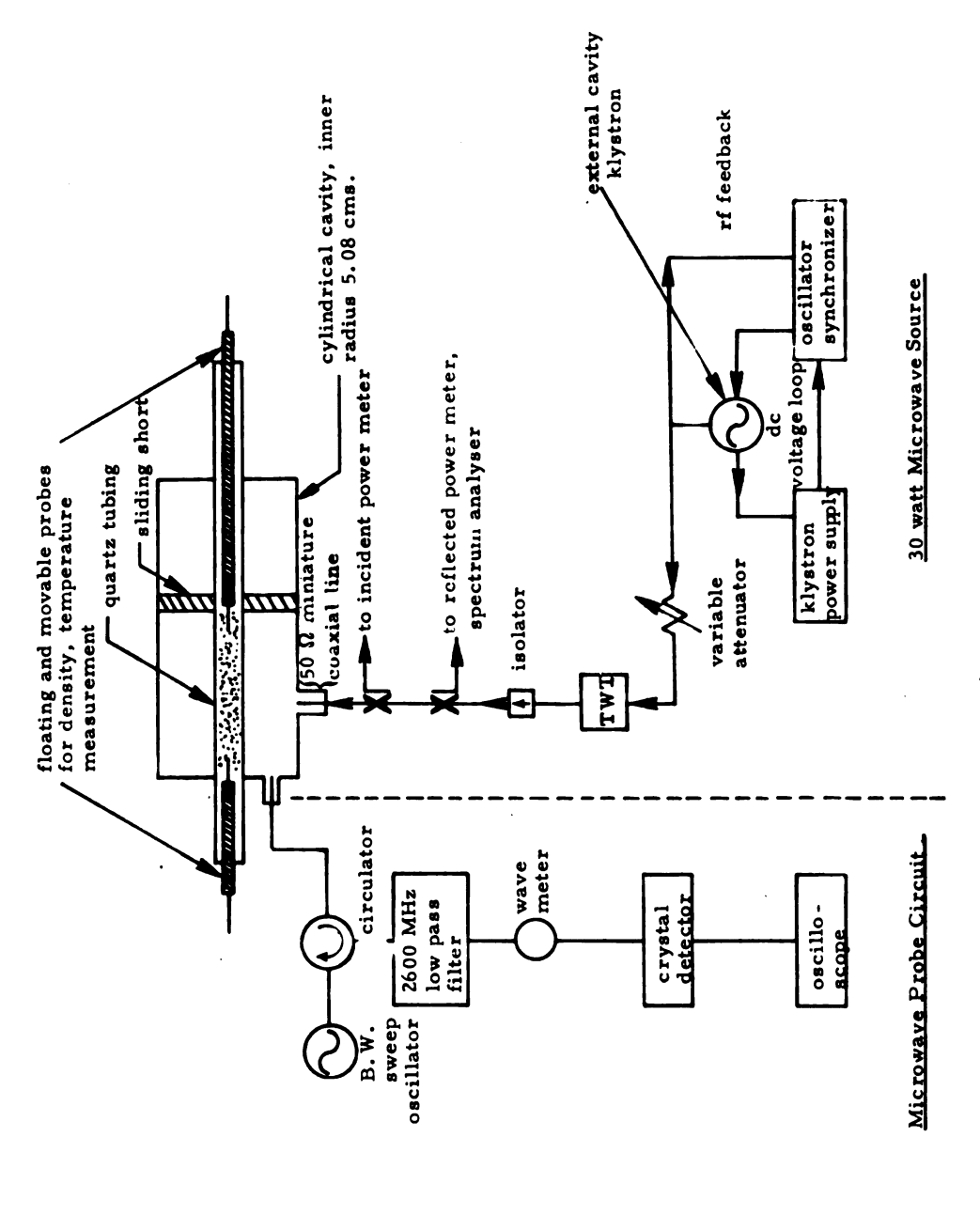
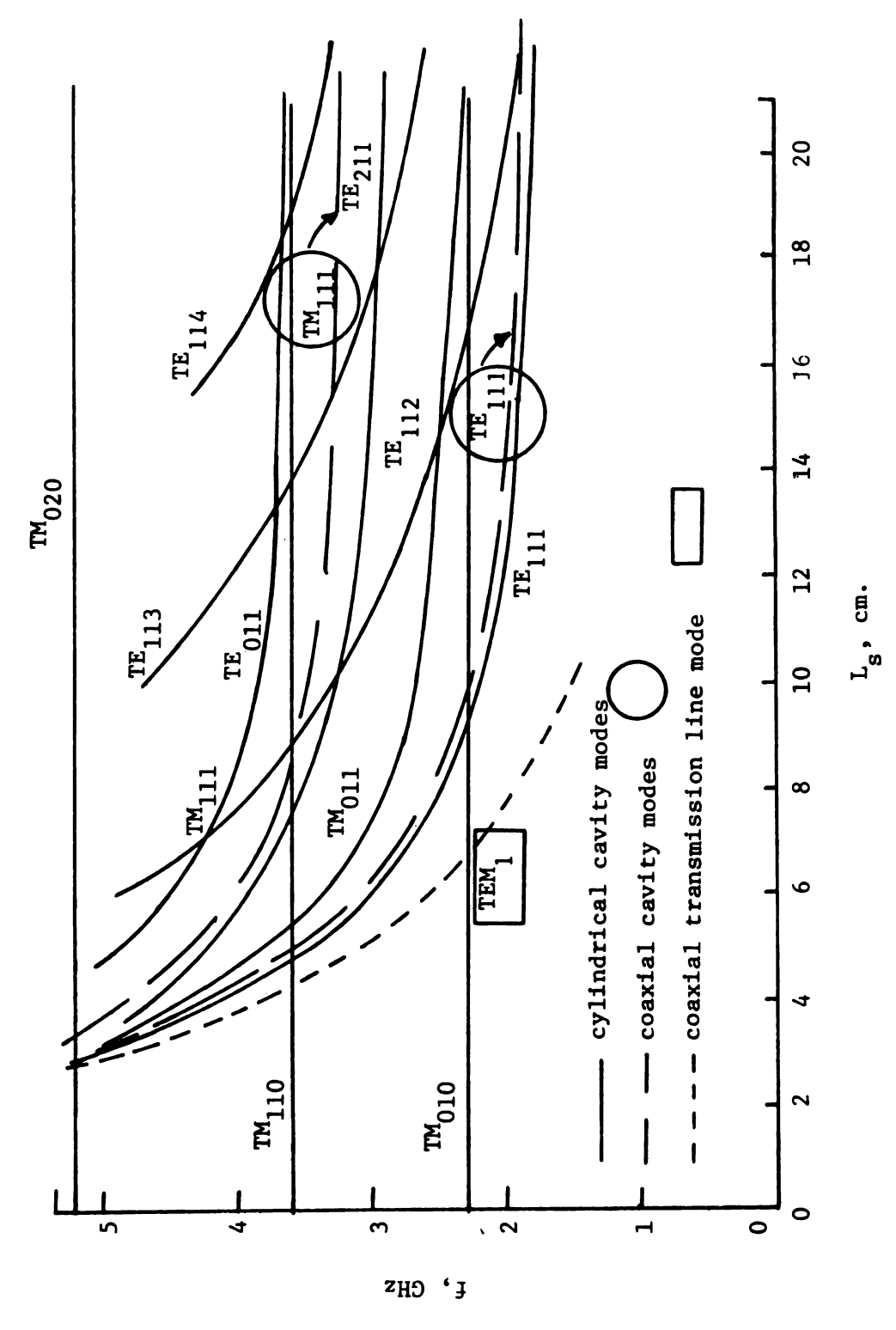


Figure 5.1. Cross section of the cylindrical cavity, 30 watt microwave source, and plasma diagnostic circuits.



c = 5.08 cms. Figure 5.2. Resonant frequency versus cavity size. Waveguide dimensions:

Cavity 1 is fitted with a mechanical device that smoothly varies the length and a micrometer that measures changes in cavity length of the order of .01 mm. This precise tuning arrangement enables the variation in cavity length for any changes in plasma conditions and thus enables the study of the cavity eigenlength as a function of the plasma density. This is especially useful in verification of the TE_{111}^{\star} eigenlength curves (see Chapter VI).

The cylindrical cavity is driven by the microwave system shown in Figure 5.1 by a miniature radial or loop type of probe coupling. The radial probe which excites radial electric fields in the cavity is suitable for exciting the ${\rm TE}_{111}^{\star}$ mode. The loop type of coupling can be used for generating an efficient ${\rm TM}_{011}$ plasma. The power coupled to the plasma can be adjusted by varying the depth of the probe into the cavity and in case of the loop probe, by also adjusting the orientation of the loop.

At the chosen frequency of $\omega/2\pi=3.03$ GHz, this cavity can be operated in the TE_{111}^{\star} , TM_{101}^{\star} , TM_{011}^{\star} and $\text{TM}_{\text{oop}}^{\star}$ modes. The TM_{101}^{\star} and $\text{TM}_{\text{oop}}^{\star}$ modes exist only in the presence of the plasma. It is important to study the behavior of the EM modes TE_{111}^{\star} and TM_{011}^{\star} over a wide range of pressures, because of their applications in areas such as plasma chemistry and possible applications to plasma confinement and gas discharge lasers.

All the low pressure work in this thesis has been done on plasmas generated in Cavity 1. This plasma-cavity system can be pumped down to a pressure of 10 mtorr and has a tight vacuum control. Thus, this system is ideally suited for studying warm plasma modes such as the Tonks Dattner resonances 17 , which occur at very low pressures and very low plasma densities. When driven in the TE_{111}^{\star} mode, the fields in the cavity are

overwhelmingly dipolar; and thus, the monopole and quadropole fields, which are excited in the usual scattering experiments when studying TD resonances, should not be present 24,25. Also, non-linear phenomena arising out of strong RF-bounded plasma interactions and any hysteresis effects of the plasma can be conveniently examined. The #1 plasmacavity is also ideally suited for generating space charge waves, as will be demonstrated in Chapter VI.

5.2.2 The External Microwave System for Cavity 1

A line diagram of the experimental system is shown in Figure 5.1. The incident microwave signal at a frequency of 3.03 GHz is generated by an external cavity klystron which is connected to an oscillator synchronizer to form a phase-lock loop. The synchronizer locks the klystron oscillator to a harmonic of the oscillating frequency of an internal reference crystal, to produce a frequency stable microwave source. Such a frequency source is necessary, since the plasma media is dispersive and the microwave circuits are frequency sensitive.

The stabilized RF power from the klystron is delivered to a variable attenuator, which controls the input power to a traveling wave tube amplifier (TWT). By adjusting the variable attenuator, the amplified output power from the TWT can be varied from 0 to 30 watts. An isolator protects the TWT's output helix from being damaged by reflected microwave power. Most of the experimental work on the Cavity 1 was done at an incident frequency of 3.03 GHz. However, a variable frequency source was employed whenever a number of different frequencies were required.

A pair of directional couplers were used to measure incident and reflected power from the cavity. The spectrum of the reflected power

could be analyzed by connecting a spectrum analyzer to the reflected signal directional coupler.

5.2.3 Diagnostic Circuits for Cavity 1

The #1 plasma-cavity system is provided with circuits for measuring the average plasma density and the electron temperature from a discharge pressure of 10 mtorr to 20 torr.

The microwave probe circuit shown in Figure 5.1 uses the ${\rm TM}_{010}$ frequency shift technique 26,27,28,29 to measure the average plasma density. This method can be used in the range 10 mtorr to 200 mtorr; the upper limit on the pressure being determined by the requirement that $v_{\rm e}^2<<\omega^2$, where ω , is the ${\rm TM}_{010}$ diagnostic frequency. The power from a 2 - 4 GHz backward wave oscillator is fed to a 3-port circulator. The output from the second port of the circulator is coupled via a miniature coaxial probe to the cylindrical cavity so as to excite the ${\rm TM}_{010}$ mode. The reflected power from the cavity comes out of port 3 of the circulator, and is sent through a 2600 MHz low-pass filter, which serves to cut off the cavity driving frequency (3.03 GHz). The output of the filter is rectified and fed to an oscilloscope, which is frequency swept by the BWO.

The eigenfrequency variation of the TM_{010} mode with the average plasma density and the normalized collision frequency is shown in Figure 5.3. The properties of cavity modes, including the TM_{010} mode, that are used for plasma diagnostic purposes are further discussed in Chapter VI.

For density and electron temperature measurements above 100 mtorr two double Langmuir tungsten probes are used. These probes are inserted through either ends of the quartz tube. The probes can be longitudinally moved so as to adjust the depth of the probe into the plasma. The probe

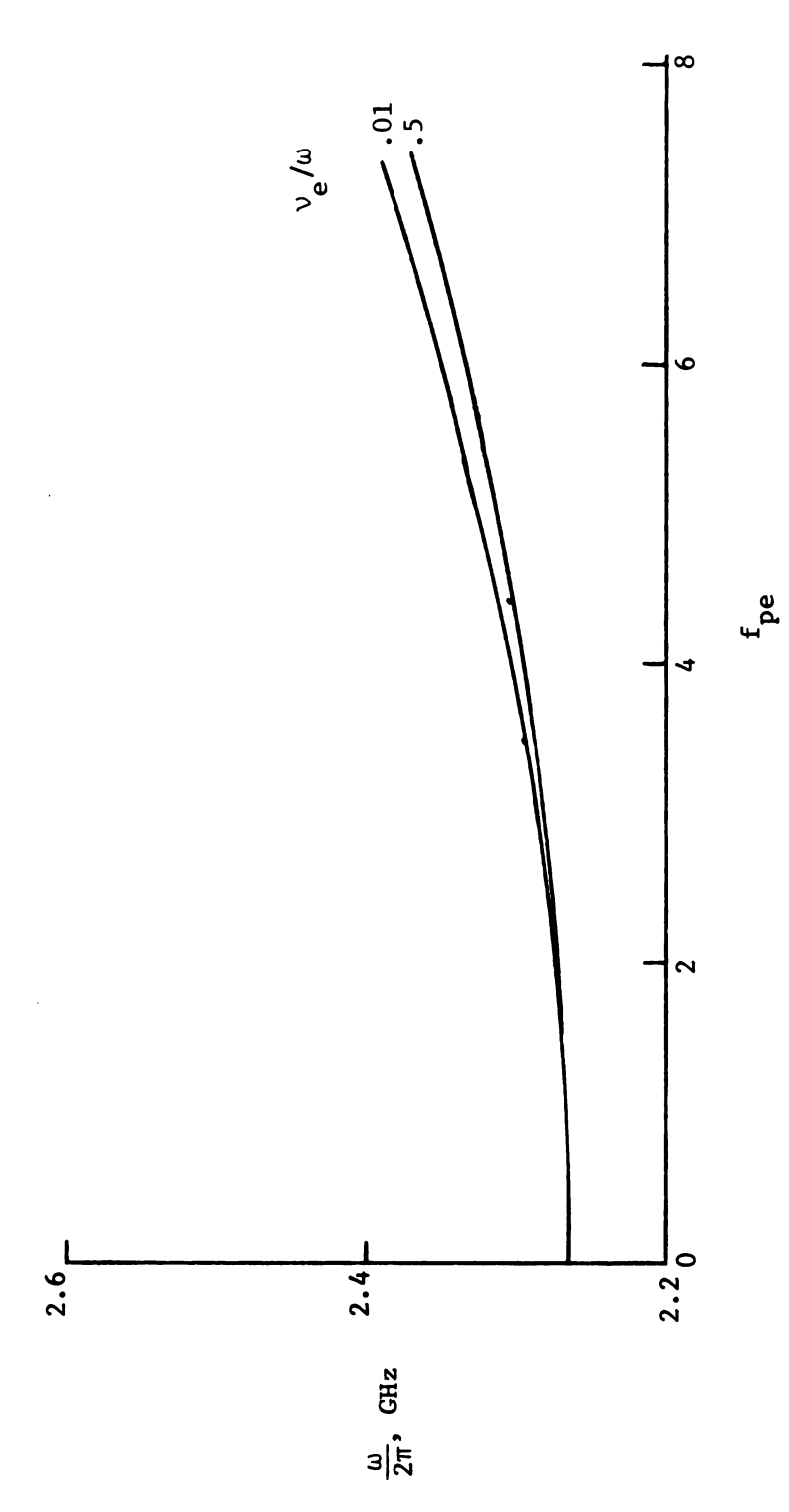


Figure 5.3. $\omega/2\pi$ vs. f and v_e/ω for the TM $_{010}$ mode. Waveguide dimensions: a=0.3 cms., b=0.3875 cms, c=5.08 cms.

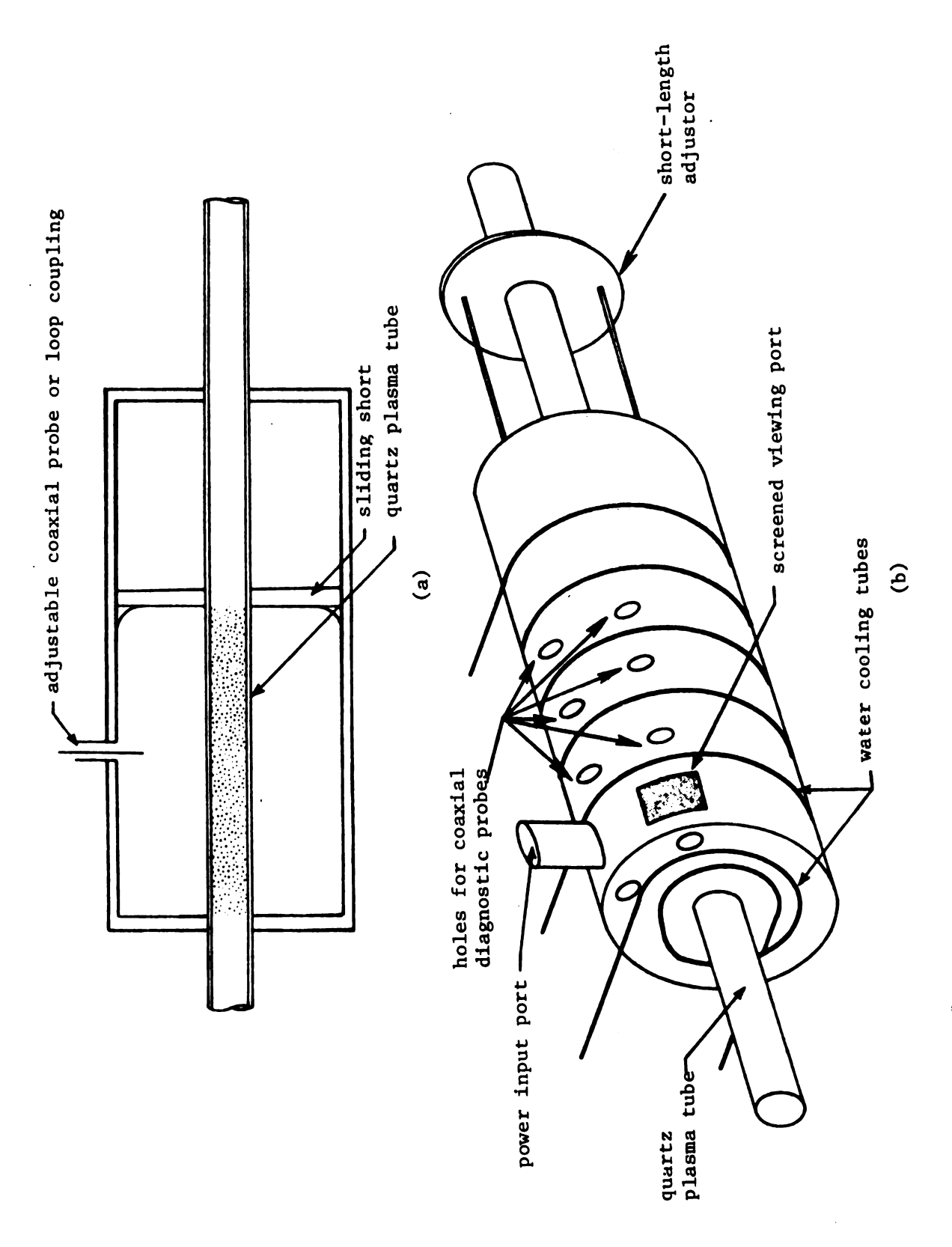
data can be analyzed by the usual double-probe theory to obtain numbers for electron density and electron temperature 30,40.

For pressures above 1 torr the probe data is usually not reliable. The plasma number density at higher pressures is obtained from the D.C. conductivity of the plasma. This is measured by introducing discs longitudinally into the quartz tube so as to be barely immersed in the plasma. Plasma diagnostics using probes and discs is further discussed in Chapter VI.

The average luminosity of the plasma can be monitored by attaching a photometer to a one mm hole drilled in the side of the cavity. By calibrating the photometer reading against a known density measurement of the plasma using another technique, it is possible to measure changes in the electron density by observing changes in the light intensity of the plasma.

5.2.4 The #2 Plasma-Cavity System

This plasma-cavity system has been used to investigate chemical reactions in microwave discharges, but is general enough to be useful for other applications such as a high-power light souce, an active plasma for lasers, and a source of free radicals for chemical lasers. The plasma is formed in the quartz tube (inside radius equals 1.25 cm.) which is located on the axis of the cylindrical plasma-cavity system (inside radius equals 10.15 cm.) as shown in Figure 5.4a. The outer walls of the cavity are water cooled by tubing attached to the exterior wall surface shown in Figure 5.4b, and the quartz tube can be forced-air cooled when necessary. A screened viewing window provides a visual viewing port. Many small holes are cut into the exterior walls providing coaxial ports required for microwave diagnostic measurements.



(a) Cross section of plasma cavity (b) Isometric drawing. Figure 5.4. The #2 plasma-cavity system.

Depending on which cavity mode is excited, two adjustable loop or probe coupling systems located in the cavity side allow the RF energy to be introduced into the cavity. These adjustable coupling systems behave like a variable impedance transformer. Thus, by adjusting the depth of a probe (or rotating the loop or by varying the loop size), the plasma-cavity impedance can be continuously adjusted.

The cavity length, which is continuously adjustable up to 35 cm., can be varied as the plasma conditions change. The inside cavity length could be determined from a centimeter scale, which was adjusted to read absolute cavity length by using the short length adjustor as a reference (see Figure 5.4). The variable cavity length allows the production of a variable high-density plasma inside the cavity operating from pressures of 1 torr to 1 atm (argon gas). This retuning can be achieved even under widely varying plasma loading conditions, and in practice, the length changes required to retune the cavity from no load to full load vary, depending on the cavity mode, from as much as 1 - 2 cm. to less than several millimeters. This small retuning length results from the fact that the ratio of plasma diameter to cavity diameter is much less than one. Thus, the presence of the plasma inside the cavity only slightly perturbs the cavity resonance frequency.

Since the plasma fills only part of the cavity, the plasma and the external metallic cavity walls combine to form the resonant circuit. This plasma-cavity system is a high-frequency equivalent of Babat's RF plasma systems 32. However, one cannot think of system performance in terms of lumped circuit elements, i.e., inductors and capacitors, because of the short electromagnetic wavelength of microwaves. The plasma-cavity system is a distributed parameter resonant circuit since the length of

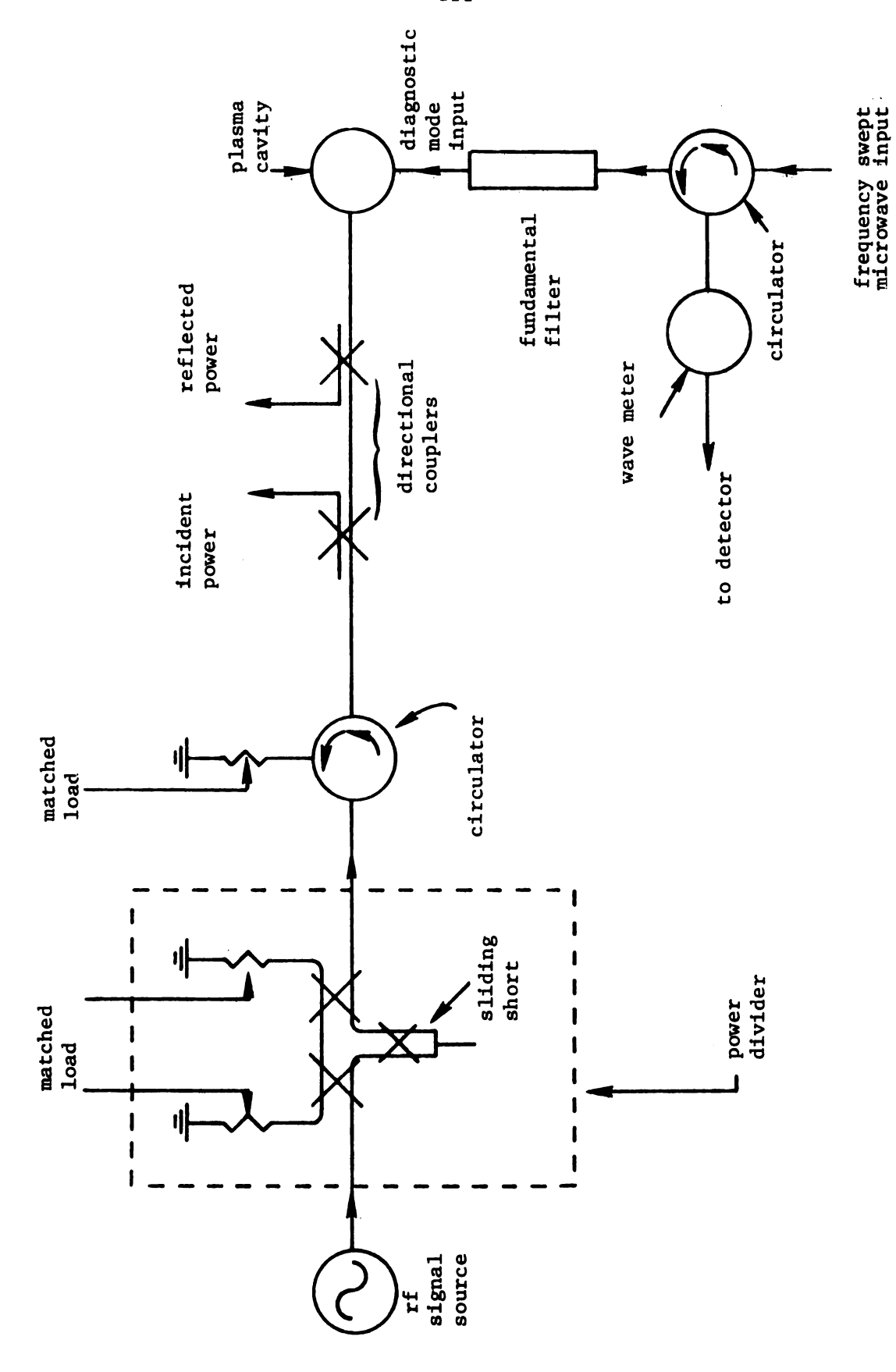
the plasma can be of the same order of magnitude or larger than the free-space electromagnetic wavelength. Thus, an active RF discharge has certain short sections of the plasma behaving similar to an E or an H discharge (as defined by $Babat^{32}$).

The fact that the plasma does not fill the entire cavity allows an RF plasma to be sustained inside the cavity with densities much greater than the critical density. If the plasma were allowed to fill the entire cavity, the plasma density would be limited to approximately the critical density or less (except in the region near the coupling ports where evanescent fields exist), since all homogenous isotropic waveguide modes are cut off at frequencies below the plasma frequency 11.

5.2.5 The external microwave system for Cavity 2

A line diagram of the external RF system is shown in Figure 5.5. The RF signal source is a fixed frequency, 2.45 GHz magnetron oscillator capable of delivering 1.3 kW of continuous wave power. As shown in Figure 5.5, the RF power from the oscillator is incident on a power divider circuit. This power divider is constructed from three 3-dB sidewall hybrid couplers, two matched dummy loads, and a tandem sliding short. By moving the sliding short, the power delivered to the power divider output arm can be continuously varied from zero to full magnetron output. This divider is designed so that the input port will always be matched for any sliding short position if the other three ports are matched.

The power output from the divider passes through a three-port circulator, through the incident and reflected directional couplers, and is incident on the plasma-cavity system. The power that is reflected from the cavity travels back into the dummy load attached to the third



The external microwave system for the #2 plasma-cavity Figure 5.5.

arm of the circulator. Thus, the circulator protects the magnetron from the large amounts of reflected power that may be present during certain phases of experimentation. Furthermore, it allows the magnetron to work into a matched system independent of the plasma-cavity load. The two-directional couplers monitor the power in the main waveguide arms and thereby provide a means to measure the incident, reflected, and absorbed power in the cavity.

The power incident on the cavity is fed into a coaxial system, and an adjustable length, radial probe, or loop couples the power into the resonant modes of the plasma-cavity system. The cavity diameter and excitation frequency were chosen to allow only one cavity mode to be excited for a given cavity length. Coupling power into a given mode was accomplished by orientation of the loop or depth of the probe. Tuning stubs which are used in some plasma-cavity experiments will not be required since adjustments in the coupling probe and cavity length will produce the impedance match necessary for all modes of operation.

5.2.6 Diagnostic circuits for Cavity 2

A diagnostic cavity mode can also be excited in addition to the driving mode to measure the average plasma density 26 . This circuit is also shown in Figure 5.5. The diagnostic input is coupled into the cavity through a small coaxial coupling loop inserted into an appropriate coupling hole shown in Figure 5.4b. This loop is positioned to minimize the coupling of the RF sustained mode energy out of the cavity and maximize the coupling of the diagnostic mode energy into the cavity. The length independent $^{\rm TM}_{010}$ and $^{\rm TM}_{020}$ modes are convenient for diagnostic purposes and the average plasma density can be obtained from standard

perturbation formulas 26 or from exact computer solutions of the lossy plasma-cavity model discussed in Chapter IV.

CHAPTER VI

EXPERIMENTAL PERFORMANCE OF THE MICROWAVE PLASMA SOURCE

6.1 Introduction

In this chapter the experimental properties of the microwave plasma source are examined over a wide range of pressures, namely 10 mtorr - 500 torr. The type of experiments conducted on this source can be broadly divided into three categories:

- 1) Observation of any unusual electromagnetic phenomena such as the appearance of sidebands and the qualitative explanation of these phenomena using the linear theory derived in Chapters II, III, and IV.
- 2) Measurement of the plasma parameters N and T $_{\rm e}$, and the calculation of an effective electric field, E $_{\rm e}$, in the plasma.
- 3) Study of the absorbed power characteristics of the plasma source and its dependence on background pressure, gas flow rate, incident power and eigenlength of the cavity.

Cavity 1 has been used in the pressure range of 10 mtorr - 20 torr to examine the linear and non-linear electromagnetic properties of the plasma cavity. This is described in Section 6.2. Eigenlength curves of the TE_{111}^{\star} mode are verified and space charge waves are excited in the cavity. Two different types of sidebands are detected in the reflected spectrum and speculation as to the cause of these is presented.

In applications of this plasma source in plasma chemistry, or gas discharge lasers, it is important to measure the effective electric field $\mathbf{E}_{\mathbf{e}}$ vs. the discharge pressure. This parameter is obtained by

measuring N_o and T_e , i.e. the average electron density and electron temperature of the ionized gas. The low power and the efficient low pressure operation of Cavity 1 make it ideally suitable for plasma diagnostics by the conventional probe 30 , disc 7 , and frequency shift techniques $^{26,33-36}$. The measurement of N_o , T_e over the pressure range 40 mtorr - 20 torr, the calculation of E_e , and the accuracy and limitations of these measurements are described in section 6.3.

The absorbed power characteristics of the plasma source as a function of the background pressure, gas flow rate, incident power and eigenlength of the cavity are examined in section 6.4. Cavity 2 is used to perform these experiments, because of its operation over a broad pressure range (1-500 torr), large variation in flow rates (0-14,000 cc/min) and high incident power levels (up to 1.3 KW). These experiments are performed on two different modes:

- a) TE $_{011}$. In this mode, the eigenlength is dependent on $(\omega_{pe}/\omega)^2$ and (v_a/ω) .
- b) TE $_{112}^{\star}$. The eigenlength is almost independent of $(\omega_{\rm pe}/\omega)^2$ and $(\nu_{\rm p}/\omega)$ for critical densities beyond 10 (see Figure 4.2).

The theory of Chapters II through IV is used to qualitatively explain some of the experiments described in this chapter. This theory cannot fully explain all experimental phenomena because of its restriction to:

1) small signal linear phenomena, 2) ionized gases with a zero flow rate. However, the theory does take into account the collision frequency losses, i.e., the pressure dependence of the experimental phenomena.

6.2 Linear and Non-Linear Operation of Cavity 1

6.2.1 Introduction

Cavity 1 is driven by a 30W, 3.03 GHz microwave source as shown in Figure 5.1. The RF plasma source is excited by a Tesla coil, and the linear resonances of the plasma-cavity are observed by monitoring the reflected power. At the fixed operating frequency of 3.03 GHz, it is possible to excite the following plasma cavity modes: dipole EM modes, TE_{111}^* and TM_{101}^* , the rotationally symmetric EM mode, TM_{011}^* , and the space charge modes TM_{00p}^* , p = 1, 2, 3 ... etc. The empty cavity resonance of the TE_{111}^* mode occurs at L_s = 6.0 cms. and the TE_{111}^* coaxial cavity resonance at L_s = 5.92 cms. The TM_{011}^* mode has an empty cavity resonance at L_s = 7.42 cms. (see Figures 4.1 and 5.2).

Based on experiments conducted in the low pressure regime, (10 mtorr-1 torr) four different types of experimental results are reported here.

They are:

- 1) The presence of two resonant plasma densities for a single resonant length while operating in the ${\rm TE}_{111}^{\star}$ mode.
- 2) Ejection of the plasma from the ends of the cavity while operating at specific resonant lengths in the ${\rm TE}_{111}^{\star}$ and ${\rm TM}_{011}$ modes and in a specific range of plasma densities and collision frequencies.
- 3) Formation of short wavelength standing waves ($\lambda_g \approx 1$ cm.) in the plasma when the plasma cavity operates in the off resonance region of the TE_{111}^* or TM_{011} modes.
- 4) Detection of two different types of sidebands in the reflected power spectrum.

Each of these experimental phenomena is explained in detail on the following pages.

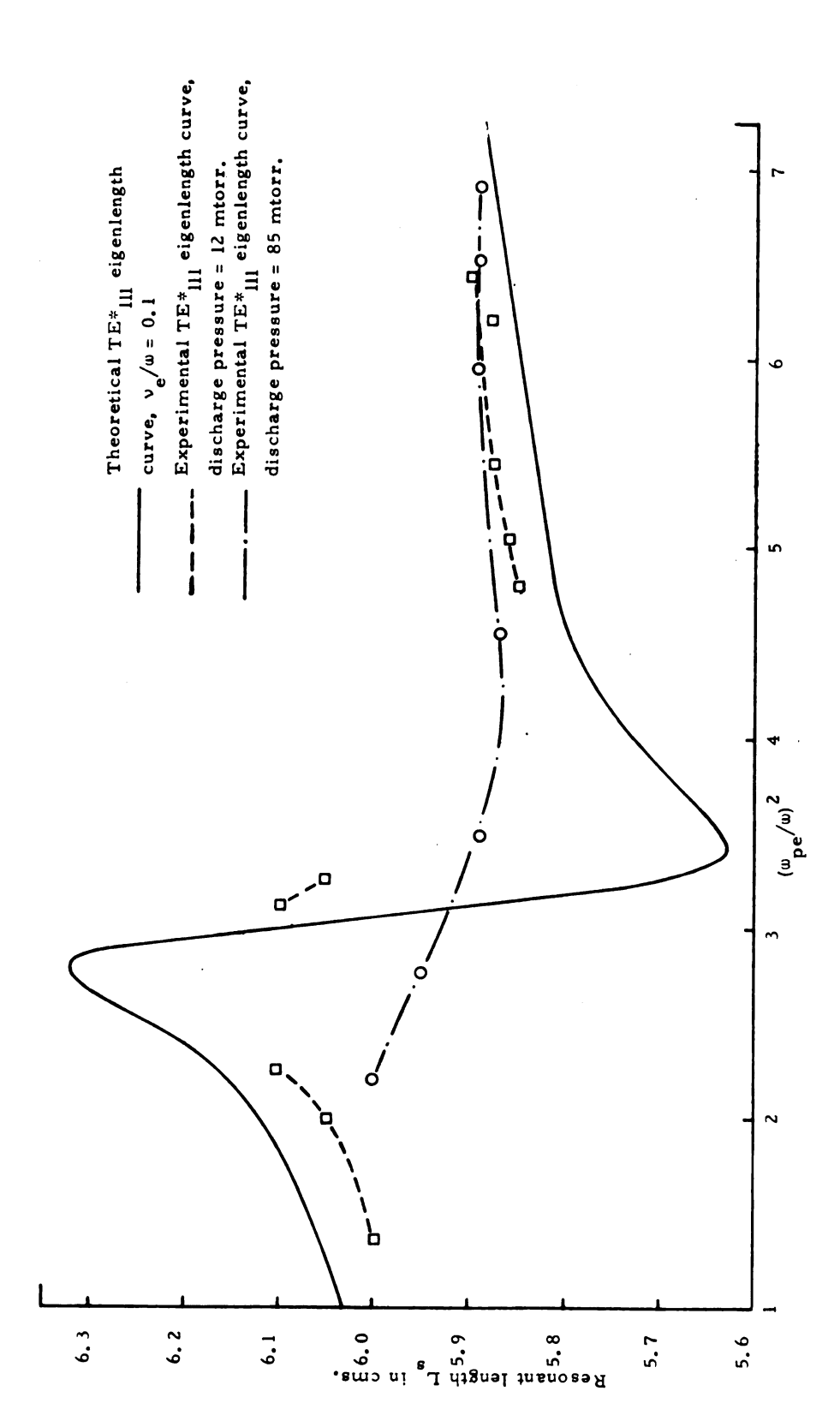
6.2.2 Excitation of Two Resonant Plasma-Density Operating Points for a Single Resonant Length

It was shown in Chapter IV that the resonant length vs. $(\omega_{\rm pe}/\omega)^2$ for a low loss ${\rm TE}_{111}^{\star}$ mode first rises, falls and then rises again to become asymptotic to the ${\rm TE}_{111}$ coaxial mode. The theoretical curve for $v_{\rm e}/\omega$ = 0.1, is shown on an expanded scale in Figure 6.1. Experimental curves at discharge pressures of 12 mtorr and 85 mtorr are also plotted on Figure 6.1. All electron density measurements in this experiment have been made using the ${\rm TM}_{010}$ frequency shift method.

The experiment is conducted by starting the discharge at a pressure of 100 mtorr, an incident power of 30W, resonant length of 6 cms. and then tuning the resonant length to 5.92 cms. by maximizing the photometer reading. The discharge pressure is now gradually reduced to a low value say 12 mtorr. Such a low pressure is necessary to provide a suitable comparison with the low collisional loss (v_{α}/ω = 0.1) theoretical curve.

At a pressure of 12 mtorr and with the maximum avaliable incident power of 26W, the resonantly-tuned operating point is at $L_s=5.90$ cms. and $(\omega_{pe}/\omega)^2=6.42$. As the incident power is gradually reduced and the resonant length tuned at the same time, the dashed curve as shown in Figure 6.1 is obtained. At $(\omega_{pe}/\omega)^2=4.8$ and $L_s=5.85$ cms., the plasma cavity abruptly jumps to the operating point of $L_s=5.85$ cms. and $(\omega_{pe}/\omega)^2=1.73$ (not shown in figure). This point corresponds to a low density non-maximized resonant length operation in the TE_{111}^* mode.

As the resonant length is increased so as to retune the plasma, the operating point shifts to $L_s=6.05$ cms. and $(\omega_{pe}/\omega)^2=3.26$. The incident power is gradually reduced, but the operating point does not shift. However, once the incident power falls below a certain threshold, the operating point jumps abruptly to $L_s=6.05$ cms. and $(\omega_{pe}/\omega)^2=1.99$. This experimentally verifies the fact that for a single resonant length



vs. $(\omega_{pe}/\omega)^2$ for the TE₁₁₁ mode. Waveguide dimensions: a = 0.3 cms., b = 0.3875 cms., Comparison of the theoretical and experimental curves of the cavity resonant length ${f L}_{f s}$ c = 5.08 cms. Figure 6.1

		·	

operation in the TE_{111}^{\star} mode it is possible to have two different plasma densities. If the resonant length and the incident power are increased the operating point moves to $L_s=6.1$ cms. and $(\omega_{pe}/\omega)^2=3.12$. When the incident power is once again gradually reduced below a certain threshold power level, the operating point jumps to $L_s=6.1$ cms. and $(\omega_{pe}/\omega)^2=2.25$. At very low incident powers the plasma can be resonantly sustained at $L_s=6$ cms. and $(\omega_{pe}/\omega)^2=1.37$.

The dotted curve is drawn to fit all the experimental points. Obviously, an exact match cannot be obtained between the 12 mtorr experimental curve and the ν_e/ω = 0.1 theoretical curve. However, the experimental curve closely follows the theoretical curve and has the same general shape. It was not possible to sustain a plasma in the region below L_s = 6 cms. and in the density range $3 \le (\omega_{pe}/\omega)^2 \le 3.5$, where the theoretical resonant length decreases with increasing plasma density.

A similar experiment is conducted at a pressure of 85 mtorr and a curve as shown in Figure 6.1 is obtained. The double density region in the neighborhood of $(\omega_{\rm pe}/\omega)^2$ = 3 does not appear to be prominent at this pressure. This experimentally verifies the theoretical eigenlength curves for collision frequencies greater than 0.1 (see Figure 4.1).

6.2.3 Formation of long plasma columns

The RF plasma in the 30W cavity is electromagnetically excited in the TE_{111}^* or TM_{011} modes. The cavity length is tuned for resonance. It is found that while operating in the pressure range of 20 mtorr - 200 mtorr and an electron density range of $(\omega_{pe}/\omega)^2 = 5$ to $(\omega_{pe}/\omega)^2 = 15$, the plasma is ejected out of the cavity at either ends (see Figure 6.2). It is possible to more than double the plasma volume internal to the cavity in this mode of operation. The length of the plasma column

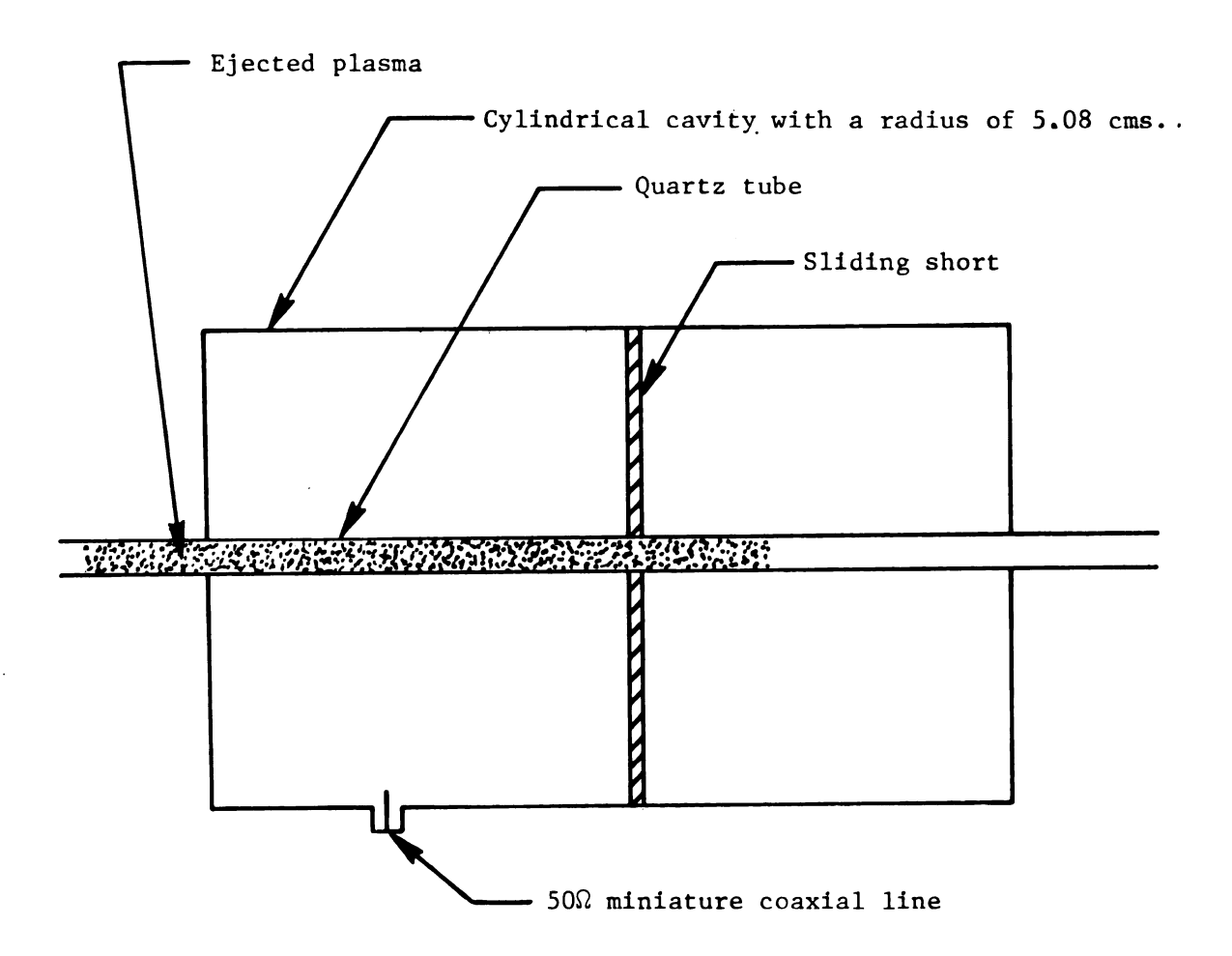


Figure 6.2. Plasma being ejected out of cavity as a result of efficient coupling to the space charge wave through an electromagnetic excitation of the cavity or $^{\text{TM}}_{011}$ mode).

ejected out of the cavity is a direct function of the power input to the cavity.

As might be expected, there is an enhanced power absorption by the plasma in the region where the plasma column is ejected. This is clearly demonstrated in Figure 6.3. This figure shows an experimental plot of the absorbed power in watts vs. the discharge pressure in torr for the TM_{011} mode with the resonant length L_s held constant at 8.6 cms. The curves have been obtained for different incident powers P_i = 25W, 20W and 15W. The curves clearly show two peaks in the absorbed power, one in the low pressure region (around 80 mtorr) and one in the high pressure region (around 90 torr).

The low pressure peaks occur at the same time that the plasma is ejected out of the cavity, the absorbed power in this region being directly proportional to the length of the plasma column ejected out of the cavity. More than 90% of the incident power is absorbed by the plasma in this region of operation. The high pressure peak in the absorbed power curves is a result of increasing collisional losses in the TM₀₁₁ plasma. At very high pressures when the plasma assumes conductor-like properties, the power absorbed gradually decreases.

A similar set of curves for the TM_{011} mode but, at a different length, L_s = 8.1 cms., are shown in Figure 6.4. Again, distinct peaks in the absorbed power can be noted at low and high pressures. These two set of curves for the TM_{011} mode, i.e., at L_s = 8.6 cms. and L_s = 8.1 cms., demonstrate that the plasma cavity when excited in this mode proves to be a useful RF plasma source that can be operated over a wide range of resonant lengths, pressures and electron densities. No tuning of the resonant length is required.

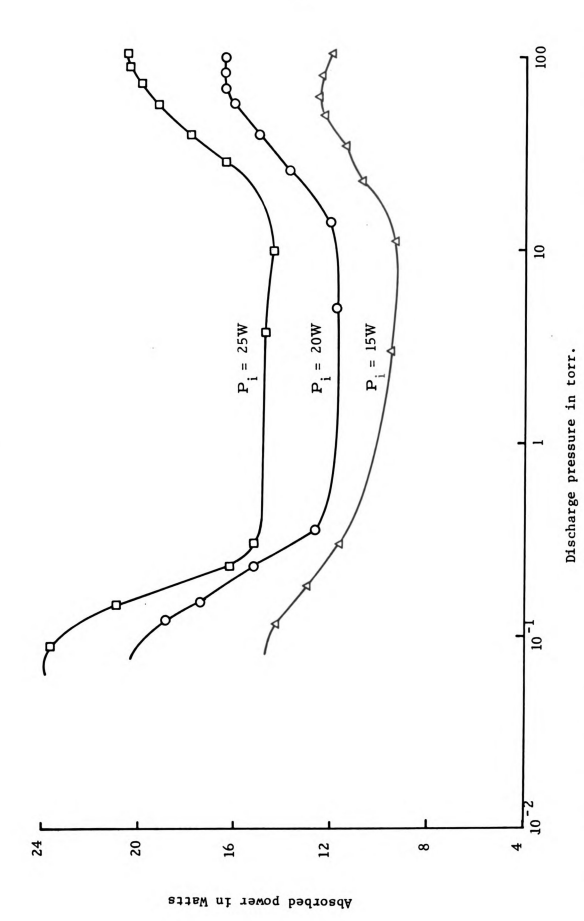
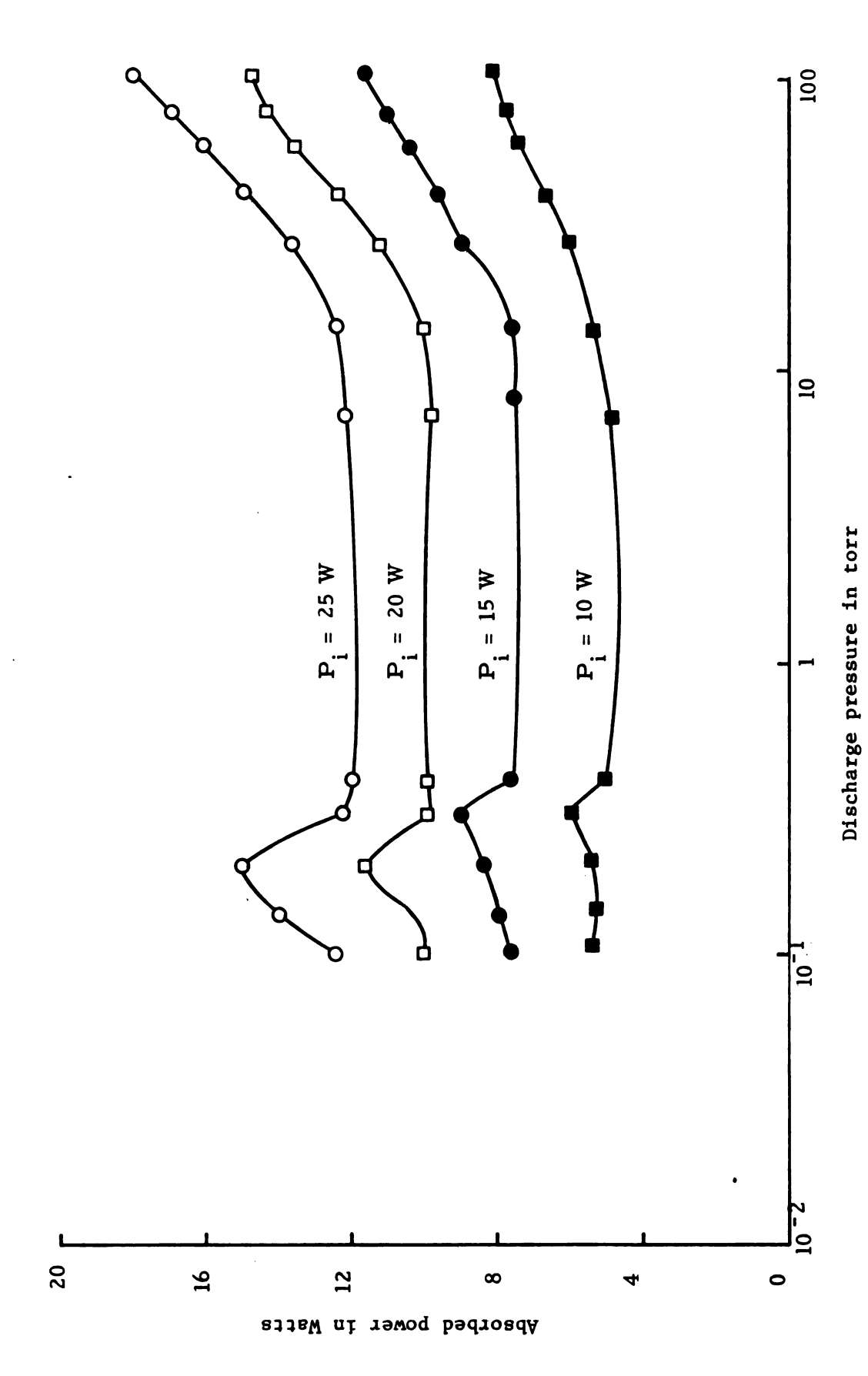


Figure 6.3. Absorbed power vs. the discharge pressure for the TM₀₁₁ mode, with the incident power P₁ held constant. The cavity resonant length $L_{\rm S}$ = 8.6 cms.



Absorbed power vs. the discharge pressure for the TM $_{011}$ mode, with the incident power $_{\rm i}$ held constant. The cavity resonant length $_{\rm s}$ = 8.1 cms. Figure 6.4.

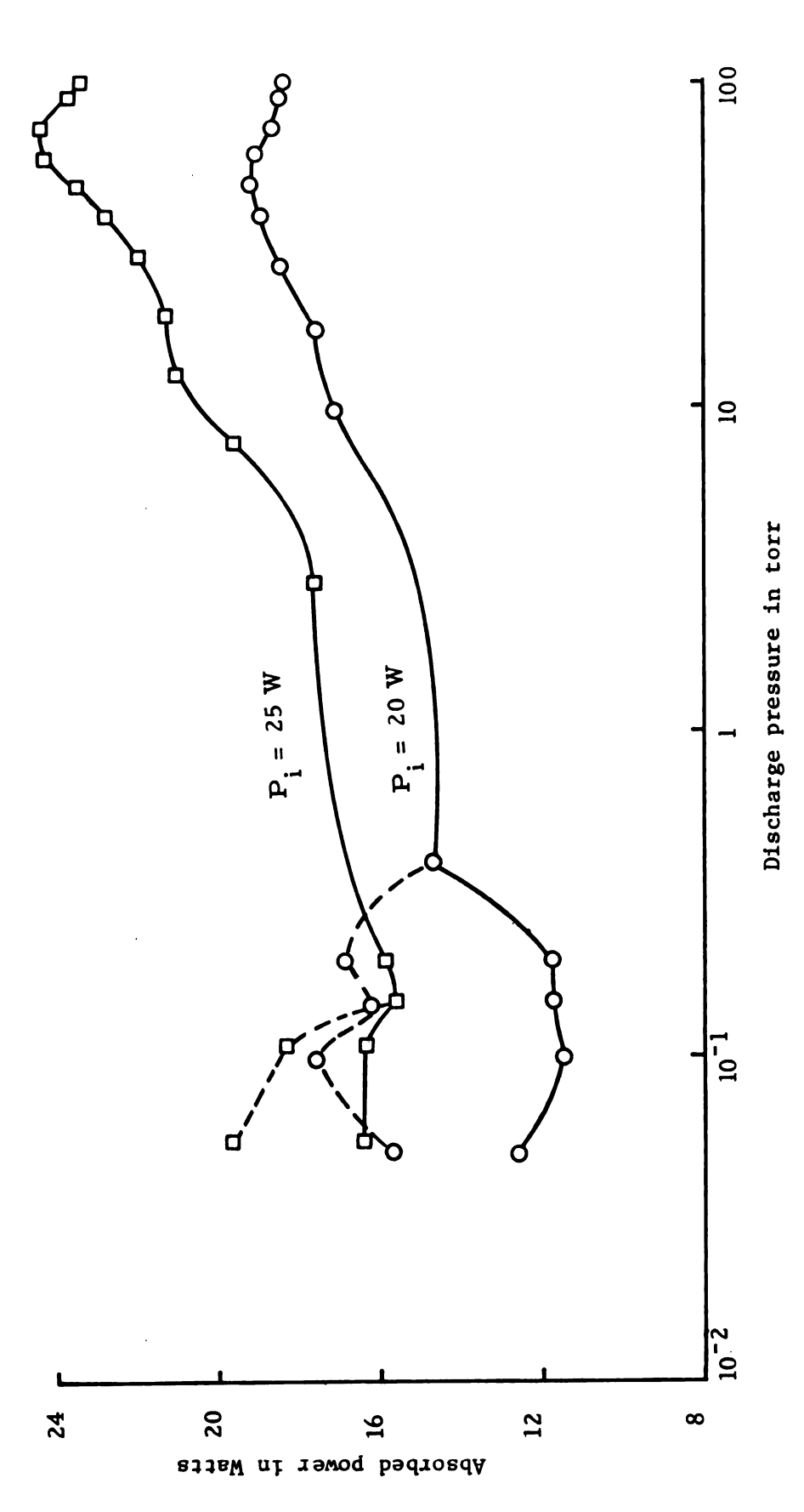


Figure 6.5. Absorbed power vs. the discharge pressure for the TE_{111}^* mode, with the incident power P_1 held constant. The cavity resonant length L_s = 5.92 cms.

A plot of the absorbed power vs. the discharge pressure has also been experimentally obtained for the ${\rm TE}_{111}^{\star}$ mode and this is shown in Figure 6.5. The dark curves show the effect of holding the resonant length constant at ${\rm L_g}$ = 5.92 cms. At high pressures, the usual peaks in the absorbed power are obtained as a result of collisional losses in the plasma. To obtain an ejection of the plasma out of the cavity at low pressures, a tuning of the cavity resonant length is required. The dotted curves show enhanced power absorption as a result of resonant length tuning.

The ejection of the RF plasma column out of the cavity at low pressures and the associated enhanced power absorption for both the TM_{011} and $\mathrm{TE}_{111}^{\star}$ modes can be explained as resulting from the coupling of EM energy to the space charge modes. This can be understood by studying the general plot of the eigenlength vs. $(\omega_{\mathrm{pe}}/\omega)^2$ for the EM modes $\mathrm{TE}_{111}^{\star}$, $\mathrm{TM}_{101}^{\star}$, TM_{011} and the space charge modes TM_{00p} (see Figure 4.1). It is observed from this plot that the TM_{00p} space charge resonances intersect the $\mathrm{TE}_{111}^{\star}$ mode resonant curves at L_{s} = 5.92 cms., and in the plasma density range of $5 \leq (\omega_{\mathrm{pe}}/\omega)^2 \leq 15$. They intersect the TM_{011} mode resonant curves in approximately the same density range, but over a wider range of resonant lengths.

Experimental measurements of resonant length, density and pressures indicate that ejection of the plasma out of the cavity takes place in the regions where the ${\rm TE}_{111}^{\star}$ and ${\rm TM}_{011}$ mode resonances intersect with the ${\rm TM}_{00p}$ space charge wave resonances. The plasma-cavity is electromagnetically excited in the ${\rm TE}_{111}^{\star}$ or ${\rm TM}_{011}$ modes. Under the right operating conditions of density, length and pressure, the EM energy is non-linearly coupled to a space charge traveling wave. This surface wave, which is

radially effenescent, propagates along the plasma column and ionizes the gas as it travels.

The ω - k diagrams of Chapter II (Figures 2.3a, 2.4a and 2.5a) indicate that the space charge mode propagates for frequencies $\omega < \omega_{pe}/\sqrt{1+k_e}$, where k_e is the dielectric constant of the quartz tube. Here k_e = 3.78. With the operating frequency at 3.03 GHz, it should be possible to propagate this mode for $(\omega_{pe}/\omega)^2 \geq (1+k_e) = 4.78$. Experimental measurements of the electron density by the TM_{010} frequency shift method (see section 6.3.1.1) verify this fact. Moisan et.al. 22 have produced similar type of long RF plasma columns at lower frequencies by exciting a surface wave in a re-entrant cavity and using a capacitive type of coupling. Thus, in a cylindrical cavity EM mode energy can be transferred to space charge wave energy. This coupling is most efficient when the EM mode is resonantly excited at low pressures, and thus, provides a large volume RF plasma source at low pressures (20 mtorr - 200 mtorr).

6.2.4 Excitation of Short Wavelength (λ_g =1cm) Standing Waves

The theoretical resonant length curves (see Figure 4.1a) indicate that it may be possible to excite space charge standing waves, i.e., ${\rm TM}_{008}, \ {\rm TM}_{009}, \ {\rm etc.}, \ {\rm as\ a\ result\ of\ the\ intersection\ of\ the\ } {\rm TE}_{111}^{\star}, \ {\rm TM}_{011}$ resonant curves with the ${\rm TM}_{00p}$ resonant curves. Experimental observations reported below appear to support the excitation of these standing waves.

Experimental observations have always shown the following to be true. Let the RF plasma be electromagnetically excited in the TE_{111}^* mode so as to efficiently couple to the traveling space charge wave. This case is illustrated in Figure 6.2. The resonant length L_g is 5.92 cms. Then if the resonant length is now gradually increased to say L_g = 6.1 cms., so that the plasma-cavity is slightly off TE_{111}^* resonance,

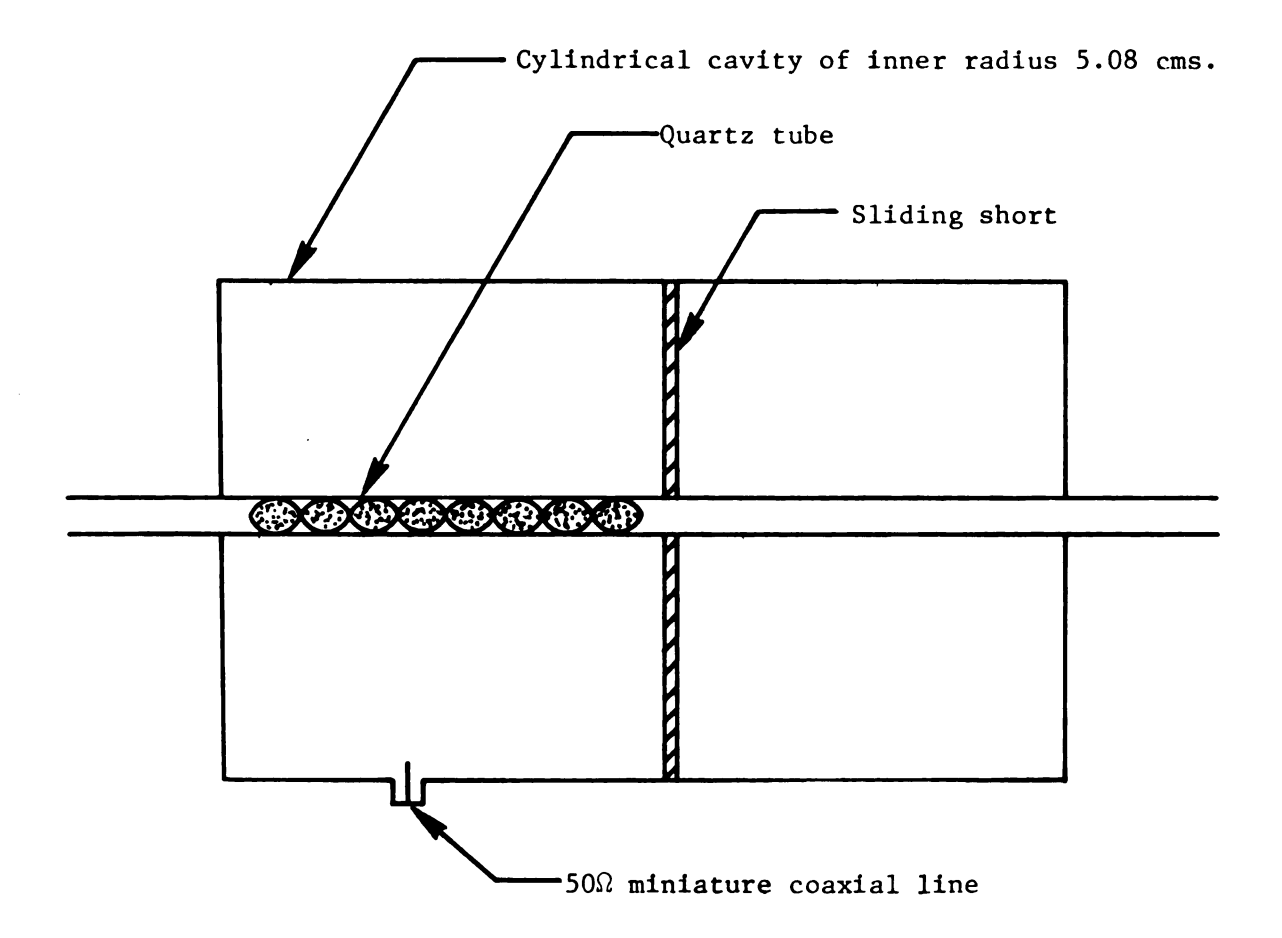


Figure 6.6. Excitation of 8 half-wave resonances of the ${\rm TM}_{00p}$ mode for an off resonance electromagnetic excitation of the cavity (${\rm TE}_{111}^{\star}$ mode).

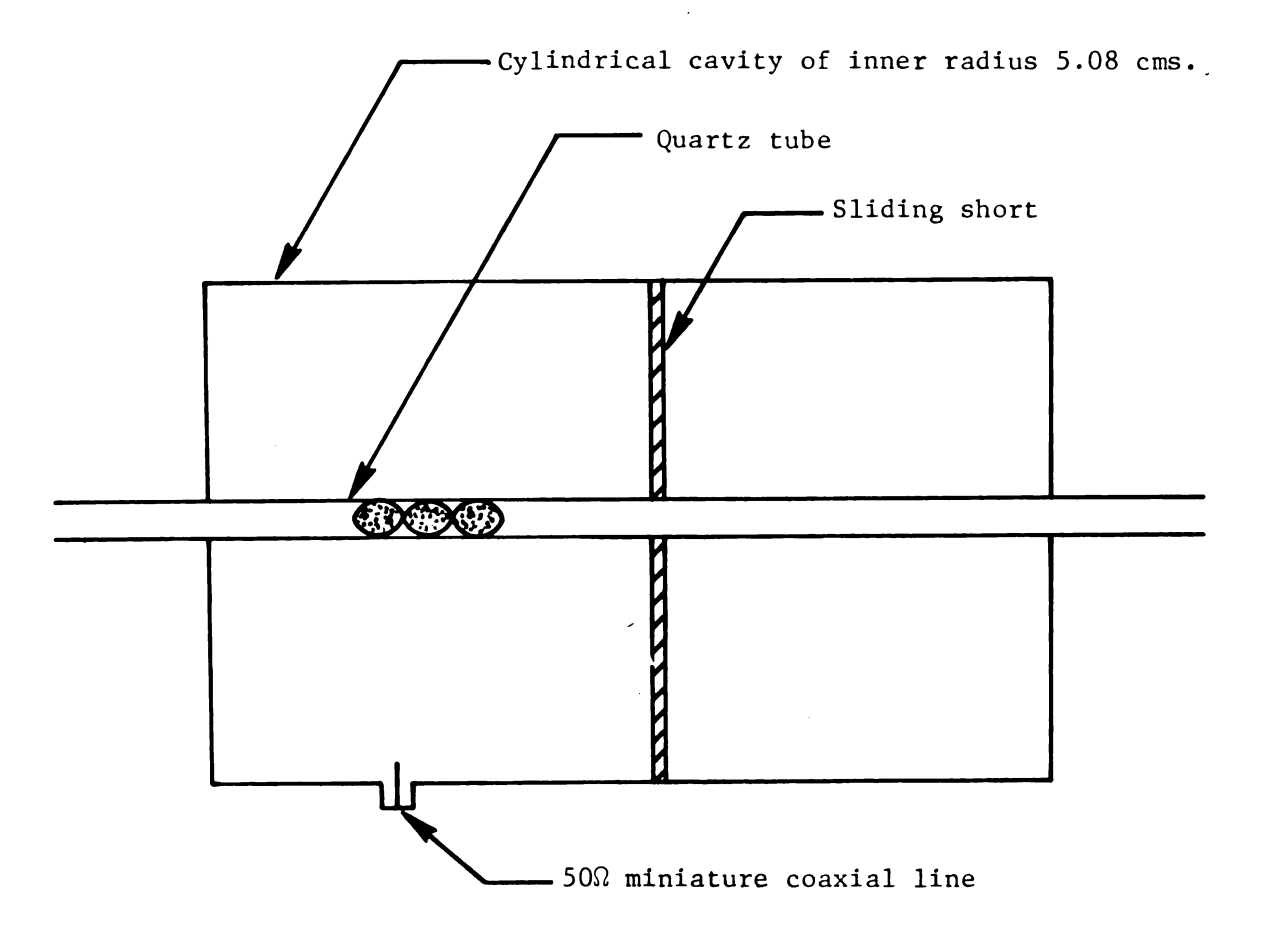


Figure 6.7. Excitation of 3 half-wave resonances of the TM_{00p} mode for a large off resonance electromagnetic excitation of the cavity (TE_{111}^{*} mode).

then the plasma contracts in volume and takes on alternate bright and dark spots. This is illustrated in Figure 6.6. The length of each of the bright spots is approximately $\frac{1}{2}$ cms. The bright spots correspond to the short wavelength standing waves of a TM_{00p} mode; λ_g being roughly 1 cm. Eight standing wave resonances of a TM_{00p} mode are shown in Figure 6.6. As the resonant length is further increased to say $L_g = 6.3$ cms., the TE_{111}^* mode becomes more effenescent and only three standing wave resonances of a TM_{00p} mode are observed. This is illustrated in Figure 6.7. A further increase in the length causes the plasma to become extinguished.

These experiments on the coupling of energy to the space charge modes indicate that it is possible to excite short wavelength standing waves of a TM_{00p} mode. These modes are excited when varying the cavity length along a TM_{00p} resonant length curve (see Figures 4.1a and 4.1b).

6.2.5 Detection of sidebands in the reflected spectrum

The RF plasma in a cylindrical cavity provides an excellent means for exciting non-linear signals. At least two different types of sidebands have been detected in the reflected power spectrum at a pressure of 12 mtorr while operating in the TE_{111}^{\star} mode. These spectra are shown in Figure 6.8a and 6.8b.

The spectrum of Figure 6.8a has a sideband separation Δf = 240 khz, a resonant length $L_{\rm g}$ = 6.0 cms., and an absorbed power of 14.2 Watts. Simultaneous density measurements with the TM_{010} frequency shift method (section 6.3.1), indicated that the value of $(\omega_{\rm pe}/\omega)^2$ fluctuated between 2.04 and 3.16 as a function of time. A plot of these experimental results on

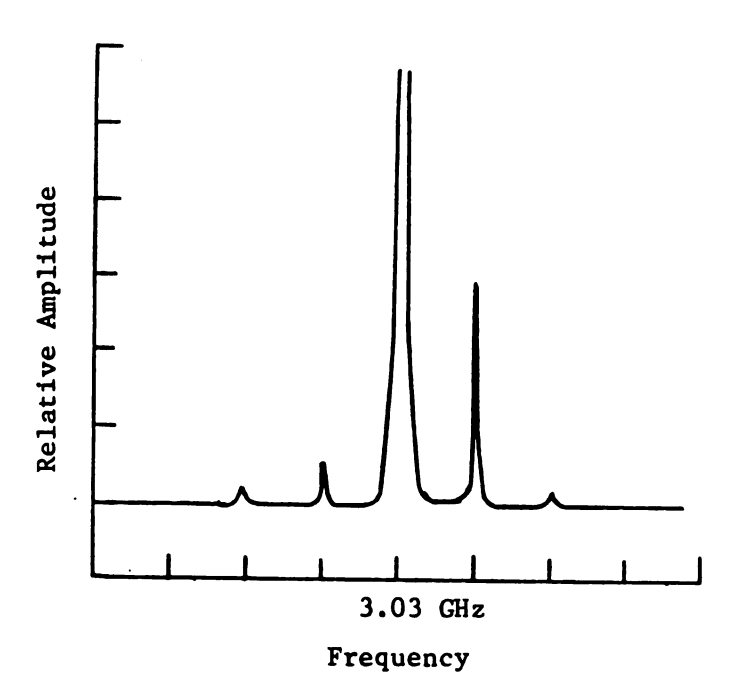


Figure 6.8a. Sidebands detected on the spectrum analyzer in the TE * 111 mode with the operating frequency $\omega/2\pi$ = 3.03 GHz. Cavity resonant length L = 6 cms. Discharge pressure = 12 mtorr. Power absorbed = 14.2 watts. Plasma electron density $(\omega_{\rm pe}/\omega)^2$ fluctuated between 2.04 - 3.16. Frequency scale: 0.2 MHz/cm.

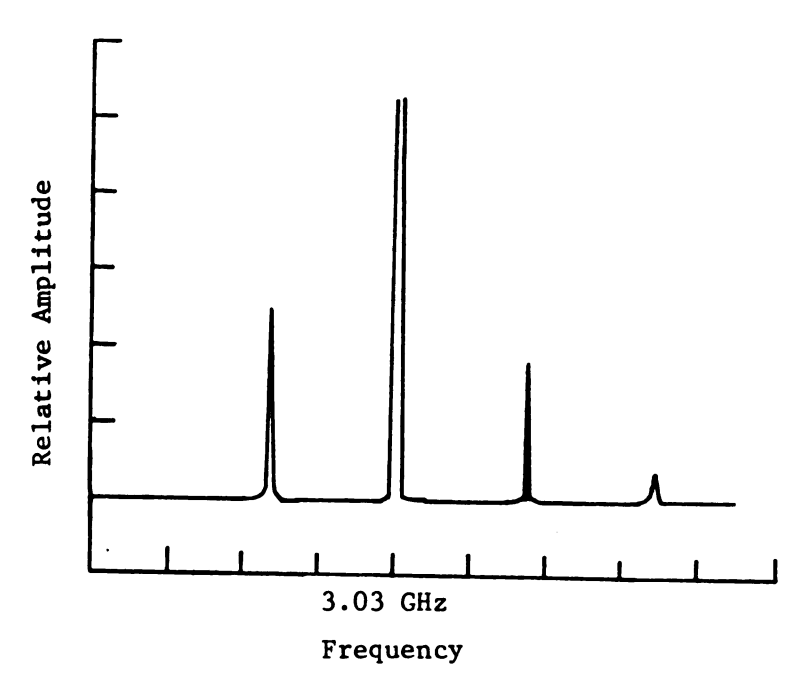


Figure 6.8b. Sidebands detected on the spectrum analyzer in the TE_{111}^{\star} mode with the operating frequency $\omega/2\pi$ = 3.03 GHz. Cavity resonant length L_s = 6.02 cms. Discharge pressure = 12 mtorr. Power absorbed = 14.1 watts. Plasma electron density $(\omega_{\text{pe}}/\omega)^2$ = 2.95. Frequency scale: 2.0 MHz/cm.

the TE_{111}^{\star} theoretical resonant curve for (v_e/ω) = 0.1 (Figure 6.2) indicates that the occurrence of these sidebands is caused by a rapid flucuation of the operating point along the same resonant length line. This phenomenon might be a result of the fact that it may not be possible to locate a stable operating on the backward wave region of the lossy TE_{111}^{\star} mode i.e., the region where the eigenlength decreases as $(\omega_{pe}/\omega)^2$ increases (see Figures 4.1 and 6.1).

Figure 6.8b displays another spectrum that was detected in the reflected power of the TE_{111}^{\star} mode. This occurs at the following operating parameters: $L_s = 6.02$ cms., discharge pressure = 12 mtorr, power absorbed = 14.1 Watts. The measured average electron density, $(\omega_{pe}/\omega)^2$, was 2.95 and the sideband separation Δf was 4 MHz. An external signal at $f \approx 4$ MHz was launched directly into the plasma by a miniature co-axial probe so as to excite signals at 3.03 GHz \pm n 4 MHz. It could not be clearly determined whether any amplification of the externally excited signals occurred in the neighborhood of the sidebands of the spectrum. The exact nature of this instability is not clearly understood and needs further investigation.

6.3 Measurement of N_0 , T_e and Calculation of E_e in the #1 Plasma-Cavity 6.3.1 Introduction

Several methods have been used to experimentally measure the average electron density and electron temperature of a microwave discharge. Each of the methods, however, are applicable to different ranges of discharge pressures. Three commonly used techniques are described on the following pages.

6.3.1.1 Use of a Microwave Cavity to Measure Electron Densities.

The cavity is usually designed to operate in the TM $_{010}$ or $^{27,28,29}_{011}$ modes. The TM $_{010}$ mode density measurement is effective for low electron-neutral collision frequencies, i.e., the condition $v_e^2 << \omega^2$ should be satisfied 33 . ω is the TM $_{010}$ driving frequency.

The ${\rm TE}_{011}$ frequency shift technique is another commonly used method for measuring electron densities. Eigenfrequency vs. $(\omega_{\rm pe}/\omega)^2~{\rm plots}^{10}$ can be used to determine the electron density provided an estimate of the electron-neutral collision frequency is available. For situations where the collision frequency can be neglected, a ${\rm TE}_{011}$ frequency shift technique using a perturbation analysis may be employed 26,35,36 . This mode may also be used for measurements in the high-electron density range. For such measurements the ${\rm TE}_{011}$ coaxial resonance of the cavity may be used as a reference frequency 34 .

Both these techniques can be employed on D.C. or various kinds of RF discharges. In the microwave plasma cavity, however, it is possible to have a multi-mode cavity operation 33 , i.e., plasma excitation in one mode, TE_{111}^{\star} or TM_{011} , and an electron density measurement with the TM_{010} or TE_{011} modes. The electron temperature cannot be measured with the cavity method and only the average value of the electron density can be determined. The diagnostic mode power input should be small compared to the primary discharge power input so as not to disturb the plasma characteristics.

6.3.1.2 Floating Double Probe Method

In this well known method³⁰ two probes connected across a variable floating potential, are immersed into the plasma. The distance between the probes should be large compared with the Debye length to avoid an

interaction of the plasma region perturbed by the two probes. In using this method to measure the plasma parameters in a microwave discharge, the probes should protrude only slightly into the plasma region so as not to distort the RF fields. Furthermore, effective shielding is required, especially in high-powered microwave discharges, to prevent the radiation of RF energy away from the active plasma region and into the external surroundings.

The average electron density and the electron energy are obtained from the I-V probe characteristics as proposed by Johnson and Malter³⁰. Their theory is valid only when the discharge pressure is low enough so that the mean free path is much larger than the probe or sheath dimensions.

Several probe theories have been suggested for collision-dominated gases. However, these theories are valid only for certain probe geometries, such as spheres ³⁷ or ellipsoids ³⁸ and are, therefore, applicable to special situations.

The characteristics of plasma-cavity I, which operates under the available incident power of 30W, can be conveniently monitored by the floating probe method at low discharge pressures (1 torr and below). This experimental system was described in Chapter V. The probes are 1.523 mm in diameter and protrude 1 cm. into the active plasma region. The electron temperature T_e is evaluated from the slope of the $\ln T_e$ -V curve while the electron density is obtained from a formula 30,39,40 that is dependent on T_e and the saturation ion current T_e . This is given by:

$$N_{o} = 4 \times 10^{16} \frac{i_{ri}}{(T_{e})^{\frac{1}{2}}}$$
 6.1

for the probe dimensions used here. N_{o} is obtained in electrons/cm 3 .

The D.C. floating I-V probe characteristics made here are likely to be modified to some extent by the RF fields of the microwave discharge. This problem has been examined by several workers for RF discharges operating in the frequency range 1-10 MHz.

Crawford 41, Garscadden and Emeleus 42, Chen 43 have all studied the effect of fluctuations in N_O, kT_e and space potential V_S on the time-average Langmuir probe characteristics in RF or unstable plasmas. Their results indicate that if kT_e is a constant for a given set of plasma conditions, then the slope of the I-V curve is unchanged by the fluctuating quantities and the electron temperature measurement is unaffected. Sugawara and Hatta 44 have shown that if kT_e cannot be assumed constant in an RF discharge, then its average value cannot be obtained from the slope of the I-V characteristics. It has been assumed for probe measurements described in this chapter that kT_e is constant. Garscadden and Emeleus 42, Boschi and Magistrelli 45 have demonstrated that for large amplitude RF oscillations the shape of the I-V characteristic near the saturation region tends to be rounded as compared to that of an ideal discharge.

The classical method of plasma diagnostics by the floating double probes suffers from two drawbacks 43: (1) only a small number of electrons in the tail of the velocity distribution is sampled (2) the I-V probe characteristics are likely to be modified by the stray capacitance between the floating probe circuitry and ground.

Gagne' and Cantin^{46,47} have experimentally demonstrated that the D.C. floating probe characteristics in their RF discharge tend to be modified by the RF voltage. These modifications include the enhancement

of the ion current by as much as 40% and an apparent increase in the electron temperature by a factor of 2-3. The perturbation of the probe characteristics is directly related to the amplitude of the RF voltage existing between the probe and the plasma. This voltage was minimized by making the ratio Z_p/Z_s very small, where Z_p is the impedance of the plasma-probe junction or RF sheath and Z_s is the overall impedance between the probe collecting surface and the reference ground plane. These experiments, however, do not explain the physical mechanism responsible for the observed modifications of the probe I-V characteristics. Also, these results are not totally consistent with the work done by others $^{41-45}$ regarding modifications of the Langmuir probe characteristics by RF fields.

All the work reported in the literature has been done in the low RF region. The effect of these observations on the probe characteristics of the 3.03 GHz microwave discharge is not clear. The probe diagnostics conducted on Cavity 1 have been done using the TE to mode of operation. For this mode, the electric fields are most strongly concentrated at the center of the cavity and away from the two probes. It appears that further investigations are required, especially for microwave discharges, to demonstrate any RF perturbation of the probe characteristics and if so to obtain the physical mechanism responsible for it.

6.3.1.3 Measurement of the D.C. Electrical Conductivity

Two flat brass electrodes of surface area 0.203 cm² have been used to determine the D.C. electrical conductivity and the electron temperature of the microwave discharge in the #1 plasma-cavity. This method has been used to obtain the plasma characteristics up to a discharge pressure of 20 torr.

This measurement technique is similar to the one used by Maksimov to obtain electron densities and energies in a microwave helium discharge at an operating frequency of 3.0 GHz.

The voltage applied to the plasma between the brass electrodes divides itself across two regions: a uniform plasma zone and small saturation regions adjacent to the electrodes. Under the assumption that the charged particles are lost in volume recombination, Thomson obtained the total voltage drop across the electrodes (V) as a function of the current density (i) in the uniform plasma zone as:

$$V = Ai + Bi^2 . 6.2$$

The linear term describes the voltage drop in the uniform plasma zone and the quadratic term gives the voltage drop in the sheath regions. Maksimov finds that the non-linear term in the above equation does not make a significant contribution to the voltage drop. The presence of cathode emission under the impact of metastable atoms and under the action of ultraviolet radiation of the discharge considerably reduces the length of the saturation region. Thus, the non-linear term in the above equation is neglected and the entire plasma zone is assumed to be uniform for purposes of calculating the electrical conductivity.

The D.C. electrical conductivity of a weakly ionized gas is given by the following expression:

$$\sigma = \frac{N_o e^2}{m_e v_e}$$
 6.3

where N_0 = average electron density

 m_{α} = mass of electron

e = charge of electron

 v_e = electron-neutral collisional frequency.

The electron temperature T_e is obtained from the slope of the I-V characteristics of the discs and is used to calculate ν_e at the given pressure from the curves 50 shown in Figure 6.9.

Possible sources of error in this method are that the probe theory has been applied to the disc I-V characteristics to obtain the electron-temperature and a uniform voltage drop has been assumed across the electrodes. Thus, the experimental numbers obtained from this method cannot be relied upon for their accuracy, but can be taken as representing the orders of magnitude of the plasma parameters.

6.3.1.4 Evaluation of
$$v_e$$
 and E_e from v_o and v_e

The dependence of electron density and electron energy on the average power density, W_a , can be used to calculate the effective electric field E_e and the reduced field E_e/p as a function of the discharge pressure p. The average power absorbed per unit volume of a cold microwave plasma¹, expressed in terms of the electric field strength E(r),

is

$$W_a = \frac{n_e(r)e^2}{2m_e v_e} - \frac{v_e^2 E(r)^2}{(\omega^2 + v_e^2)}$$
 6.4

where,

 $n_e(r)$ = spatially dependent electron density.

 ω = operating frequency

 $v_{\rm p}$ = effective electron-neutral collision frequency.

Integrating the above equation over the plasma volume, we obtain an expression for the power absorbed $\mathbf{P}_{\mathbf{a}}$ as:

$$P_{a} = \int_{V} W_{a} dv = \frac{e^{2}}{2m_{e}v_{e}} \frac{v_{e}^{2}}{(\omega^{2} + v_{e}^{2})} \int_{V} n_{e}(r) E^{2}(r) dv.$$
 6.5

 ν_e is assumed to be independent of position. An effective electric field E_ρ is defined for the entire plasma volume so that

$$\int_{V} n_{e}(r) E^{2}(r) dv = E_{e}^{2} \int_{V} n_{e}(r) dv = N_{o}E_{e}^{2}V$$
 6.6

where N_0 = average plasma density. Therefore, in terms of E_e , W_a becomes:

$$W_{a} = \frac{N_{o}e^{2}v_{e}^{2}E_{e}^{2}}{2m_{e}v_{e}(\omega^{2} + v_{e}^{2})} = \frac{\omega_{pe}^{2}\varepsilon_{o}v_{e}E_{e}^{2}}{2\omega^{2}(1 + (\frac{v_{e}}{\omega})^{2})}$$
6.7

E can, therefore, be evaluated from:

$$E_{e} = \sqrt{\frac{2W_{a} (1 + (v_{e}/\omega)^{2})}{(\omega_{pe}/\omega)^{2} v_{e} \varepsilon_{o}}}.$$
6.8

A knowledge of the average electron density, the electron temperature, and the type of gas are, thus, necessary to determine the effective field strength $\mathbf{E_e}$. $\mathbf{v_e}$, the electron-neutral collision frequency can be estimated from the electron temperature. The effective field strength, as defined here, can be treated as a figure of merit field strength. This definition is likely to yield meaningful results in the low pressure, low density regions where the electric field could be assumed to be uniform over the cross-section of the plasma. In a collision-dominated plasma with high electron densities, the electric fields would penetrate only a skin-depth thickness into the plasma. The electric field strength in such a plasma would be large at the boundary, but negligibly small in the interior. In such a situation, a measurement of the spatially dependent field $\mathbf{E}(\mathbf{r})$ would prove to be useful.

The effective electron-neutral collision frequency is obtained from the velocity dependent collision frequency $\nu_{m}(v)$, as

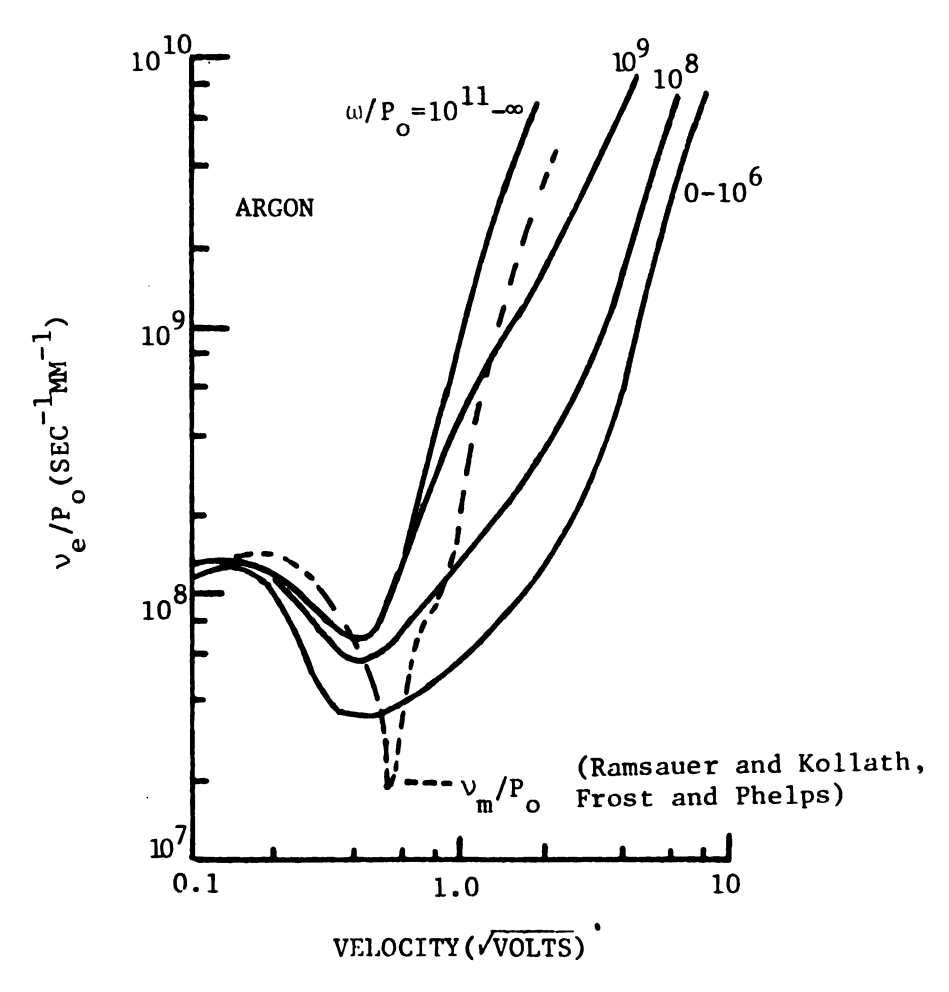


Figure 6.9. The effective collision frequency in A as a function of velocity and frequency. Reproduced from Whitmer and Herman 50 .

$$v_{e} = \frac{\int_{0}^{\infty} \frac{v_{m}(v)}{\left[v_{m}^{2}(v) + \omega^{2}\right]} v^{3} \frac{\partial f_{o}}{\partial v} dv}{\int_{0}^{\infty} \frac{1}{\left[v_{m}^{2}(v) + \omega^{2}\right]} v^{3} \frac{\partial f_{o}}{\partial v} dv}.$$

$$6.9$$

The above equation can be integrated for different gases assuming a Maxwellian distribution for f_o . $v_m(v)$ is calculated from measured crosssections, available from the data of Ramsauer and Kollath 48 , Frost and Phelps 49 , provided electron temperature numbers are available from separate measurements. As an example, Figure 6.9 shows a plot of v_e/p_o vs. the RMS value of the velocity, $v_e^2>=3kT_e/m_e$, for different values of ω/p_o in argon gas. This curve has been reproduced from Whitmer and Herrmann v_e .

6.3.2 Experimental Results

The plasma parameters N $_{\rm o}$ and T $_{\rm e}$ have been measured in the TE $_{\rm 111}^{\star}$ mode operation of Cavity 1 over the pressure range 40 mtorr to 20 torr. Using argon gas as outlined earlier three different measuring techniques have been used to cover this pressure range.

1) Discharge pressure 40 mtorr - 240 mtorr. The ${
m TM}_{010}$ frequency shift method was found to be effective in this range. Beyond a pressure of 240 mtorr the ${
m TM}_{010}$ mode was highly damped because of increasing collisional losses in the plasma.

The normalized electron density vs. discharge pressure for three different absorbed powers P_a = 16W, 12W and 8W are shown in Figure 6.10a, for this pressure range. As expected, the electron density steadily increases with pressure and absorbed power. At a pressure of 235 mtorr and for P_a = 16W, the value of N_o is 1.65 x $10^{12}/cm^3$.

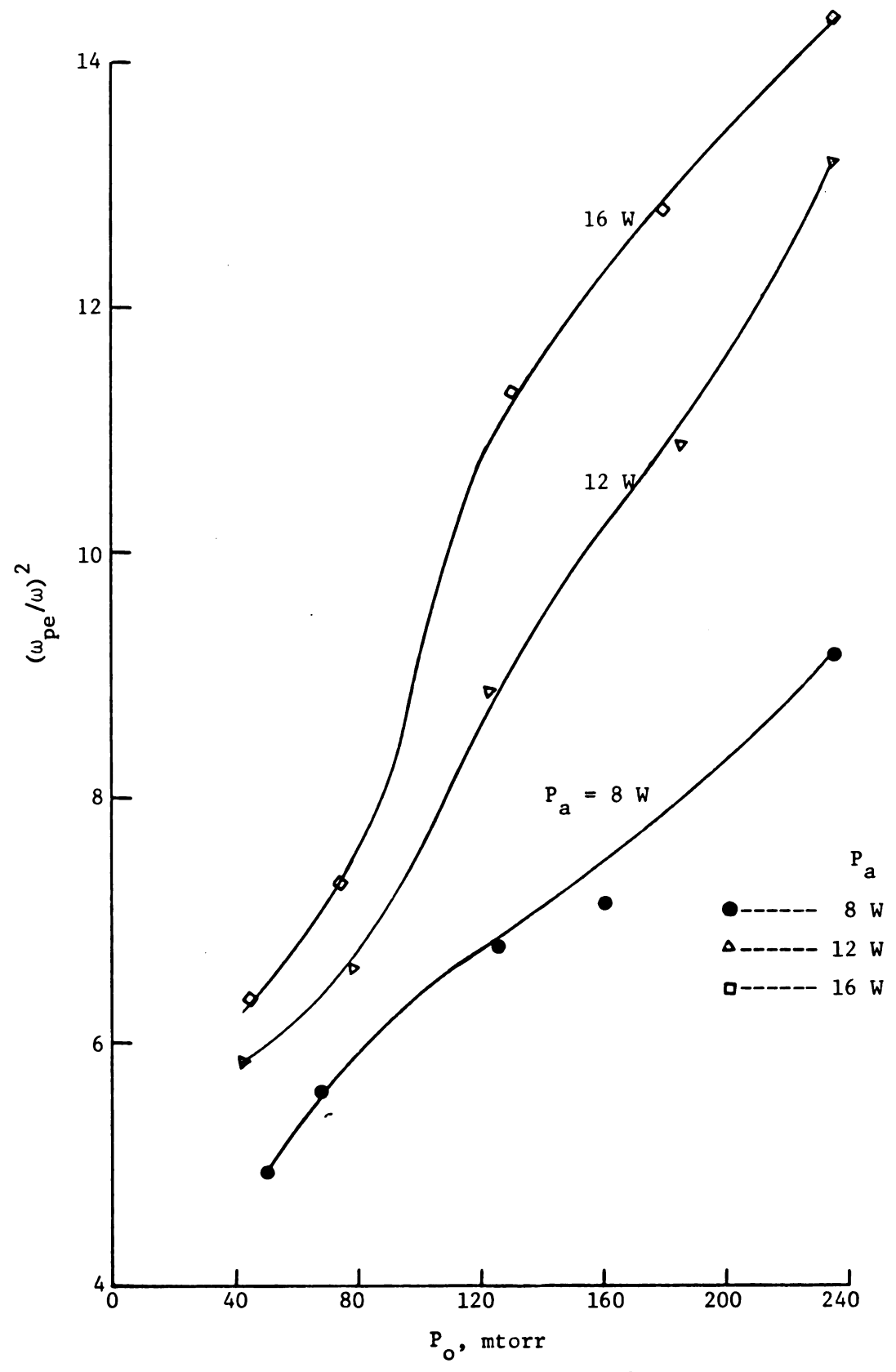


Figure 6.10a. Normalized electron density $(\omega_{pe}/\omega)^2$ vs. discharge pressure P_o and the absorbed power P_a using the TM_{010} frequency shift method.

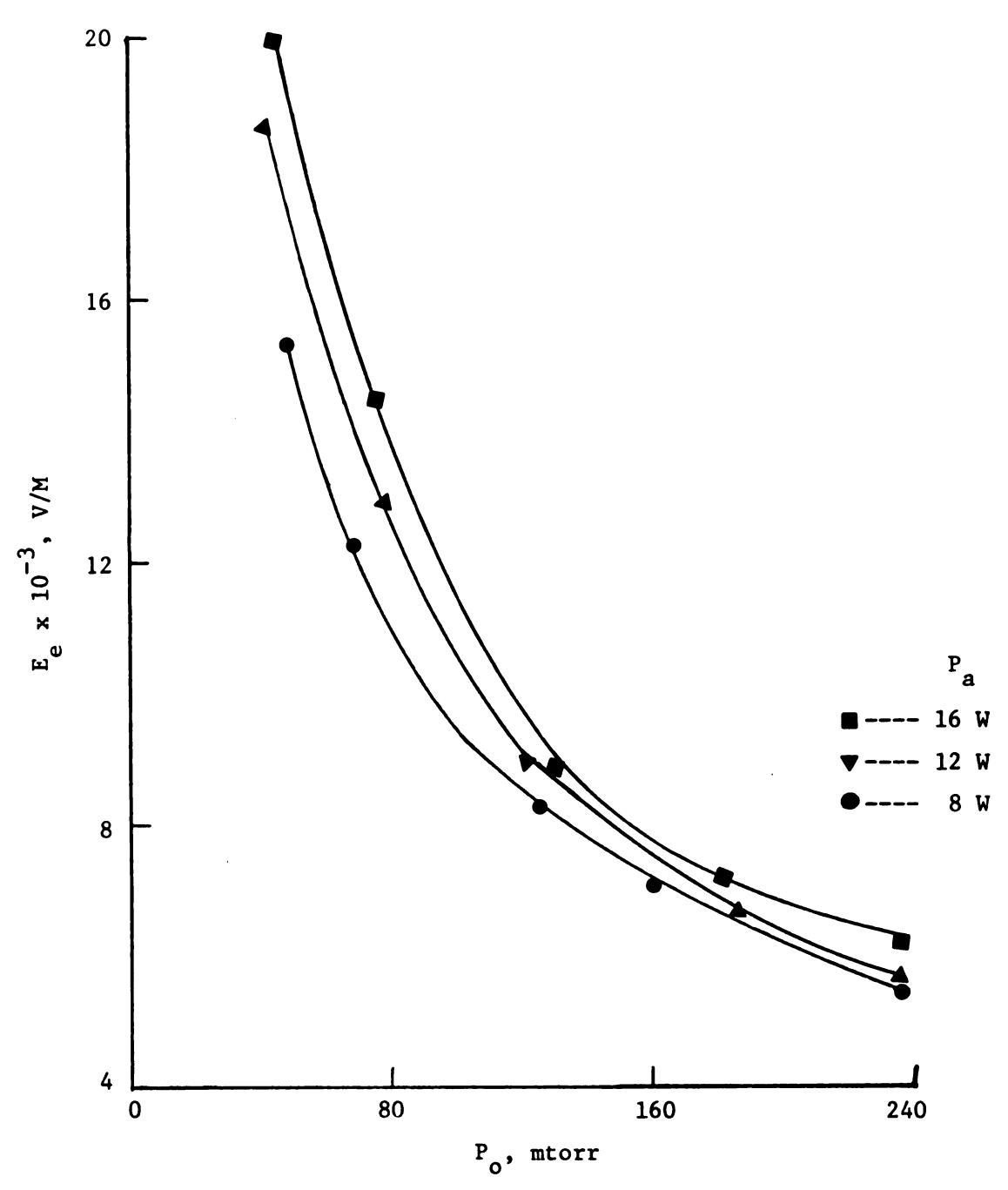


Figure 6.10b. Effective electric field $\rm E_e$ vs. discharge pressure $\rm P_o$ and absorbed power $\rm P_a$, from the $\rm TM_{010}$ frequency shift method.

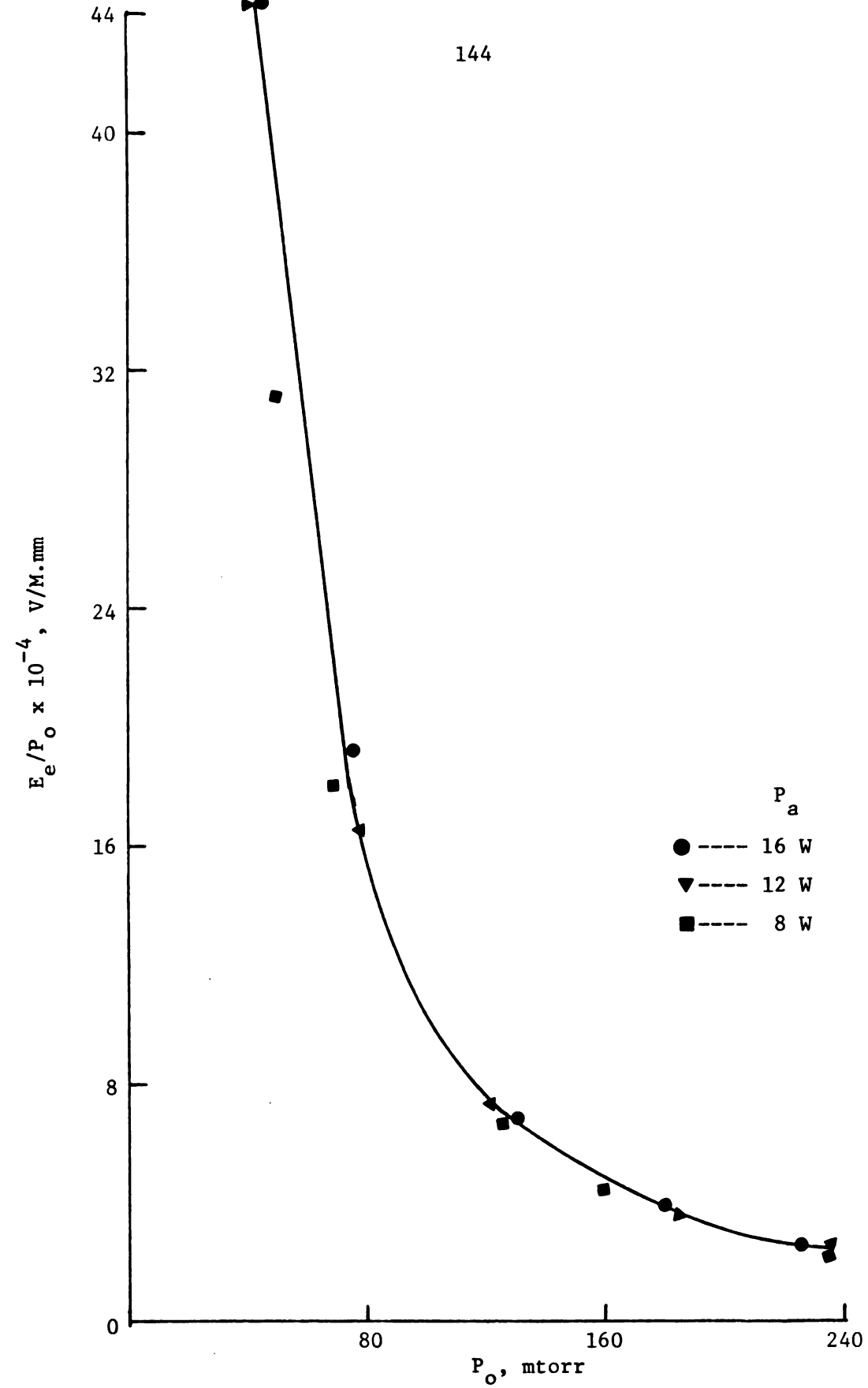
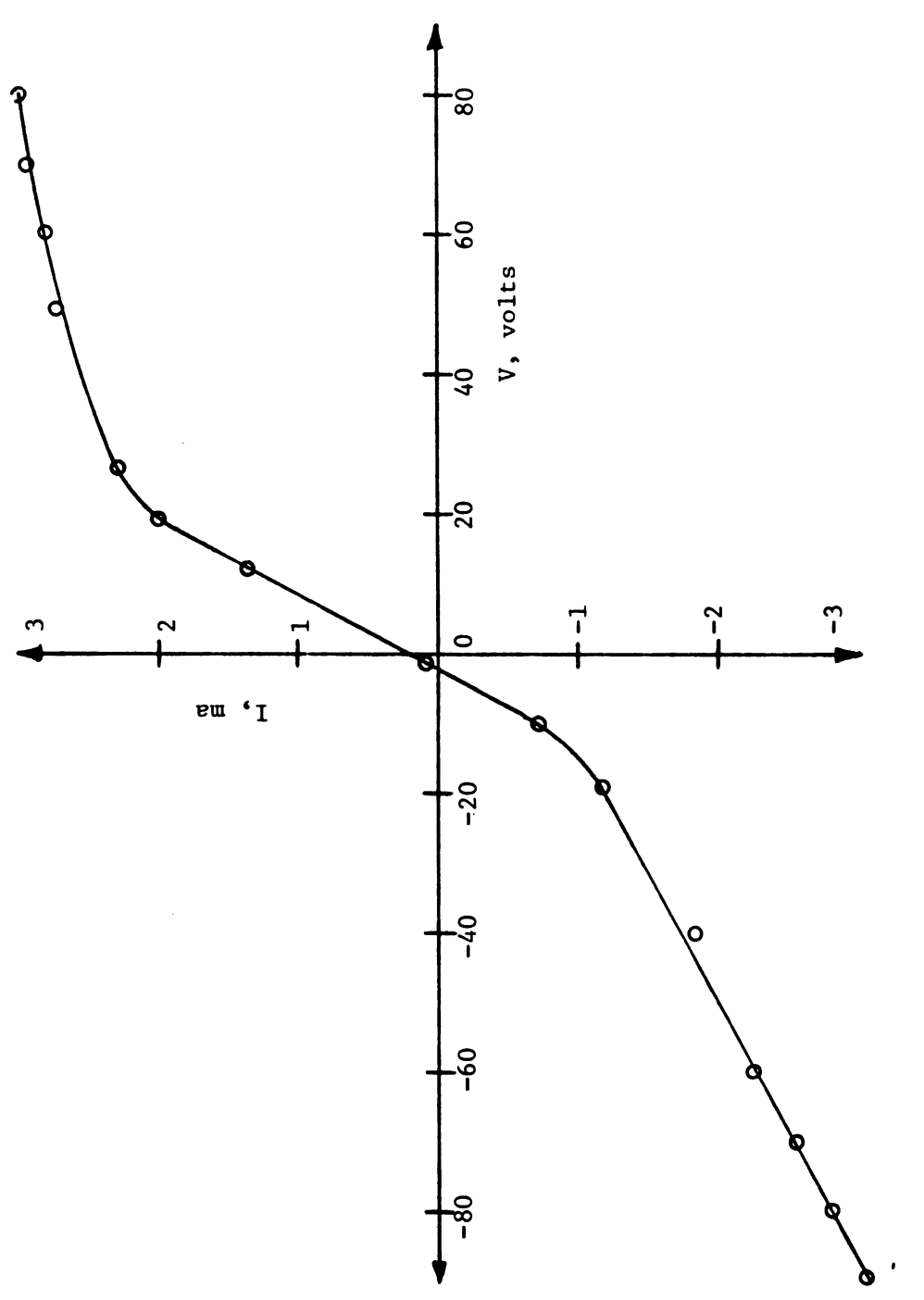


Figure 6.10c. Reduced field $\rm E_e/P_o$ vs. discharge pressure $\rm P_o$ and absorbed power $\rm P_a$, from the $\rm TM_{010}$ frequency shift method.

Since the electron temperature cannot be measured using this technique, a value of $90,000^{\circ}$ K has been used for T_{e} on the pressure range 40 mtorr - 240 mtorr. This estimate for T_{e} has been obtained from probe data measurements to be described later.

Plots of E_e and E_e/p calculated from equation 6.8 are shown in Figures 6.10b and 6.10c, respectively. E_e and E_e/p decrease with increasing pressure and electron density and appear to be almost independent of the absorbed power. E_e varies from 2 x 10⁴ V/M at 45 mtorr to 6.3 x 10³ V/M at 235 mtorr for a P_a = 16W.

2) Discharge pressure 140 mtorr to 1.05 torr. The double floating probe method has been used to measure the electron density and electron temperature in this range. At very low pressures (below 100 mtorr) and in the high pressure regime (above 1 torr) the probe data did not provide reliable results. A typical double probe I-V curve at a pressure of 86 mtorr is shown in Figure 6.11a. It is clear that the saturation regions are not clearly defined, thereby causing an error in the density calculation. At high pressures, the saturation current was too small as a result of the collision-dominated plasma. This is demonstrated by two I-V characteristics at pressures of 5 torr and 11 torr where the ion saturation current decreases with an increase in pressure from 5 to 11 torr, see Figure 6.11b. In the pressure range 100 mtorr to 1 torr, the I-V curves are more conventional, with well defined linear and saturation regions. A typical set of such curves is shown for different power levels and different pressures in Figures 6.11c and 6.11d.



Typical floating double probe I-V characteristics at a discharge pressure of 86 mtorr. Absorbed power $P_a=20~\text{W}$. Figure 6.11a.

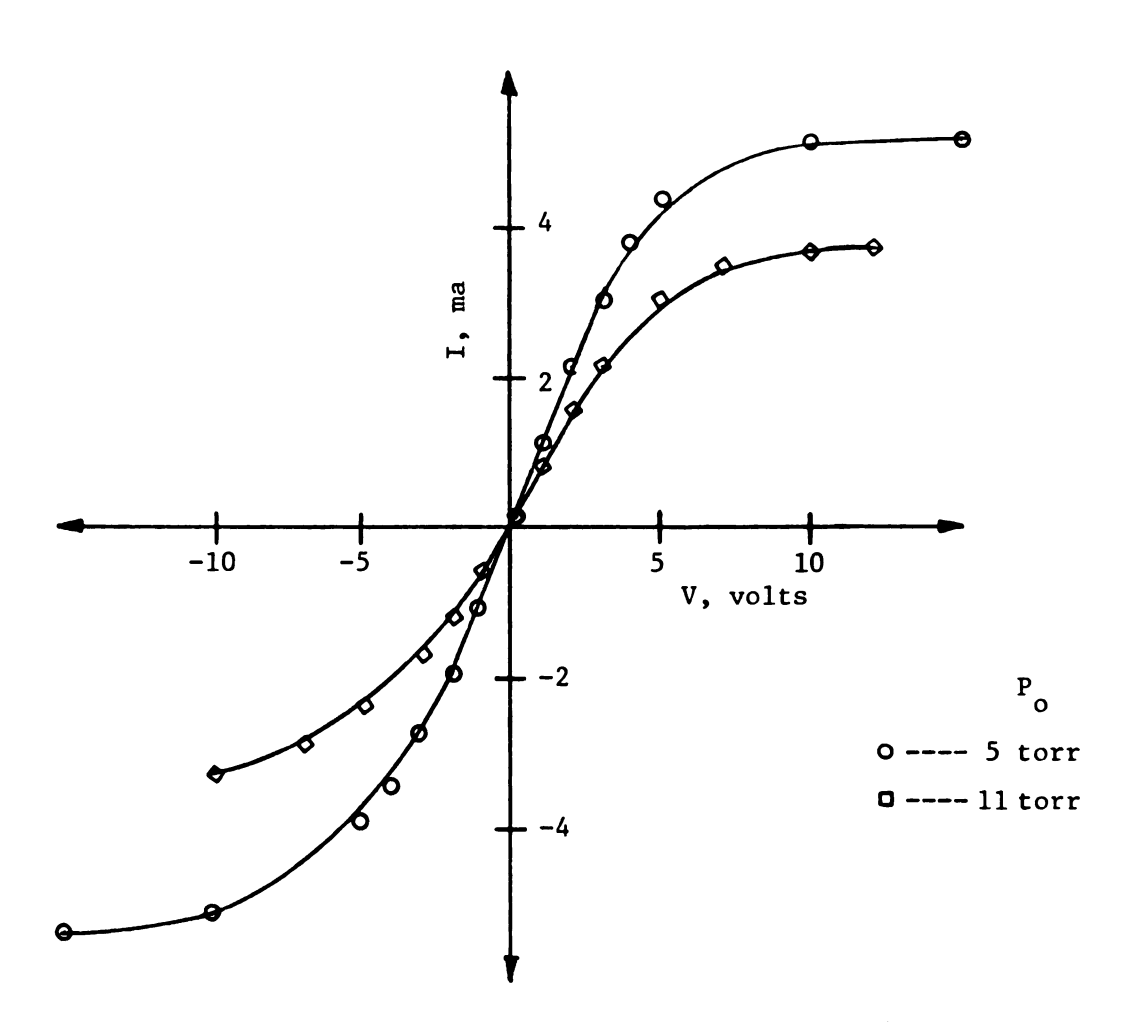


Figure 6.11b. Typical floating double probe I-V characteristics for pressures above 1 torr. Absorbed power P_a = 20 W.

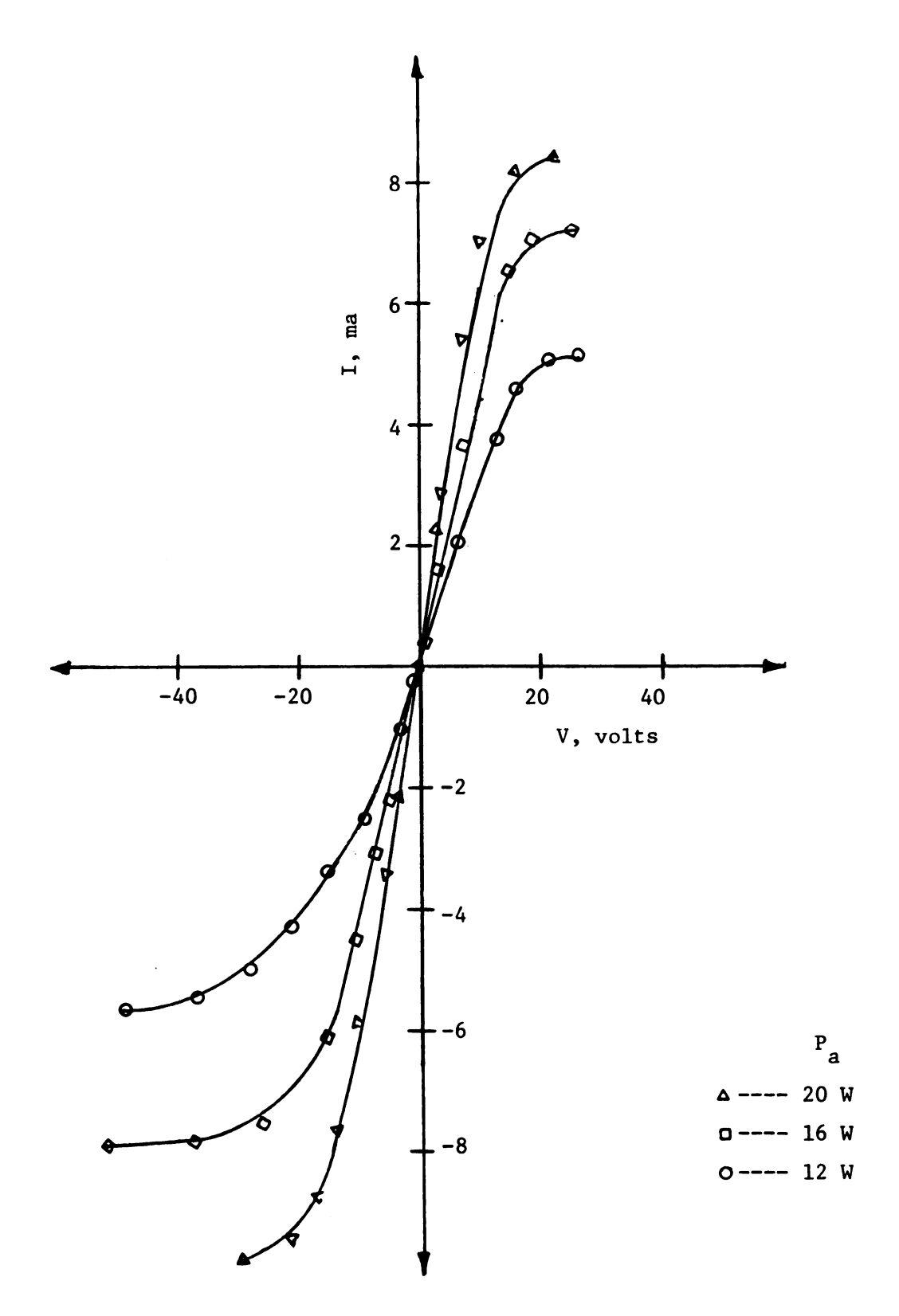


Figure 6.11c. Typical floating double probe I-V characteristics at a discharge pressure of 140 mtorr and different absorbed power levels.

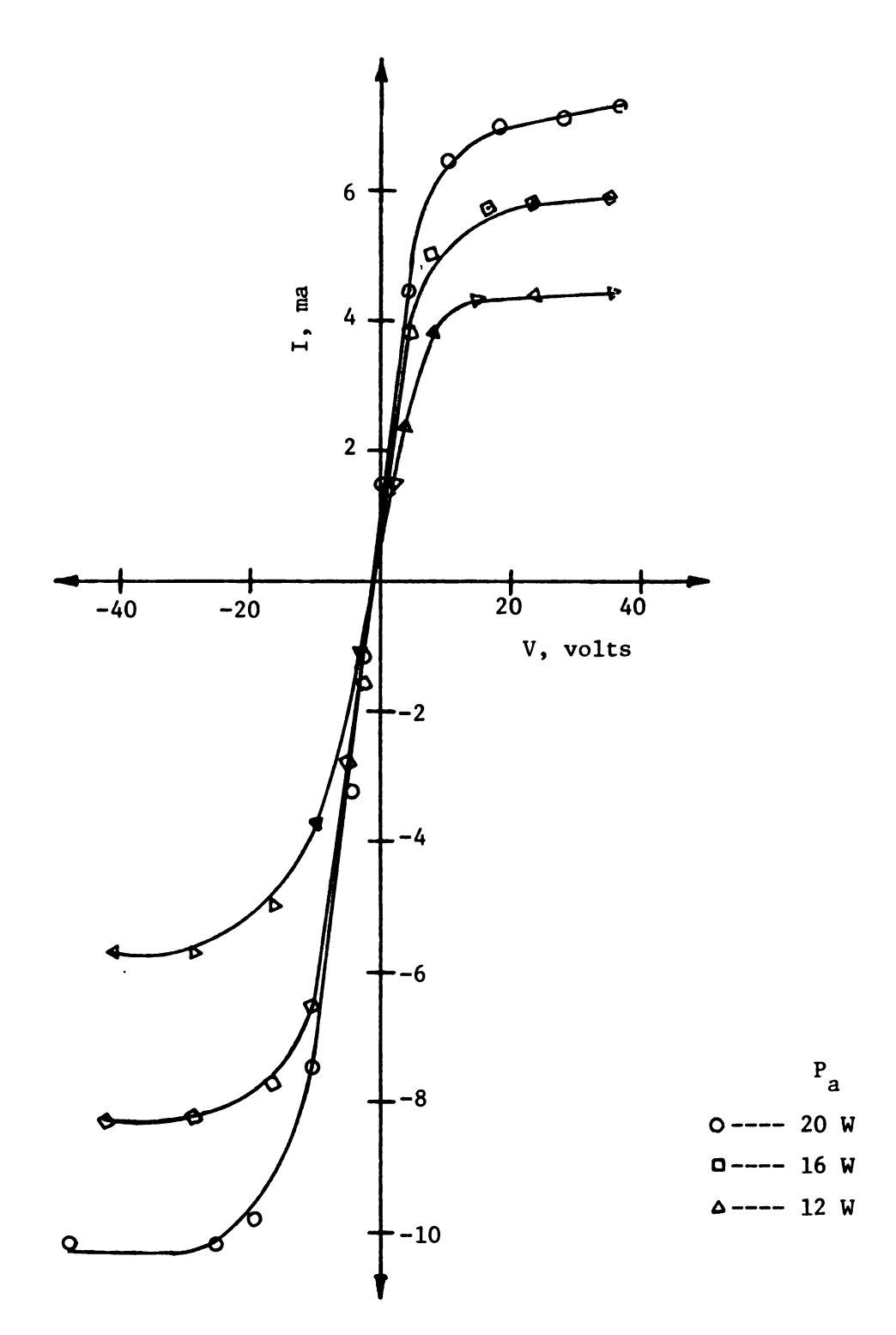


Figure 6.11d. Typical floating double probe I-V characteristics at a discharge pressure of 730 mtorr and different absorbed power levels.

The experimentally measured electron density and electron temperature vs. discharge pressure for $P_2 = 20W$, 16W, 12W are shown in Figures 6.12a and 6.12b. It is observed from Figure 6.12a that in the pressure range 100-400 mtorr, the electron density decreases and then rises again with pressure. As explained in section 6.2.3, the unusual behavior in this low pressure range is believed to be a result of coupling of the TE_{111}^* electromagnetic energy to the TM_{00p} space charge wave. Normally, this space charge wave would propagate along the plasma column and ionize the gas as it travels (see Figure 6.2). However, in this diagnostic technique, the location of the two probes (see Figure 5.1) prevents the plasma volume from increasing longitudinally. As a result, the absorbed power per unit volume increases causing a peak in the electron density vs. pressure curve. Beyond 400 mtorr, the electron density rises steadily with pressure and appears to saturate around 1 torr. However, probe measurements beyond a pressure of 800 mtorr tend to yield lower than actual values for the electron density because at these pressures, the collisionless probe theory may not be applicable. At 800 mtorr and P_{a} = 20W, the value of N_o is 1.85 x $10^{12}/cm^3$.

The electron temperature (see Figure 6.12b) appears to be almost independent of the power absorbed by the plasma, but decreases steadily with pressure. At 1 torr, T_e is approximately $60,000^{\circ}$ K. The effective electric field (Figure 6.12c) and the reduced field E_e/p (Figure 6.12d) are also independent of the power absorbed, but decrease with an increase in electron density and pressure.

The floating double-probe measurements obtained follow the same general variation with pressure as those obtained by ${\tt Maksimov}^7$ in a

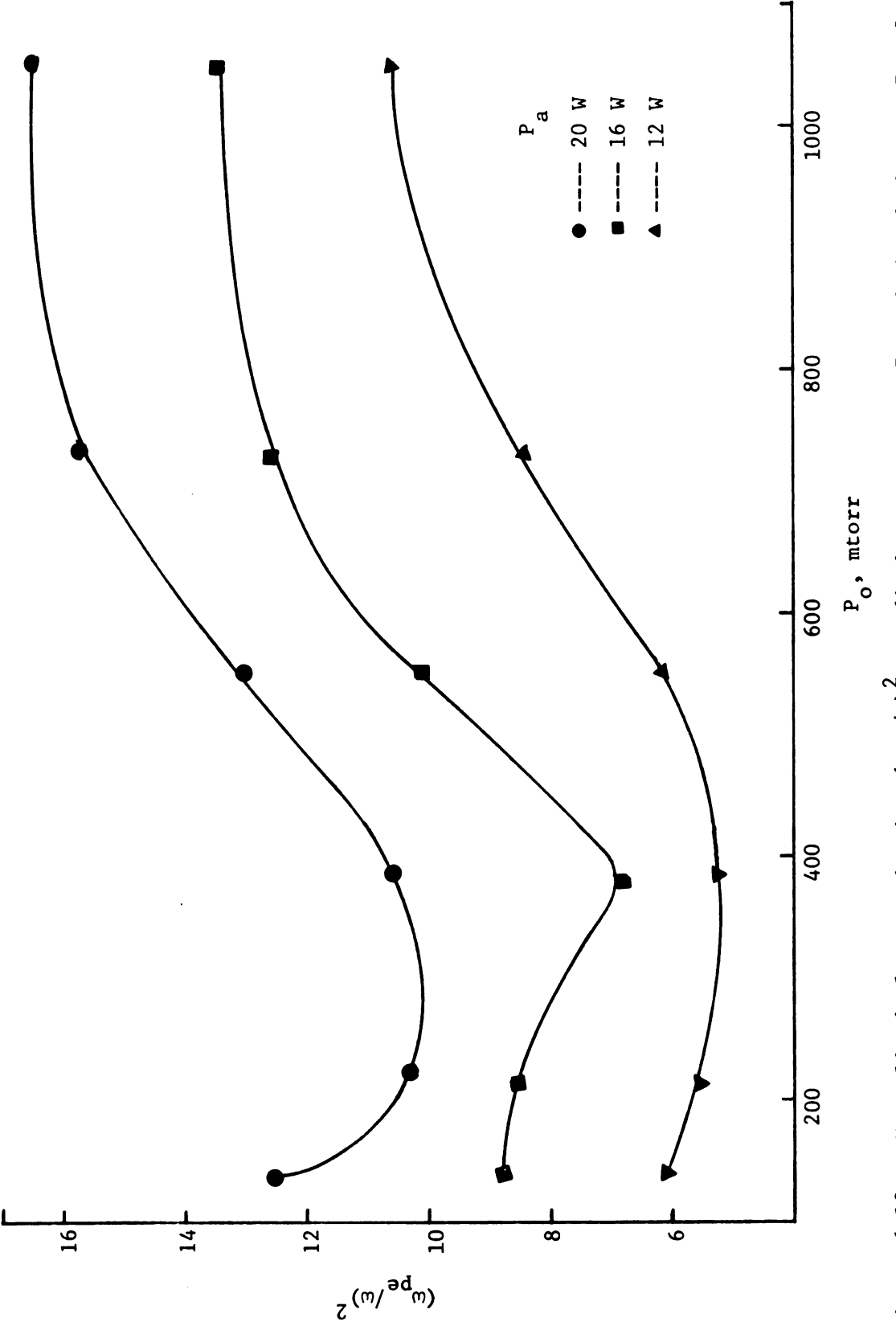


Figure 6.12a. Normalized electron density $(\omega_{
m pe}/\omega)^2$ vs. discharge pressure P $_{
m o}$ and absorbed power P $_{
m a}$, from the floating double probe measurements.

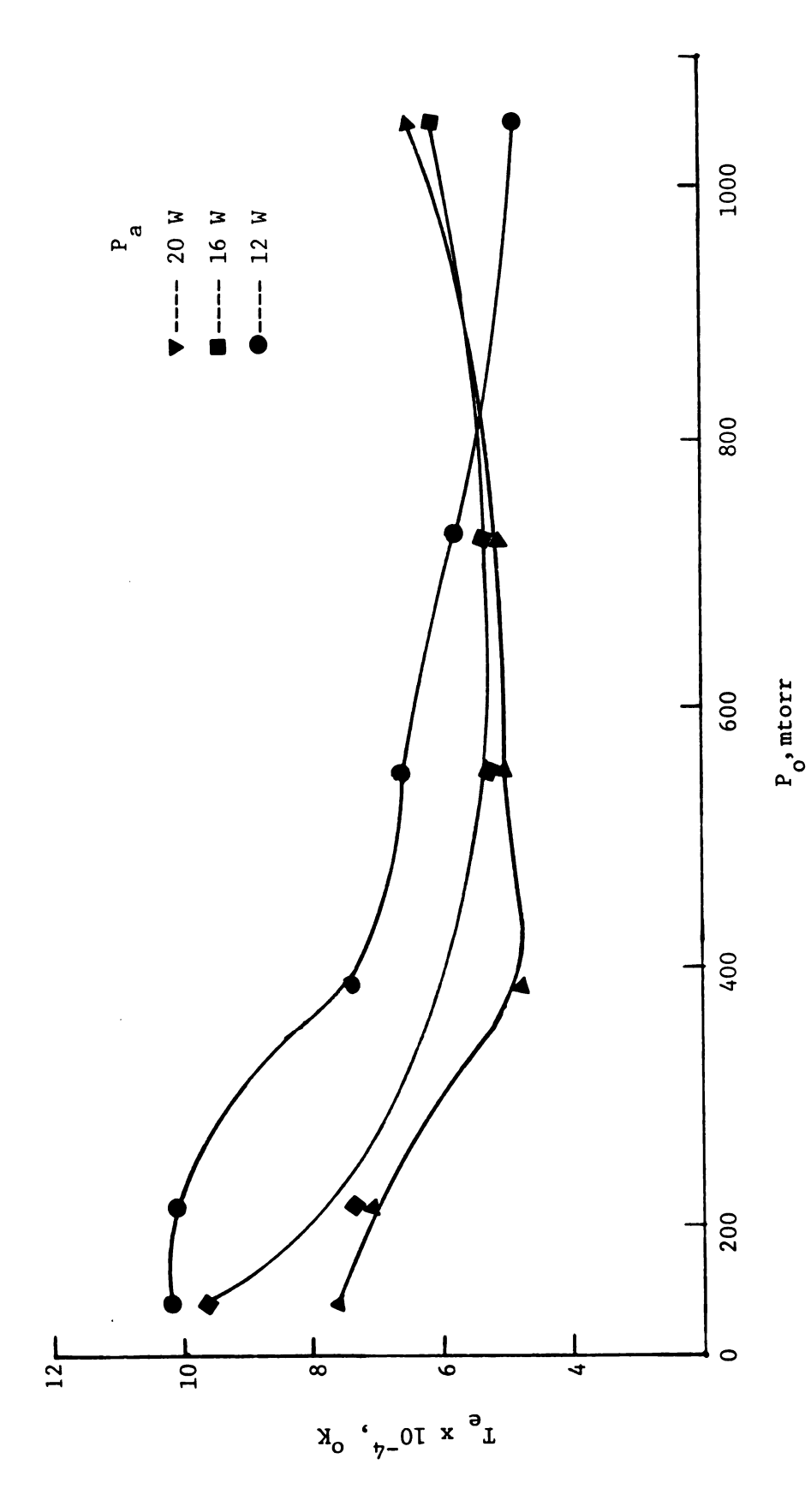


Figure 6.12b. Electron temperature T vs. discharge pressure $_{0}^{\rm P}$ and absorbed power $_{\rm a}^{\rm A}$, from the floating double probe measurements.

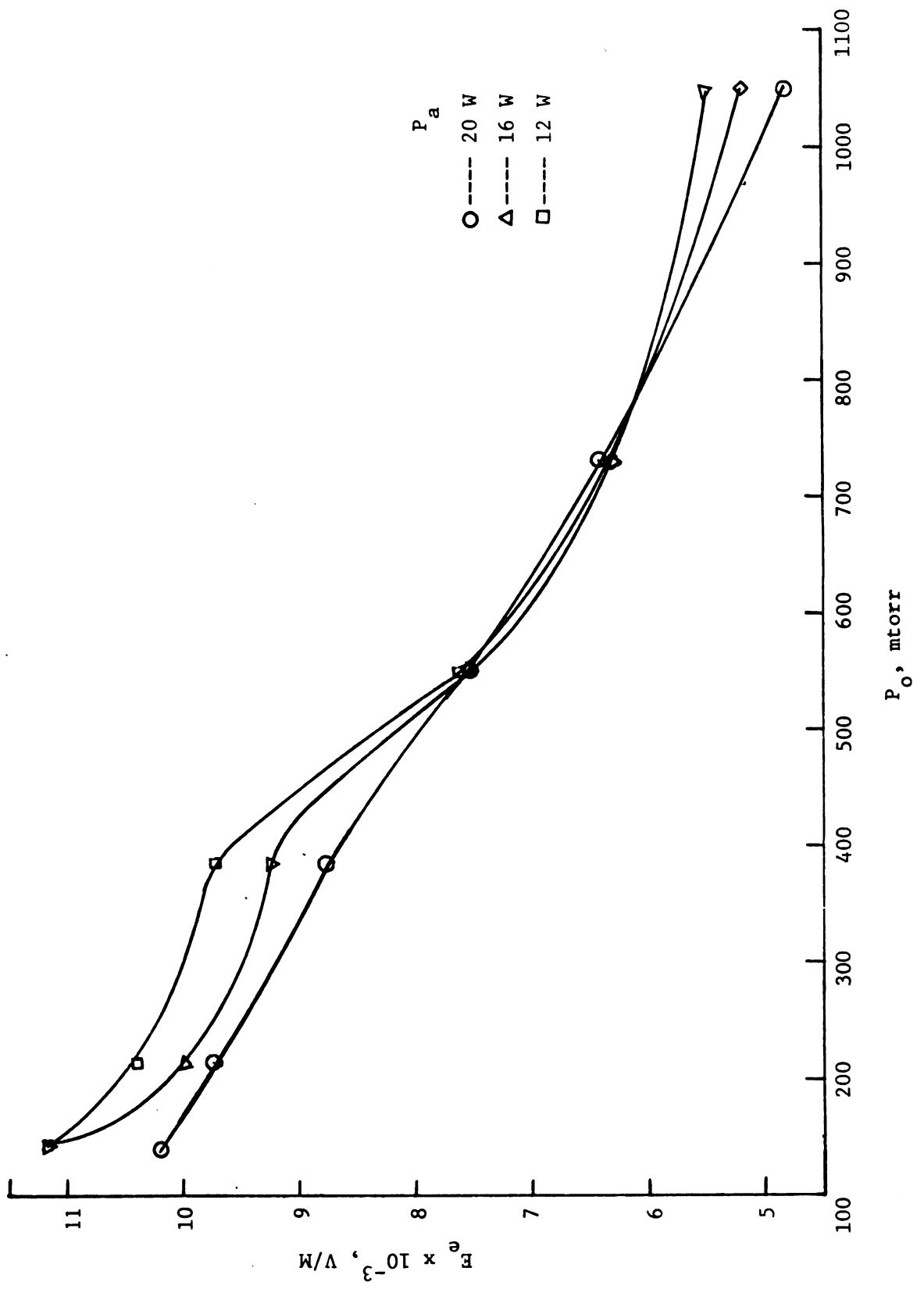


Figure 6.12c. Effective electric field E vs. discharge $_{\rm O}$ and absorbed power $_{\rm a}$, from the floating double probe measurements.

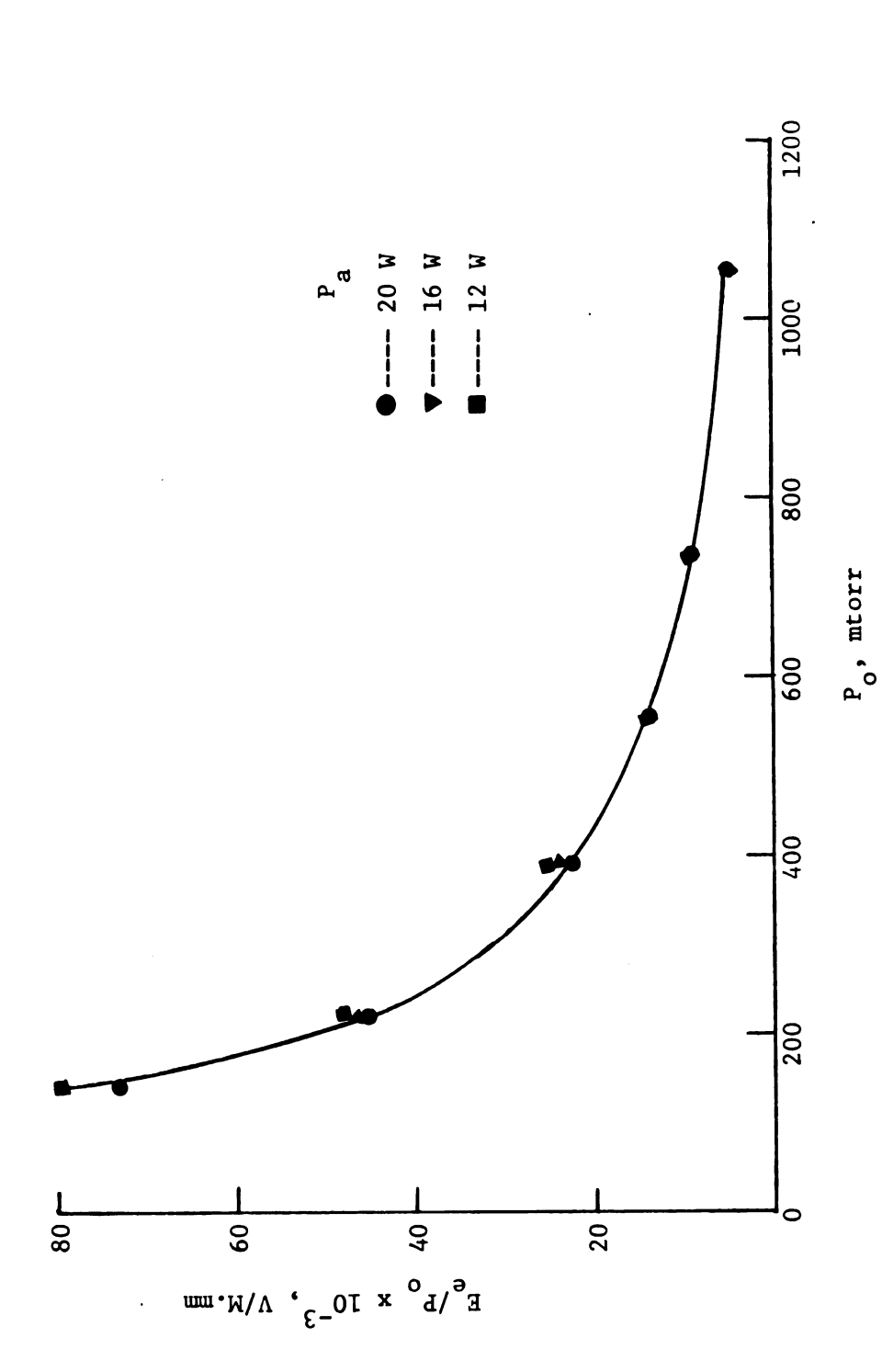


Figure 6.12d. Reduced field $E_{\rm e}/P_{\rm o}$ vs. discharge pressure $P_{\rm o}$ and absorbed power $P_{\rm a}$, from floating double probe measurements.

- 3.0 GHz Helium microwave discharge and by Bell⁵⁵ in a 20 MHz Helium discharge. Since argon gas has been used in the plasma cavity, an absolute comparison between the results of this section with those of Maksimov and Bell is not possible.
- 3) Discharge pressures above 1 torr. Most of the commonly used techniques for measuring the plasma parameters (probes, frequency shift method) fail in this pressure region because of the collision-dominated plasma.

However, a simple technique using discs to measure the conductivity has been found to be useful in estimating the electron density up to a pressure of 20 torr. Discs of different cross-sections were tried and a disc of almost the same cross-sectional area as that of the quartz tube of Cavity 1, gave numbers for electron density that seemed to match the results obtained by the double probe measurement at a pressure of 1 torr.

The results of the electron density measurement from conductivity calculations are shown in Figure 6.13a. At a pressure of 20 torr, and $P_a = 20$ W, the value of N_o is $7.84 \times 10^{12}/\text{cm}^3$. The electron temperature was estimated from the slope and the saturation current of the I-V characteristics of the discs. The results obtained by this method match those obtained by the probe measurements at 1 torr. The electron temperature is slightly dependent on the power absorbed and reaches a uniform value as pressure increases.

Plots of E_e and E_e/p vs. pressure are shown in Figures 6.13c and 6.13d, respectively. Both the effective field and the reduced field reach a steady value at a pressure of 20 torr. At this pressure E_e is 2.5 x 10^3 V/M and is independent of the power absorbed.

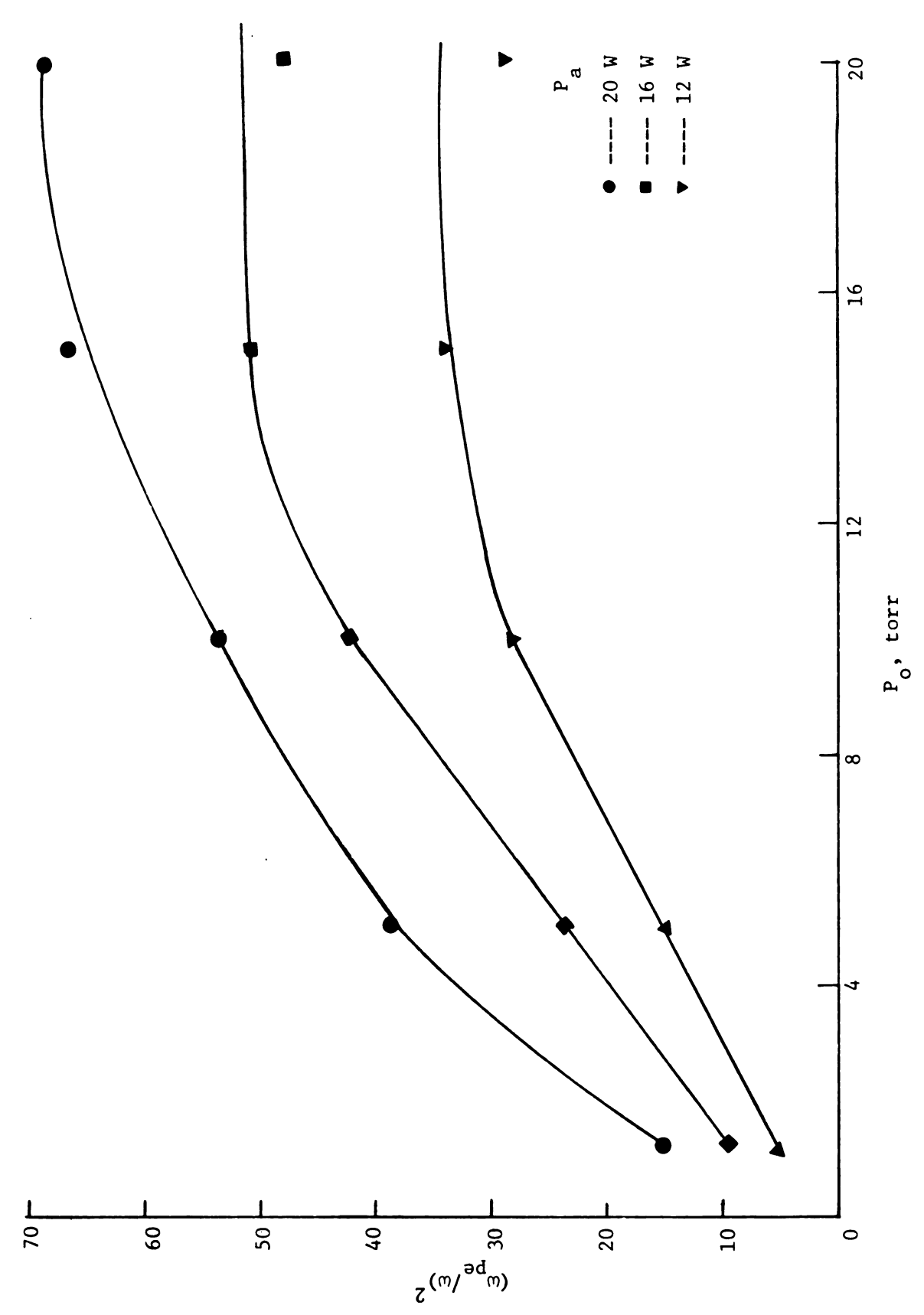


Figure 6.13a. Normalized electron density $(\omega_{
m pe}/\omega)^2$ vs. discharge pressure P and absorbed power P , from measurements using discs.

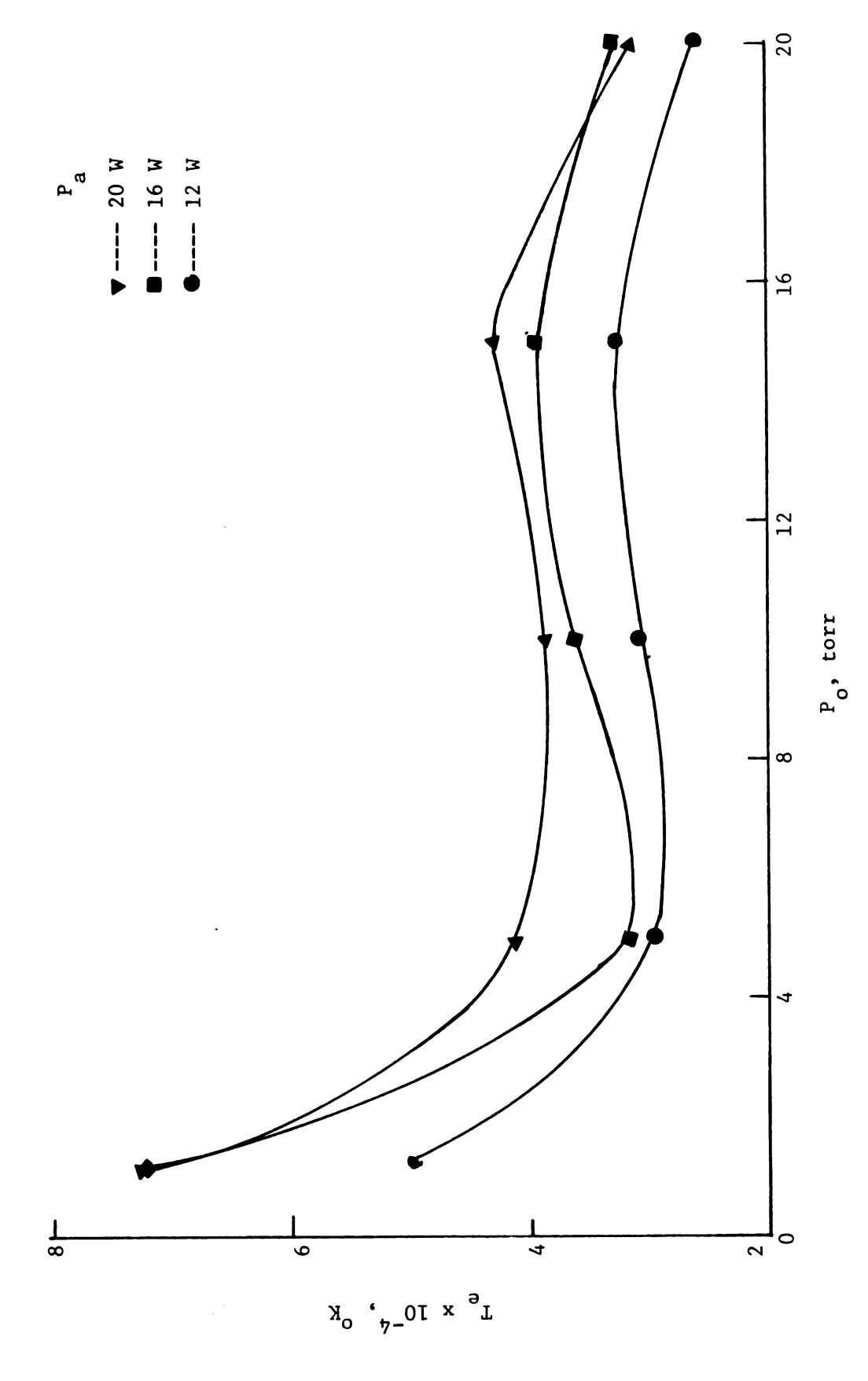


Figure 6.13b. Electron temperature T $_{\rm e}$ vs. discharge pressure P $_{\rm o}$ and absorbed power P $_{\rm a}$, from measurements using discs.

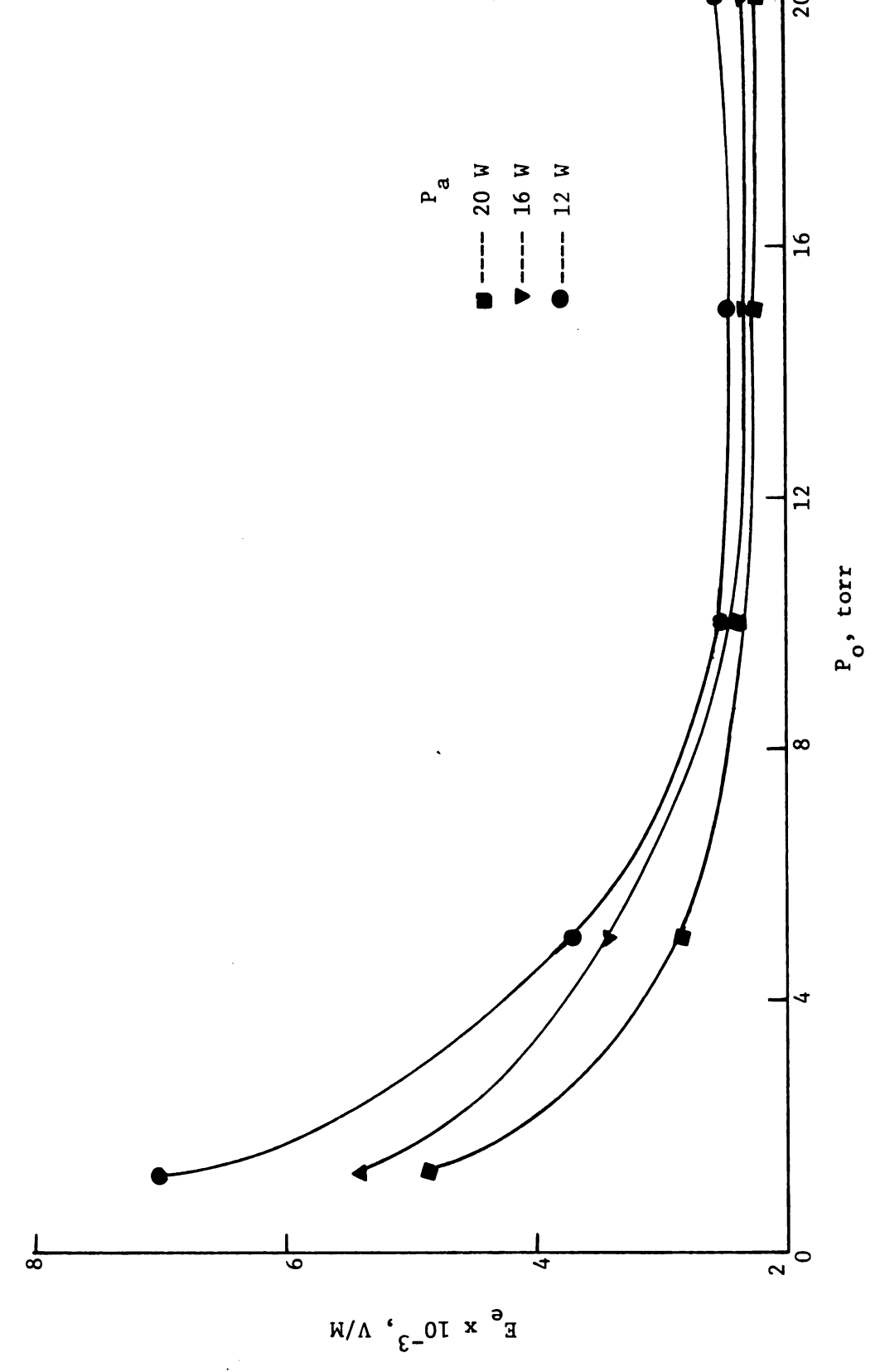


Figure 6.13c. Effective electric field $E_{\rm e}$ vs. discharge pressure $P_{\rm o}$ and absorbed power $P_{\rm a}$, from measurements using discs.

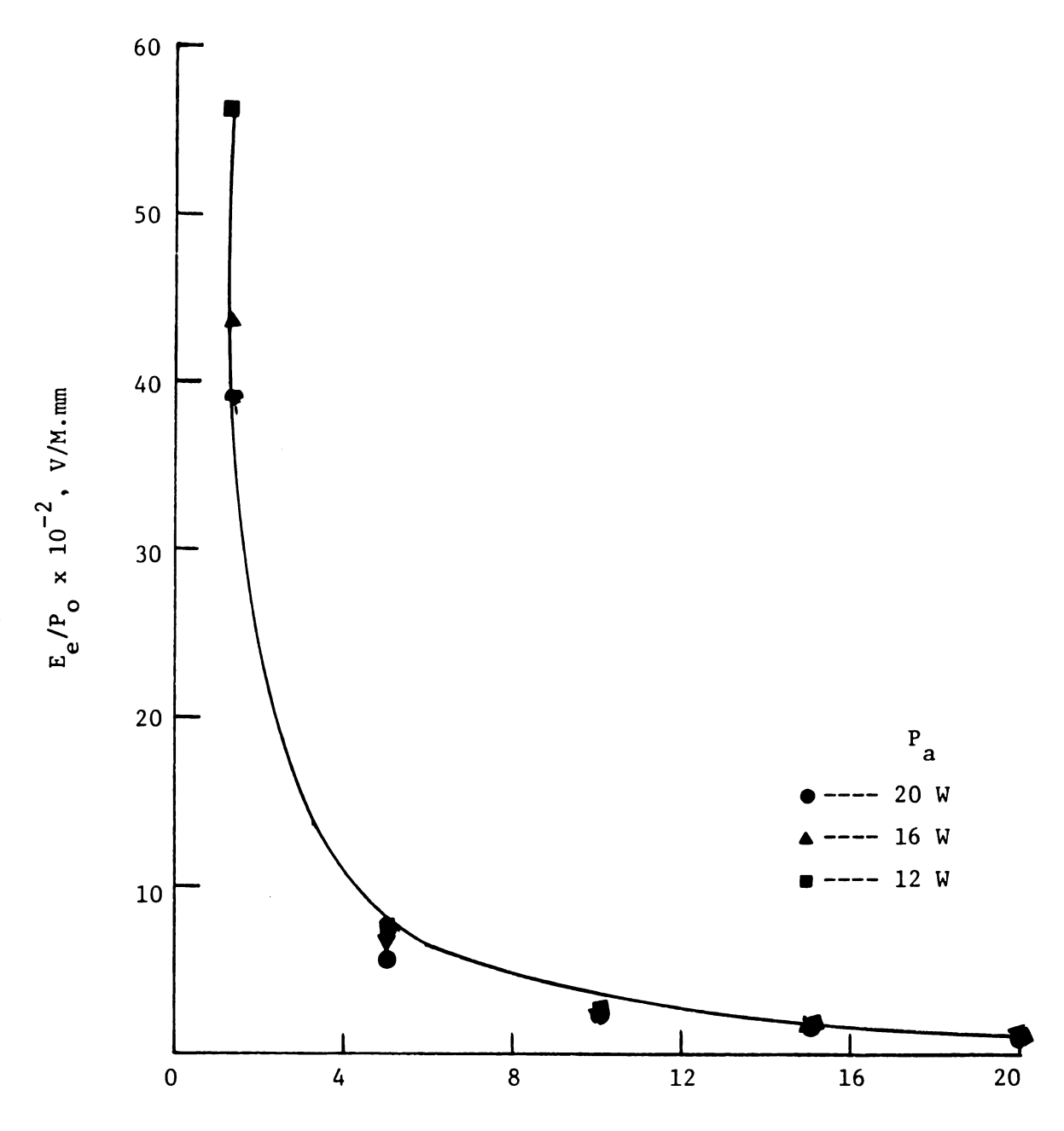


Figure 6.13d. Reduced field $\rm E_e/P_o$ vs. discharge pressure $\rm P_o$ and absorbed power $\rm P_a$, from measurements using discs.

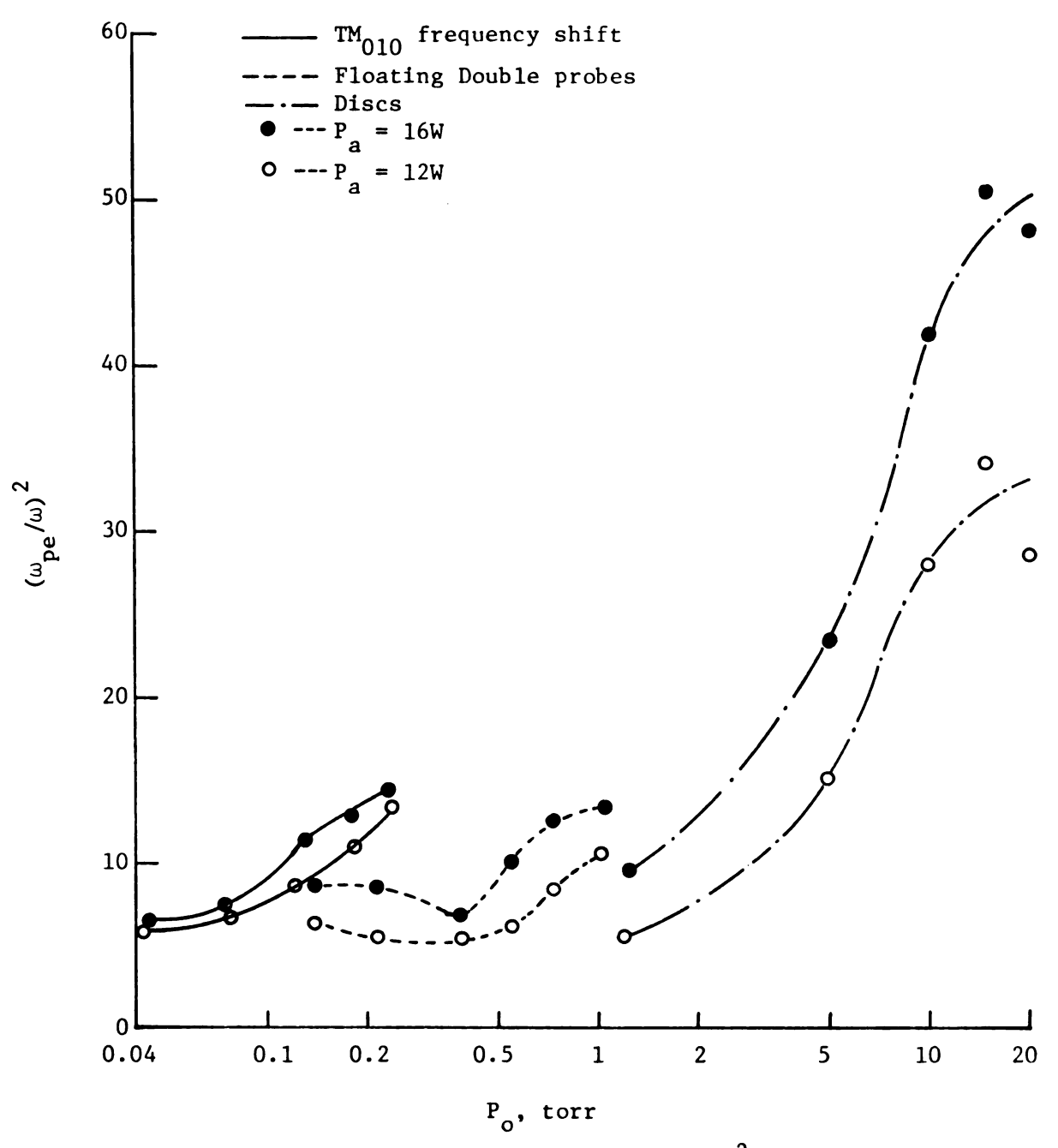


Figure 6.14a. Normalized electron density $(\omega_{pe}/\omega)^2$ vs. discharge pressure P_o and absorbed power P_a over the pressure range 40 mtorr - 20 torr, from three different diagnostic methods.

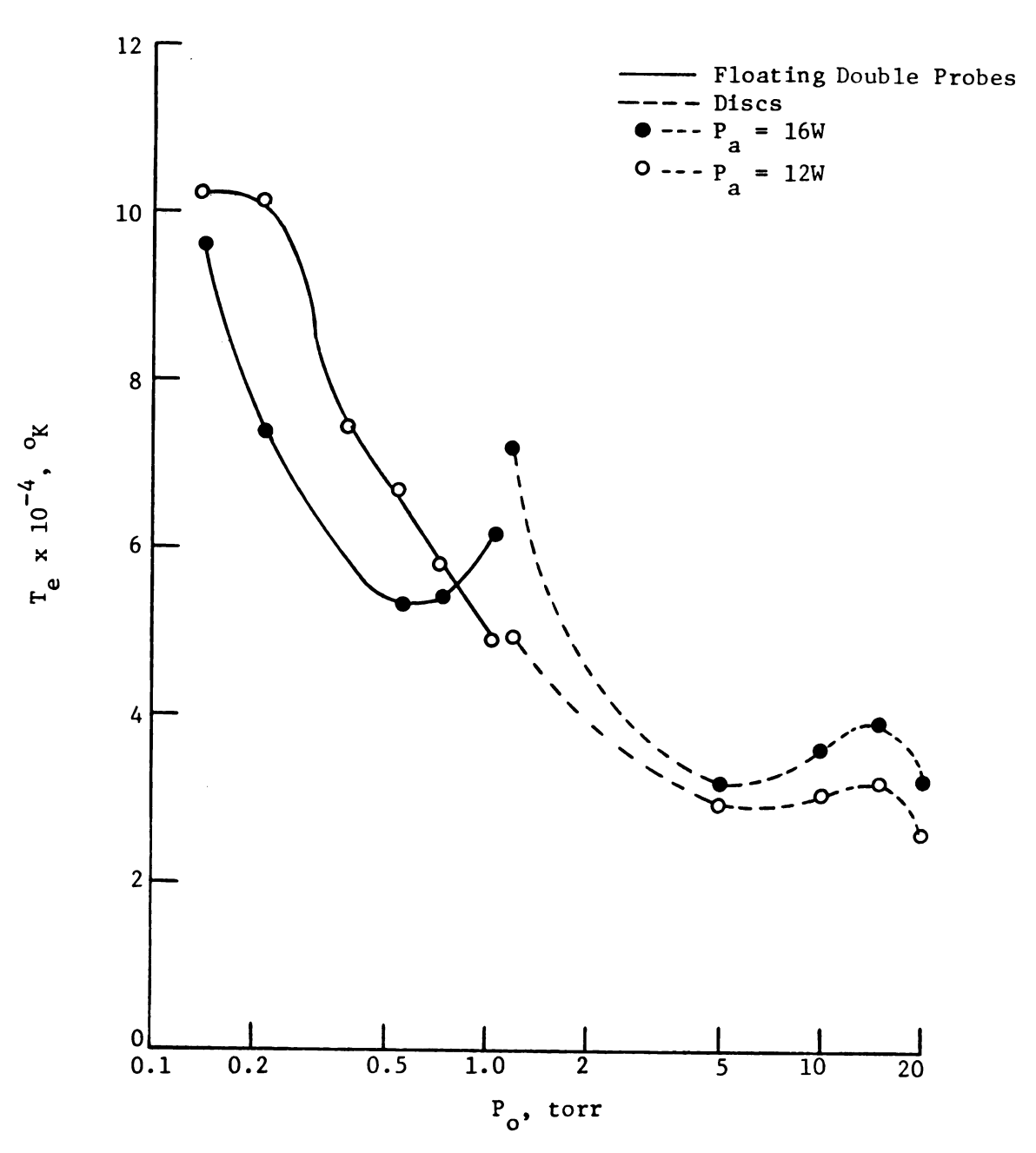


Figure 6.14b. Electron temperature T_e vs. discharge pressure P_o and absorbed P_a over the pressure range 0.1 - 20 torr, from two different diagnostic methods.

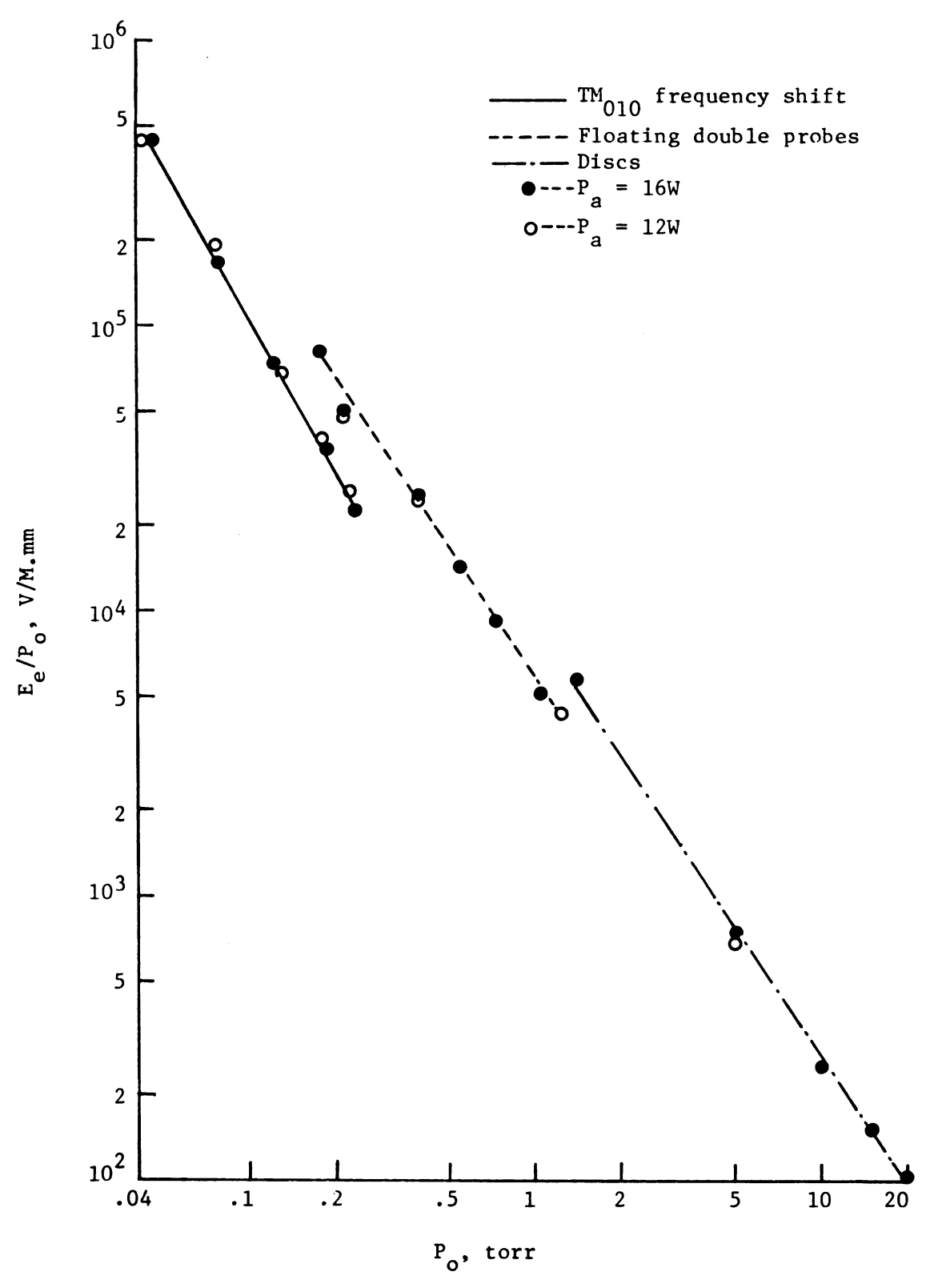


Figure 6.14c. Reduced field $\rm E_e/P_o$ vs. discharge pressure $\rm P_o$ and absorbed power $\rm P_a$ over the pressure range 0.04 - 20 torr, from three different diagnostic methods.

For purposes of comparison, the plasma parameters and the reduced fields obtained from the three different measurement techniques are displayed over the entire pressure range in Figures 6.14a, 6.14b, and 6.14c.

6.4 Absorbed Power Characteristics of the Microwave Plasma Source 6.4.1 Introduction

The #2 plasma-cavity system has been used to study the absorbed power characteristics of the microwave plasma source. The plasma-cavity was tested in argon gas. The quartz center tube was connected to a vacuum system which could be pumped down to several microns of Hg. Once evacuated to low pressures, argon was inserted into the system and plasma initiation was achieved by 1) adjusting the pressure of the argon gas somewhere between 0.5 to 10 mm Hg., 2) applying the high microwave power, and 3) length tuning the empty cavity for resonance at the oscillator frequency of 2.450 GHz. The microwave source and a cross-section of Cavity 2 are shown in Figures 5.4 and 5.5.

Gas breakdown was achieved near precalculated cavity resonant lengths. Once breakdown was accomplished, the pressure, RF power, cavity length, and cavity coupling adjustments could be varied to produce the desired plasma conditions. With a little experimental experience, this tuning procedure could be achieved in less than one-half minute without fear of extinguishing the plasma. By varying the input gas flow and exhaust pumping rate, a plasma could be established in the flowing gaseous environment. The flow rate could be continuously varied from zero to over 14,000 cm³/minute, the upper limit of the experimental flow measurement capability.

The plasma cavity could be operated in many different cavity resonances simply by adjusting the cavity length and input coupling. For

example, the following empty cavity modes have eigenfrequencies equal to 2.450 GHz when the cavity length is varied from 6 to 20 cm.: TE_{111} , TM_{011} , TE_{211} , TE_{011} , TM_{111} , TE_{112} , TM_{012} , TE_{212} , TE_{012} , TM_{112} , TE_{113} , etc. With the proper cavity length and RF coaxial coupling (i.e., loop or probe), the plasma cavity system will sustain a plasma on any of these modes. However, only the TM_{01p} , TE_{01p} , and TE_{11p} modes, where p = 1, 2, or 3 were studied extensively.

All three of these modes were able to maintain microwave plasmas in argon gas over a wide range of pressures and flowing gas conditions. The appearance of the plasma varied considerably as the pressure and power were varied. At pressures less than 5 mm Hg, the discharge could be resonantly sustained 51,52 in a TD resonance or in a pure electromagnetic resonance. In either case, the discharge took on a dull to bright reddish pink as the power was increased. In the pressure range of 5 to 80 mm Hg, the discharge color varied from dull pink to blue to a bluish white at high power levels (1 KW). At pressures of 80 mm Hg or more, thin intense discharge streamers appear following paths which have high displacement currents in the absence of a plasma. When exciting the TE $_{01n}$ resonance at pressures greater than 200 mm Hg hot plasmas, similar to low-frequency induction plasmas 32,53 , can be formed inside the quartz tube.

6.4.2 Experimental Results

Two different types of experiments were performed to study the absorbed power characteristics of the argon plasma maintained in Cavity 2.

1) In the first of these experiments, the absorbed power of the plasma was studied as a function of the cavity length with the gas discharge pressure (p_0) and the gas flow rate as the variable parameters

(see Figures 6.15 and 6.16). These experiments were conducted using the ${\rm TE}_{\rm Oll}$ mode, because of its usefulness in plasma chemistry experiments and also because of its gradual variation in eigenlength vs. electron density (see Figure 6.17). Because of equipment limitations, only the following parameters have been measured in these experiments: the gas flow rate, discharge pressure and the length of the cavity. It was not possible to make density and temperature measurements using the conventional probe and TM_{010} frequency shift diagnostic techniques. Probe measurements on the high pressure plasma of Cavity 2 yielded erroneous results because of high electron-neutral collision frequencies. Also, the insertion of a probe into the plasma of Cavity 2, caused a significant amount of power to be coupled to the external surroundings. This was considered to be a safety hazard. The use of the TM₀₁₀ frequency shift method was also limited by the high pressures employed in Cavity 2. The failure of these methods and the absence of more sophisticated techniques required that all arguments used in explaining the experimental phenomena be based on the above-mentioned experimental quantities and on estimates of the electron density and temperature.

In the absence of direct measurements of the electron density, collision frequency, rate of ionization and other parameters involving a flowing gas, the arguments presented below are speculative. However, these explanations may provide the background on which further theoretical and experimental research may be based to fully understand this problem.

Figure 6.15 displays the experimental absorbed power P_a vs. the cavity eigenlength L_s for the TE_{011} mode. All experimental points in Figure 6.15 were measured at a constant flow rate of 1,000 cc/min. and

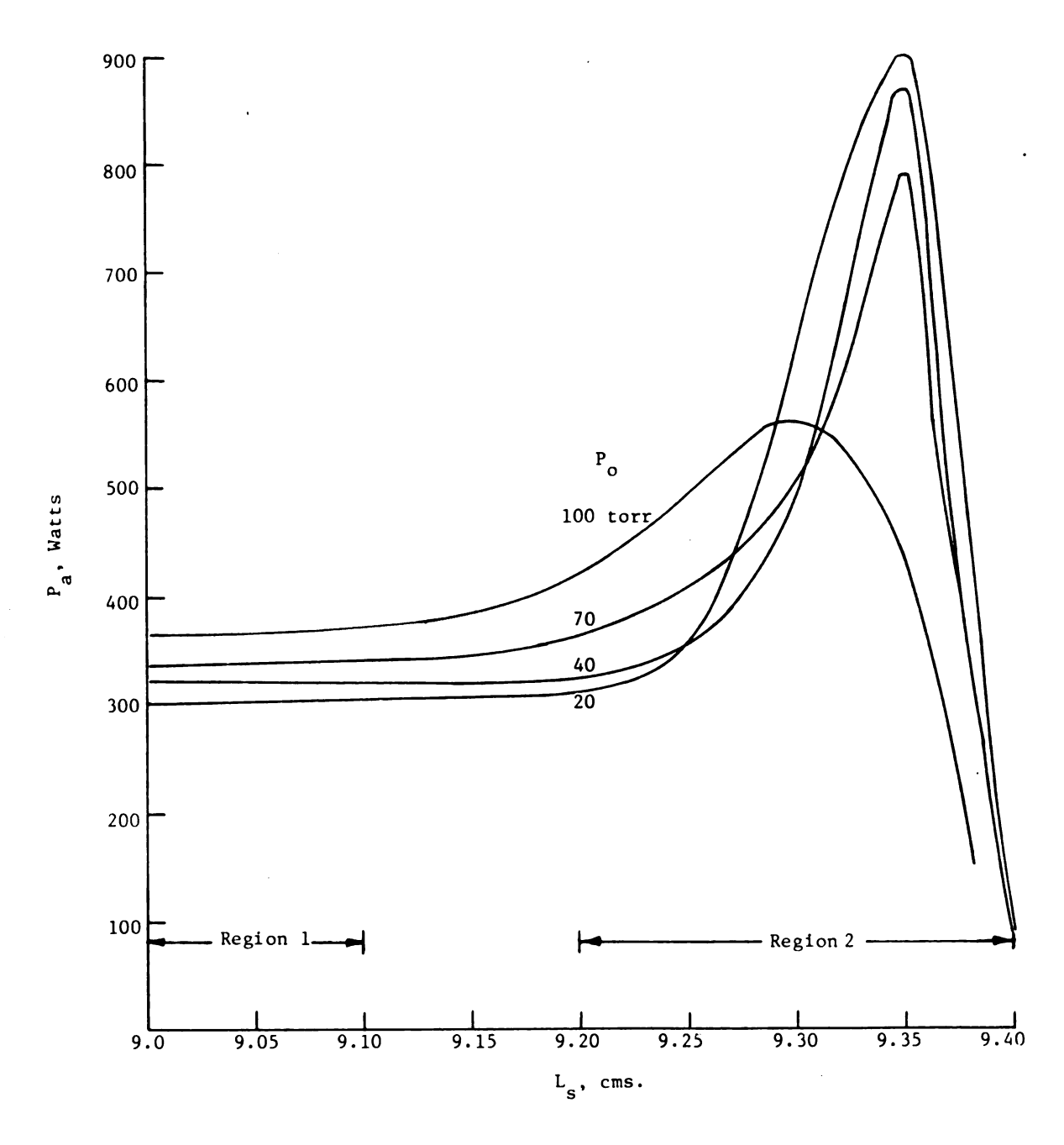


Figure 6.15. Absorbed power P_a vs. eigenlength L_s and different discharge pressures P_o , for the TE_{011} mode plasma of Cavity 2. Flow rate = 1000 cc/min, Incident power P_i = 1.2 KW.

each curve represents the power absorbed vs. cavity length for a different pressure.

Two regions of operation can be clearly distinguished in these curves. In region 1, which covers the approximate eigenlength 9.0 cms - 9.1 cms., the absorbed power increases as a function of the discharge pressure. In region 2, which includes eigenlengths from 9.2 - 9.4 cms. the absorbed power increases inversely as the discharge pressure. These experimental observations can be explained by studying the theoretical TE_{01} absorbed power vs. (ω/ω_{pe}) curve for different (ν_e/ω_{pe}) , as described in Chapter III and shown in Figure 3.5. Note that the curve of Figure 3.5 has been plotted for a plasma density of f_{pe} = 10.5 GHz and for the waveguide dimensions of Cavity 1. However, the behavior of the curve is general enough, so that it can be used to qualitatively explain the variation of absorbed power and plasma density vs. pressure in Cavity 2.

In region 1 of Figure 6.15 the cavity operates close to the empty cavity resonance. The electron density in this region is small and, hence, $(\omega/\omega_{\rm pe})$ becomes large. This experimental region of operation corresponds to the right end of the theoretical ${\rm TE}_{01}$ absorbed power curves shown in Figure 3.5. In this region of the theoretical curves, the normalized absorbed power increases with the collision frequency. (Compare curves for $({}^{\vee}_{\rm e}/{}^{\omega}_{\rm pe})$ = 0.1 and 1.0). This type of behavior would be more apparent at still higher values of $({}^{\vee}_{\rm e}/{}^{\omega}_{\rm pe})$. This seems to justify the experimental observations made in region 1 of Figure 6.15.

In region 2 of Figure 6.15, the electron density is large and, hence, (ω/ω_{pe}) is small. This region of experimental operation would lie to the left of the theoretical TE $_{01}$ absorbed power curves (Figure 3.5). In

this part of Figure 3.5, the normalized absorbed power increases inversely with the collision frequency. This theoretical behavior explains the experimental observations made in region 2 of Figure 6.15.

Figure 6.16 shows the absorbed power, P_a , vs. the cavity eigenlength, L_s , with the discharge pressure held constant at 10 mm. Each of the curves of Figure 6.16 have been plotted for different gas flow rates. These curves show that for a given flow rate, the absorbed power reaches a peak at a certain eigenlength. For example, when the flow rate is zero, the peak occurs at $L_s = 9.15$ cms. and the absorbed power is only 490W. As the flow rate increases, the absorbed power peak shifts towards higher eigenlengths and for flow rates of 250 cc/min and beyond, the absorbed power peak remains at $L_s = 9.35$ cms. At the same time, the absorbed power also increases with the flow rate and is highest for a flow rate of 2000 cc/min.

In providing a qualitative explanation for the shift in cavity eigenlength, with changes in flow rate, the eigenlength plot of the ${\rm TE}_{011}$ mode for Cavity 2 (Figure 6.17) will be used. Before using the curves of Figure 6.17, it must be noted that the experimental ${\rm TE}_{011}$ empty cavity and coaxial resonances are lower by .05 cms. than the corresponding theoretical values due to the finite thickness of the plasma enclosing quartz tube, holes in the cavity for diagnostic purposes, wall imperfections, etc. Hence, .05 cms. should be added to all ${\rm TE}_{011}$ experimental eigenlengths for a direct comparison with the theoretical curves of Figure 6.17. The ${\rm TE}_{011}$ eigenlength curves have been evaluated for a zero flow rate. The applicability of these curves to a non-zero flow rate situation is not clearly understood. It is expected that a non-zero flow rate, would modify the values of electron density and the collision frequency from their zero flow rate values. However, a flowing plasma

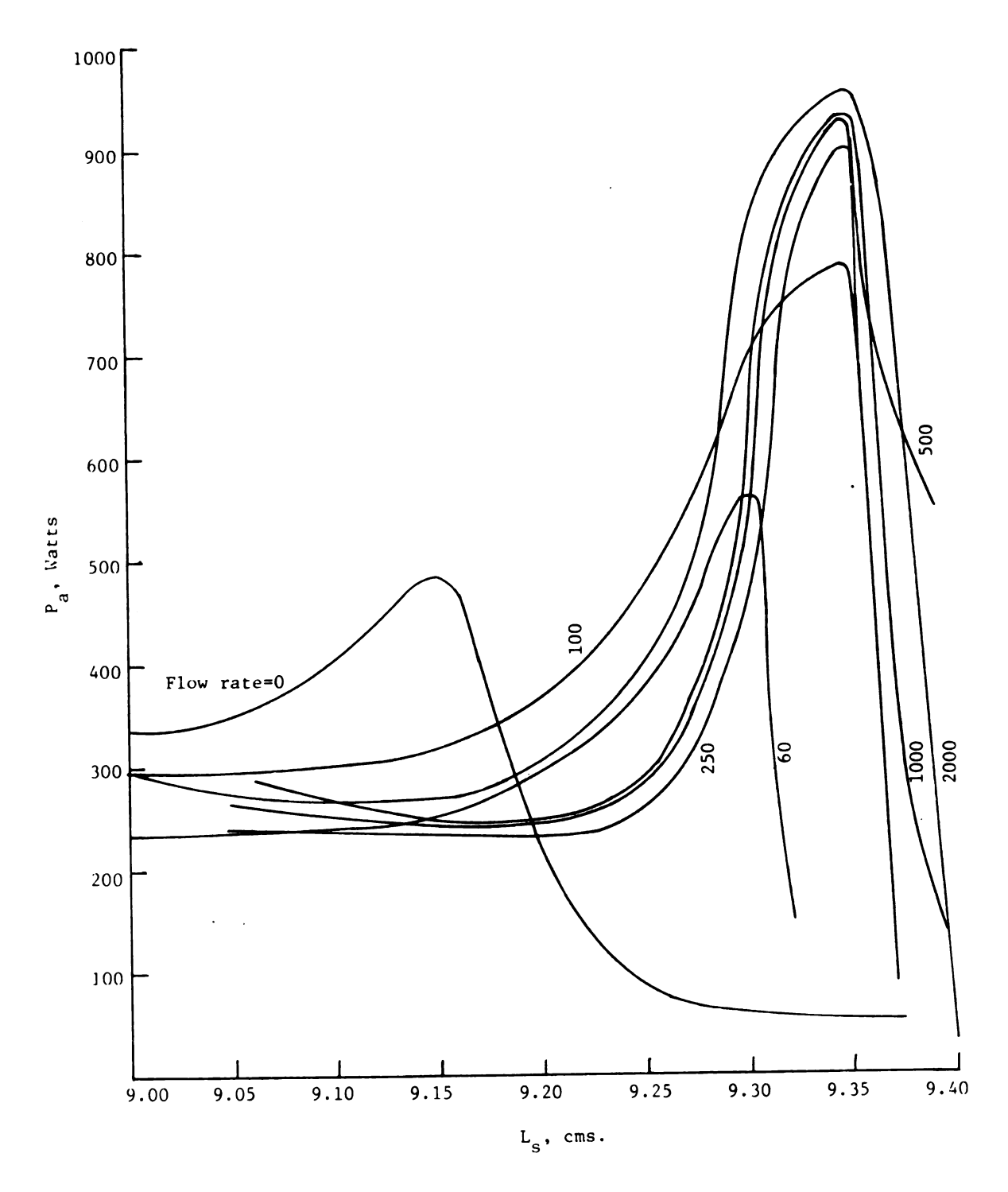


Figure 6.16. Power absorbed P_a vs. eigenlength L_s , and flow rate (cc/min) for the TE_{011} mode plasma of Cavity 2. Discharge pressure, P_o = 10 torr. Incident power P_i = 1.2 KW.

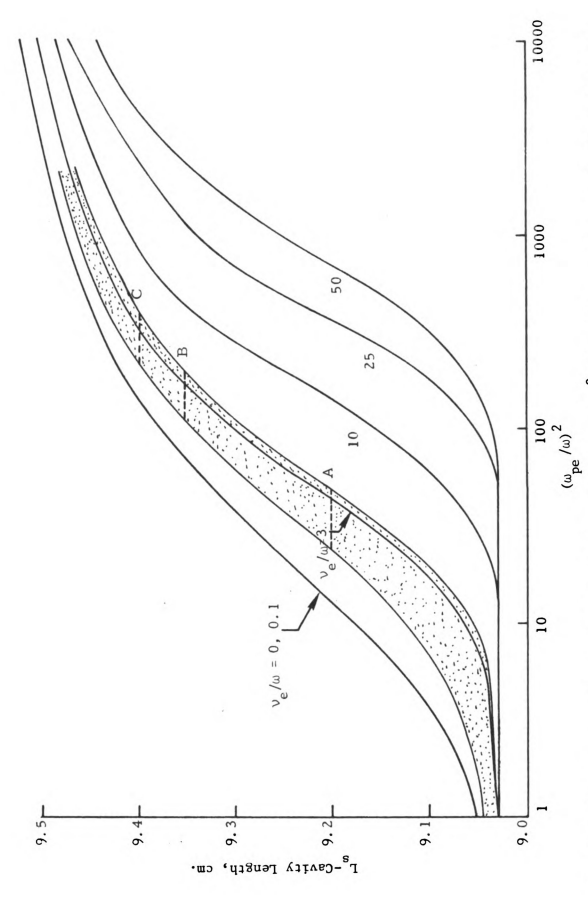


Figure 6.17. TE $_{011}$ resonant length vs. plasma density $(\omega_{
m pe}/\omega)^2$ and collision frequency (ν_e/ω) for Cavity 2. $\omega/2\pi$ = 2.45 GHz.

still has a discrete electron density, temperature and collision frequency, i.e., its steady state operation can be represented as a single point on Figure 6.17. Assuming that the electron temperature may vary between $20,000^{\circ}$ K and $90,000^{\circ}$ K, the normalized electron neutral collision frequency, (ν_e/ω) , can be estimated from Figure 6.9 to vary between 1 and 3.5. This band of collision frequencies would correspond to the shaded region of operation shown in Figure 6.17.

The experimental curves of Figure 6.16 can best be explained by classifying the curves of different flow rates into three different groups: 1) Flow rate = 0 cc/min. 2) Flow rate = 60 cc/min. 3) Flow rates = 100, 250, 500, 1,000, 2,000 cc/min.

- 1) The peak-absorbed power for a zero flow rate occurs at $L_{\rm sc}$ = 9.20 cms., and the operating point lies on line A, as shown in Figure 6.17. $L_{\rm sc}$ is the corrected eigenlength.
- 2) With an increase in the flow rate to 60 cc/min., the eigenlength of the peak of the curve shifts to $L_{\rm sc}$ = 9.35 cms. The peak-absorbed power also increases as a result of the increase in the ionized gas volume. This contributes to a rise in the electron density and the operating point lies along line B (Figure 6.17).
- 3) A further increase in the flow rate to 100 cc/min. causes the peak absorbed power to increase from 560W to 790W. The new eigenlength of the peak of the curve occurs at $L_{\text{SC}} = 9.395 \text{ cms.}$ This dramatic rise in absorbed power is attributed mainly to the increase in the volume of ionization because of the large flow rate. The operating point now lies along line C (Figure 6.17).

The flow rate is now increased gradually in the range 250 cc/min. to 2000 cc/min. It is observed that for this large variation in the

flow rate, that the eigenlength of the peak-absorbed power remains constant at $L_{\rm sc}$ = 9.40 cms. and the peak-absorbed power varies only from 900W to 950W. A possible explanation for this strange behavior is that the substantial increase in the flow rate may not cause a proportional increase in the volume of the ionized gas.

As the flow rate is varied in the range 0 to 250 cc/min, the volume of the ionized gas increases directly with the flow rate. This fact has been experimentally verified by observing that the light intensity of the gas increases with the flow rate. This implies that there must be a large increase in the absorbed power (see Figure 6.16 for flow rates 0, 60, 100, 250 cc/min.) and, hence, an increase in the electron density. The electron density at 250 cc/min. may be sufficiently large to form a high density plasma next to the inside of the quartz tube. This plasma would prevent the penetration of the fields into the internal volume of the gas and thus, have the effect of preventing the rest of the gas from ionization. This shielding effect of the outer layer of the plasma allows a large volume of the incoming gas to bypass the excitation region in the cavity. Thus, a dramatic increase in the flow rate from 250 cc/min. to 2000 cc/min. has little or no effect on the peak power absorbed by the plasma.

2) In the second type of experiments the behavior of the absorbed power of a TE_{112}^{\star} mode plasma was studied as a function of the discharge pressure with the incident power P_{1} and the gas flow rate as the variable parameters. The values used for the incident power P_{1} were 966W, 759W, 552W and 276W. A family of such curves was obtained by varying the pressure with flow rate constant. The flow rate values used were 147, 520, 955, 1480, and 2500 cc/min. These curves are shown in Figures

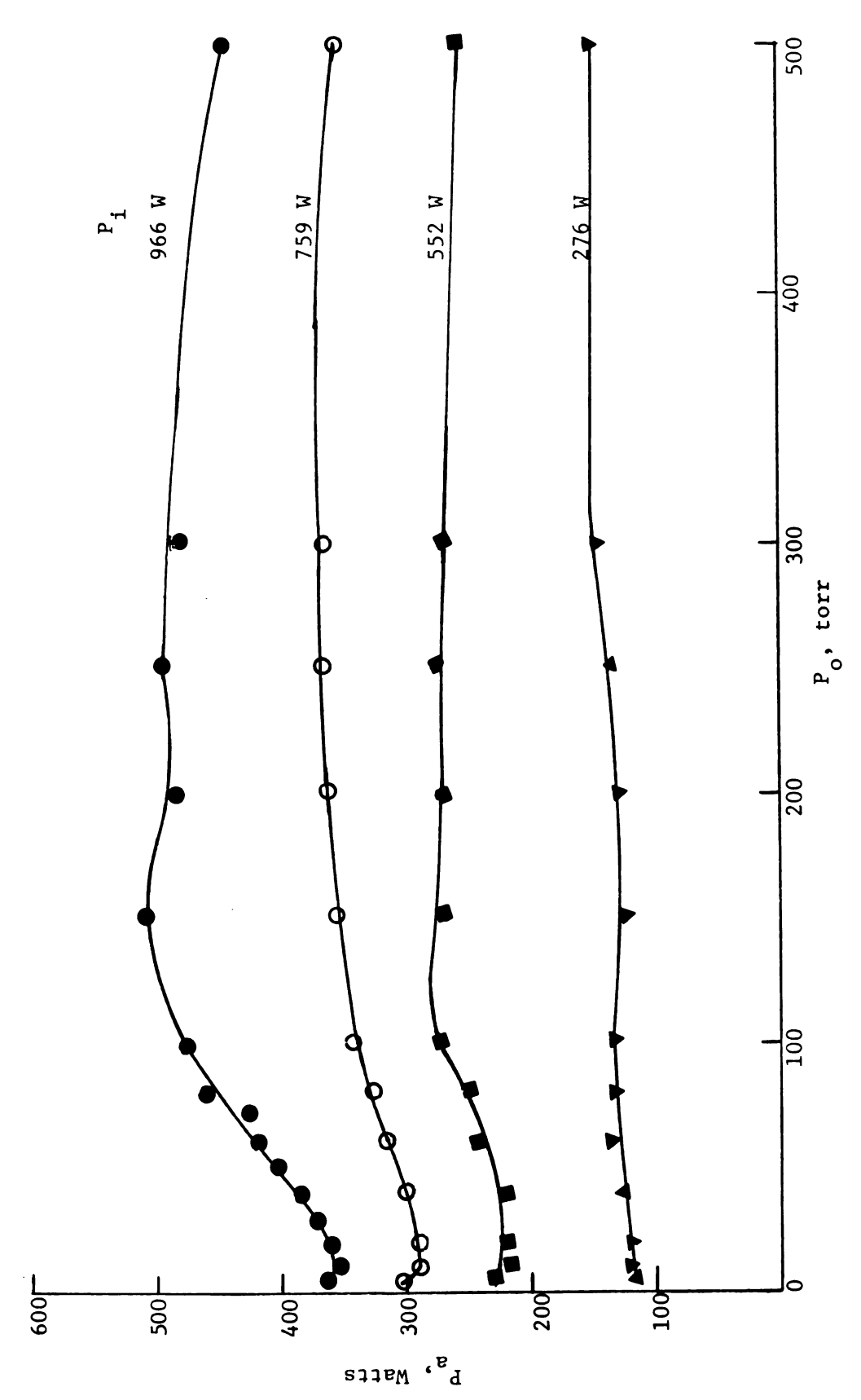


Figure 6.18. Power absorbed P $_{
m a}$ vs. discharge pressure P $_{
m o}$ and incident power P $_{
m I}$ for the TE $_{
m 112}$ mode plasma of Cavity 2. Flow rate = 147 cc/min. Gas: argon.

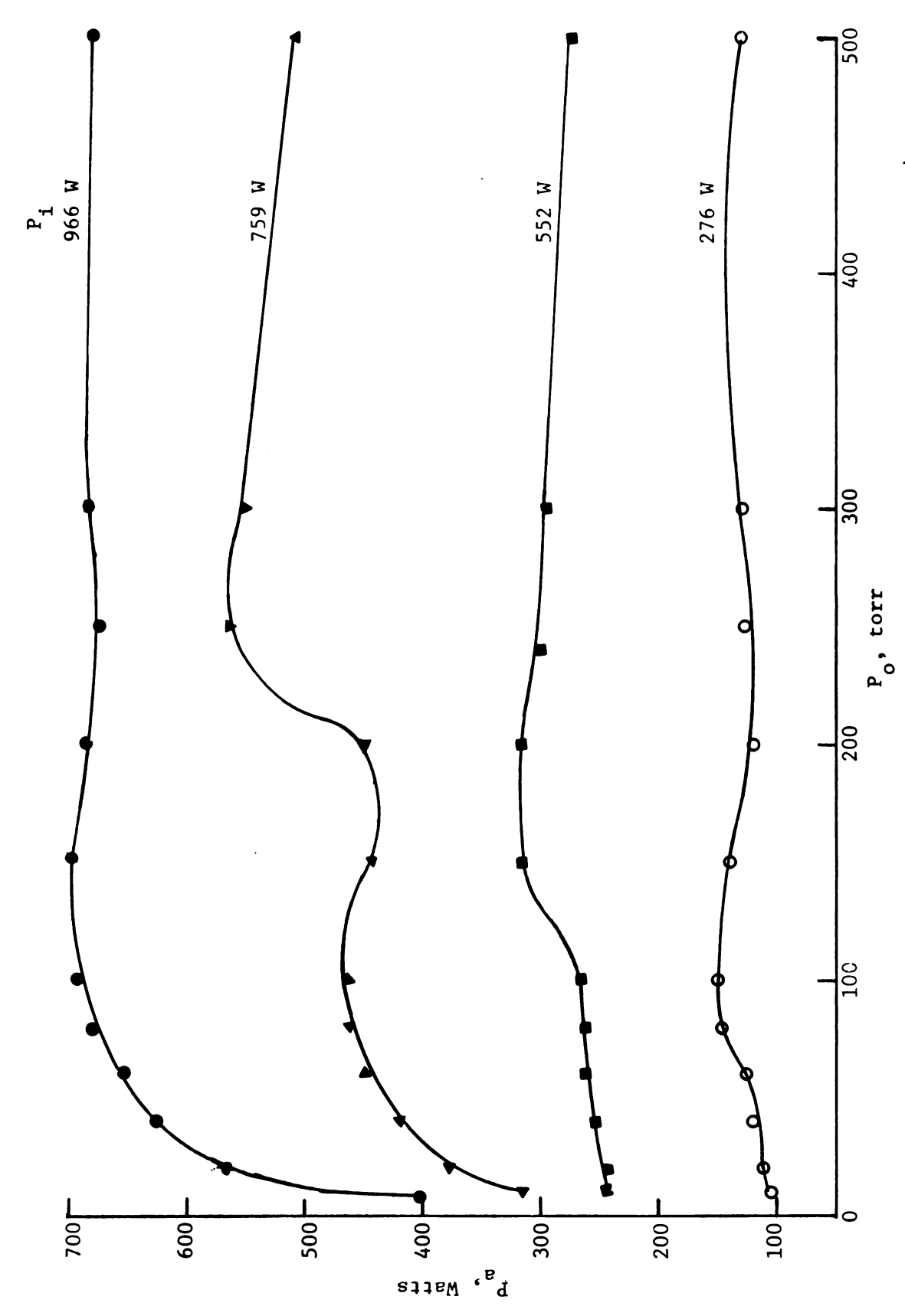


Figure 6.19. Power absorbed P vs. discharge pressure P and incident power P for the TE $^{\star}_{112}$ mode plasma of Cavity 2. Flow rate = 520 cc/min. Gas: argon.

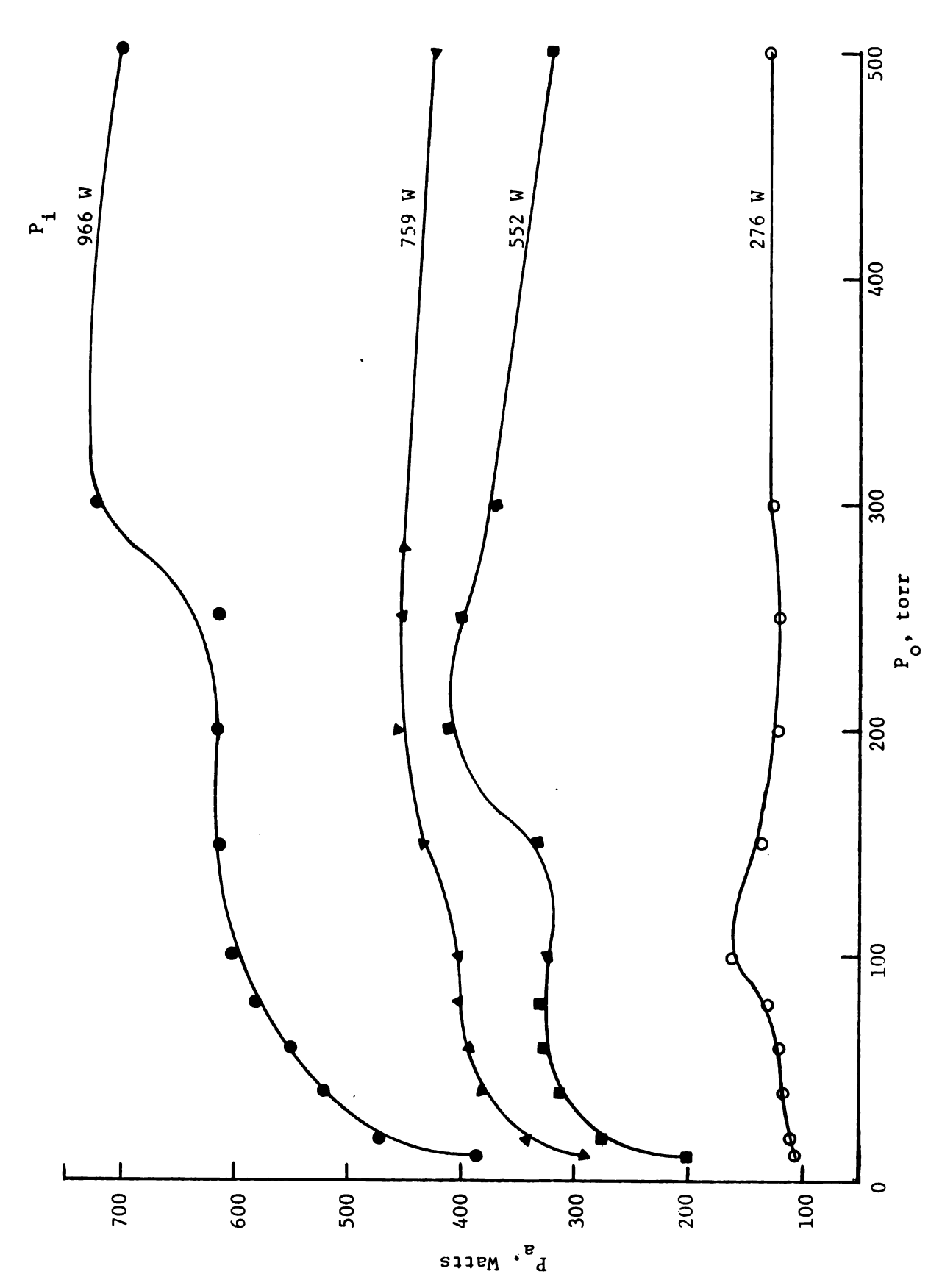


Figure 6.20. Power absorbed P_a vs. discharge pressure P_o and incident power P₁ for the TE $^{\star}_{112}$ mode plasma of Cavity 2. Flow rate = 955 cc/min. Gas: argon.

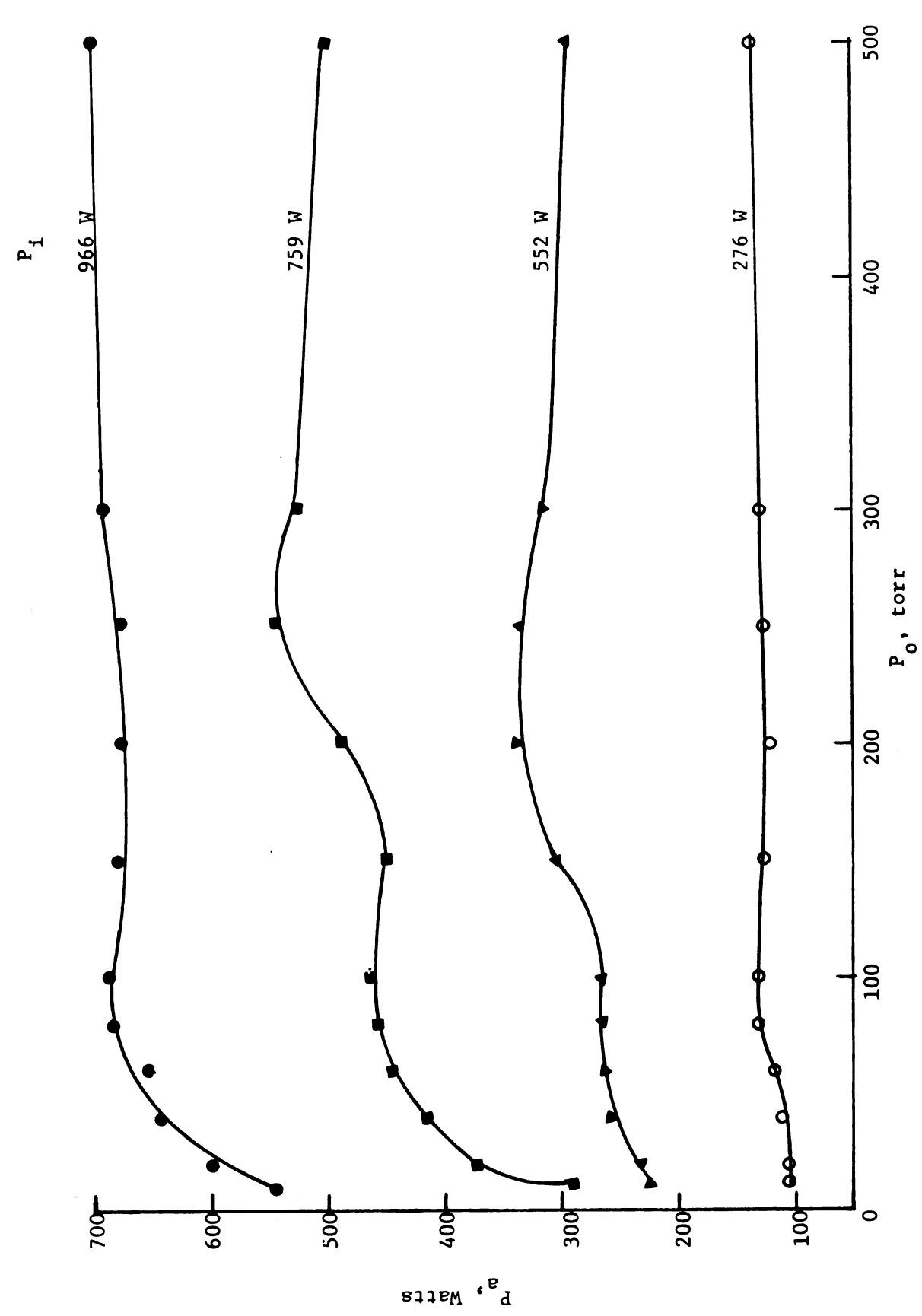


Figure 6.21. Power absorbed P vs. discharge pressure P and incident power P $_{
m I}$ for the TE $_{
m 112}^{*}$ mode plasma of Cavity 2. Flow rate = 1480 cc/min. Gas: argon.

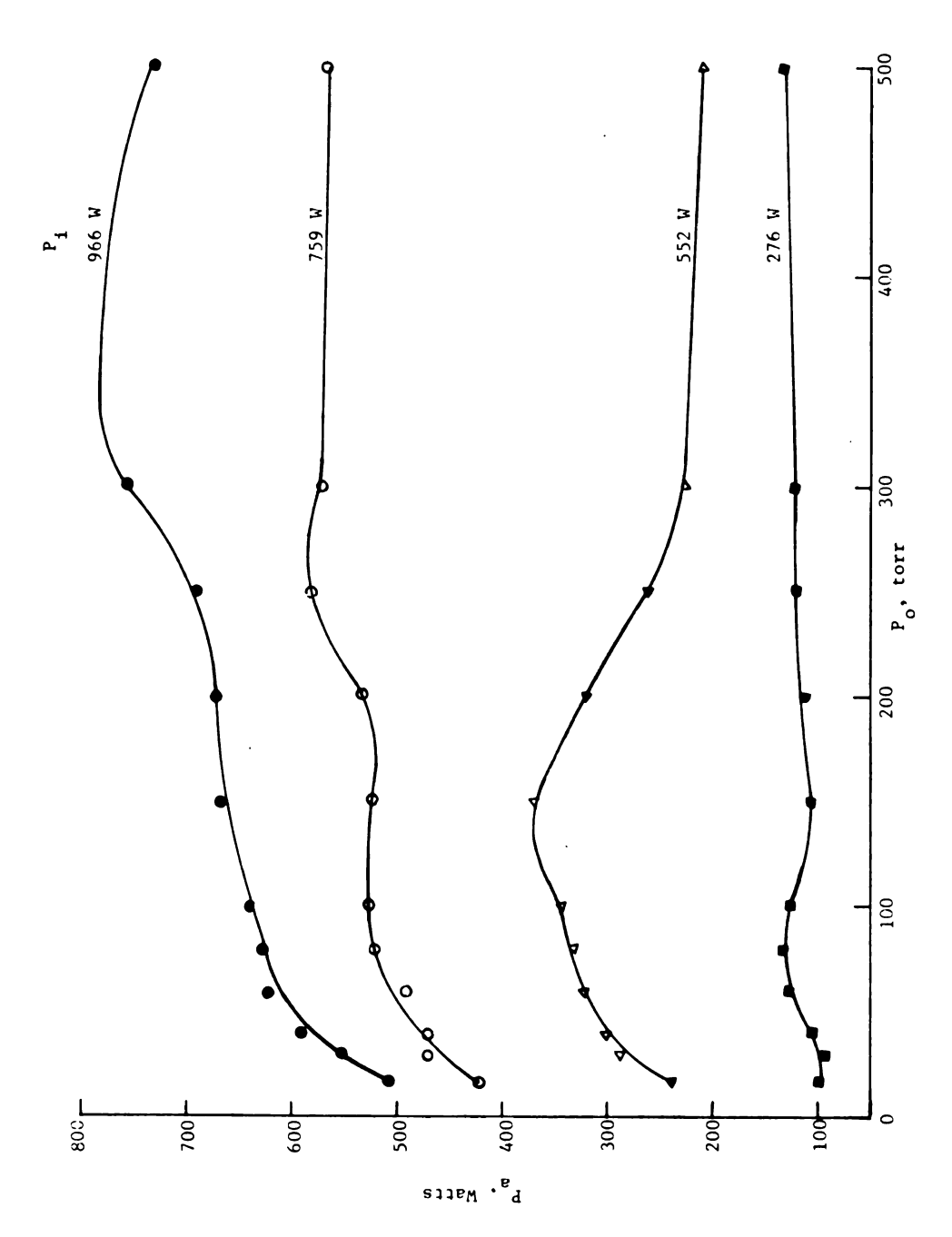


Figure 6.22. Power absorbed P $_{
m a}$ vs. discharge pressure P $_{
m o}$ and incident power P $_{
m I}$ for the T $_{
m L112}^{*}$ mode plasma of Cavity 2. Flow rate = 2500 cc/min. Gas: argon.

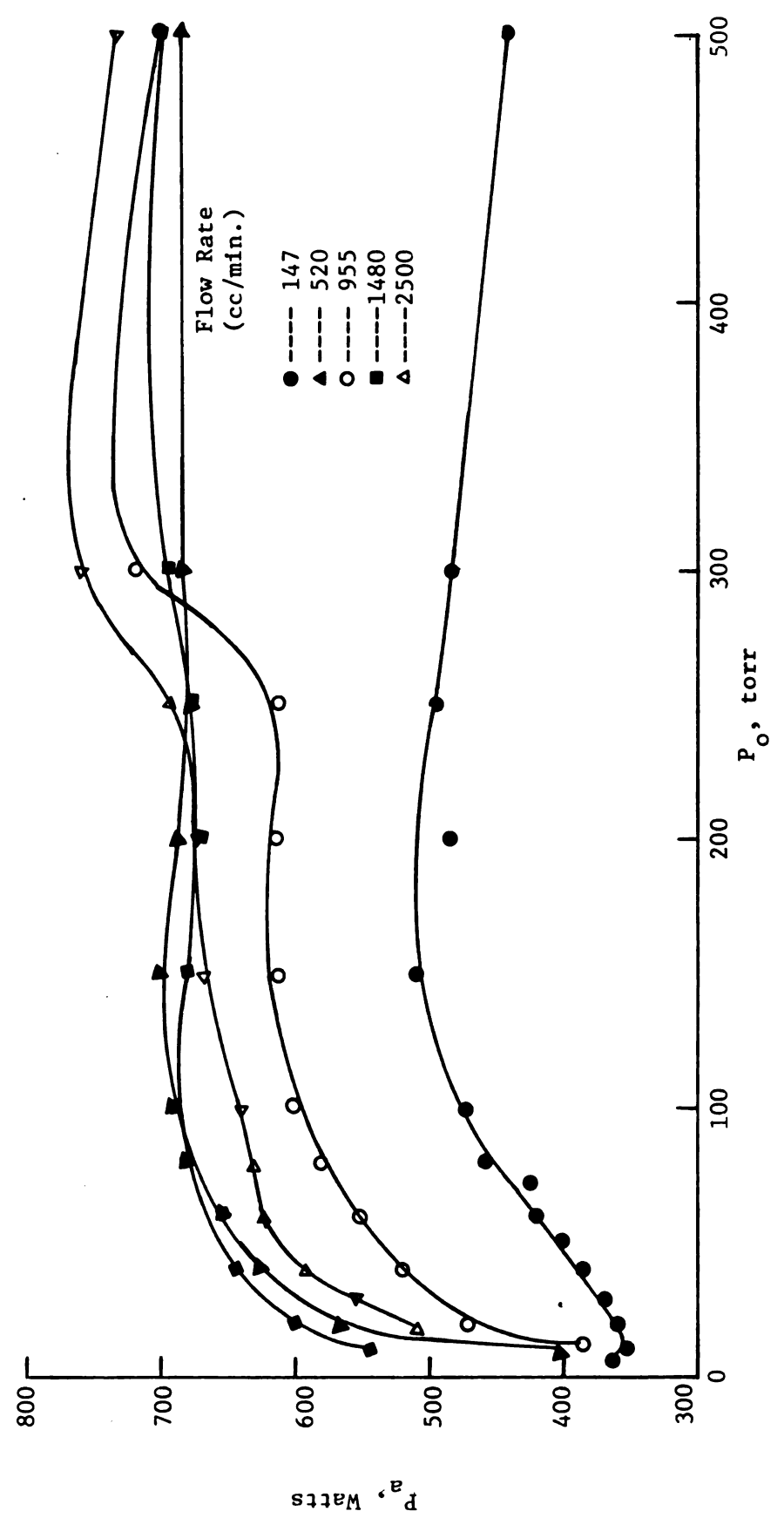


Figure 6.23. Power absorbed P vs. discharge pressure P and flow rate for the TE_{112}^* mode plasma of Cavity 2. Incident power $P_1 = 966$ W. Gas: argon.

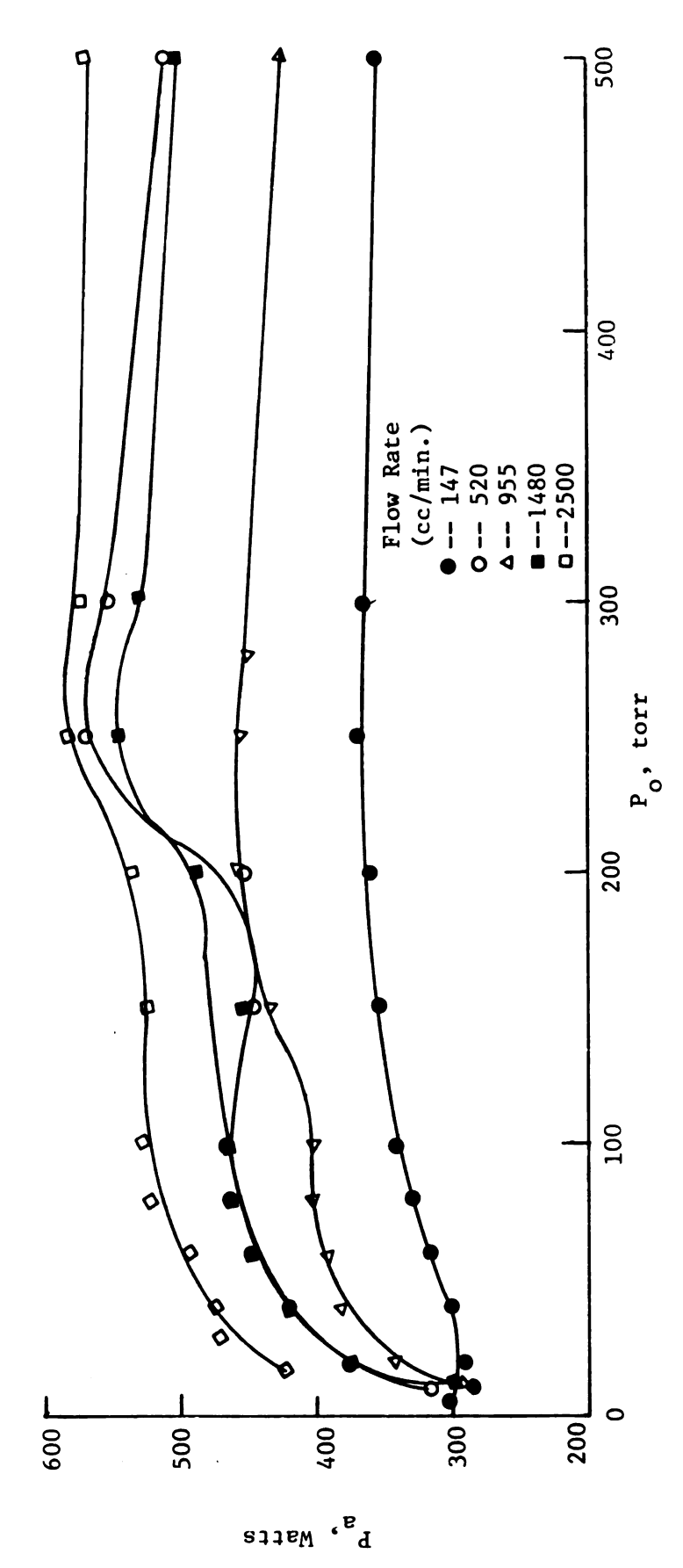


Figure 6.24. Power absorbed P vs. discharge pressure P $_{
m O}$ and flow rate for the T $_{
m 112}^{st}$ mode plasma Gas: argon. of Cavity 2. Incident power P_1 = 759 W.

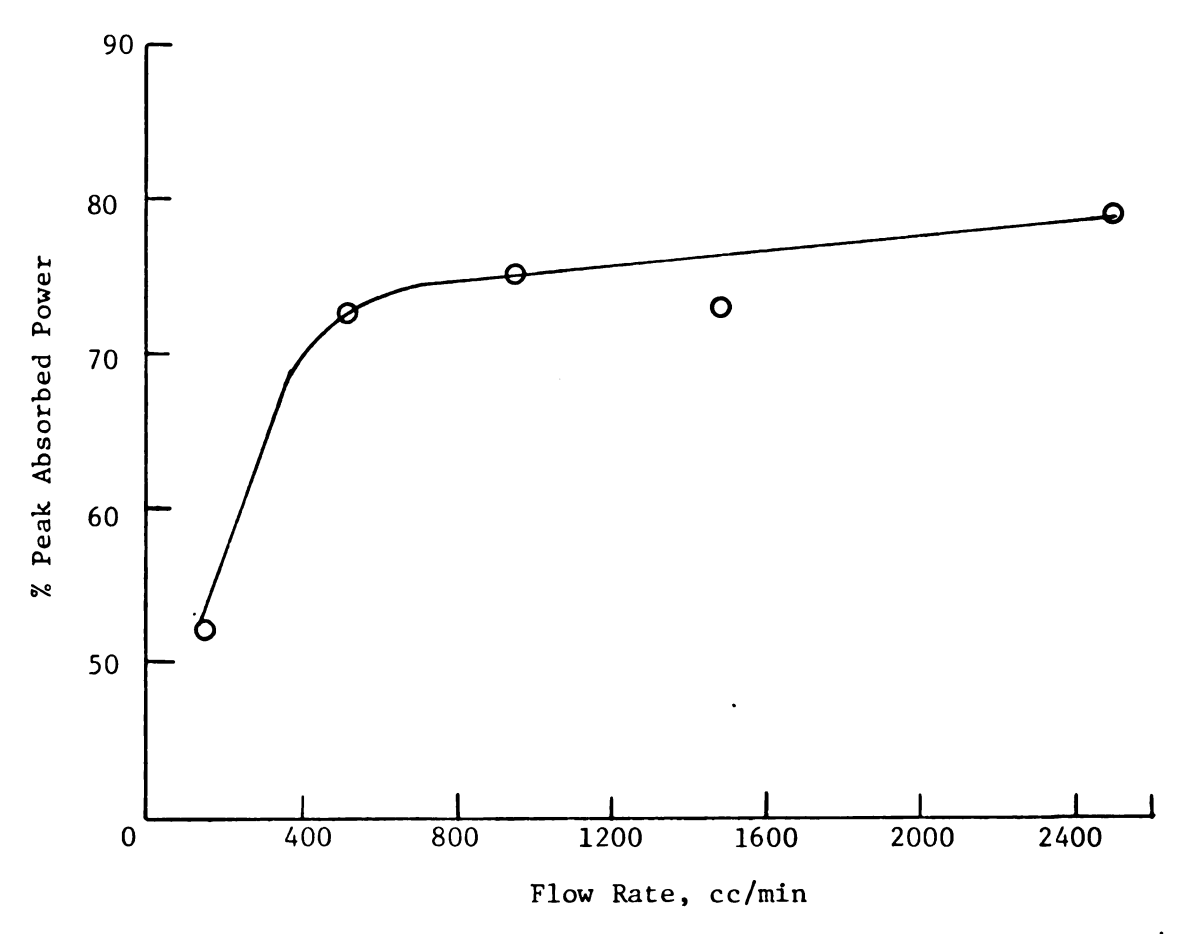


Figure 6.25. Percentage peak-absorbed power vs. flow rate for the TE_{112}^* plasma of Cavity 2. Incident power P_i = 966 W.

6.18 through 6.22. The length of the plasma-cavity during operation was held constant at $L_s = 13$ cms.

A study of the curves in Figures 6.18 - 6.22, shows that for a given flow rate and incident power, the absorbed power has a relatively flat response vs. the pressure. A minor peak in the absorbed power is seen to be present in all curves for constant flow rates. The pressure at which this peak occurs usually increases with the incident power P_i see Figure 6.22.

It is generally true that for a given incident power, the absorbed power increases with the flow rate. There is an exception to this behavior at a flow rate of 520 cc/min. as demonstrated in Figure 6.24. The curves of Figures 6.23 and 6.24 have been plotted for incident powers of P_1 = 966W and 759W. A plot of the percentage of peak-absorbed power vs. flow rate for a given incident power is shown in Figure 6.25. The curve of Figure 6.25 shows that the peak-absorbed power rises steeply with the flow rate at first and then reaches a saturation level. This behavior is consistent with the increase in peak-absorbed power with flow rate as described for the TE_{011} mode (see Figure 6.16). The saturation of the peak-absorbed power at high flow rates is probably caused by the shielding effect of the boundary plasma layer, as described earlier.

Comparison with other RF Discharges. Similar experiments were performed by Dorman and McTaggert using a resonant cavity and by Bosisio et.al. 4 using a slow wave structure. Their experiments were performed on argon gas for a zero flow rate and the results are shown in Figure 6.26. Dormand and McTaggert worked at 915 MHz and used 250W of applied power. The slow wave structure of Bosisio et.al. employed incident powers of up to 2 KW at a frequency of 2.45 GHz.

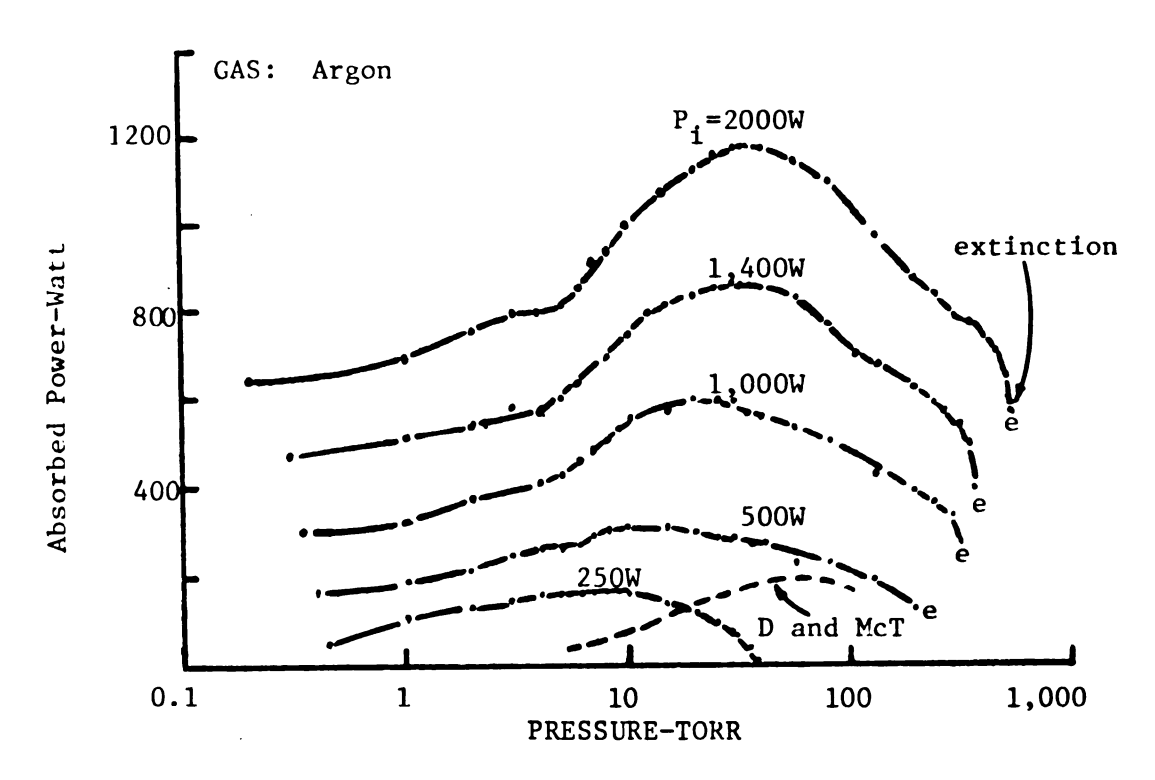


Figure 6.26. Plot of absorbed microwave power vs. pressure for argon plasmas at various incident powers. Reproduced from Bosisio et.al. ⁵⁴.

A comparison of their results with the work performed on Cavity 2 reveals the following:

1) The absorbed power variation as a function of the pressure is more uniform for the TE_{112}^{\star} microwave discharge of Cavity 2 than for a similar type of discharge in the slow wave structure of Bosisio et. al. ⁵⁴. The flat response of the absorbed power curves especially at high pressures or high values of (ν_e/ω) is a result of two phenomena. The first reason for the flat response of the experimental absorbed power curves can be obtained from typical TE_{11}^{\star} absorbed power vs. $\omega/\omega_{\text{pe}}$ curves, shown in Figure 3.6. It is apparent from these curves that the theoretical absorbed power varies very slowly with $(\omega/\omega_{\text{pe}})$ for $(\nu_e/\omega_{\text{pe}}) = 1.0$. This behavior is true for all collision frequencies greater than $(\nu_e/\omega_{\text{pe}}) = 1.0$. Thus, the plasma waveguide itself is not resonant with respect to $(\nu_e/\omega_{\text{pe}})$ and $(\omega/\omega_{\text{pe}})$.

Secondly, the property of the TE^{*}₁₁₂ mode is such that beyond a critical density of 10, there are no resonances in the eigenlength plot, (Figure 4.2), and the shift in eigenlength vs. plasma density and collision frequency is very small. It must be noted that the curves of Figure 3.6 and 4.2 have been derived from a zero flow rate condition and for the waveguide dimensions of Cavity 1. Hence, these curves cannot fully explain the experiments that have been conducted here with a non-zero flow rate. However, they can be used as a qualitative guide to understand how efficiently the incident power can be coupled to the plasma in Cavity 2. The absorbed-power curves of Bosiso et.al. (Figure 6.26) for a non-flowing argon discharge have a fairly distinct peak and this usually occurs at 40 torr. The reason for the occurrence of this absorbed-power peak at such a low pressure is attributed to the type of coupling used in their system.

Argon plasmas in microwave cavities, can be maintained at pressures over an atmosphere. However, in results presented on Cavity 2, experimental limitations prevented the measurement of pressures beyond 500 torr. In experiments conducted on the slow wave structure by Bosisio et.al., the plasma could be sustained only up to a pressure of 500 torr with the incident powers being as high as 2 KW.

2) The absorbed power curves of Cavity 2 clearly show that the coupling of the incident power to the discharge is a function of the gas flow rate. For an incident power of P_i = 966 W, the efficiency of this coupling rises from approximately 50% to as high as 79% as the flow rate increases from 147 cc/min. to 2500 cc/min. (see Figure 6.25). In these experiments, the eigenlength of the cavity mode was held constant at L_s = 13.0 cms. It is possible to couple more than 90% of the incident power to the plasma, by optimizing the length, discharge pressure, and the gas flow rate. Bosisio et.al., in their experiments on non-flowing argon plasmas report a maximum efficiency of 60% using incident powers of up to 2 KW.

Thus, these experiments conducted on Cavity 2 demonstrate that in the ${\rm TE}_{112}^{\star}$ cavity mode, the absorbed power is relatively insensitive to changes in electron density and collision frequency. The incident power can be coupled very efficiently to the plasma. No tuning stubs are required to provide an impedance match between the external microwave system and the cavity.

CHAPTER VII

SUMMARY AND CONCLUSIONS

The electromagnetic behavior of a microwave plasma source has been experimentally examined over a wide range of pressures and flow rates. A qualitative explanation has been provided to account for the experimental results using a linear, lossy, cold plasma theory. The latter theory, however, does not provide a rigorous explanation for the experimental phenomena because of its restriction to: a) small signal linear phenomena, b) ionized gases with a zero flow rate. In spite of its limitations, the theory does take into account losses in the plasma due to electron-neutral particle collisions and thus, explains the pressure dependence of the experimental results.

Three different types of experiments were conducted on the plasma-cavity to demonstrate its use as a versatile microwave plasma source. The linear and non-linear behavior of the plasma cavity in the low-pressure region was examined using Cavity 1. The presence of two plasma density operating points for a single eigenlength in the TE_{111}^{\star} mode was experimentally verified. The coupling of EM energy to the space charge waves was demonstrated and this phenomena was qualitatively explained using the eigenlength vs. $(\omega_{\text{pe}}/\omega)^2$ and (v_{e}/ω) curves obtained from the lossy, linear, cold plasma theory. A more rigorous theory, however, is required to explain the non-linear nature of this coupling mechanism. It was also observed that long plasma columns can be produced in the space charge mode of operation, with the length of the plasma column

increasing as the power input to the cavity was increased. Short wavelength standing waves of the TM_{00p} mode were also generated in the plasma cavity.

Further non-linear phenomena in the form of sidebands were detected in the reflected power spectrum of the ${\rm TE}_{111}^{\star}$ mode plasma of Cavity 1. One set of these sidebands was qualitatively explained as being caused by a fluctuation in the average plasma density as a function of time, i.e., a shift in the operating point along a constant resonant length line of the ${\rm TE}_{111}^{\star}$ mode. The reason for the occurrence of the other set of sidebands was not clearly determined and an examination of the theory of the interaction of strong RF fields with bounded plasmas may explain the latter instability.

An effective electric field vs. discharge pressure (40 mtorr-20 torr) was evaluated in the TE_{111}^{\star} mode plasma of Cavity 1, by measuring the plasma parameters N_o and T_e . The TM_{010} frequency shift method, double floating probe and disc techniques were employed to determine these parameters. The probe and disc methods yielded results that were representative of the orders of magnitude of the plasma parameters and not their exact values. The shape of the N_o , T_e , E_e and E_e/p vs. pressure curves followed the same general variation with pressure as those exhibited by Maksimov and Bell in He gas. The effect of microwave radiation on the probe and disc characteristics needs to be examined further. Plasma diagnostics on Cavity 2 using the conventional techniques proved to be unsuccessful. The TM_{010} frequency shift method and the probe techniques failed as a result of the high pressures and power levels employed in Cavity 2. Furthermore, the probes coupled significant amounts of power from the cavity into the surroundings and presented a

safety hazard. Thus, more sophisticated techniques, such as plasma spectroscopy, are needed to evaluate the plasma parameters of Cavity 2.

The absorbed power characteristics of the microwave plasma source were examined over a wide range of pressures, flow rates and incident power levels. These experiments were conducted on a length dependent mode (TE₀₁₁) and in the length independent region of the TE₁₁₁ mode. The absorbed power characteristics of a flowing plasma were shown to be significantly different from those of a non-flowing plasma. The absorbed power was shown to increase directly as a function of the flow rate at low flow rates and then reach a saturation at high flow rates. This phenomena was qualitatively explained as being caused by the shielding effect of the plasma layer adjacent to the quartz tube. Thus, the bypass region of the cavity quartz tube needs to be reduced to prevent saturation of the absorbed power at high flow rates. Also, a more exact theory incorporating the velocity of the ionized gas needs to be derived to fully explain the absorbed power characteristics of a flowing plasma.

The absorbed power variation as a function of the pressure of the microwave cavity discharge was found to be more uniform than a similar type of discharge in the slow wave structure of Bosisio et.al. ⁵⁴ The incident power could be coupled very efficiently to the plasma and no tuning stubs were required to provide an impedance match between the external microwave system and the cavity. The slow wave structure of Bosisio et.al. ⁵⁴ absorbed a maximum of 60% of the incident power and a plasma could not be sustained beyond a pressure of 500 torr. In the plasma cavity, it was possible to couple more than 90% of the incident power to the plasma by optimizing the length, discharge pressure, and gas flow rate. Operation of this plasma cavity beyond 1 atm. has been observed.

Thus, the microwave plasma source described in this thesis has been shown to operate efficiently over a wide range of pressures, flow rates, incident power levels and in different electromagnetic modes. This source has been shown to be amenable to plasma diagnostics at low power levels and for pressures up to 20 torr. At high pressures and high power levels it should be possible to conduct diagnostics using spectroscopic techniques. The simplicity of the plasma cavity structure has made it possible to conduct a linear electromagnetic analysis of the microwave plasma source, incorporating the collisional losses within the plasma.



APPENDIX A

In this appendix, the numerical techniques used in evaluating the roots of the characteristic equation of a cylindrical waveguide partially filled with a cold, lossy, isotropic plasma (See equation 2.62), are briefly discussed. A study of equation 2.62, reveals that this equation is transcendental in nature and involves Bessel functions with complex arguments. A main program and two subroutines are used to evaluate the roots of this equation.

FROOT is a subroutine that searches for roots of the transcendental equation F(Z) = 0 by an iterative process. The argument Z is, in general, complex. COMBES is a subroutine that evaluates the real and imaginary parts of a Bessel function for a given order and complex argument. DIS-PERSION is a main program which together with FROOT and COMBES evaluates a typical $\omega - \beta$ or $\omega - \alpha$ diagram (See Chapter II), i.e., it obtains the complex propagation constant k_Z for a given frequency ω , as a function of the plasma parameters ω_{pe} and ν_e . HYBRIDMODE is another main program which together with FROOT and COMBES obtains the eigenlength for a given cavity mode as a function of ω_{pe} and ν_e , with the driving frequency ω fixed (See Chapter IV).

An initial guess value for a given mode is required to obtain the dispersion curves of Chapter II or the eigenlength plots of Chapter IV. For example, to evaluate the eigenlength curves of the ${\rm TE}_{011}$ cavity mode (Figure 4.2), the value of ${\rm k}_{\rm z}$ corresponding to the empty cavity resonant length of this mode is used as the initial guess value. The ${\rm TE}_{011}$ curve

for a given v_e/ω is then obtained for different values of $(\omega_{pe}/\omega)^2$ by increasing $(\omega_{pe}/\omega)^2$ in small increments. The size of the increment depends on the value of the gradient of the curve at a given point and, therefore, on the ability of FROOT to converge. The size of the increment is decreased until convergence is eventually obtained. The resonant length of the TE_{011} curve at high values of $(\omega_{pe}/\omega)^2$ and for a given v_e/ω is then compared with the resonant length of the corresponding TE_{011} coaxial cavity mode. These two values are found to match. Thus, the empty cavity and coaxial cavity resonant lengths of a given mode serve as checkpoints in determining the accuracy of the numerical solutions.

LIST OF REFERENCES

LIST OF REFERENCES

- 1. S. C. Brown, <u>Basic Data in Plasma Physics</u>, Cambridge, Massachusetts, MIT Press (1959).
- 2. F. K. McTaggart, <u>Plasma Chemistry in Electrical Discharges</u>, London, England: Elsevier (1967).
- 3. A. I. Maksimov, Sov. Phys.-Tech. Phys., 11, 1116 (1967).
- 4. A. J. Hatch, "Plasma Heating and Confinement Controlled Nuclear Fusion," in Microwave Power Engineering, Vol. II.
- 5. R. G. Bosisio, C. F. Weissfloch and M. R. Wertheimer, J. Micr. Power, 7(4), 325 (1972).
- 6. F. C. Fehsenfeld, K. M. Evenson, and H. P. Broida, Rev. Sci. Instrum., 36, 294 (1965).
- 7. A. I. Maksimov, Sov. Phys.-Tech. Phys., 11(10), 1316 (1967).
- 8. F. H. Dorman and F. K. McTaggart, J. Micr. Power, 5, 4 (1970).
- 9. D. J. Rose and S. C. Brown, J. Appl. Phys., 23, 1028 (1952).
- 10. J. Asmussen, R. Mallavarpu, J. R. Hamann and H. C. Park, Proc. IEEE, 62, 109 (1974).
- 11. W. P. Allis, S. J. Buchsbaum, A. Bers, <u>Waves in Anisotropic Plasmas</u>, Cambridge, Massachusetts, MIT Press (1963).
- 12. A. W. Trivelpiece, Slow Wave Propagation in Plasma Waveguides, San Francisco Press (1967).
- 13. B. Agdur and B. Eneander, J. Appl. Phys., 33, 575 (1962).
- 14. J. L. Shohet and C. Moskowitz, J. Appl. Phys., 36, 1756 (1965).
- 15. P. Diament, V. L. Granatstein and S. P. Schlesinger, J. Appl. Phys., 37, 1771 (1966).
- 16. P. E. Vandenplas, <u>Electron Waves and Resonances in Bounded Plasmas</u>, John Wiley, (1968).
- 17. R. M. Fredericks, Ph.D Dissertation, Michigan State University (1971).

- 18. R. F. Harrington, <u>Time-Harmonic Electromagnetic Fields</u>, McGraw-Hill, 1961.
- 19. D. E. Baldwin, Phys. Flds., 12, 279 (1969).
- 20. S. C. Brown and D. J. Rose, J. Appl. Phys., 23, 711, 719, 1028 (1952).
- 21. P. Leprince, Laboratoire de Physique des Plasmas Rapport L. P. 100, University of Paris (1969).
- 22. M. Moisan, C. Beaudry and P. Leprince, IEEE Trans. Plasma Science, PS-3 (2), 55 (1975).
- 23. R. K. M. Landshoff, The Plasma in a Magnetic Field, Stanford University Press, 1958.
- 24. J. E. Butterworth and R. L. Moore, J. Appl. Phys., 40, 5076 (1969).
- 25. B. Kezar and P. Weissglas, J. Appl. Phys., 36, 2479 (1965).
- 26. S. J. Buchsbaum, L. Mower, and S. C. Brown, Phys. Fluids, 35, 806 (1960).
- 27. M. A. W. Vlachos and H. C. S. Hsuan, J. Appl. Phys., 39, 5009 (1968).
- 28. C. J. Burkley and M. C. Sexton, J. Appl. Phys., 39, 5013 (1968).
- 29. C. C. Johnson, Field and Wave Electrodynamics, McGraw-Hill, 1965.
- 30. E. Johnson and L. Malter, Phys. Rev., 8(1), 56(1950).
- 31. J. L. Altman, Microwave Circuits, Princeton, N.J.: Van Nostrand, 1964.
- 32. G. I. Babat, J. Inst. Elec. Eng., 94, 27 (1947).
- 33. P. D. Francis, J. Appl. Phys., 5, 235 (1972).
- 34. L. D. Pleasance and E. V. George, Appl. Phys. Lett., 18, 557 (1971).
- 35. K. B. Persson, Phys. Rev., 106, 191 (1957).
- 36. S. J. Buchsbaum and S. C. Brown, Phys. Rev., 106, 196 (1957).
- 37. I. M. Cohen, Phys. Fluids, 6 (10), 1492 (1963).
- 38. I. M. Cohen, AIAA Journal, 5 (1), 63 (1967).
- 39. R. H. Huddlestone and S. L. Leonard, <u>Plasma Diagnostic Techniques</u>, Academic Press, 1965.
- 40. S. Glasstone and R. H. Loveberg, <u>Controlled Thermonuclear Reactions</u>, D. Van Nostrand Company, Inc., 1960.

- 41. F. W. Crawford, J. Appl. Phys., 34, 1897 (1963).
- 42. A. Garscadden and Emeleus, Proc. Phys. Soc. (London) 79, 535 (1962).
- 43. F. F. Chen, Rev. Sci. Instr. 35, 1208 (1964).
- 44. M. Sugawara and Y. Hatta, Inst. Plasma Phys. (Nagoya Univ., Japan), Res. Rept. No. IPPJ-4 (1963).
- 45. A. Boschi and F. Magistrelli, Nuovo Cimento 29, 487 (1963).
- 46. A. Cantin and R. R. J. Gagne', IEEE Trans. Antennas Propagation AP-16, 279 (1968).
- 47. R. R. J. Gagne' and A. Cantin, J. Appl. Phys., 43 (6), 2639 (1972).
- 48. C. Ramsauer and R. Kollath, Ann. Physik 3, 536 (1929).
- 49. L. S. Frost and A. V. Phelps, Phys. Rev. 136, A1538 (1964).
- 50. R. F. Whittmer and G. F. Herrman, Phys. Fluids, 9 (4), 768 (1966).
- 51. J. Taillet, Am. J. Phys., 37, 423 (1969).
- 52. A. M. Messian and P. E. Vandenplas, Phys. Fluids, 12, 2406 (1969).
- 53. T. B. Reed, J. Appl. Phys., 32, 821 (1961).
- 54. R. G. Bosisio, M. Nachmann, and J. Spooner, IEEE Trans. on Plasma Science, PS-2 (4), 273 (1974).
- 55. A. T. Bell, I & EC Fundamentals, 9 (1), 160 (1970).

MICHIGAN STATE UNIV. LIBRARIÉS
31293008217881